DETERMINATION AND CHARACTERIZATION OF ICE PROPAGATION MECHANISMS ON SURFACES UNDERGOING DROPWISE CONDENSATION

A Dissertation

by

JEFFREY BRANDON DOOLEY

Submitted to the Office of Graduate Studies of
Texas A&M University
in partial fulfillment of the requirements for the degree of

DOCTOR OF PHILOSOPHY

May 2010

Major Subject: Mechanical Engineering

DETERMINATION AND CHARACTERIZATION OF ICE PROPAGATION MECHANISMS ON SURFACES UNDERGOING DROPWISE CONDENSATION

A Dissertation

by

JEFFREY BRANDON DOOLEY

Submitted to the Office of Graduate Studies of
Texas A&M University
in partial fulfillment of the requirements for the degree of

DOCTOR OF PHILOSOPHY

Approved by:

Chair of Committee,	Dennis L. O'Neal
Committee Members,	Debjyoti Banerjee
	Sarah D. Brooks
	Thomas R. Lalk
Head of Department,	Dennis L. O'Neal

May 2010

Major Subject: Mechanical Engineering

ABSTRACT

Determination and Characterization of Ice Propagation Mechanisms on Surfaces Undergoing Dropwise Condensation. (May 2010)

Jeffrey Brandon Dooley, B.S., Texas A&M University;
M.S., Texas A&M University
Chair of Advisory Committee: Dennis L. O'Neal

The mechanisms responsible for ice propagation on surfaces undergoing dropwise condensation have been determined and characterized. Based on experimental data acquired non-invasively with high speed quantitative microscopy, the freezing process was determined to occur by two distinct mechanisms: inter-droplet and intra-droplet ice crystal growth. The inter-droplet crystal growth mechanism was responsible for the propagation of the ice phase between droplets while the intra-droplet crystal growth mechanism was responsible for the propagation of ice within individual droplets. The larger scale manifestation of these two mechanisms cooperating in tandem was designated as the aggregate freezing process.

The dynamics of the aggregate freezing process were characterized in terms of the substrate thermal diffusivity, the substrate temperature, the free stream air humidity ratio, and the interfacial substrate properties of roughness and contact angle, which were combined into a single surface energy parameter. Results showed that for a given thermal diffusivity, the aggregate freezing velocity increased asymptotically towards a constant value with decreasing surface temperature, increasing humidity, and decreasing surface energy. The inter-droplet freezing velocity was found to be independent of substrate temperature and only slightly dependent on humidity and surface energy. The intra-droplet freezing velocity was determined to be a strong function of substrate temperature, a weaker function of surface energy, and independent of humidity. From the data, a set of correlational models were developed to predict the three freezing velocities in terms of the independent variables. These models predicted the majority of the measured aggregate, inter- and intra-droplet freezing velocities to within 15%, 10%, and 35%, respectively.

Basic thermodynamic analyses of the inter- and intra-droplet freezing mechanisms showed that the dynamics of these processes were consistent with the kinetics of crystal growth from the vapor and supercooled liquid phases, respectively. The aggregate freezing process was also analyzed in terms of its constituent mechanisms; those results suggested that the distribution of liquid condensate on the surface has the largest impact on the aggregate freezing dynamics.

To Noreen, McKenna, and Shaylen, and to my parents J.B. and Virginia

ACKNOWLEDGMENTS

I wish to express sincere gratitude to my advisor, Dr. Dennis O'Neal, for recruiting me into the graduate program in mechanical engineering at Texas A&M and for his unwavering support and guidance throughout the course of my studies. I'm particularly grateful for the considerable freedom he provided me in all phases of my research as well as the friendship we forged along the way. I also extend my heartfelt appreciation to Dr. Debjyoti Banerjee, Dr. Sarah Brooks, and Dr. Tom Lalk for serving on my committee.

A number of other people within the mechanical engineering department are due special thanks as well: Bernie Koronka, Peggy McCarty, Dori Wilson, Mitch Wittneben, Brian Bachmeyer, Johnny Hallford, and the late Mike Walker all provided invaluable assistance and support for me and my research program at various junctures.

I would like to thank Bonnie Stern for helping me to organize the plethora of data I generated in my studies, Juan Cornejo for assisting me with some of the day-to-day operations in my lab during those times when I could not be there, and Matt Bell for his extensive efforts in helping to prepare and characterize the test surfaces used in this study.

I gratefully acknowledge the professional opportunities afforded to me by Heat Transfer Research, Inc. (HTRI) in College Station. Since joining the technical staff at HTRI, I have learned a great deal about industrially-focused research and software development from a cache of very talented technicians and engineers. I offer my sincere thanks to each of them for offering their support and encouragement to me throughout my doctoral studies.

Finally, words cannot begin to express the profound appreciation I have for my wonderful family and the love and support they have directed at me throughout this arduous journey. In particular, I wish to thank my uncle, Martin Reese Luhn II, for helping to foster my love of learning, my sister, Gayle Dooley Rodgers, for her uncompromising support throughout my life, and of course my parents, J.B. and the late Virginia Harris Dooley, for not only their love, but also the sacrifices they both made to ensure I was able to attend college. Above all, I thank my wife Noreen for her steadfast love, patience, and support, and our two beautiful daughters, McKenna and Shaylen, for never failing to remind me of what is most important in life.

NOMENCLATURE

A	area (m^2)
$\mathbf{A}$	matrix representation of digital image
$\hat{\mathbf{A}}$	matrix representation of binary image
a_{ij}	components of $\mathbf{A}$
a_1-a_8	constants
Bi	Biot number $\left(\frac{h\delta_0}{k}\right)$
Bi$_m$	Mass transfer Biot number $\left(\frac{h_m\delta_0}{\mathcal{D}_m}\right)$
C	heat capacity (J/K)
C_n	correlating parameter
$\mathbf{C}$	image calibration matrix
C_1-C_9	correlating parameters (Equations 5.9, 5.11, and 5.14)
D	diameter (m)
$\bar{D}_k$	average droplet diameter (μm)
$\mathcal{D}$	diffusion coefficient (m^2/s)
d	diameter; displacement; thickness (m)
$\mathcal{E}_{ad}$	activation energy barrier for molecular adsorption (J)

f	focal length (m)
f_{ad}, f_{ds}	unit area molecular adsorption/desorption flux (s^{-1})
f_w	surface roughness contact area ratio (*dimensionless*)
G	Gibbs free energy (J)
g	specific Gibbs free energy (J/g)
H	enthalpy (J)
h	specific enthalpy (J/g); heat transfer coefficient ($\mathrm{W/m^2{\cdot}K}$)
$\hat{h}$	molecular enthalpy (J/molecule)
Ja	Jakob number $\left(\frac{c_p \Delta T}{h_{lv}}\right)$
K	number of droplets detected within ROI
K_T	kinetic coefficient (m/s·K)
$\hat{K}$	proximal droplet count
k	thermal conductivity (W/m·K)
k_B	Boltzmann's constant ($= 1.38066 \times 10^{-23}$ J/K)
$\mathcal{L}$	latent heat of formation (J)
$\hat{l}$	molecular latent heat of formation (J/molecule)
ℓ_r	latent heat conduction length scale (m)
M	magnification power (*dimensionless*)
m	mass (g)

$\dot{m}$	mass flow rate (kg/s)
N	number
n	mean number density (m^{-3}); refractive index (*dimensionless*)
$\mathbf{n}$	unit normal vector (*dimensionless*)
$N.A.$	numerical aperture (*dimensionless*)
P	pressure (N/m^2)
$\mathcal{P}$	probability
p	generic field variable
Q	heat transfer (J)
$q'', \mathbf{q}''$	heat flux (**vector**) (W/m^2)
R, r	radius (m)
R^2	coefficient of determination
R_a	average surface roughness (μm)
R_{res}	optical resolution (μm)
$\mathbf{R}_k^n$	vector of droplet center x, y coordinates
$\hat{\mathcal{R}}_{k\rightarrow\hat{k}}$	set of inter-droplet spacings (μm)
r_c	inter-droplet ice crystal tip position (μm)
$\bar{r}_k$	average droplet radius (μm)
$\hat{r}_{k\rightarrow\hat{k}}$	discrete center-to-center droplet spacing (μm)

r_{sl}	intra-droplet ice front position (μm)
r_ψ	spatial proximity (μm)
Re_x	local Reynolds number $\left(\frac{U_\infty x}{\nu}\right)$
RH	relative humidity (%)
S	entropy (J/K); separation distance (m); sample standard deviation
S_m	microscope focal plane position (m)
$\bar{S}$	sample standard error
s	specific entropy (J/g·K)
$\hat{s}$	molecular entropy (J/molecule·K)
SSD	supersaturation degree, (*dimensionless*)
T	temperature (K)
t	time (s); value from t-distribution
t_ψ	temporal surface (s)
U	velocity (m/s); internal energy (J)
$\mathcal{U}_b$	bias limit for overall uncertainty interval $\mathcal{U}_Y$
$\mathcal{U}_p$	precision limit for overall uncertainty interval $\mathcal{U}_Y$
$\mathcal{U}_Y$	overall uncertainty interval for variable Y
u	specific internal energy (J/g); generic field variable
V	velocity (m/s); volume (m^3)

$\mathbf{V}, \mathbf{v}$	velocity vectors (m/s)
$\bar{V}_n$	average aggregate freezing velocity (μm/s)
$\mathcal{V}$	velocity (μm/s)
v	velocity (m/s); specific volume, (m^3/kg)
v_c	instantaneous inter-droplet crystal growth velocity (μm/s)
v_{HK}	crystal growth rate given by Hertz-Knudsen formula (Equations 6.28, 6.30, 6.31 and 6.32) (μm/s)
v_{WF}	crystal growth rate given by Wilson-Frenkel formula (Equations 6.19 and 6.20) (μm/s)
$\hat{v}$	discrete velocity (μm/s)
$\hat{v}_{k,\bar{D}}$	discrete inter-droplet freezing velocity based on $\bar{D}_k$ (μm/s)
$\hat{v}_{k\rightarrow\hat{k}_\psi}$	discrete center-to-center droplet freezing velocity (μm/s)
$\hat{v}_{\Delta\hat{r}}$	discrete inter-droplet freezing velocity (μm/s)
$\bar{v}_c$	average inter-droplet crystal growth velocity (μm/s)
$\bar{v}_{k,\bar{D}}$	average inter-droplet freezing velocity (μm/s)
$\bar{v}_{sl}$	average intra-droplet crystal growth velocity (μm/s)
$\mathbb{X}$	droplet freezing history data structure
x	coordinate or distance (m); mass fraction (*dimensionless*)
Y	arbitrary measured variable

$\bar{Y}$	mean value of sample set Y_i
y	coordinate or distance (m)
z	coordinate or distance (m)

Greek Symbols

α	thermal diffusivity (m^2/s)
α_{cond}	condensation coefficient (*dimensionless*)
β	angle (°)
Γ	interface (m)
γ	surface tension (N/m)
Δr	local inter-droplet spacing (μm)
$\Delta \hat{r}_{k \rightarrow \hat{k}_{\psi}}$	discrete edge-to-edge inter-droplet spacings (μm)
ΔT	supercooling degree (K)
Δt	time step (s)
$\Delta \hat{t}_{k \rightarrow \hat{k}}$	discrete inter-droplet freezing time (s)
$\Delta \hat{\tau}_{k \rightarrow \hat{k}}$	set of inter-droplet freezing times (s)
$\Delta \hat{v}_{k,\bar{D}}$	bin width for inter-droplet freezing velocity distribution (μm)
Δx_{ψ}	variable unit length (μm)
δ	thickness; displacement (m)
ϵ	average inter-droplet velocity cutoff threshold (%)

ϵ_f	depth of focus (μm)
ζ	generic variable
η	viscosity (N·s/m^2); generic variable
Θ_0, Θ_1	correlating offset parameters (Equations 5.8 and 5.13) (*dimensionless*)
θ	angle; contact angle (°)
θ_{app}	apparent contact angle (°)
θ_{ave}	volume-averaged contact angle (°)
θ_c	effective contact angle (°)
θ_w	corrected contact angle (°)
κ	curvature (μm^{-1})
λ	latent heat (J/g·K); wavelength (nm)
μ	chemical potential (J/molecule)
ν	molecular vibrational frequency (s^{-1}); kinematic viscosity (m^2/s)
ξ	pixel intensity threshold
ρ	density (kg/m^3)
σ	supersaturation ratio (*dimensionless*)
ϕ	angle; half-angle (°)
$\mathbf{\Psi}_k^n$	vector of droplet states (frozen or unfrozen)
ψ	droplet state (frozen or unfrozen)

Ω	area or domain (m^2)
ω	absolute humidity ratio (g/kg)

Superscripts

$*$	reference value
n	frame number

Subscripts

0	reference value
∞	ambient or free stream value
a, b	mediums a or b
β	ice phase
γ	air-water vapor phase
$cond$	condensation; condensate
d	droplet
dew	dew point
f	frost; final
fus	fusion
i	ice phase; incidence; initial; general index
$inter$	inter-droplet
$intra$	intra-droplet

j	general index; phase j
$k, \hat{k}$	droplet k or $\hat{k}$
l	liquid phase; lower
lv	liquid-to-vapor
M	phase equilibrium condition
m	mass; mass transfer; molecular
max	maximum
min	minimum
n	normal; frame number
$norm$	normalized
N, T	normal or tangential component
r	refracted
ROI	region of interest
s	surface or substrate; solid phase
sat	saturated
sl	solid-to-liquid
sv	solid-to-vapor
td	target droplet
u	upper

v	vapor
w	water

Abbreviations

CNT	carbon nanotubes
DACS	data acquisition and control system
HVAC	Heating, ventilating, and air-conditioning
ISF	isotropic superfinishing
LED	light emitting diode
PID	proportional-integral-derivative
RSS	root-sum-square
TFT	thin-film thermocouple

TABLE OF CONTENTS

CHAPTER Page

LIST OF TABLES

LIST OF FIGURES

FIGURE Page

FIGURE Page

CHAPTER I

INTRODUCTION

When an object below 0°C is exposed to humid air, frost will eventually form on its surface. Well known for its numerous (and often beautiful) manifestations in nature, frost is also a common feature or by-product of many engineered products or processes. Heat exchangers, airfoils, electrical power lines, road surfaces, and pipelines represent a broad class of engineering devices or systems that may be affected by the presence of frost or ice. Refrigerant-to-air heat exchangers commonly employed in heating, ventilating, and air conditioning (HVAC) applications offer a prime example. Because many heat exchangers of this type are designed to operate in humid air streams, frosting conditions are likely to exist if refrigerant temperatures are below 0°C. Unfortunately, frost accumulation on heat exchangers generally degrades performance by obstructing airflow and insulating the heat transfer surface; the combination of these effects can reduce heat exchanger performance by as much as 75% [1].

In broad terms, the physical structure of frost can be described as a collection of interwoven ice crystals which grow outward from the substrate on which it forms, ultimately producing a porous, three-dimensional matrix. In air temperatures below the triple point of water, frost tends to form on surfaces as the result of ice deposition directly from the vapor phase. For air temperatures above the triple point, the development of frost may be preceded by condensation of an intermediate supercooled liquid phase (often in the form of discrete droplets) that subsequently freezes to form an ice sub-layer [2]. The former process is often referred to simply as *deposition* while the latter is commonly known as *condensation frosting* [3]. The combination of

---

The journal model is the *AIAA Journal of Thermophysics and Heat Transfer.*

air conditions and surface properties encountered in many industrial applications is usually more conducive to condensation frosting than deposition. Despite the considerable differences in the incipient stages of each scenario, the macrostructures of fully developed frost resulting from both processes share many similarities. As a result, the impact of frost on the overall thermal problem has generally been presumed to be independent of the initial growth mechanism. Thus, the vast majority of engineering research conducted in this area during the last several decades has largely overlooked the incipient mechanism and focused on the later stages of frost growth and its resulting impact on device performance.

Analytical and experimental studies devoted to modeling the frost growth process are abundant [4–23]. Historically, the scope of this research has been geared toward empirically correlating parameters such as frost layer thickness, thermal conductivity, and density with environmental variables and time. While many of these studies have aided the design engineer by providing methods to predict thermal performance under frosting conditions, they offer little insight into the phenomena affecting the initial stages of frost formation and how the early stages may affect the overall frost formation process. Because the spatial and temporal connections between a mature frost layer and its underlying substrate lie within these so-called early stage occurrences, it stands to reason that research aimed at mitigating or even preventing frost formation should necessarily consider the earliest stage when frost just begins to form.

Surprisingly, there are relatively few investigations which consider the earliest stages of frost formation exclusively. One reason for this disproportionality stems from the fact that a primary interest in frost research to date seems to have been in characterizing, not necessarily preventing, the formation of frost. But another, and perhaps more pertinent, reason is that the physical mechanisms governing condensation, ice nucleation, and deposition on surfaces are intrinsically microscopic, a fact that tends to complicate rigorous experimental and theoretical analyses. Of the known studies dedicated solely to the early periods, most are either largely qualitative in nature or only consider the inceptive stages indirectly [2, 24–26]. A few investigations have specifically assessed the impact that the liquid precursor phase has on the later stages of the condensation frosting process [27–29]; however, the general emphasis in these studies was placed more on the distribution of the condensate rather than the actual inception of the ice phase.

In the study of early stage phenomena, the condensation frosting process is of considerable interest because the liquid phase that exists prior to the formation of frost represents the medium in which ice first appears on the surface. In fact, frost cannot grow at all until the liquid condensate freezes. For many surfaces, the morphology of the initial liquid phase manifests as the result of dropwise condensation. Accordingly, the surface may be covered with numerous liquid droplets that grow through coalescence with neighboring droplets or through continued condensation from the vapor phase [30]. Because the temperature of the surface is below freezing, these droplets exist in a metastable, supercooled state. When a given droplet finally nucleates to ice, a surprising event transpires: freezing is subsequently triggered in the surrounding droplets. As each droplet freezes, it in turn induces freezing in its unfrozen neighbors and so on. The resulting “chain reaction” migrates along the surface in the form of a bulk freezing front that demarcates a boundary on the surface where frost can and cannot form. This phenomenon has been observed by other researchers [2, 27], but the mechanisms responsible for it are not currently understood and, to the author’s knowledge, have not been studied. Because ice propagation in this manner represents a truly incipient event (i.e. a localized transition to the solid phase), a considerable amount of insight into the earliest stage of frost formation stands to be gained from further study of it.

The purpose of this study was to determine and characterize the mechanisms responsible for ice propagation between naturally occurring condensate droplets on horizontal surfaces. To satisfy this objective, a high speed digital microscopy system was employed to non-invasively probe the small length and time scales associated with ice inception and propagation within and between discrete liquid droplets. In addition, a novel visualization technique was developed which allowed the aggregate and discrete motions of inter-droplet freezing fronts to be tracked and quantified. This work has revealed previously unknown details about the inception and propagation of the solid ice phase on cold surfaces when both the liquid and vapor parent phases are present. Collectively, this research should increase the overall understanding of the inceptive stages of frost formation and serve as a basis for future studies. It is also hoped that this research will eventually contribute towards a more generalized frost model and better ice and frost control or prevention strategies.

This dissertation is divided into seven chapters. Chapter II presents a review of supporting background material and pertinent literature. Chapter III describes the apparatus and general operating procedures developed for the experimental portion of the work. Chapter IV outlines the data reduction and analysis procedures, including an overview of a new visualization technique conceived specifically for tracking aggregate and inter-droplet ice propagation during nucleation. Chapter V presents the reduced data as well as a set of correlational methods which characterize the freezing dynamics in terms of environmental and surface parameters. Chapter VI provides an analysis of the thermophysics associated with the underlying mechanisms. Chapter VII rounds out this investigation with the overall conclusions and recommendations for future work.

CHAPTER II

BACKGROUND AND LITERATURE REVIEW

The study of frost has been an active area of research for over 60 years and numerous models and experimental data have been generated during that time. While fundamental studies do exist, most of the work in this area has focused on characterizing the overall effects of frost accumulation or ice accretion on the performance of devices such as heat exchangers, airfoils, ships, and other structures such as buildings, bridges, and electrical power transmission lines. Few investigations have focused exclusively on the earliest stages of frost growth. In addition, there appears to be a lack of literature concerned with the inception and propagation of the ice phase on surfaces as it pertains to the frost formation process.

In this chapter, a review of the background material central to this research is presented, followed by a survey of the open literature.

A. Overview of the Frost Formation Process

Frost can be described as the product of two competing processes [3]:

1. ice deposition directly from the vapor phase
2. condensation of an intermediate liquid phase that eventually freezes, followed by ice crystal growth from the vapor phase

The first process is sometimes referred to as deposition or desublimation frosting while the second is more commonly known as condensation frosting. Condensation frosting tends to be the more dominant mechanism for air temperatures or partial pressures above the triple point of water (0.01°C or 0.611 kPa, respectively) and surface temperatures above −20°C. On the other hand, desublimation frosting typically dominates for air temperatures below the triple point or for surface temperatures below −40°C. Under intermediate conditions, these two mechanisms may contribute to frost growth in a parallel fashion [3].

1. Thermodynamics of Frost Growth

The phase change processes associated with both the deposition and condensation frost formation mechanisms can be understood within the framework of classical thermodynamics. The first law of thermodynamics for a closed system can be expressed as

$$dU = \delta Q - \delta W \tag{2.1}$$

which can be combined with the second law definition of entropy change $dS \geq \int \left(\frac{\delta Q}{T}\right)$ and the assumption of reversible, compressible boundary work $\delta W = PdV$ to yield the relation

$$dU + PdV - TdS \geq 0 \tag{2.2}$$

The Gibbs free energy of the system is defined as

$$G(T, P) = U + PV - TS \tag{2.3}$$

from which it follows that

$$dG = VdP - SdT + (dU + PdV - TdS) \tag{2.4}$$

The terms in parentheses shown in Equation 2.4 have been so grouped to emphasize their equivalency with Equation 2.2. Comparing Equations 2.2 and 2.4 reveals that for an isothermal ($dT = 0$), isobaric ($dP = 0$) process, a necessary condition for stable equilibrium is $dG \geq 0$. This criterion implies that the Gibbs free energy of any system in stable equilibrium will be minimized. For a two-phase system (a mixture of the solid and vapor phases, perhaps), the Gibbs free energy of the system on a per unit mass basis is given by

$$g = xg_1 + (1-x)g_2 \tag{2.5}$$

where x is the mass fraction of phase 1. The minimum Gibbs free energy of this two-phase system may be defined by $\frac{\partial g}{\partial x} = 0$; thus, evaluating the derivative of g with respect to x in Equation 2.5 yields

$$\left(\frac{\partial g}{\partial x}\right)_{T,P} = g_1 - g_2 = 0 \tag{2.6}$$

where the subscripts T and P denote that this expression is valid for a constant temperature, constant pressure process. Therefore, during an equilibrium phase transition,

$$g_1 = g_2 \Longrightarrow dg_1 = dg_2 \tag{2.7}$$

With the intensive form of Equation 2.4, $dg = vdP - sdT$, it follows that

$$v_1(dP)_1 - s_1(dT)_1 = v_2(dP)_2 - s_1(dT)_2 \tag{2.8}$$

Thus, with $(dP)_1 = (dP)_2$ and $(dT)_1 = (dT)_2$ for an equilibrium process, an expression for the coexistence or saturation boundary between phases 1 and 2 emerges:

$$\frac{dP}{dT} = \left(\frac{\Delta s}{\Delta v}\right)_{1\to 2} \tag{2.9}$$

Using the definition of isobaric specific enthalpy change, $dh = du + Pdv$, the intensive form of Equation 2.2 can be rearranged to yield an expression for the specific entropy change

$$ds = \frac{dh}{T} \Longrightarrow \Delta s_{1\to 2} = \left(\frac{\Delta h}{T}\right)_{1\to 2} \tag{2.10}$$

Substituting this expression into Equation 2.9 produces the well known Clausius-Clapeyron equation, given by

$$\frac{dP}{dT} = \frac{h_1 - h_2}{T(v_1 - v_2)} \tag{2.11}$$

The Clausius-Clapeyron equation expresses the slope of the pressure-temperature curve along which phases 1 and 2 can coexist in thermodynamic equilibrium. A representative pressure-temperature (PT) diagram for water is shown in Figure 2.1.

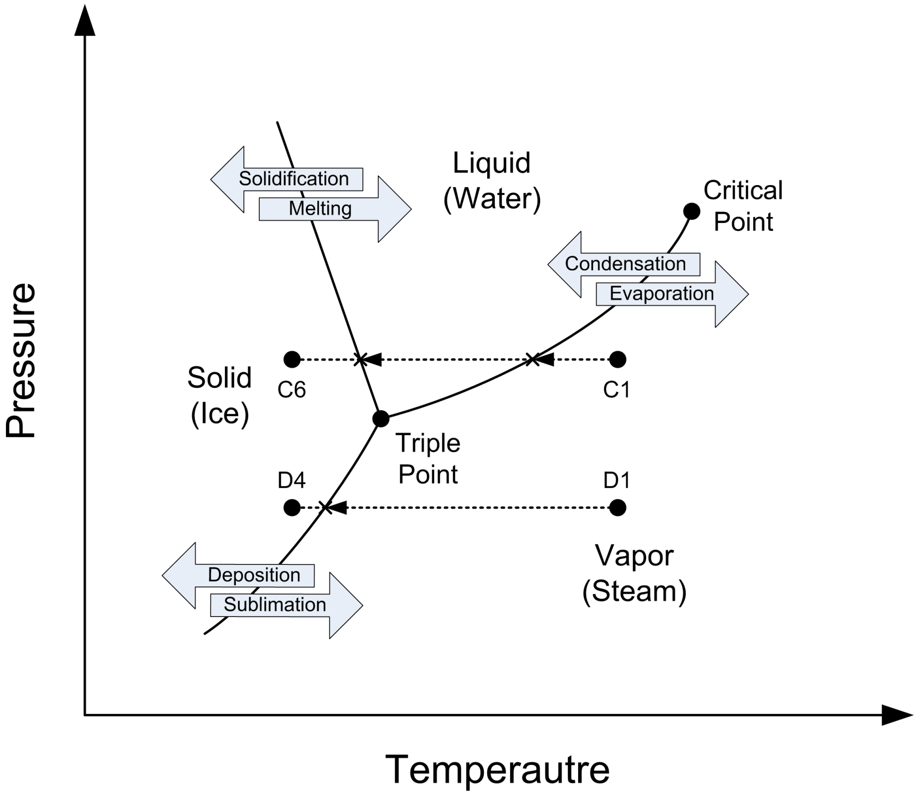

Figure 2.1: Two isobaric frost formation paths within the PT diagram for water

The lines shown emanating from the triple point in the PT diagram shown in Figure 2.1 stem directly from Equation 2.11 for a given specific volume change $v_1 - v_2$. These are known as the coexistence curves for a given substance, which in this case is water. The line shown separating the solid (ice) and liquid (water) phases is generally referred to as the fusion curve. Likewise, the boundary between the liquid (water) and vapor (steam) phases is known as the vaporization curve while the line separating the solid (ice) and vapor (steam) phases is often called the sublimation curve. As the name implies, the triple point is defined as the pressure and temperature combination at which all three phases can coexist in equilibrium. The critical point represents the pressure and temperature combination at which the vaporization curve ceases to exist; thus for pressures and temperatures beyond the critical values, the liquid and vapor phases are no long distinct. The most common names for the phase change processes that occur from one phase to another are denoted by the arrows overlaid across each coexistence curve shown.

Two ideal, isobaric phase change processes associated with deposition and condensation frosting are illustrated in the PT diagram of Figure 2.1 by the lines starting with points D1 and C1, respectively. Here it can be readily seen that the initial conditions required for deposition frosting to occur must lie below the triple point pressure, but not necessarily below the triple point temperature. Conversely, the condensation frosting mechanism is seen to proceed through an intermediate liquid phase prior to the transition to ice. In addition, Figure 2.1 clearly shows that for condensation frosting to occur, the initial water vapor pressure and temperature must both be in excess of the corresponding triple point values.

The PT diagram for water shown in Figure 2.1 provides a good overall picture of how the coexistence of dual phases is constrained by the pressure-temperature coupling associated with the equilibrium assumptions. An important characteristic of the Clausius-Clapeyron equation is that it implies a change in volume and evolution of latent heat are both necessary conditions for a phase change to occur. However, as a strict definition of equilibrium phase change, this equation does not describe how specific volume is coupled with the other thermodynamic state variables of pressure and temperature. To understand this relationship, an equation of state for a given substance needs to be considered. Many equations of state have been developed from theoretical and experimental considerations, but no single one yet conceived can adequately describe the coupling of pressure, volume, and temperature for all three classical states of matter[1]. Nonetheless, the idea of state equations formulated as functions of pressure, volume, and temperature gives rise to the concept of equilibrium surfaces on which transitions between thermodynamic states are valid. Such equilibrium surfaces are known as pressure-volume-temperature (PVT) phase diagrams. A representative PVT surface for water is shown in Figure 2.2.

With the inclusion of volume as a state variable, the appropriate equation of state expresses the equilibrium conditions for singe-phase as well as phase transition processes in terms of a three-dimensional surface, as shown in Figure 2.2. In fact, the PT digram shown in Figure 2.1 is merely a two-dimensional projection of the PVT surface aligned with the volume axis. In addition, two additional phase diagrams can be derived from the PVT surface: a pressure-volume (PV) and a temperature-volume (TV) diagram.

Additional details about the deposition and frosting mechanisms can be obtained by considering these process paths on the PVT diagram. The two ideal, isobaric phase change processes previously illustrated in the PT diagram of Figure 2.1 are displayed on the PVT surface for water shown in Figure 2.2.

For illustrative purposes, it is assumed that both processes shown in Figure 2.2 originate in the vapor region at the points C1 and D1 at the same, above-freezing temperature, but at two different pressures. In the case of humid air, which is a multi-component system, these isobars would correspond to the partial pressures of

---

[1] Solids, liquids, and gases.

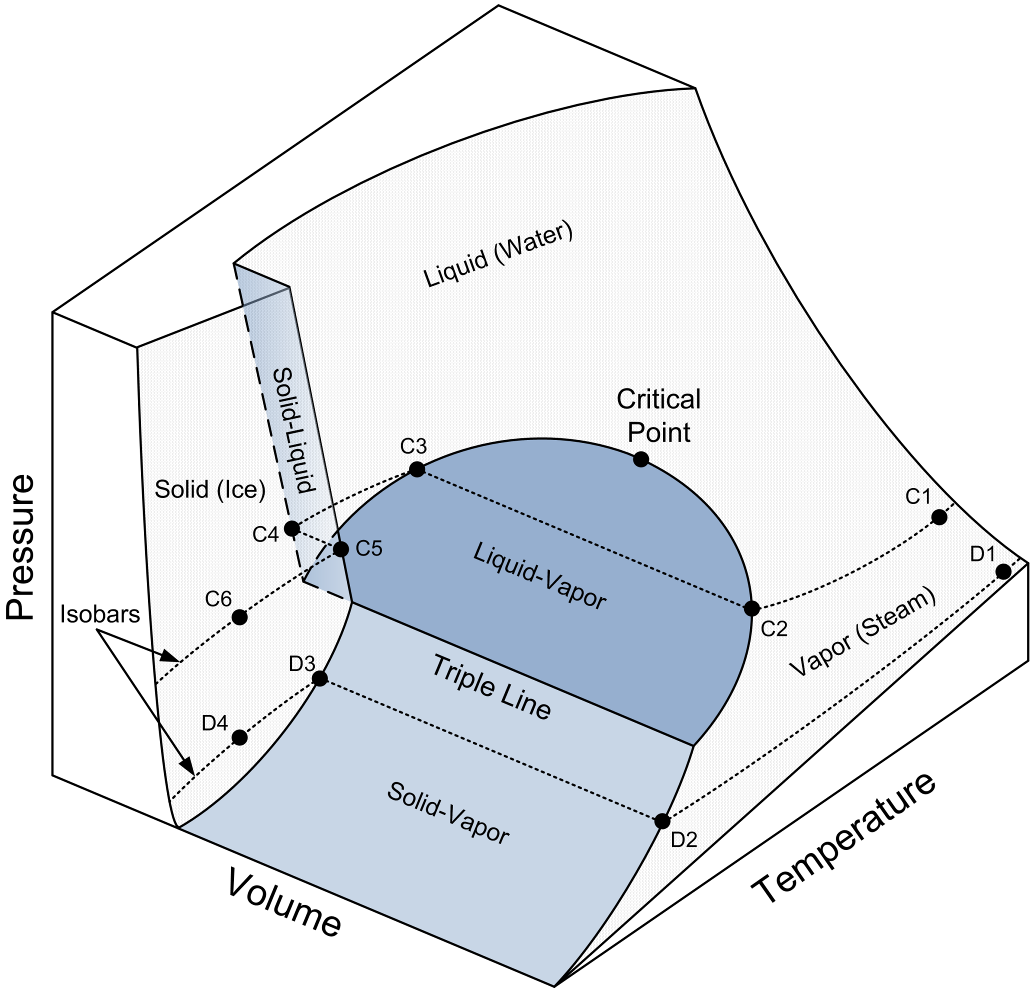

Figure 2.2: Two isobaric frost formation paths along the PVT surface for water

water vapor in each case (which would manifest as a specific humidity difference). If water vapor at these two conditions is brought into contact with a below freezing substrate in an isobaric fashion, two strikingly different paths emerge: C1-C6 and D1-D4. It is assumed that the temperatures at C6 and D4 are identical and equal to that of the substrate.

The pressure for process D1-D4 lies below the triple point value; therefore the deposition frosting mechanism is represented by this path. Inspection of Figure 2.2 shows that sensible cooling of the water vapor from point D1 along line D1-D2 yields saturated vapor at point D2. The saturated vapor at this point, however, is saturated with respect to ice and further cooling from point D2 initiates a phase change process from water vapor to ice, represented by line D2-D3. At the point D3, the resulting ice phase exists as a saturated solid and further cooling to the substrate temperature at D4 produces subcooled[2] ice.

The pressure for process C1-C6 lies above the triple point value; thus, this path represents the condensation frosting mechanism. Figure 2.2 shows that cooling of the water vapor along this isobar follows an entirely different path from that of the previous case. Sensible cooling of the vapor from points C1 to C2 produces saturated vapor at point C2, but unlike in the previous instance, the vapor is saturated with respect to liquid water, not ice. Further cooling from point C2 results in condensation, producing saturated liquid at point C3. Additional cooling from this point eventually produces liquid at point C4 which is subcooled with respect to water vapor but saturated with respect to ice. Removing additional energy from the liquid at this point initiates the freezing process, C4-C5, and further cooling from the saturated solid state at C5 to the substrate temperature at C6 results in subcooled ice.

2. Dynamics of Frost Growth

Although the thermophysics involved in the inceptive stages of deposition and condensation frosting are considerably different, the overall macrostructure of the frost in both cases generally evolves into that of a fragile matrix of ice crystals which continually grow and accumulate in a direction normal to the substrate. A simplified overview of this problem is illustrated in Figure 2.3.

The impact that frost has on the thermal problem can be inferred from the frost

---

[2] The terms *subcooled* and *supercooled* are used synonymously in this context.

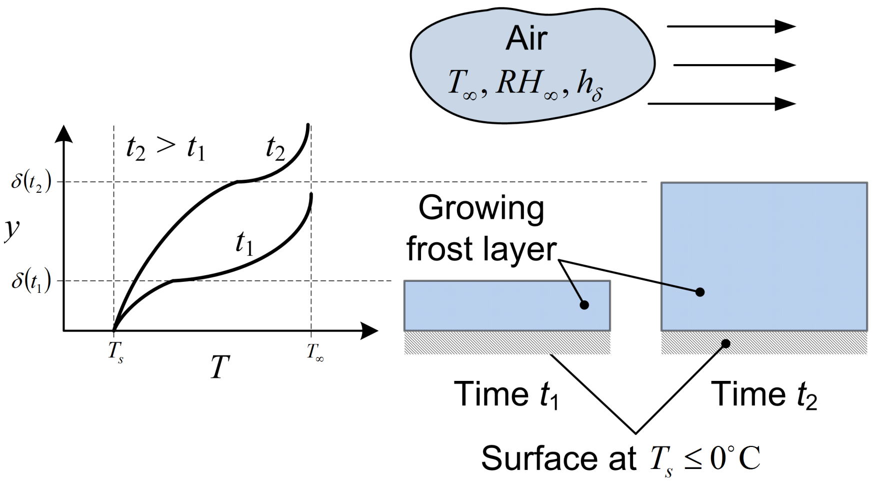

Figure 2.3: Illustration of frost layer growth and corresponding temperature profiles as a function of time

layer temperature profiles depicted in Figure 2.3. As shown, the mere presence of a frost layer of thickness δ represents an impedance to heat transfer between the air stream and the surface. Because the frost layer continually grows outward from the surface, the thermal resistance imposed by the frost layer increases with time. Thus, in general terms, the formation of frost can be classified as a type of fouling process. Compared to many other fouling processes, however, a notable complication associated with frost is that the interaction of all three phases of water during the crystal growth stage can significantly alter the physical structure of the frost layer [31]. As an example, consider the implications of the frost layer depicted in Figure 2.3 growing on a below-freezing substrate in an above-freezing air stream. As the frost layer continues to grow away from the surface, the free boundary temperature of the frost, $T_f(\delta, t)$, eventually rises to 0°C. At this point, the ice at the free boundary $(y = \delta)$ melts, soaks into the surrounding structure, and then refreezes. This cyclical melting and refreezing process, combined with interstitial water vapor diffusion and condensation on the free boundary, can substantially affect the growth dynamics of the frost layer. These interactions ultimately result in the frost layer evolving into a highly anisotropic medium with time-dependent physical properties [32].

Once the initial growth stage has passed, the influence of interstitial heat and mass transfer decreases and the overall growth dynamics of the frost layer is dominated by ice deposition at the free surface. As a result, the problem can be idealized as a type of moving boundary problem originally applied to the stable freezing of water by Stefan [33]. Applying an energy balance to the free surface of the frost at $y = \delta$ yields an expression for the growth rate of the frost layer of the form

$$k_{ice} \frac{\partial T_{ice}}{\partial y}\bigg|_{y=\delta} = \bar{\rho}_f \lambda_{sv} \frac{\partial \delta}{\partial t} + k_{air} \frac{\partial T_{air}}{\partial y}\bigg|_{y=\delta} \tag{2.12}$$

where the frost density is given by $\bar{\rho}_f = \rho_{ice}\left(1 - \chi\right)$, ρ_{ice} is the density of solid ice and χ is the porosity of the frost matrix. Because $k_{ice} \gg k_{air}$, it follows that as long as $\mathcal{O}\left(\frac{\partial T_{air}}{\partial y}\right) \leq \mathcal{O}\left(\frac{\partial T_{ice}}{\partial y}\right)$, the frost growth rate will not be very sensitive to the ambient air conditions. In this case, the solution to Equation 2.12 can be approximated by the classical one-dimensional Stefan solution, from which it can be shown that

$$\delta \propto t^{\frac{1}{2}} \tag{2.13}$$

The relation given by Equation 2.13 has been confirmed experimentally by Schneider [5].

3. The Condensation Frosting Process

For the operating conditions found in most industrial settings, condensation frosting is generally the predominant growth mechanism. This mode of frost formation can be conceptualized to occur in three sequential stages [2]:

1. a condensation stage in which liquid water droplets initially form, supercool,

grow, and coalesce

2. a nucleation stage in which these droplets suddenly freeze
3. a crystal growth stage in which ice dendrites grow away from the surface, toward the humid air stream, and accumulate to form a porous crystalline matrix otherwise known as frost

The first two stages, sometimes referred to collectively as the early stages of frost formation, are technically precursors to the crystal growth stage in which frost actually emerges. This third and final stage is more commonly known as the mature growth stage and, from a pragmatic viewpoint, has historically been of greater concern to the design engineer because of the resulting reduction in both air flow and heat transfer often caused by frost.

The physical characteristics of the surface play an important role in condensation frosting [2, 27, 29]. At its inception, condensation begins as a molecular phenomenon at discrete nucleation sites on the surface where the vapor phase becomes locally supersaturated. Whether or not the condensation process proceeds in a filmwise or dropwise manner depends on the relative difference between the internal cohesive forces (surface tension) in the liquid condensate and the adhesive forces (a function of the interfacial free energy of the surface) between the condensate and the surface. The affinity that a liquid possesses for a particular solid surface is known as the wettability of that fluid. In terms of surface tension, the wettability can be quantified in terms of the angle formed between the liquid-vapor and solid-liquid interfaces at three-phase contact line depicted in Figure 2.4.

Neglecting the contribution of gravity, a static force balance of the interfacial tensions at the solid-liquid-vapor contact line shown in Figure 2.4 yields Young's

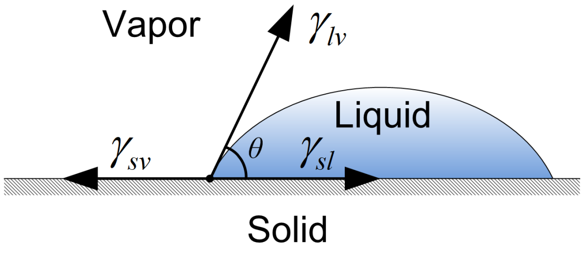

Figure 2.4: Definition of liquid droplet contact angle in terms of interfacial lines of tension

relation:

$$\cos\theta = \frac{\gamma_{sv} - \gamma_{sl}}{\gamma_{lv}} \tag{2.14}$$

Because surfaces with higher free energies naturally experience stronger adhesive forces with the liquid phase, high energy surfaces are more easily wetted than low energy surfaces by a particular liquid under similar conditions. In general, high energy surfaces are hydrophilic in nature and are classified by contact angles in the range of $\theta \leq 90°$. By contrast, low energy surfaces can usually be classified as hydrophobic, resulting in higher contact angles in the range of $\theta \leq 90°$. In the limit of $\theta = 0°$ and $\theta = 180°$, surfaces are classified as completely wettable or non-wettable by a given liquid, respectively. An overall sense of the difference between these two surface types is illusrated in Figure 2.5.

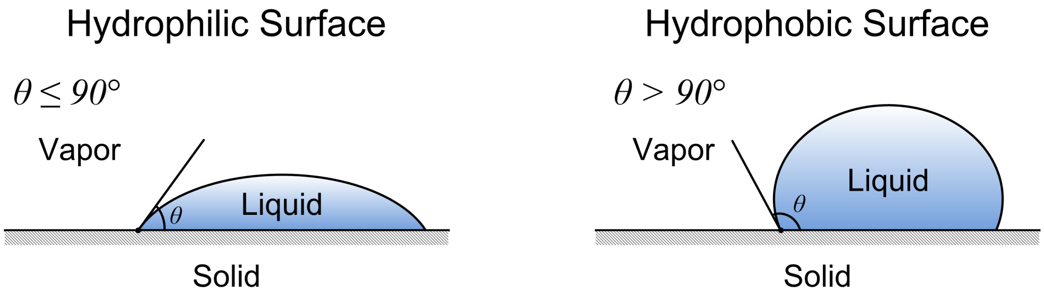

Figure 2.5: Droplet contact angles for hydrophillic (wetting) and hydrophobic (non-wetting) surfaces

Conceptually, the dominant condensation process for highly wettable surfaces would be expected to follow the filmwise mechanism exclusively. As the wettability of the surface decreases, the condensation process appropriately shifts towards the dropwise mechanism. Interestingly, the metals common to most heat transfer equipment generally constitute high energy surfaces and ideally, contact angles should be relatively low for polar liquids such as water. However, one consequence of their high surface energy is that such metals are easily wetted by various organic contaminants that can be present in the surroundings. The thin film of contamination that often results can cause such metal surfaces to experience localized hydrophobicity and therefore promote dropwise condensation to a larger extent, particularly in the early stages while the droplets are still small [30].

The contact angle given by Young's relation in Equation 2.14 provides a macroscopic measurement of an intrinsically microscopic quantity: the interfacical free energy between the liquid and the substrate. However, Young's equation only applies to ideal, perfectly smooth surfaces. By contrast, the morphology of all real surfaces features microscopic defects which give rise to the concept of surface roughness. The interaction between these asperities and the liquid phase may produce a scenario in which the measured contact angle does not accurately represent the actual surface energy [34]. For example, on a rough surface, it is possible to imagine how the contact angle of a droplet grown from condensation might vary considerably from that of a manually implanted droplet of comparable mass or size.

In the case of condensation, the resulting droplet will grow from sub-microscopic nucleation sites, many of which are the surface defects themselves. Therefore, the resulting condensate droplet will likely be in good physical contact with the local topology of the surface and the actual contact area between the droplet and the substrate will be greater than that of a perfectly smooth surface. In this case, the measured contact angle is more appropriately expressed in terms of a corrected value, as in the model of Wenzel [35]

$$\cos\theta_w = f_w \cos\theta \tag{2.15}$$

where f_w is the ratio of the actual to projected contact area between the droplet and substrate. Because f_w increases from unity with surface roughness, Equation 2.15 implies that the underlying wetting properties of the surface are always magnified by roughness. Thus, if $\theta < 90°$, $\theta_w < \theta$ whereas if $\theta > 90°$, $\theta_w > \theta$. In other words, for droplets in the Wenzel state, hydrophillic surfaces become more hydrophillic and hydrophobic surfaces become more hydrophobic as surface roughness increases.

In the case of a manually implanted water droplet, a different physical situation emerges. When placed onto the surface, the droplet will naturally trap air within some of the microvoids on the surface. The resulting interface between the droplet and the surface is therefore a composite of solid and air. Depending on the wetability and roughness of the substrate, the Cassie-Baxter model [36] shows that the effective contact angle can be expressed as

$$\cos\theta_c = \gamma_{sl} \cos\theta - \gamma_{lv} \tag{2.16}$$

For frosting to occur, the temperature of the surface must be at or below the freezing point of water. In the case of condensation frosting in above-freezing humid air, portions of the growing water droplets on the surface can actually be supercooled to a metastable liquid state below the freezing temperature [3]. Theoretically, the lowest temperature to which pure water can be cooled before undergoing homogeneous nucleation to ice is about −45°C [37]. However, even in precisely controlled laboratory conditions, a supercooled water droplet growing on a surface is much more likely to undergo heterogeneous nucleation at substrate temperatures well above this theoretical limit. Heterogeneous nucleation can attributed to active nucleation sites provided by contaminating particles, surface morphology, or even localized disturbances arising from internal temperature gradients and convection currents. Fundamentally, the degree of supercooling that a water droplet can tolerate before ice nucleation occurs is strongly dependent on droplet size, ambient temperature, and relative humidity [3]. For condensation frosting on surfaces, the substrate temperature and surface energy also affect the amount of droplet supercooling that can occur before freezing begins [27, 38].

When a supercooled water droplet suddenly nucleates to ice, the entire droplet does not freeze instantly. Experiments have shown that the coldest portion nearest the surface freezes first while the upper portion remains in the liquid phase [39]. After nucleation, the solid ice phase that initially forms at the interface grows upward until the entire droplet is frozen. An interesting phenomenon that occurs as a result of this non-uniform freezing is the formation of a characteristic "spire" projection at the top of the completely frozen droplet, as depicted in Figure 2.6. Frozen droplets such as these have been reported by several researchers for various aqueous mixtures and droplet sizes [26, 27, 29, 39–41].

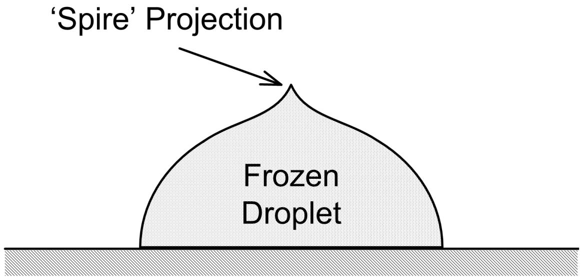

Figure 2.6: Example of a completely frozen water droplet with characteristic spire-like projection

Another important aspect of droplet freezing pertains to larger regions on the surface. When a single droplet nucleates to ice, it can induce nucleation in the surrounding droplets. In turn, each of these surrounding droplets triggers nucleation in neighboring droplets and so on, as illustrated in Figure 2.7. The resulting chain reaction has been observed to advance outwards from the point of origin with an aggregated wavelike motion [27]. The so-called "freezing front" associated with this process is important because it represents a distinct local phase transition boundary from metastable liquid to stable crystalline solid and therefore defines the regions on the surface where frost can and cannot begin to form during the earliest stage. The mechanisms responsible for freezing front propagation between droplets are not currently known and have not been the subject of any known research to date.

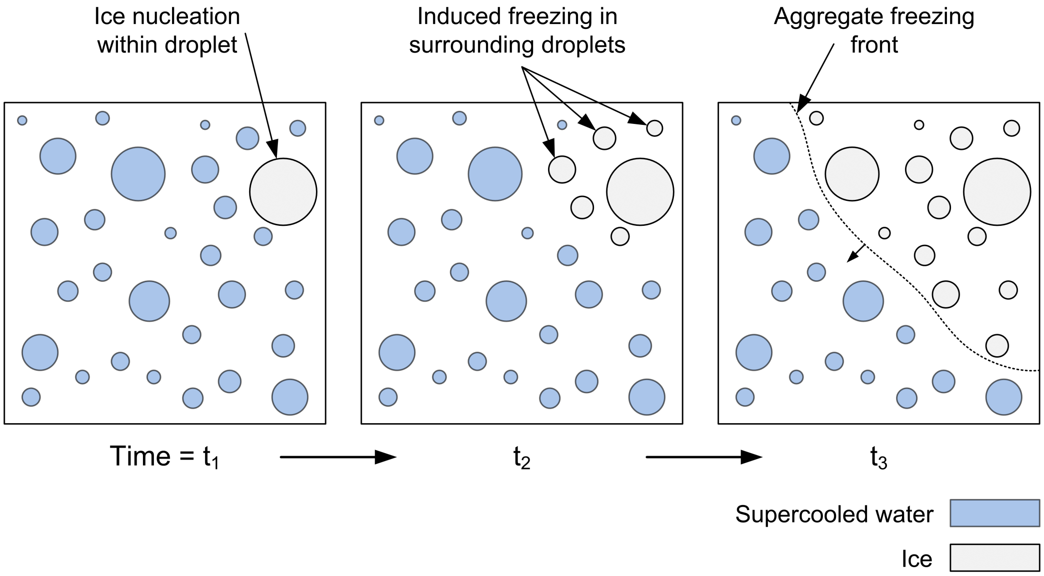

Figure 2.7: Propagation of an aggregate inter-droplet freezing front during the earliest stage of the condensation frosting process

In regions where the condensate droplets have completely frozen, the mature growth period begins. It is not uncommon for some degree of heat transfer enhancement to occur at the beginning of this period because of turbulence promotion and the fin effect resulting from the presence of newly frozen condensate droplets [39,42]. However, any benefit is quickly negated as the growth of a porous matrix of dendritic ice crystals proceeds outward from the frozen droplets. As time progresses, the resulting frost layer becomes thicker and more uniform in the direction normal to the surface. At this point, the characteristics of the frost layer approach those of the moving boundary problem described in Figure 2.3. A summary of the three stages of the condensation frosting process used in the present discussion is illustrated in Figure 2.8.

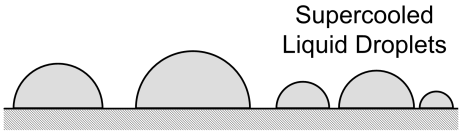

Stage 1: Condensation

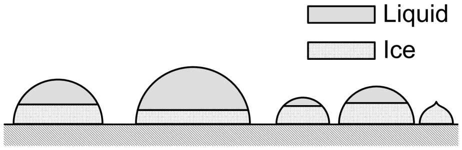

Stage 2: Ice Nucleation

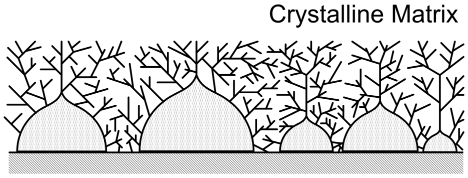

Stage 3: Mature Frost Growth

Figure 2.8: Summary of the three stages of the condensation frosting process

B. Literature Review

The literature identified as relevant to the this work was divided into the following sections:

1. Frost modeling
2. Frost experimentation
3. Dropwise condensation
4. Ice nucleation
5. Ice propagation

1. Frost Modeling

The scope and complexity of frost models available in the literature vary widely. A number of investigators have developed models that attempt to characterize frost formation on surfaces from inception to mature growth. However, the majority of these so-called comprehensive models ultimately focus on frost growth in the later stage while treating the early stages superficially. A few noteworthy studies have considered frost growth in the early stages to various extents [9, 38, 43–45].

An analytical and experimental study of the early stages of the frost formation process was conducted by Seki et al. [43]. Their investigation considered heat and mass transfer in both the condensation and frost growth stage. The energy equation used in their condensation model accounted for droplet growth as well as heat and mass transfer through a convective coefficient and water vapor pressure differential, respectively. The nucleation events associated with droplet freezing were not considered; rather, frost growth in their later stage model was assumed to occur on an ice layer generated by the frozen droplets. Results showed that both the condensation and frost growth models tended to under-predict their experimental data. They attributed the former discrepancy to the fact that their condensation model did not account for droplet coalescence, and the latter was explained by the inability of their frost growth model to account for changes in frost density over time.

Tao et al. [9] attempted to create a comprehensive frost model by dividing the problem into two distinct periods: an early crystal growth period and a later fully developed frost layer growth period. Their early crystal growth model was based on circular ice column growth upwards from the freezing surface at locations where supercooled water droplets had previously resided. As shown in Figure 2.9, the ice columns were mathematically modeled as growing fins by the simplified energy equation

$$\frac{\partial T_\beta}{\partial t} = d\frac{\partial^2 T_\beta}{\partial z^2} + 2\frac{\partial T_\beta}{\partial z}\frac{\partial d}{\partial z} - 4\mathrm{Bi}_\beta \left(T_\beta - T_\gamma\right) + \frac{2}{\mathrm{Ja}}\frac{\partial d}{\partial t} \tag{2.17}$$

and the mass balance equation

$$\frac{\partial d}{\partial t} = 2\mathrm{Bi}_m \left(\omega_\gamma - \omega\right) \tag{2.18}$$

where the subscripts β and γ denote the ice and air-water vapor phases, respectively. The evolution of the ice column height, δ_f, was implicit in the boundary condition given by

$$\frac{d\delta_f}{dt} = \mathrm{Bi}_{m\beta} \left(\omega_\infty - \omega|_{z=\delta_f}\right) \tag{2.19}$$

where $\mathrm{Bi}_{m\beta}$ is the mass transfer Biot number for the ice phase. The numerical solutions to this set of equations provided the ice column diameter, height, and one-dimensional temperature distribution as a function of time. However, use of this ice column model within the framework of the authors' comprehensive model hinged on knowing the droplet distribution prior to freezing. This parameter was not reported in the study; therefore, a droplet distribution was assumed.

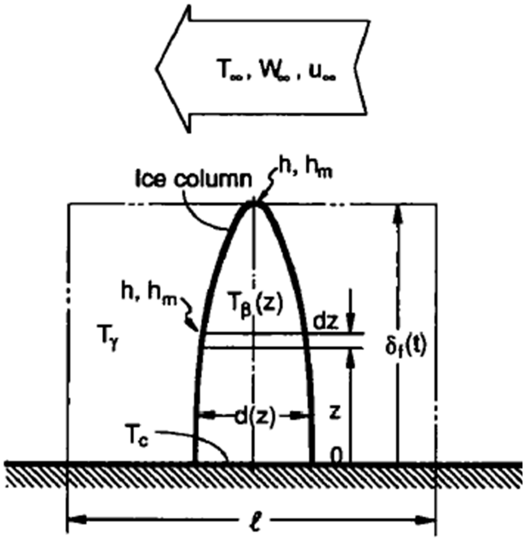

Figure 2.9: An early stage frost formation model describing ice column growth into the vapor phase [42]

Olsen and Hilding [44] presented a detailed model for freezing on horizontal surfaces. They analyzed what was effectively a three-phase heat transfer problem, which involved the condensation of saturated water vapor onto a freezing substrate and the subsequent growth of an ice layer beneath the condensate and vapor layers (Figure 2.10). Their analysis used a simplified form of the energy equation for each phase, given by

$$\rho_j C_j \left(\frac{\partial T_j}{\partial t} + v_j \frac{\partial T_j}{\partial y} \right) = k_j \frac{\partial^2 T_j}{\partial y^2} \tag{2.20}$$

where the subscript j represents the particular phase (solid, liquid, or vapor).

The authors obtained a set of exact solutions for the one dimensional, transient temperature distributions in the growing ice, liquid, and vapor layers for the case of a constant, uniform wall temperature. Results agreed to within 15% of a preliminary experiment, but as evidenced by the formulation, their model was only applicable to filmwise condensation for a pure vapor and solid ice layer growth.

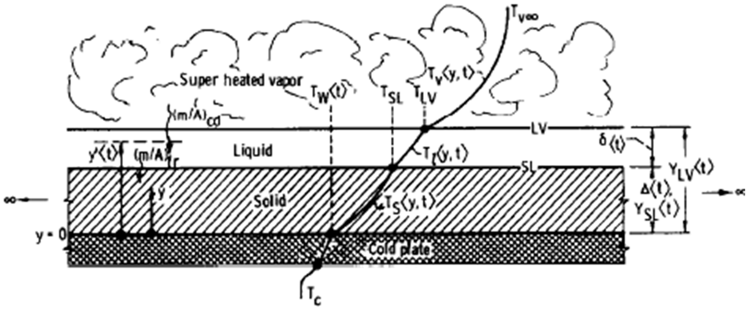

Figure 2.10: A three-phase heat transfer model used to model ice growth from the vapor phase [44]

In contrast to earlier models that assume water vapor is saturated at the surface during frost formation, recent work by Na and Webb [38] has shown that the water vapor must be locally supersaturated for frost to form. Applying the nucleation model of Fletcher [46], the authors analyzed some of the key limiting factors that govern frost inception for both condensation frosting and desublimation (deposition) on surfaces. Two important results from their analysis are shown in Figure 2.11.

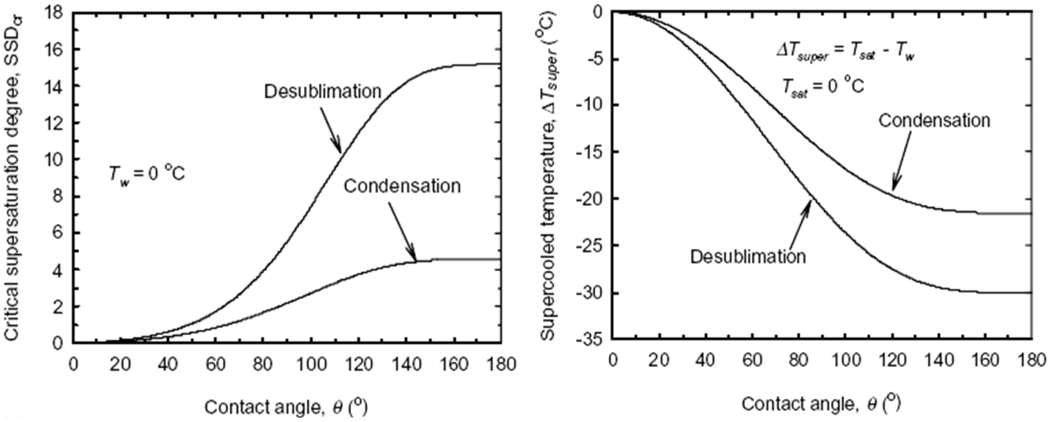

(a) (b)

Figure 2.11: Predicted supersaturation degree (a) and supercooled temperature limits (b) for water as a function of contact angle [38]

The critical supersaturation degree shown in Figure 2.11(a) is given by the relation

$$SSD = \frac{P_v - P_{v,sat}}{P_{v,sat}} \tag{2.21}$$

where P_v is is the local partial pressure of water vapor in the air. For a surface temperature of 0°C, Figure 2.11(a) shows the degree of water vapor supersaturation required for frost nucleation as a function of the contact angle θ previously defined in Figure 2.4. Conversely, for water vapor with a saturation temperature of 0°C, Figure 2.11(b) shows the supercooled temperature required for frost nucleation as a function of θ. A major conclusion from their study was that lower energy surfaces (large θ) require a higher degree of supersaturation for frost nucleation than higher energy surfaces (small θ). In a separate but related study, Na [45] used a boundary-layer analysis to develop a model capable of predicting the degree of supersaturation at the surface under different frosting conditions. He indicated that models using the saturated water vapor assumption at the interface may over-predict measured mass transfer rates by factors of as high as 30.

2. Frost Experimentation

Experimental studies into the general nature of frost formation on surfaces are numerous. As with the case for frost modeling, most of the available experimental work has focused on the mature growth period, with any consideration of the early stages being incidental for the most part. A few investigations which consider early stage frost formation to varying degrees are discussed in this section [2, 24, 26, 40, 47, 48]

Hayashi et al. [47] studied frost formation on a flat, horizontal surface using time-lapsed photography. The authors divided the frost growth process into three periods: the crystal growth period, the frost layer growth period, and the frost layer full growth period. Based on extensive measurements, they devised a system to classify frost formation types based on the ambient-to-wall water vapor concentration gradient (ΔC) and the surface temperature (t_s). The resulting frost regime map, along with a corresponding illustration of the general growth process for each frost type, is shown in Figure 2.12. The authors observed how ice column growth in the crystal growth period served as a basis for subsequent frost layer development, but due to a lack of resolution in their visualization system, they were not able to consider liquid supercooling or ice nucleation in the early stages.

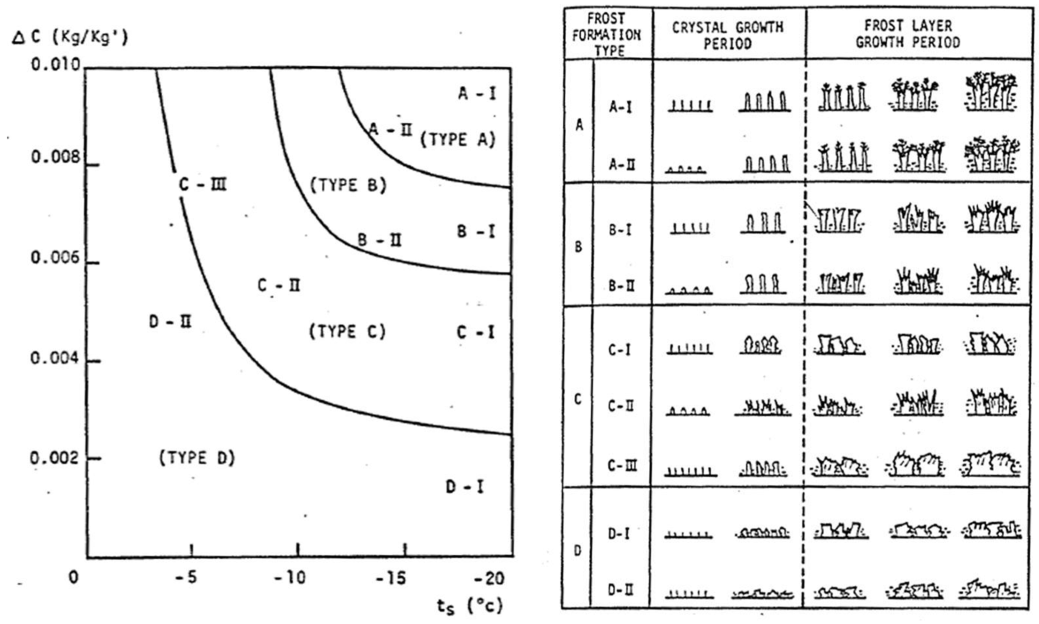

(a) (b)

Figure 2.12: Frost regime map based on water vapor concentration gradient-surface temperature profiles (a) and an illustration of frost formation types (b) [47]

Tao and Besant [48] used a closed loop psychrometric wind tunnel to study frost growth on a horizontal flat plate under moist laminar airflow conditions. They used a laser beam profilometry system to obtain in situ measurements of the frost layer thickness and directly measured the spatial and temporal frost layer density with removable, flush-mount disks tailored for their testing surface. Although this study was primarily concerned with the characterization of frost properties in the mature growth period, the experimental techniques did produce some qualitative data regarding early stage crystal (ice column) growth that corroborated some of the authors' previous models.

A study of frost inception at the microscale was conducted by Georgiadis [2] and later by Georgiadis and Hoke [26]. In these investigations, scanning confoncal microscopy was used to observe the growth and subsequent freezing of supercooled condensate droplets on a horizontal surface. Quantitative data were obtained by synchronizing the visualization system with real time temperature and heat flux measurements at the surface. An interesting observation from both of these studies was the sudden disappearance of near-micron sized liquid droplets neighboring larger freezing droplets. The researchers attributed this phenomenon to evaporation incited by a localized vapor pressure gradient resulting from the formation of ice.

An investigation by Dyer et al. [24] studied the effects of surface energy (hydrophobicity) on the rate of frost growth on surfaces. The authors used a closed loop wind tunnel to obtain quantitative measurements of frost height as a function of time for surfaces with various liquid contact angles. In addition, they conducted a series of qualitative experiments with a scanning confocal microscope to study the impact of surface energy on the condensation and freezing processes involved in the early stages. The results of this study agreed with similar investigations [25,27,49] in that the frost growth rate on hydrophobic surfaces was measured to be less than on hydrophilic surfaces. However, the authors also found that the frost growth rate varied appreciably between surfaces made of different materials but with similar surface energies.

3. Dropwise Condensation

The study of vapor condensation on surfaces is a well established research topic. Numerous aspects of filmwise condensation have been modeled analytically with great success, but despite continual progress over the last several decades, the theory associated with dropwise condensation is still riddled with uncertainties. Nonetheless, analytical and experimental studies devoted to the dropwise mechanism abound and several have been identified as relevant to the present discussion [30, 50–53].

The two most widely accepted dropwise condensation models are discussed by Carey [30]. The first model is based on the assumption that droplet embryos form and grow at discrete nucleation sites on the surface while the area between droplets remains dry. For this model, further condensation occurs only on the droplets, not the surface. In the second model, it is presumed that filmwise condensation occurs initially and that droplets are formed only after the film ruptures upon reaching some critical thickness. Subsequent condensation in this model is postulated to occur only on the surface between droplets, with the resulting condensate film being continuously drawn into the existing droplets through capillary forces. Unfortunately, a great deal of ambiguity between these two models still exists because experimental evidence supporting both views is available [54, 55].

In an effort to understand the mechanisms associated with droplet formation and growth, Song et al. [50] used an optical technique to measure reflectance from horizontal copper and stainless steel test surfaces during dropwise condensation. Their results suggested that both of the dropwise condensation models previously described may be valid under certain conditions. They found that a thin, invisible condensate film coexisted with droplets on the substrate as long as condensation was occurring (i.e. there was net mass transfer to the surface), as depicted in Figure 2.13. However, when the condensation process was stopped (i.e. zero mass transfer to the surface), the film disappeared and the surface was found to be essentially dry between droplets.

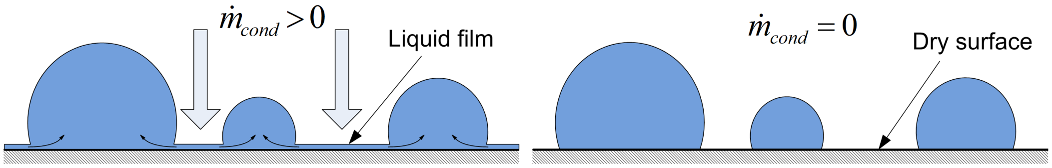

(a) $T_s < T_{dew}$ (b) $T_s \geq T_{dew}$

Figure 2.13: Conceptual illustration of an inter-droplet liquid film present for condensation (a) and absent for no condensation (b)

Investigating ways to promote dropwise condensation in heat transfer applications has long been a research topic of practical importance. Marto et al. [51] studied the effects of organic and noble metal coatings on condensation in steam systems. Their data showed that even moderately hydrophobic coatings tended to promote excellent dropwise condensation in steam systems, resulting in overall heat transfer coefficients at least 3-6 times greater than comparable uncoated surfaces. Tsuruta et al. [53] studied the theoretical aspects of constriction resistances resulting from surface heat flux non-uniformities. Their analysis showed that the dropwise heat transfer coefficient decreased with decreasing surface thermal conductivity because of increasing constriction resistance. Numerical results from their study agreed with an earlier experimental investigation by Hannemann and Mikic [52] in which a thin-film thermometer was used to characterize the effects of substrate and coating thermal conductivity on the dropwise condensation process.

4. Ice Nucleation

Literature pertaining to the nucleation of ice in supercooled water droplets on surfaces is sparse. However, there are a number of studies dedicated to homogeneous and heterogeneous ice nucleation in microscopic cloud droplets [3, 56–60]. Although the bulk of the available literature on this subject stems from the atmospheric sciences, the basic mechanisms are applicable to the present topic.

A detailed discussion of the thermophysics involved in homogeneous and heterogeneous ice nucleation in small droplets was presented by Hobbs [3]. In homogeneous nucleation, microscopic ice embryos spontaneously form and disintegrate in supercooled water droplets until an embryo larger than some critical size eventually forms. If conditions make it more thermodynamically favorable for this larger embryo to continue growing rather than dissociating back to the liquid phase, a stable ice nucleus forms and the entire droplet will then proceed to freeze. In heterogeneous nucleation, extraneous solid particles in the droplets tend to promote the formation of ice nuclei long before the homogeneous mechanism becomes significant. Consequently, the temperatures at which heterogeneous nucleation occur are notably higher than for homogeneous nucleation.

A complete theory of heterogeneous ice nucleation is hindered by the fact that a daunting amount of information would be required to properly account for the countless substances that could act as ice nuclei [56]. Nonetheless, a number of experimental investigations have studied the various mechanisms associated with heterogeneous ice nucleation in supercooled water droplets. Early investigations by Gokhale and Goold [57] and Fukuta [58] showed that when nucleating particles are placed on the surface of supercooled water droplets, they freeze at temperatures which are 2 to 10°C warmer than when immersed within the droplets. A more recent investigation by Shaw et al. [59] showed that when a single nucleating particle is located on the outer surface of a droplet, the freezing temperature of that droplet will be 4 to 5°C higher than when the same particle is completely immersed within that droplet. The authors explained this phenomenon in terms of preferential surface crystallization catalyzed by the nucleating particle. A related study by Durant and Shaw [60] revealed that it does not matter if the nucleating particle contacts the droplet surface from the inside out or the outside in; the probability of inducing nucleation on the surface is the same. This phenomenon has been observed in molecular dynamics simulations (MDS) of liquids other than water [61]. A more recent MDS study by Vrbka and Jungwirth [62] showed that ice nucleation preferentially begins in the subsurface (i.e. within a few monolayers of the surface layer) of liquid water droplets as opposed to the surface itself.

5. Ice Propagation

There is a plethora of research focused on the propagation of crystallization fronts in melts. Most of this work is derived from the field of materials science and engineering and is largely concerned with solidification in metals and semiconductors as it pertains to casting processes. Interestingly, the foundation for this subject area dates back to 1891 when Stefan first studied the problem one-dimensional ice propagation in water [33]. In recent years, the development of numerous sophisticated modeling techniques, including enthalpy methods, volume-of-fluid (VOF) models, and level set and phase field methods, has advanced largely out of the need to simulate solidification problems in two and three dimensions.

Several studies concerned specifically with the propagation of ice in droplet geometries were identified as relevant to the process of frost inception [39, 63–65]. An analytical and numerical study of a single, supercooled droplet undergoing freezing was conducted by Feuillebois et al. [63]. They developed their models based on the a priori assumption that the freezing process consists of two steps: 1) a very fast process in which the droplet returns to the melting temperature upon beginning to freeze and 2) a slower process dominated by heat conduction through the evolving solid-liquid interface. For their physical model, they used the one-dimensional, one-phase Stefan problem cast in spherical coordinates, which is given by the heat conduction equation

$$\frac{\partial^2(rT)}{\partial r^2} = \frac{1}{\alpha_s}\frac{\partial(rT)}{\partial t} \tag{2.22}$$

and the associated energy balance along the interface Γ

$$\left.\frac{\partial T(r,t)}{\partial r}\right|_{r=\Gamma} = \frac{\rho_s \Delta h_{fus}}{k_s}\frac{dr_\Gamma(t)}{dt} \tag{2.23}$$

The authors solved Equations 2.22 and 2.23 analytically with a perturbation method and numerically using a fully implicit finite differencing scheme. The results of their study showed excellent agreement between the analytical and numerical solutions. More recently, Tabakova and Feuillebois [64] extended this work by solving the same problem with an enthalpy method in two-dimensions and found that the results agreed with the analytical solutions derived in [63] to within 0.5%.

Gong [39] studied the unsteady freezing process associated with a single droplet installed on a cold horizontal surface. He used a two-dimensional finite control volume formulation to develop a numerical model capable of predicting the rate of heat transfer, the temperature distribution, and the position of the phase-change region as functions of position and time in the droplet during solidification. His model allowed the use of a prescribed convective heat transfer boundary condition along the droplet-air interface and a uniform temperature boundary condition along the droplet base. For a hemispherical droplet with a radius of 1.4 mm, results of his analysis showed that for several seconds after ice nucleation began, the maximum local heat flux at the droplet base occurred between the center ($r = 0$) and the perimeter ($r = R$) of the droplet (Figure 2.14).

A recent investigation by Zhong [65] characterized the growth of condensate and the evolution of freezing fronts on micro-grooved surfaces. The test surfaces used for

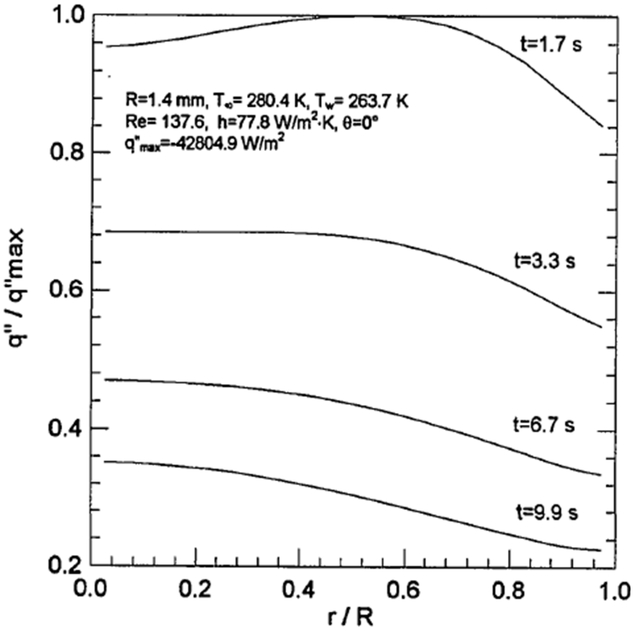

Figure 2.14: Radial heat flux distribution at the droplet base during nucleation [39]

the freezing experiments consisted of silicon wafers fabricated with a series of parallel micro channels spanning the entire width of the substrate. Freezing was induced within a uniform layer of water deposited onto the surface in the manner depicted in Figure 2.15. As indicated in the diagram, each end of the test surface was maintained a different temperature.

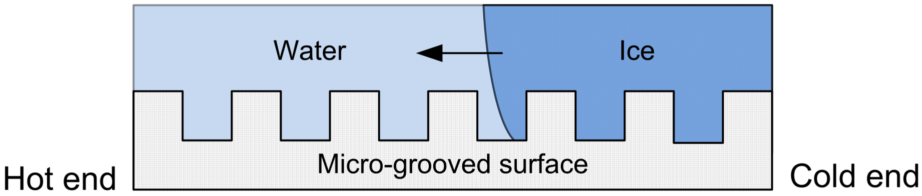

Figure 2.15: Illustration of ice propagation on a micro-grooved surface [65]

Using an visualization system to quantitatively track the evolution of ice, Zhong found that the velocity of the freezing front oscillated as it traversed the substrate.

Subsequent analysis with finite element simulations revealed that this oscillation occured because the local freezing front velocity accelerated and decelerated as it passed over the crests and troughs of the micro-grooves, respectively. Based on the simulation results and a statistical analysis of the experimental data, the author deduced that this effect was due primarily to thermal effects in the two-phase system, namely heat conduction.

C. Conclusions

A number of conclusions can be drawn from the literature review:

1. Typical treatments of the so-called early stage in comprehensive frost models largely neglect the interaction between freezing water droplets and the substrate. As a result, such models cannot effectively predict the effects of substrate properties such as surface energy or roughness on frost accretion in the later stages.
2. Water vapor must be locally supersaturated at the surface for deposition or condensation frosting to occur. Thus, the degree of supersaturation required for frost to form by either mechanism is strongly dependent on the free energy of the surface.
3. The rate of frost growth on substrates with similar surface energies, but made of different materials, has been measured to be different under carefully controlled conditions. This implies that the interaction between the frost and the substrate is not fully characterized by surface energy alone.
4. When a supercooled water droplet nucleates to ice on a substrate, smaller liquid droplets in its immediate vicinity may rapidly evaporate and deposit onto the surface of the larger drop. It has been postulated that these evaporated droplets

serve as the initial source of mass for the dendritic ice columns that form on frozen droplets at the beginning of the mature growth stage. However, no consideration has been given to the role that these evaporating droplets may have in the propagation of ice between droplets.

5. Some experiments have shown that during dropwise condensation, a very thin liquid film may coexist with visible condensate droplets on the surface. No studies have been conducted to determine if such a liquid film could participate in the propagation of ice along surfaces undergoing dropwise condensation.

6. Several studies have suggested that ice nucleation is more thermodynamically favorable when occurring at or very near the surface of supercooled liquid droplets as opposed to the bulk interior. However, these investigations focus on contact or heterogeneous ice nucleation at the liquid-vapor interface (e.g. cloud droplets). No references were found that considered contact nucleation at the interface between a droplet and a solid substrate.

These conclusions have provided much of the motivation for this research. The chapters that follow discuss the experimental work and subsequent analyses used to determine and characterize the mechanisms associated with ice propagation on surfaces undergoing dropwise condensation.

CHAPTER III

EXPERIMENTAL FACILITY AND PROCEDURE

To study the underlying thermophysical phenomena responsible for ice propagation on surfaces undergoing dropwise condensation, extensive experimental work was required. To carry out the necessary experiments, factors known to affect frost formation on surfaces, such as air temperature, humidity, and velocity, had to be reliably simulated and controlled as well as accurately measured. In addition, diagnostically resolving the length and time scales characteristic of ice inception and propagation required the use of high speed digital microscopy. Because of the considerable effort directed towards the experimental portion of this study, this chapter focuses exclusively on the facility and associated procedures used.

A. Experimental Apparatus

The experimental facility consisted of three main components:

1. a closed-loop pyschrometric wind tunnel
2. a digital microscopy system
3. a data acquisition and control system.

Major components of the wind tunnel loop included an optically-accessible test section and an air conditioning system. The wind tunnel was designed to provide continuous, conditioned airflow over an interchangeable test surface flush-mounted to the bottom side of the test section. This surface was affixed to a thermal stage which provided precise control of the test surface temperature. The test surface was viewed *in situ* with a digital microscopy system, which was comprised of a customized high speed imaging system integrated with a boom-mounted compound microscope. This boom-mounted configuration allowed the surface under test to be imaged from either top- or side-view orientations. The data acquisition and control system (DACS) was a commercially-available setup capable of handling multiple analog input and output signals. With the DACS, measurements from various instruments could be recorded simultaneously while other elements were being manually or automatically controlled. An overall view of the experimental apparatus is shown in Figure 3.1.

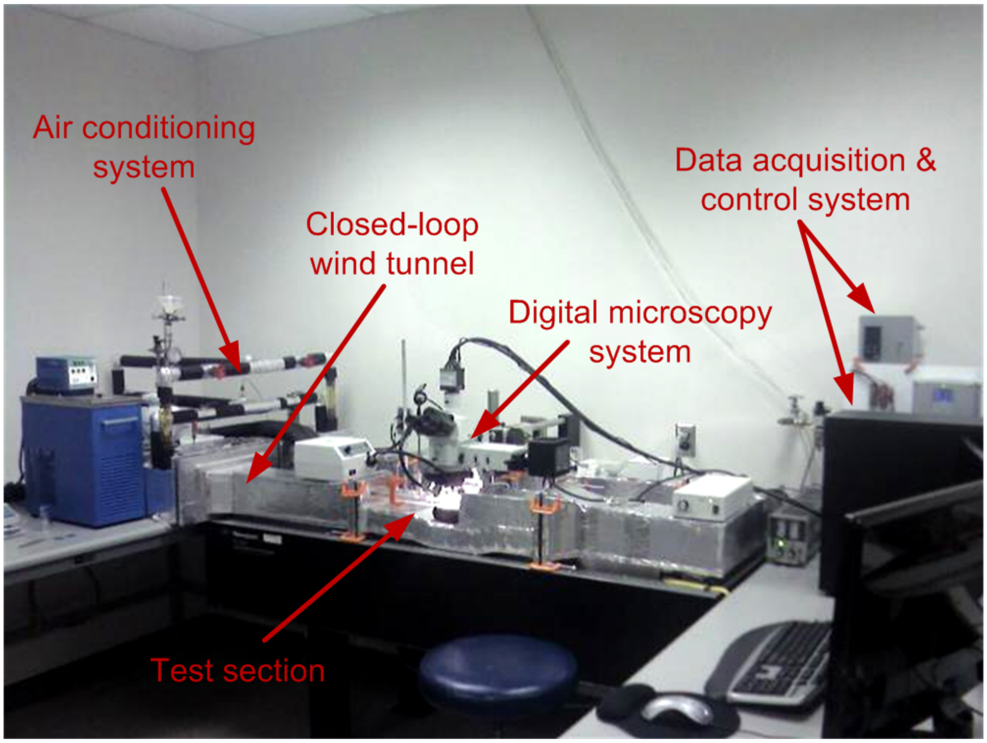

Figure 3.1: Overall view of experimental apparatus

Details surrounding the design and functionality of each main component in the facility and the associated subsystems are discussed in the sections that follow.

1. Psychrometric Wind Tunnel

The psychrometric wind tunnel was designed and constructed as a closed-loop bench-top apparatus with modular sections. A schematic of the wind tunnel loop and its primary components is shown in Figure 3.2. With the exception of the clear test section, each module was fabricated from rigid insulated ductboard. Raised flanges sealed with soft foam gasket material were incorporated into the termini of each module to facilitate assembly of the airflow loop. In addition, each major component of the air conditioning system was housed in its own module. As seen in Figure 3.2, this modular concept made it possible to isolate the most vibration-prone components of the air conditioning system (e.g. blower) from the microscope and test section.

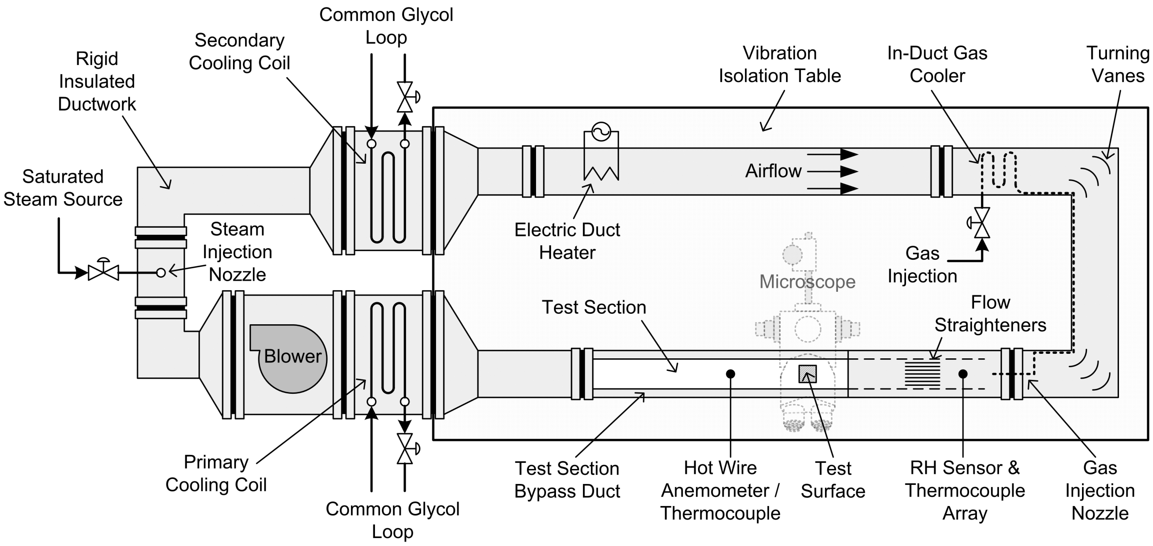

Figure 3.2: Schematic overview of pyschrometric wind tunnel loop and components

a. Air Conditioning System

The air conditioning system consisted of an adjustable-speed blower, two cooling coils, a duct heater, a humidification system and a dry gas injection system. These components were housed in discrete modules, the relative locations of which are shown in Figure 3.2. Thus the air conditioning system was compartmentalized into the following five main modules:

1. Primary and Secondary Cooling Modules
2. Blower Module
3. Humidification Module
4. Reheat Module
5. Moisture Trim Module

Beginning at the outlet of the test section depicted in Figure 3.2, air was inducted through the primary cooling module into the blower module. From there, air was sent through the humidification module and subsequently into the secondary cooling module. Air then passed through the reheat and moisture trim modules before entering the test section. The resulting ranges of bulk air temperature, humidity, and velocity that could be generated and sustained in the test section by the air conditioning system are summarized in Table 3.1.

Table 3.1: Bulk air temperature, humidity, and velocity ranges of experimental facility

Parameter	Operating Range		Control Accuracy
	Lower	Upper	
Dry Bulb Temperature, °C	-5	55	$\pm\,0.5$
Relative Humidity, %	25	95	$\pm\,2$
Air Velocity, m/s	0	15	$\pm\,0.05$

Each module in the air conditioning system is described in more detail in the sections that follow.

Primary and Secondary Cooling Modules

Sensible cooling and moisture removal in the bulk air stream were provided by a primary and a secondary cooling module. The coil used in the primary cooling module was a four-circuit, four-tube pass continuous plate fin and tube heat exchanger with a projected airside face area of 0.06 m^2 and a fin density of 700 fins per meter (fpm). The secondary cooling coil was of the same type as the primary coil but with a two-circuit configuration and a face area and fin density of 0.05 m^2 and 680 fpm, respectively. Cooling for both modules was provided by a centralized 8.8 kW laboratory chiller system that delivered a single-phase glycol/water mixture to each coil from a common 23 liter reservoir. The chiller was capable of producing coolant temperatures as low as -15°C while still maintaining the capacity required for steady operating conditions with a 10°C coolant-to-air temperature approach. Standard laboratory-grade rotameters and globe valves located in the return lines of each heat exchanger were used to measure and control the coolant flow rate through each coil, respectively.

With this cooling system configuration, it was possible to precisely tune the capacities of each cooling section to match the overall cooling load of the wind tunnel loop for a specific set of testing conditions. A distinct advantage of the dual coil approach used here was the ability to cool downstream of the humidification module on demand. This made it possible to increase humidity in the air stream without increasing the dry bulb temperature or vise versa.

Blower Module

Air circulation in the wind tunnel loop was provided by a 120 VAC centrifugal blower located immediately downstream of the primary cooling coil. While most of the blower enclosure was constructed out of the same rigid insulated ductboard used in the other wind tunnel modules, sheet metal struts were used to reinforce the blower mounting structure. Rubber isolators were used on the blower mounts to provide vibration attenuation. The speed of the blower was controlled manually with a silicon controlled rectifier (SCR).

At full power, the blower was capable of providing centerline air velocities as high as 15 m/s through the test section.

Humidification Module

The primary means of adding moisture to the air stream was by injecting saturated steam directly into the wind tunnel. The humidification module was located downstream of the primary cooling module and upstream of the secondary cooling module. The steam originated from a 1000 W miniature boiler with a 250 mL reservoir and was delivered to the air stream through a manually controlled needle valve and atomizing nozzle assembly.

When operated at maximum capacity, the humidification system was capable of sustaining a bulk air stream relative humidity in excess of 95% for up to 45 minutes at a time.

Reheat Module

Any sensible heat addition needed to maintain steady operating conditions in the system was provided by the reheat module. Located immediately downstream of the secondary cooling module, the reheat module employed a 120 VAC, 500 W electric duct heater powered by a programmable Red Lion Model TCU controller. The feedback temperature for the controller was measured by a 9-element thermocouple array located at the inlet of the test section module.

Under most testing conditions, use of the reheat module in conjunction with the rest of the air conditioning system enhanced the precision with which the the test section dry bulb air temperature could be controlled. Bulk air temperatures as high as 55°C were possible with this setup.

Moisture Trim Module

Fine control of the air stream humidity in the test section was accomplished by injecting conditioned gas directly into the wind tunnel immediately upstream of the test section inlet. The moisture trim module consisted of a gas injection line that fed into a duct-mounted coil. From the coil, gas flow was directed through a tube around two 90° bends in the wind tunnel ductwork and delivered to a nozzle. The nozzle was oriented parallel to the airflow and aligned co-linearly with the centerline of the test section inlet. The function of the coil was to bring the temperature of the injected gas to the temperature of the air stream before introducing it to the test section.

Depending on the humidity requirements of a particular test condition, saturated gas from a bubbler or dry gas filtered with a desiccating cartridge could be pumped into the moisture trim module at an adjustable flow rate to provide isothermal humidification or dehumidification, respectively. For this study, zero-grade nitrogen (N_2) or air was used as the injection gas.

b. Test Section

The test section module was the central component of the wind tunnel loop. As implied in Figures 3.1 and 3.2, this module featured two parallel ducts: a test section and a bypass duct. A more detailed schematic showing the side and cross-sectional views of the test section module is presented in Figure 3.3.

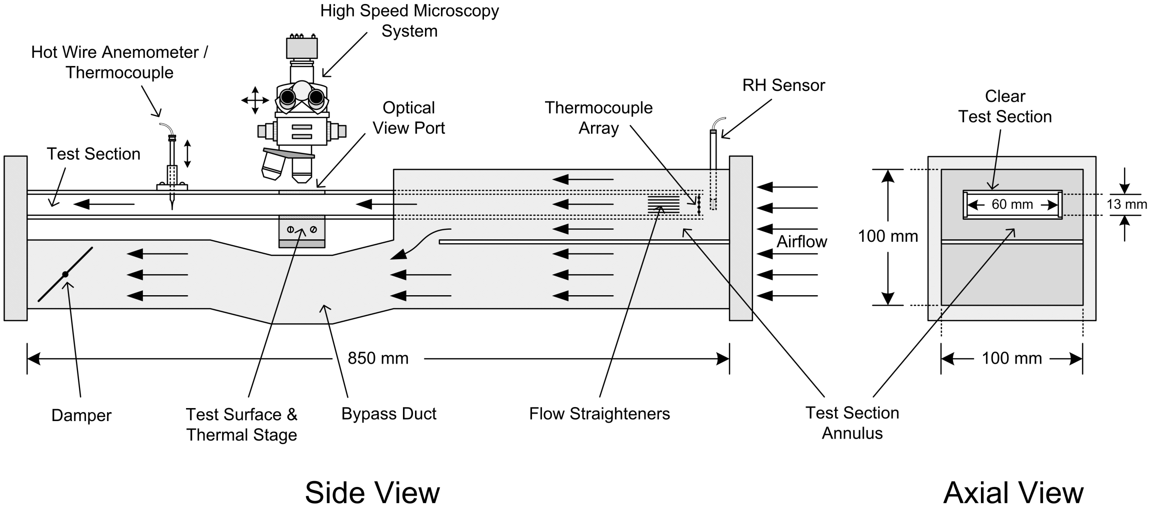

Figure 3.3: Detailed schematic of test section module

Conditioned air entering the test section module was split into two flow paths by a partition that divided the cross section of the main entry duct into two halves. The lower half of the this partition directed airflow through the bypass duct. The entrance to the test section was centered within the upper half of the main duct so as to form a rectangular annulus, as depicted in Figure 3.3. A controllable portion of the air flowing through this section was inducted through the test section while the remainder returned to the bypass duct through a break in the partition. This annular construction was used to insulate the entry region of the clear test section, ensuring that the temperature of the air inducted over the test surface was uniform. Use of the bypass arrangement provided the flexibility to adjust the airflow velocity through the test section over a wide range while ensuring that sufficient airflow was maintained over the primary and secondary cooling coils in the air conditioning system. In addition to the SCR controller used with the blower, an adjustable damper located at the outlet of the bypass duct provided additional control over the air velocity in the test section.

The test section was constructed out of precision machined acrylic glass panels which were fused together with dichloromethane (CH_2Cl_2). The relative humidity (RH) and dry bulb temperature of the air entering the test section was measured with a duct-mounted RH sensor and a 5-element thermocouple array, respectively. A bank of 1.5 mm diameter, 20 mm long flow straighteners was positioned near the inlet of the test section, just downstream from the thermocouple array. A hotwire anemometer and 0.16 mm diameter thermocouple were used to make traversing air velocity and temperature measurements downstream from the test surface. The test surface was flush-mounted to the bottom of the test section with a thermal stage, which itself was secured to the test section structure with a mounting bracket. A view port was machined into the upper acrylic panel of the test section directly above the surface to allow in-situ, top-down viewing with the microscopy system. A single pane of optical quality glass, 0.17 mm thick, was used as the window in this view port. A similar configuration was used with the side panels of the test section when the surface was viewed from the side. When needed, a stream of dry nitrogen gas was directed over the outside of the observation window in use to prevent fogging during low air temperature tests.

Thermal Stage

The thermal stage used to control the test surface temperature was constructed out of several components, including some instrumentation. The functional components consisted of a Peltier module and a copper heat sink. Instrumentation included two thermocouples and a thin-film heat flux gage. An assembled and exploded view of the thermal stage is shown in Figure 3.4.

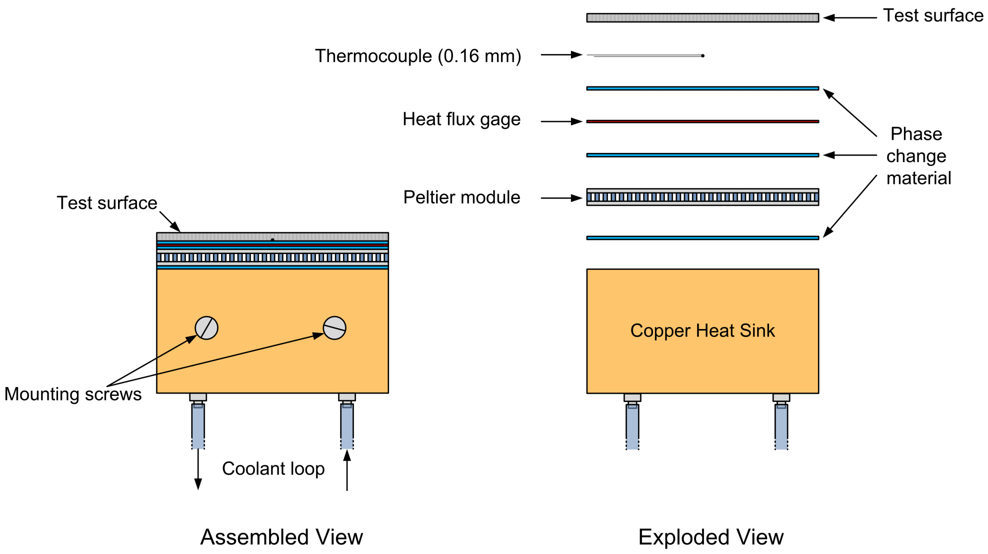

Figure 3.4: Assembled and exploded view of thermal stage

The heat sink was machined from copper stock and featured an internal serpentine conduit to maximize heat transfer to the coolant. The coolant was a propylene glycol/water mixture and was supplied to the heat sink from a small benchtop circulating chiller with a 100 W cooling capacity at $-10°$C. The Peltier module was a commercially available 36 W thermoelectric cooler powered by a 100 W analog-controlled regulated DC power supply. A reed relay and double pole, double throw electromechanical switch was used in conjunction with this power supply to change the polarity of the power supplied to the Peltier module, thereby allowing it to be used in both a heating and cooling mode.

A small type-T thermocouple with a bead diameter of 0.16 mm was used to measure the underside temperature (T_l) at the center of the test surface. In addition, a thin-film heat flux sensor was used to directly measure the instantaneous heat flux (q'') through the thermal stage assembly. These two measurements allowed the upper surface temperature (T_u) of the test surface to be calculated by the DACS in real time by the simple plane wall conduction equation

$$T_u = \frac{q''\Delta y}{k} + T_l \tag{3.1}$$

A second type-T thermocouple was epoxy-bonded to the bottom of the heat sink to monitor transient loading of the thermal stage assembly during cool-down and heat-up sequences: this measurement was used for diagnostic purposes only.

All thermal stage components were joined together with a thin layer of thermally conductive phase change material (PCM), as shown in Figure 3.4. The PCM was a pliable solid that remained semi-tacky at room temperature. At temperatures above 52°C, the PCM underwent a phase change and flowed, thoroughly wetting the thermal interfaces. Upon cooling, it re-solidified and held the various thermal stage components rigidly in place with good thermal contact, without the need for external clamping or permanent adhesives. A key benefit this provided in practice was that once the thermal stage was assembled and installed, the test surface could be quickly changed from the top side without having to disassemble or remove the entire thermal stage from the test section. This eliminated the potential for surface contamination by other media such as thermal grease. The specifications for the PCM used are presented in Table 3.2.

Table 3.2: Specifications for phase change material used in thermal stage

Specification	Value
Film thickness, mm	0.254
Phase change temperature, °C	52
Thermal conductivity, $\frac{\mathrm{W}}{\mathrm{m\,K}}$	3.0

2. Digital Microscopy System

A digital microscopy system provided quantitative in-situ visualization of the test surface during all experiments. It consisted of two primary items: a high resolution optical microscope and a high speed digital imaging system. Additional details about these components are provided in the following sections.

a. Optical Microscope

A custom Nikon compound microscope was used to view the test surfaces through the viewing ports in the test section. Because the test surfaces were opaque, brightfield relfected light microscopy was used. The primary light source was a Phillips LUXEON K2-TFFC 220 lumen high intensity light emitting diode (LED) which was directed to the test surface through an episcopic beam tube integrated into the microscope optics. With this approach, light could be delivered to the test surface on-axis through the objective lens. When needed, secondary illumination from a 150 W infrared-filtered halogen lamp was delivered to the test surface through a pair of fiber optic light guides. These features are denoted in a photograph of the microscope setup shown in Figure 3.5.

As indicated in Figures 3.2 and 3.3, the microscope was mounted on a telescoping boom stand and was free-floating with respect to the test surface. This configuration made it possible to mount the microscope in a variety of orientations so that the test surface could be viewed from either directly above or from the side. One consequence of the test section and microscope not being rigidly coupled was that vibrations generated elsewhere in the test apparatus and laboratory building were easily transmitted to the microscope. Under some conditions, this produced oscillations in the digital images. This issue was addressed by placing the microscope, test section, and the

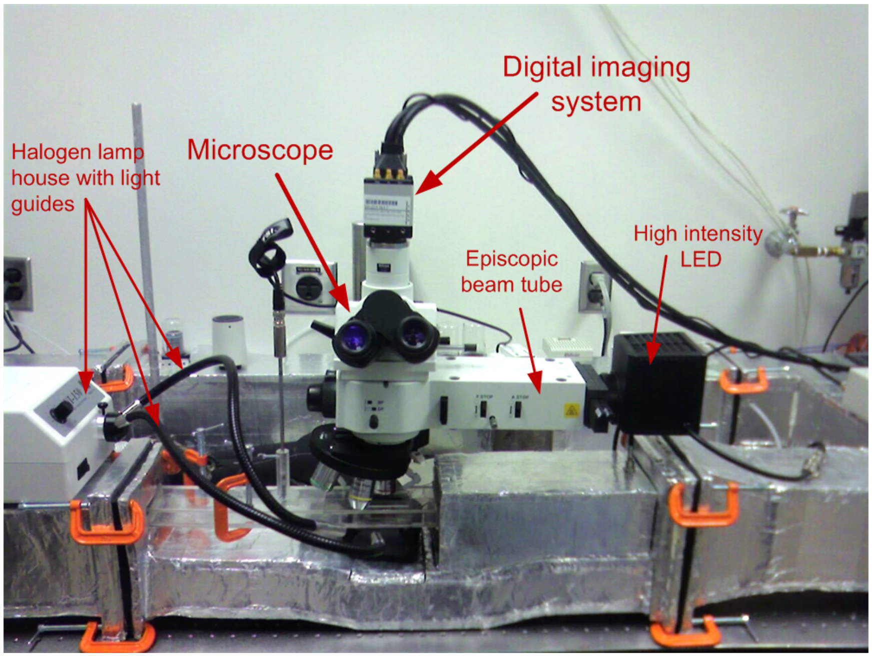

Figure 3.5: Overall view of microscope setup

other static components of the wind tunnel loop on a active pneumatic vibration isolation table (see Figure 3.2).

The optical components of the microscope consisted of a head piece and turret-style nose piece with four objective lenses. The head piece used a prismatic beam splitter in a trinocular arrangement which allowed viewing through 10X binocular eye pieces or with a mounted camera. Magnification powers of the objective lenses used were 5X, 10X, 20X, and 50X and in order to accommodate the dimensions of the test section, they were of the long working distance type. The numerical aperture for each objective lens is defined as

$$N.A. = n \sin \phi \tag{3.2}$$

where n is the refractive index of the transmissive medium ($n = 1$ for air) and ϕ is the half-angle formed by the optical axis and a light ray passing through the extreme periphery of the lens as illustrated in Figure 3.6. The numerical aperture defines the ultimate resolving power of each objective lens (i.e. the closest proximity of two objects that can be interpreted as two distinct regions of the image) through the relationship

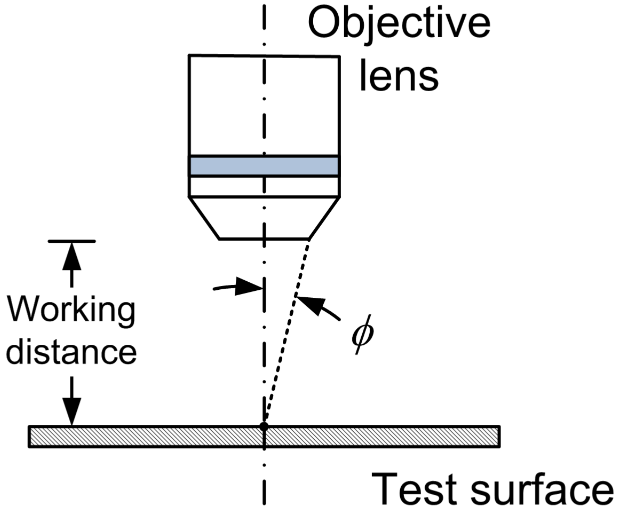

Figure 3.6: Numerical aperture half angle for an objective lens

$$R_{res} = \frac{\lambda}{2(N.A.)} \tag{3.3}$$

where λ is the wavelength of the incident light (assumed to be 550 nm for evaluation purposes). An additional expression gives the depth of focus offered by the objective:

$$\epsilon_f = \frac{n\lambda}{2(N.A.)^2} + \frac{n}{7(N.A.)(M)} \tag{3.4}$$

where M is the rated magnification power of the lens (5, 10, 20, or 50). Based on these definitions, the pertinent specifications of the objective lenses used in this study are listed in Table 3.3.

Table 3.3: Objective lens specifications

Objective, M	$N.A.$	R_{res} μm	ϵ_f μm	Working Distance mm
5X	0.15	1.83	$\pm$ 2.02	23.5
10X	0.30	0.92	$\pm$ 0.96	17.3
20X	0.35	0.79	$\pm$ 0.81	24.0
50X	0.45	0.61	$\pm$ 0.62	17.0

b. High Speed Digital Imaging System

To provide quantitative visualization of the freezing events on the test surface, a high speed digital imaging system was used in conjunction with the optical microscope. The rationale behind the imaging system design stems from experience gained during preliminary studies by the author which showed that

1. the freezing phenomena central to this research occur over a wide range of length and time scales; thus high speed image acquisitions were needed for some experiments

2. ice inception within the viewable area generally occurs suddenly; thus long record times were needed to fully capture the dynamics of the inceptive phenomena

The resulting imaging system consisted of an IDT-Redlake model M3 digital camera connected to a custom-built high performance workstation through a BitFlow-Karbon CL frame grabber card. The camera featured a 1280 by 1024 complementary metal-oxide semiconductor (CMOS) photodiode array with an individual pixel size of 12 by

12 microns. It was capable of providing acquisition speeds of up to 33,000 images per second in a reduced resolution mode. The computer used to control the camera was a purpose-built PC workstation with 32 GB of RAM and two quad-core 64-bit Xeon-class Intel CPUs running at 2.0 GHz. The frame grabber card was installed in the northbridge slot of the PCI Express bus, enabling direct throughput to the system RAM so that it could be used as a fast storage medium for the recorded image data. After a given acquisition was complete, the image data could be offloaded from the RAM onto a 2 TB, 4 disk array striped in RAID 0. Due to the lack of data redundancy associated with the RAID 0 scheme, a pair of 1 TB USB 2.0 external hard disks were used as mirrored backup drives.

The IDT Motion Studio software was used to control the camera and record image sequences. With this hardware and software combination, the imaging system was capable of recording images at rates of up to 520 Hz at full frame resolution (1280 by 1024 pixels) for up to 45 seconds at a time. Using an enhanced memory mode, it was possible to extend the full frame acquisition rate to as high as 1040 Hz for a time span of 22 seconds. One of the most important features offered by this setup was the ability to continuously record images into a preallocated circular memory buffer in a first in, first out (FIFO) fashion. While operating in this mode, image acquisition continued indefinitely until an external trigger was activated to signal that the freezing event of interest had occurred and the recording process could stop. In practice, this FIFO scheme was heavily relied upon to capture the entirety of freezing events which occurred spontaneously on the surface.

The digital camera was connected to the microscope with a standard C-mount on the upper trinocular view port of the headpiece, as shown in Figure 3.5. Unlike the eyepieces, the camera mount did not employ any additional magnifying optics. The microscope objective lenses naturally produced a circular viewing area; however, the

CMOS photodiode array used in the digital camera was rectangular (1280 by 1024 pixels). Therefore, the placement of the camera in the optical path was carefully chosen so that the entire CMOS sensor was fully illuminated by the image with no circular cropping in the corner regions. The length scale viewed by the camera through each objective lens was calibrated with a Nikon stage micrometer with 0.01 mm divisions. The relative sizes of the resulting rectangular regions of interest (ROIs) provided by each objective lens listed in Table 3.3 are illustrated in the scaled diagram shown in Figure 3.7. In addition, the camera calibrations along with the geometric extents of each ROI shown in Figure 3.7 are listed in Table 3.4.

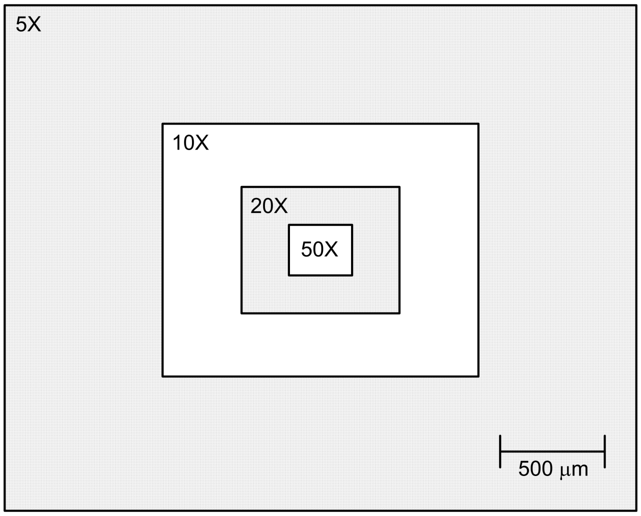

Figure 3.7: Relative sizes of ROIs for various objective lenses (drawn to scale)

3. Data Acquisition and Control System

A multichannel data acquisition and control system (DACS) for the test apparatus was developed with National Instruments (NI) hardware and software. The hardware interface with the instrumentation was handled with one 8 channel cFP-TC-120 thermocouple module and one 8 channel cFP-AIO-610 analog input/output module which

Table 3.4: ROI specifications for various microscope objective lenses

Objective	Camera Calibration μm/pixel	ROI Width μm	ROI Length μm	ROI Area μm^2
5X	2.38	2437	3046	7.423×10^6
10X	1.19	1219	1523	1.857×10^6
20X	0.60	614	768	4.716×10^5
50X	0.24	246	308	7.577×10^4

were connected to an NI Compact FieldPoint cFP-1804 controller. The controller was connected to the imaging workstation through a dedicated Ethernet crossover cable and managed by a data acquisition and control program developed in NI LabVIEW. This DACS software was designed to run simultaneously with the camera control software for synchronous image and data acquisition.

a. Instrumentation

A variety of instrumentation were employed in the test apparatus to measure temperature, humidity, and velocity. Type-T thermocouples (copper-constantan) were used to measure multiple temperatures in the test section, including the underside temperature of the test surface (see Figure 3.4), the test section inlet air temperature, and the test section traverse air temperature (see Figure 3.3). An Omega Engineering HFS-4 thin-film heat flux sensor was used to measure the heat flux though the thermal stage. A Vaisala HMT333 duct-mounted thin-film capacitive relative humidity (RH) transmitter was used to measure the moisture content of the air entering into the test section. In addition, the air velocity in the test section was measured with a TSI model 1750 constant temperature anemometer and 1201 hot film probe. Other parameters were also measured throughout the wind tunnel loop, such as the cooling coil supply and heat sink temperatures and the Peltier module supply voltage; however, these quantities were merely tracked for diagnostic and control purposes and were not recorded by the DACS for data reduction.

The DACS software was set up to accept standard polynomial calibration curves for all instrument channels used. All thermocouples were calibrated in an circulating glycol bath against a NIST-traceable 100 Ω platinum resistance temperature device (RTD). The hot wire anemometer was calibrated in situ with a TSI 8346 VelociCalc thermal anemometer probe which was itself calibrated against pitot-static pressure measurements in a low speed wind tunnel. The heat flux gage and RH transmitter were brand new at the onset of the study and were each shipped with a factory calibration certificate; as such, no additional calibrations were carried out for these instruments. The calibrated ranges and estimated uncertainties associated with each measurement type are reported in Table 3.5,

Table 3.5: Calibrated ranges and estimated uncertainties for test section measurements

Measurement	Calibrated Range		Max. Uncertainty
	Lower	Upper	
Temperature, °C	−30	50	± 0.2
Relative Humidity, %	25	95	± 1.7
Heat Flux, $\frac{\mathrm{W}}{\mathrm{cm}^2}$	−9.5	9.5	± 0.06
Air Velocity, $\frac{\mathrm{m}}{\mathrm{s}}$	0	12	± 0.36

As a particularly important measurement in this study, the calculated test surface temperature was further validated by conducting a series of melting point experiments with three pure substances. For this procedure, small droplets of o-Xylene, distilled/deionized water, and p-Xylene were placed on multiple locations on the upper side of each test surface after installation onto the thermal stage. The temperature of the test surface was then lowered until the droplets of each substance were completely frozen. Then, the surface temperature was gradually increased until the first signs of melting could be observed with the digital microscopy system. The upper surface temperature, as calculated by Equation 3.1, was subsequently recorded and validated against the appropriate melting temperatures. The accepted melting temperatures at standard pressure for each calibration standard used are reported in Table 3.6 [66]. For all test surfaces considered, the maximum deviation between the calculated surface temperature and the melting temperatures of the standards was ± 0.08°C.

Table 3.6: Accepted melting temperatures for three pure calibration standards at standard pressure (from [66])

Substance	Melting Temperature °C
o-Xylene	-25.3
Water	0.0
p-Xylene	13.2

Silicon-based integrated thin-film thermocouples (TFTs) were also explored as a type of quantitative, non-invasive, mircoscopic surface thermometry technique for use in this study. TFTs have been used successfully in numerous boiling investigations to provide high spatio-temporal resolution of the interfacial substrate temperature without significantly affecting the underlying thermophysical phenomena [67]. In this investigation, TFTs would have likely provided very valuable measurements of nearly-instantaneous substrate temepatures during the freezing process. Unfortunately, every bank of TFTs fabricated for this study failed prematurely due to what were presumed to be thermally-induced stresses associated with repeated heating and cooling cycles.

b. Surface Temperature Control Schemata

For added consistency and flexibility in the experimental work, an option was developed in the DACS software that provided automatic control of the test surface temperature. To accomplish this, an adaptive proportional-integral-derivative (PID) algorithm was created to modulate the calculated temperature of the test surface (Equation 3.1) toward a user specified setpoint quickly and with minimal error. Temperature control was achieved by linking the output of the PID algorithm directly to the Peltier module power supply voltage level and polarity; controlling the latter parameter allowed the DACS to invoke heating or cooling as required. Alternative schemes were also created that allowed the setpoint variable to track other test section temperatures with a user-specified offset. For example, the user could set the test surface temperature to track, say, 5°C above the instantaneously calculated dew point temperature and the control system would maintain the split, even in rapidly changing air conditions. This feature also made it possible to switch back and forth between testing conditions rapidly and with high repeatability. An example of how the PID control responded to step changes in temperature setpoint is shown in Figure 3.8. For the transient profiles shown, the initial surface temperature was steady at around 10°C when the setpoint was suddenly changed to the target values indicated by the labeled curves. The data shown in Figure 3.8 were derived from a set of actual test runs, with each curve ending when the freezing process was complete within the ROI. These transient surface temperature profiles are representative of all experiments conducted in this study.

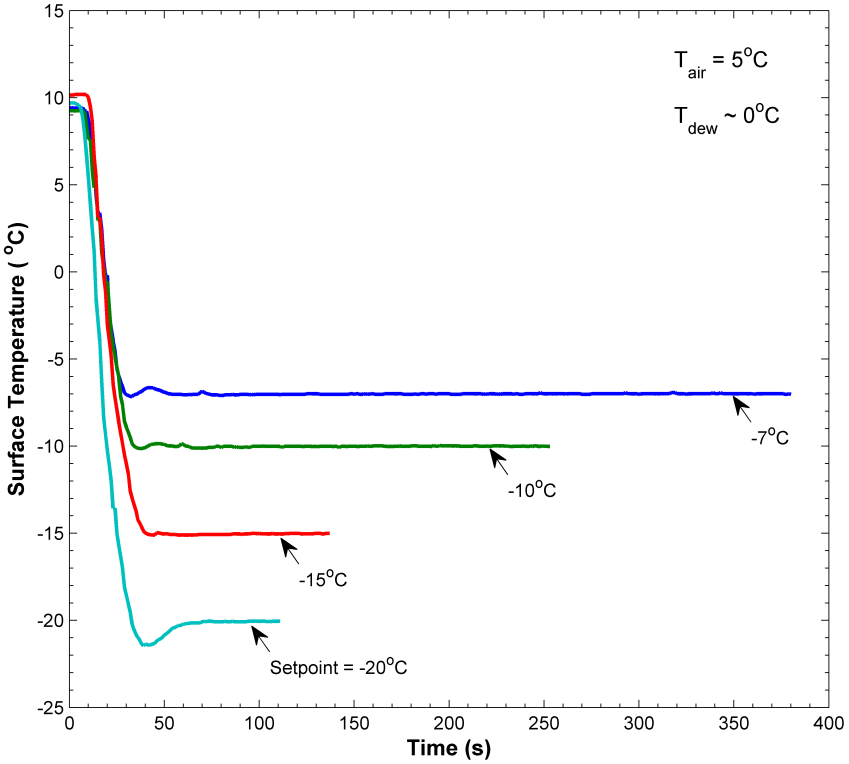

Figure 3.8: Example of test surface temperature response to step changes in setpoint under PID control

B. Test Surfaces

To characterize the impact of surface roughness and wettability (hydrophobicity) on the propagation of ice between condensate droplets, four test surfaces consisting of three materials were ultimately considered: two silicon surfaces, one copper surface, and one aluminum surface. The copper and aluminum surfaces were initially shear-cut from standard grade sheet stock (non-alloy) and subsequently machined to the final dimensions (length and width) required for use on the thermal stage. The silicon surfaces were cut from a standard 76 mm lab grade wafer with a water-cooled diamond saw. In all cases, the final size of each test surface was 30 by 30 mm. The identification (ID) numbers, material compositions, measured thicknesses, and thermal diffusivities for the surfaces selected for this study are reported in Table 3.7.

Table 3.7: Composition, thickness, and thermal conductivity of test surfaces

Surface ID	Composition	Thickness, b_s mm	Thermal Diffusivity, α_s $\frac{\text{m}^2}{\text{s}}$
SiA1	99.5% Si: Wafer Grade	0.412	8.92×10^{-5}
SiA2	99.5% Si: Wafer Grade	0.407	8.92×10^{-5}
CuA5	98.5% Cu: Sheet Stock	0.621	1.17×10^{-4}
AlA2	97.8% Al: Sheet Stock	0.672	9.71×10^{-5}

A fifth test surface consisting of an array of carbon nanotubes (CNTs) grown vertically on a silicon substrate was also considered for use in this investigation. Stable carbon nanotube forests have been shown to possess exotic *superhydrophobic* properites, producing static contact angles for deposited water droplets in excess of 165° [68]. While it would have been highly desirable to investigate the effects of superhydrophobicity on the freezing process, all attempts to conduct experiments with such a surface in this study were unsuccessful because the CNTs were actually found to exhibit *superhydrophillic* behavior when subjected to condensing conditions. The reason this occurred was thought to stem from the fact that 1) the surfaces of the CNTs themselves are actually hydrophillic[1] and 2) the condensation process occurs

---

[1] Carbon (i.e. graphite) itself is actually hydrophillic; it's the interfacial topology of the resulting CNT forest that is thought to produce the superhydrophobic effect characteristic of these surfaces [68].

at a molecular level, thus allowing the formation of the liquid phase deep within the hydrophillic interior of the CNT forests.

1. Surface Preparation

Close inspection of the raw metallic surfaces (copper and aluminum) revealed the presence of unidirectional grain patterns which resulted from the manufacturing processes associated with the production of the source sheet stock. To ensure surface homogeneity in the experiments, one side of each metallic specimen was treated with a special chemomechanical polishing technique known as ISF (isotropic superfinishing) developed by REM Surface Engineering. Using the ISF process, the grain patterns in the raw material were completely eliminated, yielding an highly isotropic surface of uniform roughness. An additional advantage afforded by the ISF technique was that it was possible to converge on specific surface roughness values with repeated roughening and polishing stages.

Because the source wafers were highly isotropic to begin with, the surfaces of the silicon specimens were not physically altered in any way. However, a thin hydrophobic coating of a silcon-based conformal polymer was applied to one of the silicon surfaces to significantly alter its wettability. By depositing 0.5 μl of the solvated polymer onto the surface as it turned in a spin-coating apparatus, a uniform coating with a thickness of 0.5 - 0.6 μm was formed on the surface. Immediately following the spin-coating process, the surface was cured at 200°C for 24 hours.

After preparation, all test surfaces were stored in a vacuum canister until they were ready to be tested. To ensure that any residual surface contamination was removed just prior to testing, the prepared specimens were installed on the thermal stage, gently swabbed with a lint-free clean room-quality cloth saturated in acetone, thoroughly rinsed with methanol, and then heated to 40°C with the Peltier module and dried for 15 minutes. After this final cleaning step, the test surfaces were not touched again until after all testing had been completed.

2. Surface Characterization

Prior to testing, each prepared surface was characterized in terms of the average surface roughness (R_a) and droplet contact angles (θ). The equipment and procedures used to perform these characterizations are outlined in the sections that follow.

a. Surface Roughness

A Hommelwerke model W55 direct contact profilometer was used to measure roughness in small regions on each test surface. The probe used a small diamond-tipped stylus which was first brought into contact with the surface and then subsequently traced through a distance of 1.5 mm. The resulting vertical displacement profile provided a direct measure of the local surface roughness along the line of interrogation. An example of one such profilometry scan for the AlA2 surface is shown in Figure 3.9.

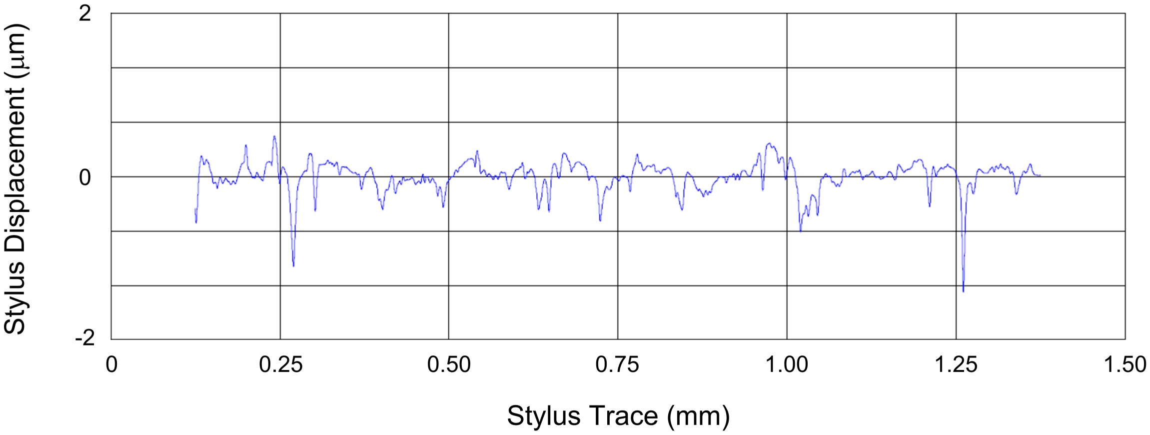

Figure 3.9: Local profilometry profile for one region on surface AlA2

These measurements were repeated in all four corners of each specimen to verify surface isotropy. The overall average roughness for a given surface, R_a, was taken to be the arithmetic average of the values measured in the corner regions. Because it was the primary region of interest in the freezing experiments, roughness measurements were not taken in or around the surface centers to eliminate the risk of scratching. The inherent smoothness of the silicon surfaces made it very difficult to accurately measure surface roughness for these specimens with the direct contact technique. Based on the ultimate resolution of the profilometer, however, it was evident that the R_a values for the silicon surfaces were less than 0.005 μm. The average surface roughnesses for the test surfaces are listed in Table 3.8.

Table 3.8: Average surface roughness values for test surfaces

Surface ID	R_a μm
SiA1	<0.005
SiA2	<0.005
CuA5	0.0234
AlA2	0.1342

b. Droplet Contact Angle

After each test surface had been prepared, static contact angles on each specimen were measured with a FTA188 video tensiometer. The tensiometer featured a precision syringe which could implant single water droplets of known volume on the horizontally-oriented test surfaces. An integrated video system captured still images of the sessile droplet in place and an associated image analysis software package was used to measure the contact angle. Localized variations in surface energy were accounted for by dividing each square test surface into a 3 by 3 grid of equally sized cells and carrying out contact angle measurements within each subregion. The effect of droplet volume on contact angle was also considered within each subregion. A representative image taken from the tensiometer analysis for one subregion of the CuA5 surface with a droplet volume of 1.0 μl is shown in Figure 3.10. A plot of the spatially-averaged contact angles versus the implanted droplet volume for all test surfaces is shown in Figure 3.11. The volume-averaged contact angle θ_{ave}, based on the data presented in Figure 3.11, is reported in Table 3.9 for each test surface.

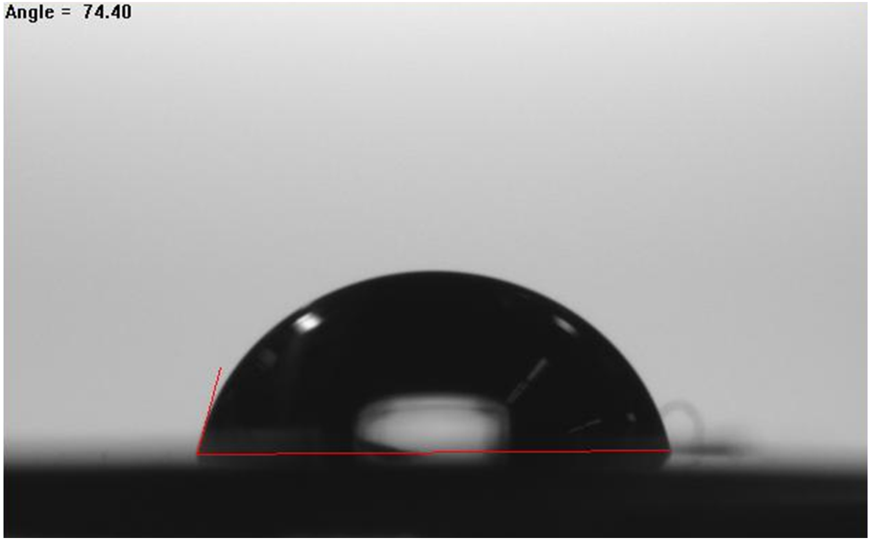

Figure 3.10: Tensiometer image for one subregion on surface CuA5 with a droplet volume of 1.0 μl

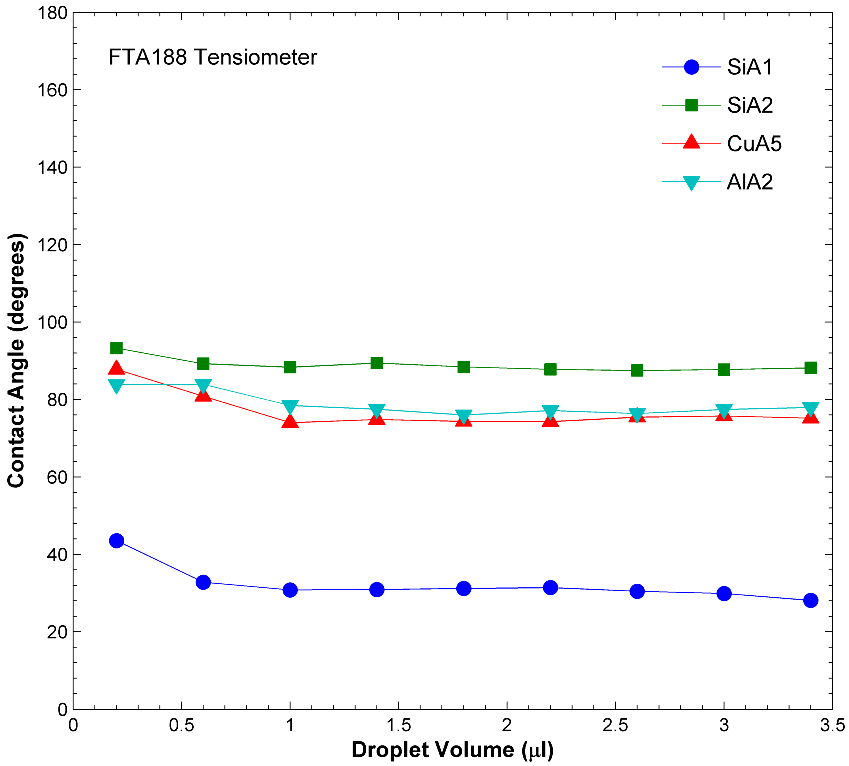

Figure 3.11: Spatially-averaged contact angle versus droplet volume for all test surfaces

Table 3.9: Volume-averaged contact angles for all test surfaces

Surface ID	θ_{ave} degrees
SiA1	32.1
SiA2	88.9
CuA5	76.9
AlA2	78.7

C. Experimental Procedure

The test apparatus was designed to reliably simulate and control various environmental parameters which are known to affect frost formation on surfaces. To characterize the mechanisms responsible for ice propagation between condensate droplets, a number of experiments and associated procedures had to be designed as well. The following sections outline the rationale behind the development of the test matrices as well as the testing procedures conceived to fully utilize the capabilities of the experimental facility.

1. Test Matrices

Environmental parameters that could be varied with the apparatus included the test surface temperautre (T_s), the test section air inlet temperature (T_{air}), the bulk relative humidity of the air stream (RH), and the test section air velocity (U_{air}). Two additional parameters implicitly linked to the test surfaces were the average surface roughness values (R_a) reported in Table 3.8 and the surface wettability or hydrophobicity given by the average contact angles (θ_{ave}) reported in Table 3.9. Therefore, a total of six parameters were available for potential inclusion into the experiments.

In considering the factors expected to be most influential on the inception and propagation of ice on the test surfaces, the air temperature T_{air} and velocity U_{air} were selected as invariant parameters in this study and were held at constant values of 5°C and 5 m/s, respectively, for all experiments. These values of T_{air} and U_{air} were selected because they were representative of nominal refrigeration and heat pump operating conditions. In addition,

1. the fact that $T_{air} > 0$°C ensured that all of the latent heat evolved by freezing droplets was rejected into the substrate and not the air stream

2. the selected value of U_{air} corresponded to an average flat plate Reynolds number of approximately 10^5 in the vicinity of the test surface; this turn corresponded to an average heat transfer coefficient of about 165 $\frac{\mathrm{W}}{\mathrm{m^2\,K}}$ along the air-substrate interface [69].

Furthermore, the region of interest (ROI) for all experiments was confined to the central region of the specimen in order to minimize any boundary-layer effects associated with the edges of the test surface

The remaining environmental parameters were varied over the following ranges:

- $-20 \leq T_s \leq -7$°C
- $60 \leq RH \leq 90\%$

while the surface parameters R_a and θ_{ave} varied with the test surface under consideration according to the values listed in Tables 3.8 and 3.9, respectively.

To investigate the pertinent freezing phenomena, three classes of experiments were ultimately conceived: Types I, II, and III. Type I experiments were focused exclusively on generating quantitative data to characterize the bulk or aggregate behavior of inter-droplet freezing events in terms of the environment and surface parameters previously discussed. The Type II experiments were designed to provide insight into the fundamental microscopic mechanisms responsible for ice propagation between individual droplets; these experiments were therefore tailored to utilize the optical resolving power of the microscope to probe small length scales. Similarly, the Type III experiments were designed to probe the small time scales associated with ice nucleation and propagation within individual droplets; thus these experiments were designed to exploit the high speed capabilities of the digital microscopy system. An overview of the test matrices associated with each experiment type is presented in the following sections.

a. Type I Experiments

The Type I experiments comprised the largest fraction of experimental work conducted in this research. These tests were designed to provide quantitative visualization data on the aggregate motion associated with ice propagation between condensate droplets on the test surfaces. All experiments of this type were conducted with the digital microscopy system configured to a magnification of 5X, a full frame image size of 1280 by 1024 pixels, and an image acquisition rate of 100 Hz. The air temperature T_{air} and velocity U_{air} were held constant at 5°C and 5 m/s, respectively, for all tests.

For each test surface with its unique values of R_a and θ_{ave}, four target surface temperatures of -7, -10, -15, and -20°C and two target RH values of 60 and 90% were considered. This combination resulted in 8 unique testing conditions for each surface. To check for repeatability, each test was repeated a minimum of two times. The overall Type I test matrix for a single surface is shown in Table 3.10.

b. Type II Experiments

A subset of the conditions investigated with the Type I experiments were revisited under higher optical magnification in what were designated as the Type II experiments. As with the Type I conditions, RH values of 60 and 90% were considered and T_{air} and U_{air} were again held constant at 5°C and 5 m/s, respectively. The principle difference for the Type II experiments was that the optical microscopy system was reconfigured to use magnifications of 20X and 50X; otherwise, the imagine parameters were the same as those used in Type I tests (i.e. full frame images acquired at 100 Hz). In addition, only two surface temperatures were considered: -10 and -20°C. The overall Type II test matrix for a single surface is shown in Table 3.11.

Table 3.10: Type I test matrix for a surface with R_a and θ_{ave} for $T_{air} = 5°\text{C}$, $U_{air} = 5$ m/s, and 5X magnification

Test Surface	Target RH %	Target T_s °C	Test Number
R_a, θ_{ave}	60	-7	1
		-10	2
		-15	3
		-20	4
	90	-7	5
		-10	6
		-15	7
		-20	8

Table 3.11: Type II test matrix for a surface with R_a and θ_{ave} for $T_{air} = 5°\text{C}$, $U_{air} = 5$ m/s

Test Surface	Target RH %	Magnification	Target T_s °C	Test Number
R_a, θ_{ave}	60	20X	-10	1
			-20	2
		50X	-10	3
			-20	4
	90	20X	-10	5
			-20	6
		50X	-10	7
			-20	8

c. Type III Experiments

Consideration of the smaller time scales associated with ice nucleation and propagation within individual droplets was provided by a set of experiments classified as Type III. The same temperature and RH conditions used in the Type II experiments were also used in these tests: RH values of 60 and 90% RH as well as surface temperatures of -10 and -20°C were considered. And as in all other tests, T_{air} and U_{air} were held constant at 5°C and 5 m/s, respectively. The main difference between the Type III experiments and the others was that the temporal emphasis was shifted to utilize the high frame rate capability of the digital microscopy system. As such, full frame images (1280 by 1024 pixels) were acquired under 5X magnification at rates of 1000 Hz and at reduced resolution (1280 by 448 pixels) at 2367 Hz. The overall Type III test matrix for a single surface is shown in Table 3.12.

Table 3.12: Type III test matrix for a surface with R_a and θ_{ave} for $T_{air} = 5$°C, $U_{air} = 5$ m/s, and 5X magnification

Test Surface	Target RH %	Target T_s °C	Frame Rate Hz	Image Resolution Pixels	Test Number
R_a, θ_{ave}	60	-10	1000	1280 × 1024	1
		-20	2367	1280 × 448	2
	90	-10	1000	1280 × 1024	3
		-20	2367	1280 × 448	4

2. Testing Procedure

The general operational procedures for the test apparatus and DACS were effectively the same for all experiments conducted. A typical startup of the test rig proceeded with the following steps:

1. The wind tunnel was initially purged with dry nitrogen gas to remove any residual moisture in the system.
2. The air conditioning chiller was turned on and set to provide coolant to the primary and secondary cooling coils at whatever temperature was needed to maintain the desired air inlet temperature in the test section.
3. The thermal stage chiller was turned on and set to deliver −15°C coolant to the thermal stage.
4. After the nitrogen purge, the blower was turned on and adjusted to provide the target air velocity in the test section. At this point, the test surface temperature was placed under automatic control in the DACS program and set to track the test section air inlet temperature.
5. After the target air temperature had been reached, the steam boiler was activated (if needed) and manually adjusted to provide the target RH value. If the RH was too high for the desired conditions, dry nitrogen could be injected into the air stream through the moisture trim module or additional coolant could be supplied to the secondary cooling module.

The time required to reach steady operating conditions in the test apparatus was approximately one hour. Once steady environmental conditions were achieved, the DACS system was set to begin acquiring physical measurements from the test section instrumentation. These data were collected in one second intervals and written to a standard text file for subsequent processing. As these data were collected, a set of user-defined statements could be "stamped" or superimposed directly into the raw time series data to denote various observations during testing (such as the onset of condensation or freezing, for example).

The procedures used to acquire the image data varied slightly from one experiment type to the next. In all cases, the digital imaging system memory had to be configured prior to recording images. For the Type I and II experiments, the camera resolution was set at full frame (1280 by 1024 pixels) and a significant portion of the RAM in the imaging workstation was preallocated for approximately 20,000 images. With an acquisition speed of 100 Hz, the resulting record time for the Type I and II experiments was about 200 seconds. The Type III experiments used a similar configuration, except that the camera resolution was reduced to 1280 by 448 pixels for the tests conducted at a frame rate of 2367 Hz. With frame rates of 1000 and 2367 Hz, the average record time for the Type III experiments was on the order of 15 seconds. Because it was not known a priori when the actual freezing events would occur within the ROI, all images were written into a circular memory buffer with the camera control software. After the freezing event of interest occurred, the circular recording was stopped by a user-activated trigger and all images stored in the buffer up until that point in time could be saved.

To capture any effects associated with the distribution of liquid condensate on the ice propagation process, the condensation stage was implicitly considered in all experiments. For consistency, each test run was initiated with a completely dry surface. The dry state of the surface was ensured by using the automatic surface temperature control to track the air dew point temperature with a +10°C offset for a minimum of 10 minutes prior to the start of a given test. The digital microscopy system was also used to visually confirm that the surface was dry at the start of each experiment. Beginning with a dry test surface and the appropriate environmental conditions, a typical test run for the Type I and II experiments proceed as follows:

1. The circular recording process in the imaging system was initiated.

2. The desired surface temperature was entered into the DACS program and the automatic control quickly lowered the temperature of the test surface to the new setpoint value. Condensation on the surface was observed as the temperature crossed the dew point threshold and this point in time was denoted with user-defined stamp in the output data file.

3. After the target conditions were established, the user watched the condensation process proceed on the computer monitor until the first signs of freezing were observed within the ROI. This point was also noted in the data file with a user-defined stamp.

4. After all of the liquid within the ROI was frozen, the camera trigger was activated, ending the recording process and storing the image sequence of the freezing events in computer memory. The data file was stamped simultaneously with the activation of the trigger to ensure synchronization between the recorded images and the time series data acquired from the test section.

5. At this point, the experiment was complete and the surface temperature was reset to the initial pre-test value with the DACS program. This process melted the ice on the test surface and subsequently evaporated all remaining liquid, returning the surface to a dry state from which the next test could begin.

6. While the DACS was returning the test surface to its initial state, the newly recorded image sequence stored in RAM was briefly interrogated, cropped if

needed, and then offloaded onto the computer hard disk array for further processing. The computer memory was then reallocated for the next test.

The image acquisition procedure for the Type III experiments followed the same steps listed above. The only difference in the general testing procedure was that three freeze-thaw cycles were used prior to data collection to grow the liquid droplets large enough to be imaged with sufficient optical contrast and clarity. This was due to the specific camera settings required and lighting restrictions inherent to high frame rate image acquisitions through the microscope optics.

CHAPTER IV

DATA REDUCTION AND ANALYSIS METHODOLOGY

A combination of quantitative visualization and conventional experimental techniques were used to study ice propagation on surfaces undergoing dropwise condensation. The resulting visualization data consisted of image sequences of the freezing events on the test surfaces captured in situ by a digital microscopy system. Likewise, the environmental parameters in the test section were quantified by pyschrometric airflow and surface temperature measurements collected synchronously with the images captured for each experiment. This ultimately generated a profusion of data, the largest portion of which consisted of over 500 GB of digital image files. Processing this information required a substantial effort; therefore, the techniques and procedures used to reduce and analyze the experimental data are discussed in this chapter.

As discussed previously, the experimental work was divided into three main categories: Types I, II, and III. To analyze the Type I data, an optical phase tracking technique was developed which allowed the aggregate and inter-droplet dynamics of ice propagation to be quantified from a millimeter-sized, mesoscopic viewpoint. Conversely, the Type II and III experiments were tailored specifically to probe the microscopic length and time scales at which the underlying phenomena responsible for ice propagation under these conditions were thought to occur. The Type I experiments can be thought of as providing the means to *characterize* the freezing dynamics in terms of environmental parameters and substrate properties while the Type II and III experiments were used to *identify* the underlying mechanisms.

A. Type I Experiments

As previously illustrated in Figure 2.7, propagation of the ice phase among supercooled condensate droplets has been observed to occur in a semi-continuous fashion in what manifests as an aggregate or bulk freezing front [27]. This phase transition front is of considerable interest in the study of frost inception because it demarcates local regions on the surface where frost can and cannot begin to form. An example of this ice propagation phenomenon is shown in the digital image sequence presented in Figure 4.1. In this figure, the images were acquired with the digital microscopy system on an arbitrary copper stock surface used for camera calibration under a set of Type I experimental conditions (listed in the figure caption). The frozen droplets can be readily identified by their darker appearance owing to the higher opacity of ice relative to water. The time stamps associated with each image shown are referenced to time $t = 0$ s, which corresponds to the time at which ice was first observed within the region of interest (ROI). A high contrast overlay has been added to each image to emphasize the position and shape of the aggregate freezing front at each time step.

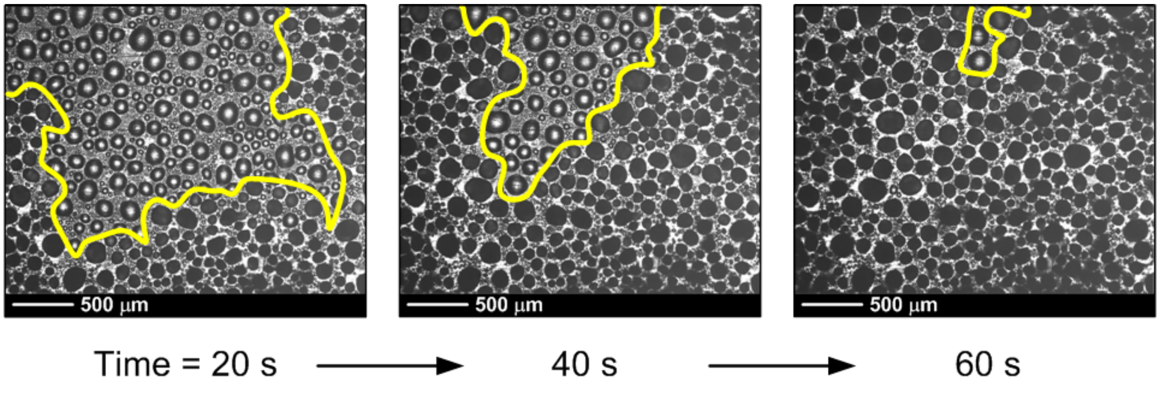

Figure 4.1: Images of freezing front position at three different times on a copper surface with $T_s = -10°\text{C}$, $T_{air} = 5°\text{C}$, and $RH = 65\%$

Two important characteristics of these aggregate freezing fronts can be observed directly from the example images shown in Figure 4.1. First, the motion of the bulk freezing front is clearly dependent on the distribution of liquid condensate on the surface and, therefore, tends to propagate in a complicated, non-uniform manner. Second, the non-uniform shape of the ice front indicates that both the magnitude and direction of freezing front velocity can vary substantially over the ROI. This latter observation naturally spurs the question of whether or not the freezing dynamics can even be meaningfully quantified so as to allow direct comparisons between different surfaces and environmental conditions. From a quantitative point of view, a combination of aggregate and inter-droplet velocity measurements offers the greatest value in terms of insight into the underlying phenomena. Unfortunately, an exhaustive literature search on this subject yielded no guidance on how this might be accomplished. This necessitated the development of an optical tracking technique, the details of which are outlined in the sections that follow.

1. Type I Data Analysis Overview

Although it was possible to roughly quantify the freezing front velocity by manually tracking the displacement of the ice-liquid interface from one frame to the next, carrying out such measurements for hundreds or thousands of images was impractical and prone to large uncertainties. Thus, it was clear that a more consistent and robust method of quantifying the evolution of the freezing fronts was needed. Automating the image analysis process was one way to accomplish this task. The simple fact that the opacity of ice differs from that of water offers a seemingly convenient way to track the freezing fronts. However, using raw images like those shown in Figure 4.1 in an automated tracking scheme presented several difficulties. To begin with, the intensity contrast between the periphery of the unfrozen and frozen droplets in these images was not high enough for conventional edge detection algorithms to reliably differentiate between the two. In addition, the intensity of the light reflected back through the unfrozen droplet centers can vary significantly with droplet size. Finally, the intensity of the light reflected from the substrate between droplets and through the unfrozen droplet centers was generally comparable, a fact which decreased the reliability of identifying discrete droplets on the surface.

To overcome these issues, a specialized technique was developed which exploited the optical properties of water droplets residing on reflective surfaces. This made it possible to directly measure the ice propagation velocity between droplets within an ROI that contained hundreds, or even thousands, of individual droplets. This approach produced statistical inter-droplet ice propagation velocity data as a function of environmental parameters and surface properties. Used with a novel temporal gradient technique, these data were further reduced to provide ice propagation velocity vector fields for each test condition and substrate combination. In this way, local aggregate freezing velocities could be evaluated for all cases and then compared on a consistent basis.

2. Optical Properties of Sessile Water Droplets and the Lensing Phenomenon

A water droplet residing on a surface shares many characteristics with a standard convex spherical lens. To illustrate these similarities, a brief discussion of geometric optics is warranted. Consider a generic convex lens with two principle radii of curvature as shown in Figure 4.2. In this scenario, a light ray traveling from left to right and parallel with the optical axis encounters the surface of incidence defined by R_1. The light ray forms an angle θ_{i1} with the normal of the surface at the point of intersection and is refracted by an amount θ_{r1} according to the relationship given by Snell's law

$$n_a \sin\theta_{i1} = n_b \sin\theta_{r1}$$

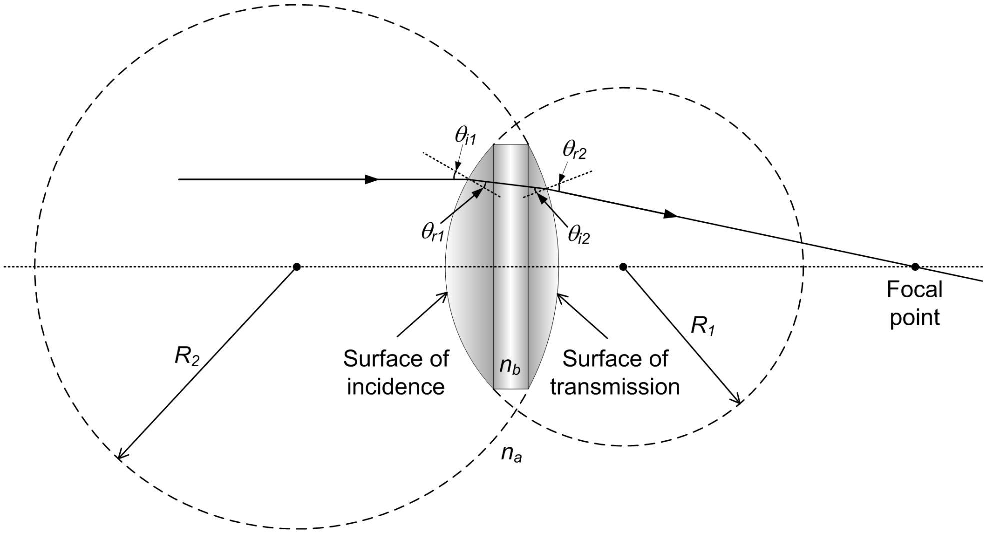

Figure 4.2: Illustration of a positive convex lens and surface curvature

or in the more familiar form

$$\frac{\sin\theta_{i1}}{\sin\theta_{r1}} = \frac{n_b}{n_a} \tag{4.1}$$

where n_a and n_b are the indices' of refraction of the surrounding medium and lens, respectively. Within the lens, the light ray forms an angle of incidence θ_{i2} with the normal of the surface of transmission defined by R_2 and upon emerging from the lens, is again refracted by an amount θ_{r2}. With the appropriate substitutions, the relationship given by Equation 4.1 is equally valid at the surface of transmission. The combined effect of this refractive phenomenon is that the collimated light entering the left side of the lens converges toward the so-called focal point located on the right side of the lens.

A more complete understanding of the optical properties of lenses is afforded by considering the ray trace of a generic lens shown in Figure 4.3. The distance from the principle planes of the lens to the focal point, known as the focal length f, can be expressed by the relationship [70]

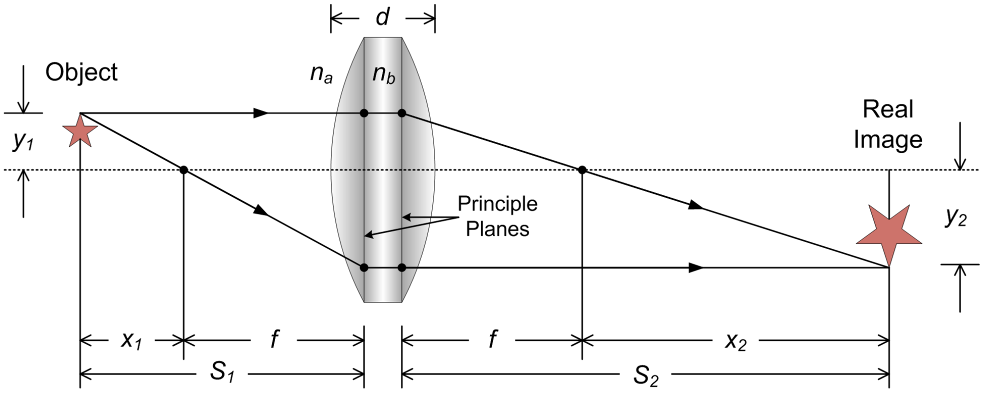

Figure 4.3: Ray trace of a real and inverted image formed by a positive convex lens

$$\frac{1}{f} = \left(\frac{n_b}{n_a} - 1\right)\left[\frac{1}{R_1} - \frac{1}{R_2} + \frac{(n_b - 1)\,d}{n_b R_1 R_2}\right] \tag{4.2}$$

Equation 4.2 is often referred to as the thick lens equation. If the thickness of the lens is negligible compared to the radii R_1 and R_2, then $d \rightarrow 0$ and Equation 4.2 can be simplified to

$$\frac{1}{f} = \left(\frac{n_b}{n_a} - 1\right)\left[\frac{1}{R_1} - \frac{1}{R_2}\right] \tag{4.3}$$

Furthermore, if the transmissive medium is air, then $n_a = 1$ and the lens equation becomes

$$\frac{1}{f} = (n - 1)\left[\frac{1}{R_1} - \frac{1}{R_2}\right] \tag{4.4}$$

where the subscript b has been dropped from the refractive index of the lens n_b. Equation 4.4 is widely known as the thin lens equation or the lensmaker's formula. Using the principle planes as a reference, it can also be shown that the lens equation can be cast in its more general Gaussian form as

$$\frac{1}{S_1} + \frac{1}{S_2} = \frac{1}{f} \tag{4.5}$$

or in the Newtonian form given by

$$f^2 = (S_1 - f)\,(S_2 - f) = x_1 x_2 \tag{4.6}$$

The focal length f calculated by Equations 4.2 - 4.6 is positive for converging lenses and negative for diverging lenses; hence, the convex lenses discussed thus far are sometimes referred to as *positive* lenses.

If the distance to the viewed object S_1 is greater than or equal to the focal length f, the image formed at S_2 will be magnified and inverted. The resulting image can be projected onto a physical surface such as a screen or camera sensor and is therefore known as a *real* image. However, if S_1 is less than f, a different situation arises because Equation 4.5 requires that $S_2 < 0$. In this instance, the image formed appears to be located a distance S_2 behind the lens, as illustrated in Figure 4.4. Because this image is not projected on the transmissive side of the lens, it is known as a *virtual* image. In both instances, the real and virtual images formed by positive lenses are magnified

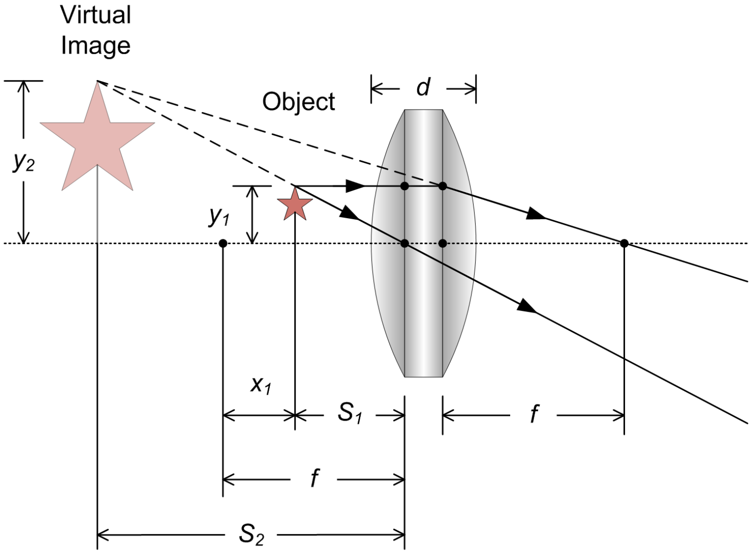

Figure 4.4: Ray trace of a virtual image formed by a positive convex lens

by an amount

$$M = \frac{y_2}{y_1}$$

From similar triangles in Figures 4.3 and 4.4, it can be seen that $\frac{y_2}{y_1} = -\frac{S_2}{S_1}$. Therefore, the lens magnification can be more appropriately expressed as

$$M = -\frac{S_2}{S_1} \tag{4.7}$$

Equation 4.7 indicates that the magnification of real images will always be negative, a fact that stems from the actual inversion of real images as illustrated in Figure 4.3. It follows that the magnification of virtual images will always be positive.

For this research, the geometric similarities between sessile water droplets and convex lenses were used to provide a reliable means of tracking the propagation of ice on the test surfaces. The basic concept behind this technique was to use the lens-like properties of unfrozen condensate droplets residing on the surface to focus the reflected light in a such a way that an automated image analysis routine would be able to easily resolve the locations and state (solid or liquid) of the individual droplets on the surface. The principles associated with this method are illustrated in Figure 4.5.

For the purposes of discussion, the droplet shown in Figure 4.5 is assumed to be perfectly hemispherical; that is, with a contact angle of 90°. In this arrangement, the water droplet mimics what is essentially a planar-convex lens. Incident light from the microscope objective lens or an external source illuminates the test surface as shown in the diagram. Owing to the luster of the test surfaces, a substantial fraction of this light is merely reflected from inter-droplet regions on the surface (outside of the droplet). Conversely, light that is incident on the droplet surface is refracted in accordance with Equation 4.1. In the absence of the surface, the light would ideally

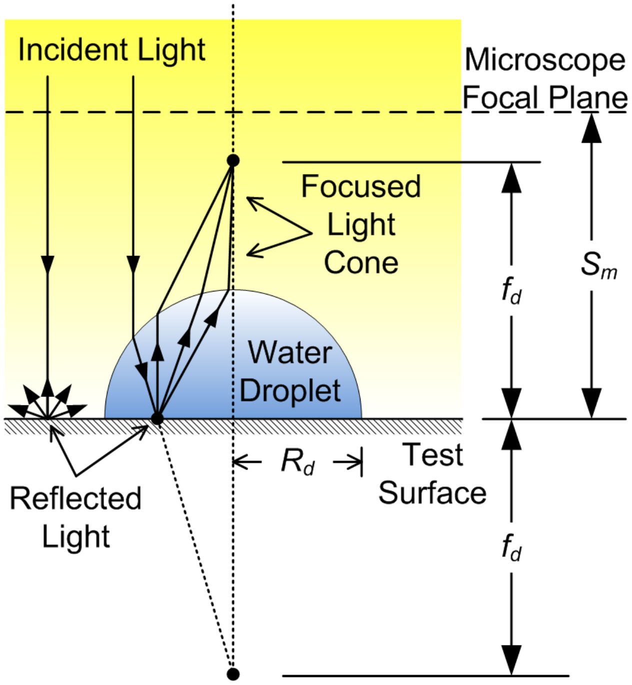

Figure 4.5: Schematic of the droplet lensing phenomenon used in the Type I image analysis

converge to the lower focal point shown; however, the substrate reflects the majority of light incident upon this interface as well. Notwithstanding any edge effects along the extreme periphery of the droplet or partial reflection at the air-droplet interface, much of light reflected internally is refracted upon reemerging from the droplet and converges to the upper focal point f_d. The focal length of the droplet can be calculated from Equation 4.4 by requiring that $R_1 \rightarrow \infty$ for the planar surface, which yields

$$f_d = -\frac{R_d}{n_w - 1} \tag{4.8}$$

where R_d is the radius of the hemispherical droplet and n_w, which is the refractive index of pure water with a value of 1.333. In accordance with the previous discussion, if the distance between the surface and the focal plane of the microscope is less than the focal length of the droplet, $S_m < f_d$, then a virtual image of underlying surface will result and the droplet will behave as what is effectively a magnifying glass. However, for $S_m \geq f_d$, the resulting image produced on the camera sensor will be real and consist of the cross sectional view of a concentrated cone of focused light that coincides with the geometric center of the droplet. As $S_m \to f_d$, the light cone reaches a minimum size and maximum intensity relative to the background. Therefore, for this so-called “lensing effect” to occur, a minimum microscope focal distance must be maintained. This minimum distance can be expressed in terms of the hemispherical droplet diameter $D_d = 2R_d$ as

$$S_{m,min} \approx \frac{D_d}{2\left(n_w - 1\right)} \tag{4.9}$$

where it is noted that because light is assumed to enter the droplet lens through the planar surface, $R_d < 0$ by sign convention and therefore $D_d = -2R_d$. The linear relationship between the minimum microscope focal distance and the droplet diameter is shown in Figure 4.6.

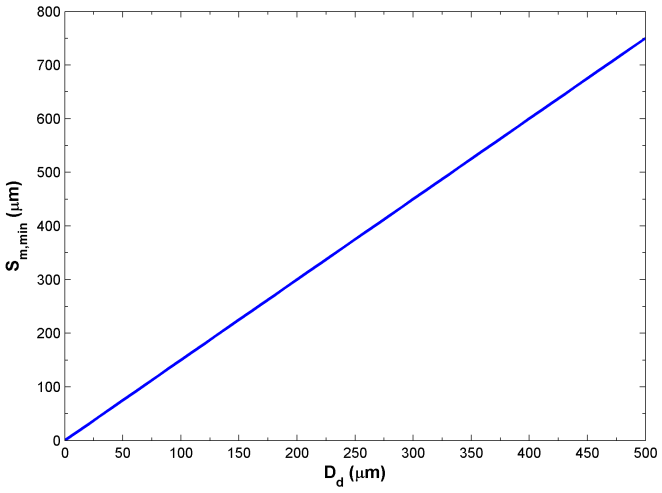

Figure 4.6: Minimum microscope focal distance versus droplet diameter required for lensing effect in hemispherical droplets

For a given droplet diameter, Figure 4.6 shows the minimum microscope focal distance required to produce the droplet lensing effect. In practice, this concept is applied to all droplets on the test surface simultaneously. Because diameter of the droplets continually increase during the condensation stage, the focal distance of the microscope must increase as well. This is achieved by manually adjusting the fine focusing unit on the microscope chassis until the focal distance is large enough to invoke the lensing effect in all droplets on the surface just prior to freezing. When used in conjunction with cross-polarized light to reduce glare from the substrate, a small high contrast region within each droplet is produced which undergoes a nearly instantaneous decrease in intensity when freezing occurs. An example of this technique applied to the same arbitrary stock surface shown in Figure 4.1 is presented in Figure 4.7.

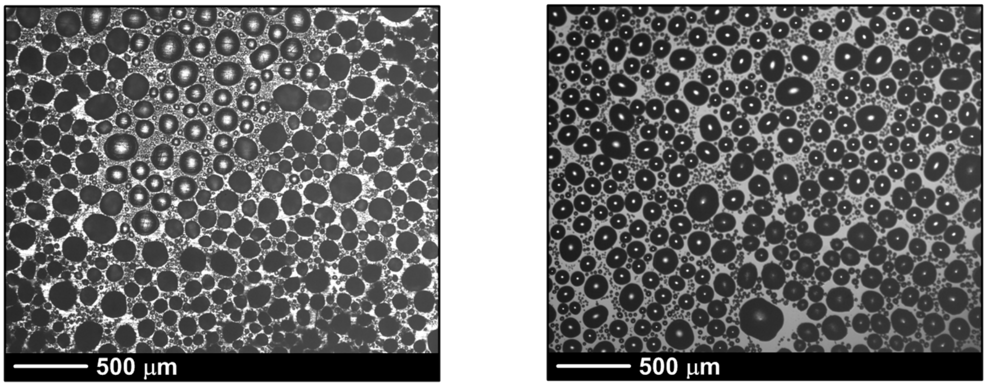

$S_m = 0$ $S_m \geq f_d$

Figure 4.7: Comparison between an image focused on the substrate ($S_m = 0$) and one invoking the droplet lensing effect ($S_m \geq f_d$) for the copper surface previously shown in Figure 4.1

Conceptually, differentiating between the frozen and unfrozen droplets in both images shown in Figure 4.7 is straightforward: the higher opacity of ice causes the frozen droplets to take on a notably darker appearance than the unfrozen droplets. However, directly comparing these images highlights the principle advantages offered by the successful application of the droplet lensing effect. In the left hand image, the microscope was focused on the substrate (i.e. $S_m = 0$); consequently, the focal distance of the microscope was less than the average droplet focal length and magnified virtual images of the substrate were observed through the larger droplets. Unfortunately, the intensity level of the droplet centers and many inter-droplet regions on the surface in this image were comparable, a fact which severely inhibited reliable edge detection in any associated image analysis procedure. Further complicating matters was the fact that the location and state of the smaller droplets could not be determined with high precision, if at all. Conversely, the microscope focal distance in the right hand image was adjusted to be slightly greater than or equal to the average droplet focal length (i.e. $S_m \geq f_d$). In this case, the observed foci were seen to be precisely aligned with the droplet centers and of much higher intensity than the background. The resulting optical system allowed the location and state of the vast majority of visible droplets on the surface, regardless of size, to be resolved with high precision.

The droplet lensing phenomenon was used to generate high contrast image sequences of the freezing events in all Type I experiments. The details behind the development of an automated image analysis algorithm designed to utilize this effect are discussed in the next section.

3. Type I Image Analysis

The grid-like, pixel-based structure of digital images makes them readily amenable to computer analysis. In general, a digital image can be represented mathematically by a matrix, the elements of which correspond to the location and intensity magnitude of each pixel in the image. For example, consider the very rudimentary digital image represented by the 3×3 unit pixel map shown in Figure 4.8. Assuming that the

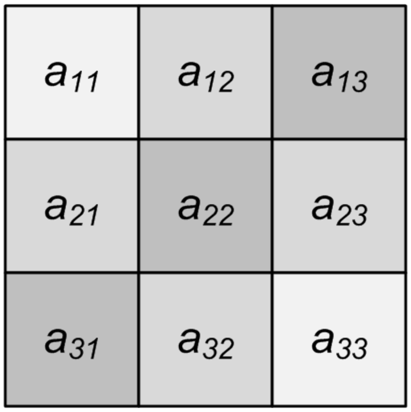

a_{11}	a_{12}	a_{13}
a_{21}	a_{22}	a_{23}
a_{31}	a_{32}	a_{33}

Figure 4.8: Unit pixel map of a simple digital image

intensity of each pixel can be represented by some real scalar value, this image can be mapped directly into a corresponding matrix **A**, defined as

$$\mathbf{A} = \begin{pmatrix} a_{11} & a_{12} & a_{13} \\ a_{21} & a_{22} & a_{23} \\ a_{31} & a_{32} & a_{33} \end{pmatrix} \tag{4.10}$$

where the value of each element a_{ij} represents the intensity magnitude of the corresponding pixel shown in Figure 4.8. As long as the pixels are uniformly spaced, the relative location of each element of **A** corresponds to the location of each pixel in the image. Monochromatic or gray scale images can be represented by a single matrix. For color images, however, as many as three equally-sized matrices may be needed to quantify the color of each pixel in terms of an additive color model such as the red-green-blue (RGB) scheme. The images acquired by the digital microscopy system for the Type I experiments were 8-bit grayscale images with a spatial resolution of 1280 pixels wide × 1024 pixels high. Each image sequence of size N acquired in this portion of the study could be suitably represented by a family of matrices $\mathbf{A}_{(1,2,\cdots,N)}$, each with dimensions of 1024 rows by 1280 columns and elements consisting of unsigned integers in the range of 0 to 255.

The application of the droplet lensing phenomenon during the image acquisition stage of experimentation provided the means to reliably track freezing events on the test surfaces. To analyze the resulting data, an image analysis algorithm was developed with MATLAB which could identify the location and state of each droplet on the surface on a frame-by-frame basis. Specifically, for each frame n in the sequence of N images, this program determined the location of each droplet k in Cartesian coordinates, $(x, y)_k^n$, and its corresponding state ψ_k^n, defined as

$$\psi_k^n = \begin{cases} 0 & \text{if frozen} \\ 1 & \text{if unfrozen} \end{cases} \tag{4.11}$$

In practice, determining $(x, y)_k^n$ and ψ_k^n was accomplished in four sequential steps:

1. calibration of each image $\mathbf{A}_n$ with a single reference image $\mathbf{A}^*$ of the dry surface under test
2. normalization of each image $\mathbf{A}_n$ with a pixel calibration multiplier and background subtraction
3. thresholding of each normalized image $\mathbf{A}_{n,norm}$ for conversion to binary images
4. distributed edge detection within each binary image $\hat{\mathbf{A}}_n$ for calculation of droplet centroid coordinates

To offset any bias in pixel intensity caused by the light source or camera sensor, a calibration matrix $\mathbf{C}_n$ for each raw image $\mathbf{A}_n$ was evaluated with respect to the reference image as

$$\mathbf{C}_n = \frac{\mathbf{A}_n(i, j)}{\mathbf{A}^*(i, j)} \tag{4.12}$$

where the i and j indices are used to denote that the matrix division operation was carried out on an elementwise basis. Each image was normalized by subtracting the final sequence image and then rescaling the resulting image to a consistent intensity level:

$$\mathbf{A}_{n,norm} = \mathbf{C}_n(i,j)\,|\mathbf{A}_n(i,j) - \mathbf{A}_N(i,j)| \tag{4.13}$$

where the condition $\mathbf{A}_{n,norm}(i,j) \leq 255$ was universally imposed. These normalized images where converted into the binary images $\hat{\mathbf{A}}_n$ by prescribing a maximum pixel intensity threshold ξ for each image sequence and comparing it to the intensity value of each pixel in a given frame. Based on this cutoff criterion,

$$\hat{\mathbf{A}}_n(i,j) = \begin{cases} 0 & \text{for } \mathbf{A}_{n,norm}(i,j) < \xi \\ 255 & \text{for } \mathbf{A}_{n,norm}(i,j) \geq \xi \end{cases} \tag{4.14}$$

All pixels that fell below this intensity threshold were set to zero while all other pixels were set to the maximum value of 255. The resulting binary images showed the light foci associated with the droplet centers as white spots on an otherwise black background. An example of the successful conversion from raw to a binary images with the image processing algorithm is shown in Figure 4.9.

After each image sequence was converted to the binary format shown in Figures 4.9(c) and (d), an edge detection algorithm was used to identify the coordinates of the droplet centers in each frame. The edge detection method used a gradient calculation for each binary image $\hat{\mathbf{A}}_n$ to locate discontinuities in pixel intensity. The gradient of a scalar field $p(x,y)$ is given by a vector field defined as

$$\nabla p = \frac{\partial p}{\partial x}\mathbf{e}_x + \frac{\partial p}{\partial y}\mathbf{e}_y = p_x\mathbf{e}_x + p_y\mathbf{e}_y \tag{4.15}$$

where $\mathbf{e}_x$ and $\mathbf{e}_y$ are unit normal vectors in the principle x and y directions, respec-

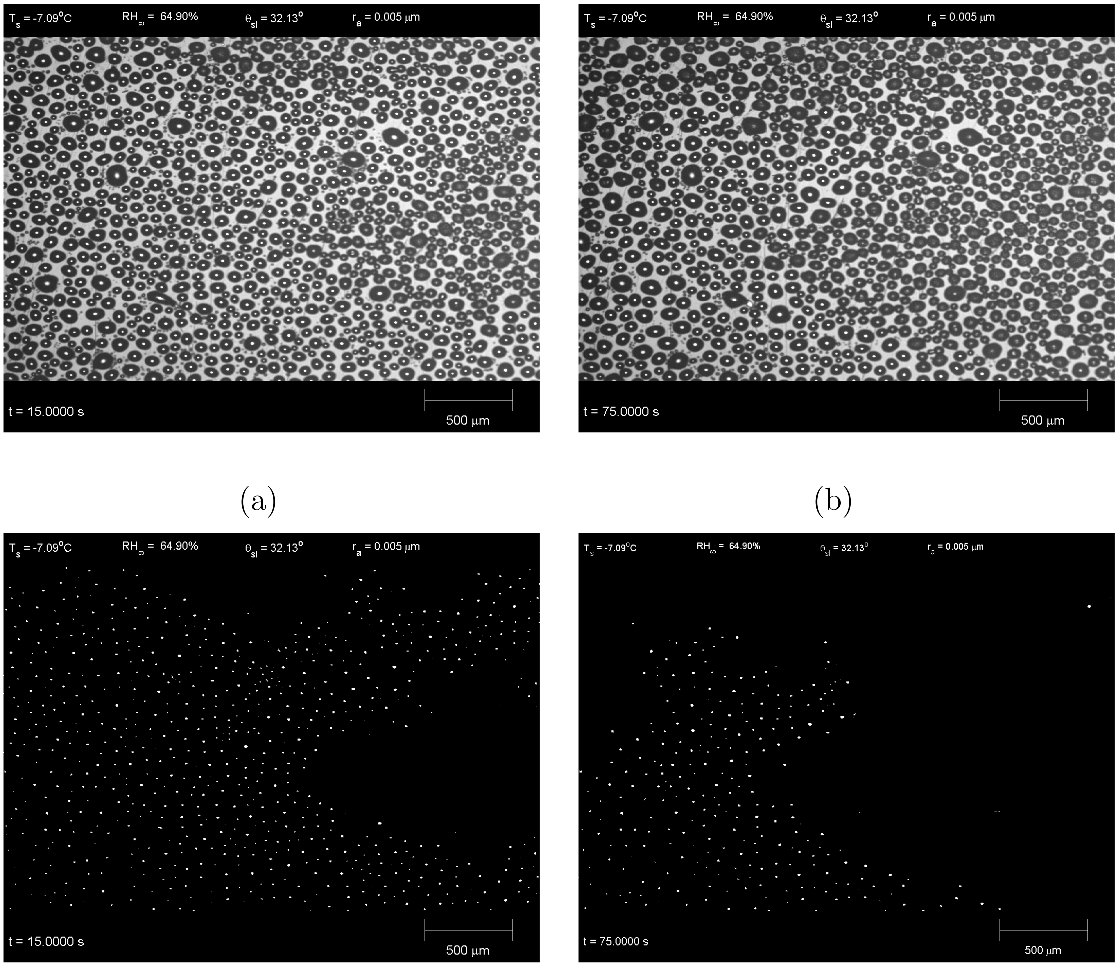

(a) (b)

(c) (d)

Figure 4.9: Calibrated raw and binary images of freezing on test surface SiA2: calibrated images at (a) $t = 15$ s and (b) $t = 75$ s; binary images at (c) $t = 15$ s and (d) $t = 75$ s

tively. The magnitude and direction of ∇p are given by

$$|\nabla p| = \sqrt{(p_x)^2 + (p_y)^2} \tag{4.16}$$

and

$$\phi_{\nabla p} = \tan^{-1}\left(\frac{p_y}{p_x}\right) \tag{4.17}$$

With Equations 4.15 - 4.17, the intensity gradient at each pixel location in a binary image $\hat{\mathbf{A}}_n$ could be evaluated numerically. Several numerical approximations to the spatial derivatives in Equation 4.15 have been crafted specifically for digital images [71]; for this study, the Sobel scheme was used. Referring to the unit pixel map shown in Figure 4.8, the Sobel derivatives for the central pixel (2,2) are defined in terms of offset central differences as

$$\begin{aligned} p_x &= (a_{31} + 2a_{32} + a_{33}) - (a_{11} + 2a_{12} + a_{13}) \\ p_y &= (a_{13} + 2a_{23} + a_{33}) - (a_{11} + 2a_{21} + a_{31}) \end{aligned} \tag{4.18}$$

According to this scheme, if $|\nabla p|_{(2,2)} \geq \alpha_T$ for some specified threshold α_T, then pixel (2,2) can be interpreted as an edge pixel. Application of this methodology to a single binary image $\hat{\mathbf{A}}_n$ produced the x and y coordinates for each pixel residing on the outer edge of each droplet's light focus, as shown in Figures 4.9 (c) and (d). With the outer boundary of each droplet's light focus known, the centroid of each focus was then computed as the area-weighted averages of the pixel x_p and y_p coordinates specific to each focus, namely

$$x_k = \frac{1}{\Omega}\int_{\Omega} x_p \; d\Omega \tag{4.19}$$

and

$$y_k = \frac{1}{\Omega}\int_{\Omega} y_p \; d\Omega \tag{4.20}$$

where Ω is the area of each droplet focus bound by the detected edge. Thus for the binary image sequence $\hat{\mathbf{A}}_{(1,2,\cdots,N)}$, the centroidal coordiantes given by Equations 4.19 and 4.20 were computed for each droplet k detected within each frame n to produce a time history of droplet location $(x, y)_k^n$ and state ψ_k^n on the surface during the freezing process. As a final step in the image analysis process, a vibration screening algorithm was applied to the $(x, y)_k^n$ data to eliminate any translational artifacts caused by microscope or test surface movements which may have occurred during the image acquisition process. For subsequent processing, the final $(x, y)_k^n$ and ψ_k^n data were mapped to the sequences represented by the vectors $\mathbf{R}_k^n$ and $\mathbf{\Psi}_k^n$ defined as

$$\mathbf{R}_k^n = \begin{pmatrix} x_k \\ y_k \end{pmatrix}_{1,2,\cdots,N} \tag{4.21}$$

and

$$\mathbf{\Psi}_k^n = \begin{pmatrix} \psi_k \end{pmatrix}_{1,2,\cdots,N} \tag{4.22}$$

4. Inter-Droplet Freezing Velocity Calculations

Because each image sequence was acquired at a uniform frequency, a finite time step Δt could be prescribed to each sequential pair of frames n and $n+1$. Therefore, knowing $\mathbf{R}_k^n$ and the variation of $\mathbf{\Psi}_k^n$ with time, it was possible to calculate the effective velocities of the inter-droplet freezing events. From a computational perspective, it was more efficient to analyze each data sequence in reverse; that is, starting with the frame N data and progressing backward in time to the first frame. In this way, the state variables $\mathbf{\Psi}_k^n$ were used to simply demarcate the single frame (and therefore the point in time) in which the corresponding droplets located at $\mathbf{R}_k^n$ began to freeze. Another important advantage offered by this approach was that it eliminated spurious inputs into the velocity calculations caused by the coalescence of water droplets prior to freezing. By analyzing the droplet position and state data in this manner, a single data array representing the freezing events of all K droplets in the entire image sequence was produced. This data structure was of the form

$$\mathbb{X}(k) = \begin{bmatrix} k & x_k & y_k & n_k & t_k \\ \vdots & \vdots & \vdots & \vdots & \vdots \\ K & x_K & y_K & n_K & t_K \end{bmatrix}_{k=(1,2,\ldots K)} \tag{4.23}$$

where each row in $\mathbb{X}(k)$ is referenced to a unique droplet number k, the coordinates x_k and y_k define the position of droplet k, n_k is the frame number in which freezing in droplet k is detected, and t_k is the absolute time corresponding to frame n_k as referenced from the first frame in the sequence.

To compute the inter-droplet freezing velocities, the natural progression of droplet freezing within the ROI had to be accurately tracked. This required the application of a spatial and temporal screening algorithm to the data array $\mathbb{X}(k)$ to identify the appropriate droplet-to-droplet interconnections. With respect to each droplet k, this screening process was carried out in two steps:

1. For each droplet $\hat{k}$ located within a distance r_ψ of droplet k, the inter-droplet spacing was calculated as

   $$\hat{r}_{k\to\hat{k}} = \sqrt{(x_k - x_{\hat{k}})^2 + (y_k - y_{\hat{k}})^2} \tag{4.24}$$

   The inter-droplet spacings defined by Equation 4.24 were assigned to the set $\hat{\mathcal{R}}_{k\to\hat{k}} = \{\hat{r}_{k\to 1}, \hat{r}_{k\to 2}, \ldots, \hat{r}_{k\to\hat{K}}\}$ where $\hat{K}$ is the total number of droplets located within a distance r_ψ of droplet k.

2. The time $t_{\hat{k}}$ corresponding to each droplet $\hat{k}$, as defined in the data sequence $\mathbb{X}(k)$, was used to calculate the freezing time differential between droplets k and

$\hat{k}$ as

$$\Delta\hat{t}_{k\to\hat{k}} = t_k - t_{\hat{k}} \tag{4.25}$$

where $\Delta\hat{t}_{k\to\hat{k}}$ was always positive because the data array $\mathbb{X}(k)$ was screened sequentially (i.e. backwards in time such that $t_k \geq t_{\hat{k}}$). Accordingly, the time differentials given by Equation 4.25 were combined to form the positive set $\Delta\hat{\tau}_{k\to\hat{k}} = \left\{\Delta\hat{t}_{k\to 1}, \Delta\hat{t}_{k\to 2}, \ldots, \Delta\hat{t}_{k\to\hat{K}}\right\}$.

Thus, the set $\hat{\mathcal{R}}_{k\to\hat{k}}$ which specified all proximal droplets on the surface that could have induced freezing in droplet k. Furthermore, the set $\Delta\hat{\tau}_{k\to\hat{k}}$ produced by the temporal screening process was then used to determine the single droplet $\hat{k}$ in $\hat{\mathcal{R}}_{k\to\hat{k}}$ that was responsible for triggering ice nucleation in droplet k. The neighboring droplet most likely to induce freezing in droplet k was assumed to be the droplet $\hat{k}$ which was in closest *temporal* proximity to droplet k; that is, the droplet corresponding to the minimum element of $\Delta\hat{\tau}_{k\to\hat{k}}$. Designating this droplet as $\hat{k}_\psi$, the center-to-center freezing velocity between droplets k and $\hat{k}_\psi$ could then be computed as

$$\hat{v}_{k\to\hat{k}_\psi} = \frac{\hat{r}_{k\to\hat{k}_\psi}}{\Delta\hat{t}_{k\to\hat{k}_\psi}} \tag{4.26}$$

Because Equation 4.26 is based on the droplet center-to-center length scale, $\hat{v}_{k\to\hat{k}_\psi}$ represents an *apparent* inter-droplet freezing velocity. While accurate in a global sense, this quantity does not account for the local length scales associated with the edge-to-edge inter-droplet spacing defined by

$$\Delta\hat{r}_{k\to\hat{k}_\psi} = \hat{r}_{k\to\hat{k}_\psi} - \left(r_k + r_{\hat{k}_\psi}\right) \tag{4.27}$$

where r_k and $r_{\hat{k}_\psi}$ are the radii of droplets k and $\hat{k}_\psi$, respectively. The inter-droplet spacing given by $\Delta\hat{r}_{k\to\hat{k}_\psi}$ is illustrated in Figure 4.10. In general, r_k and $\hat{r}_{\hat{k}_\psi}$ will be different and vary according to some droplet size distribution on the surface. In this

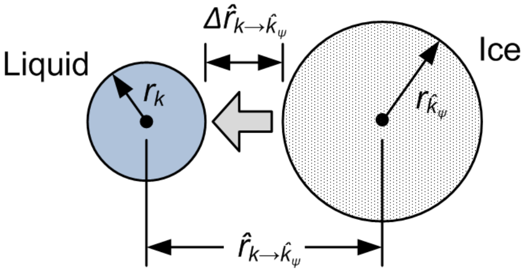

Figure 4.10: Local droplet-to-droplet spacing used for inter-droplet freezing velocity calculations

case, the inter-droplet freezing velocity is more appropriately expressed as

$$\hat{v}_{\Delta\hat{r}} = \frac{\Delta\hat{r}_{k\rightarrow\hat{k}_\psi}}{\Delta\hat{t}_{k\rightarrow\hat{k}_\psi}} \tag{4.28}$$

To apply Equation 4.28 to the data array $\mathbb{X}(k)$, the radius of each droplet just prior to freezing is needed. Unfortunately, this was not a practical quantity to obtain for a variety of reasons. First of all, individually measuring the radius of each droplet with image analysis software was impractical due to the very large number of manual interrogations that would be required to map out an entire image sequence. In addition, manual measurements were further complicated by the fact that the size and position of each unfrozen droplet was subject to change during an experiment due to growth via condensation as well as coalescence; thus, attempting to manually correlate the position of each droplet with the data stored in $\mathbb{X}(k)$ would not only be tedious, but also prone to potentially large errors. The ideal method for determining the droplet radii would have involved an automated image analysis routine capable of identifying the edges of each droplet one frame prior to freezing. However, several attempts to implement such functionality in the data analysis algorithms were met with limited success because the droplet edges were not in sharp focus, a direct consequence of invoking the droplet lensing phenomenon illustrated in Figure 4.5. To overcome these issues, the average droplet radius for each image sequence was used in the computation of a corrected inter-droplet freezing velocity defined as

$$\hat{v}_{k,\bar{D}} = \frac{\hat{r}_{k\rightarrow\hat{k}_\psi} - (\bar{r}_k + \bar{r}_k)}{\Delta\hat{t}_{k\rightarrow\hat{k}_\psi}} = \frac{\hat{r}_{k\rightarrow\hat{k}_\psi} - \bar{D}_k}{\Delta\hat{t}_{k\rightarrow\hat{k}_\psi}} \tag{4.29}$$

where $\bar{D}_k = 2\bar{r}_k$ is the average diameter of the droplets on the surface just prior to freezing. The value of $\bar{D}_k$ was obtained by manually analyzing a representative image from each sequence with the Java-based image processing program *ImageJ* developed at the National Institutes of Health (NIH). With the value of $\bar{D}_k$ known, the inter-droplet freezing velocities for all droplets were computed by Equation 4.29 with the following constraints:

1. The velocity calculations were applied progressively to the data array $\mathbb{X}(k)$ from frame N to the first frame in order to ensure that each droplet was interpreted as freezing only once during the analysis. In addition to filtering out duplicate or "false" freezing events from the velocity calculations, this process also provided the fidelity required to capture scenarios in which a single frozen droplet induced freezing in multiple nearby droplets.

2. If $\hat{r}_{k\rightarrow\hat{k}_\psi} \leq \bar{D}_k$ in Equation 4.29, it was assumed that the droplet diameter was neglible in the velocity calculation. Thus, all inter-droplet velocity calculations were carried out programmatically as

$$\hat{v}_{k,\bar{D}} = \begin{cases} \dfrac{\hat{r}_{k\rightarrow\hat{k}_\psi} - \bar{D}_k}{\Delta\hat{t}_{k\rightarrow\hat{k}_\psi}} & \text{for } \hat{r}_{k\rightarrow\hat{k}_\psi} > \bar{D}_k \\ \dfrac{\hat{r}_{k\rightarrow\hat{k}_\psi}}{\Delta\hat{t}_{k\rightarrow\hat{k}_\psi}} & \text{for } \hat{r}_{k\rightarrow\hat{k}_\psi} \leq \bar{D}_k \end{cases} \tag{4.30}$$

As an example of the results generated by the velocity calculation routines, a plot of the interpreted inter-droplet freezing pathlines for one experiment conducted with test surface SiA1 is shown in Figure 4.11.

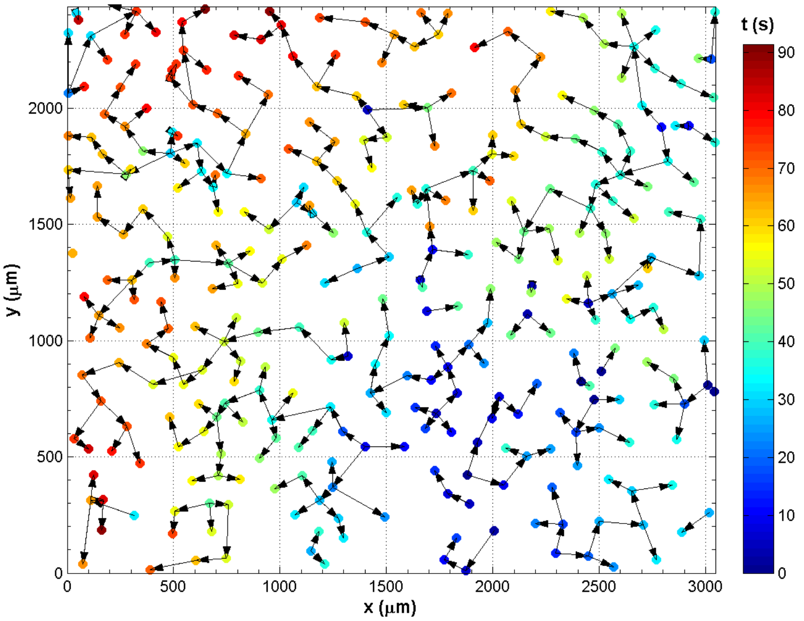

Figure 4.11: Inter-droplet freezing pathlines for surface SiA1 with $T_s = -7.1°\text{C}$, $T_{air} = 5.0°\text{C}$, and $RH = 64.9\%$

The data presented in Figure 4.11 display the freezing position (x and y coordinates) and freezing time of each droplet (indicated by the color of each data marker) while the local progression of inter-droplet freezing is demarcated by the arrows superimposed on the dataset. Although the direction of each arrow reflects the freezing direction, it should be noted that the arrow length does not represent the magnitude of the freezing velocity; as such, these arrows are *not* vectors. Rather, they are presented in this context to clearly highlight the so-called "freezing pathlines" that result from droplet-to-droplet interactions during ice nucleation. The data shown in this plot are representative of all Type I data acquired in this study.

The fidelity of the inter-droplet velocity calculations was assessed by comparing key freezing events in each raw image sequence to the corresponding pathline plot, such as that shown in Figure 4.11. For example, particular droplet-to-droplet freezing progressions in each raw image sequence were flagged as benchmark visual references and then used to evaluate the accuracy with which the velocity calculation methods could interpret the references. In all cases, the methodology described by Equations 4.23 - 4.30 was found to capture more than 90% of the benchmark freezing events within the ROI.

The freezing history shown in Figure 4.11 reveals a number of details about the freezing process on surfaces undergoing dropwise condensation. The motion of the aggregate freezing front can be inferred from the color of each data marker; those droplets which froze earliest in the image sequence are represented by the dark blue data markers while the color transitions from blue to green, green to yellow, and yellow to red represent the freezing of droplets at progressively later points in time. With this in mind, the plot indicates that the ice phase first entered the ROI from within the lower right quadrant of the frame and the corresponding freezing front propagated along a path roughly directed towards the upper left quadrant. Closer inspection of the local freezing history in the upper left quadrant shows that a few droplets in the latter sub-region froze independently of those in the former. This indicates that one or more of the droplets in that area nucleated to ice spontaneously, without being triggered by any detectable freezing front. As evidenced by the pathline arrows, these self-nucleated droplets induced freezing in the surrounding droplets, spawning new freezing fronts which propagated outward from the droplets of origin. With time, all freezing fronts on the surface merged as the entire viewable field of droplets completely froze.

A more detailed look at the freezing pathlines shown in Figure 4.11 highlights a feature that was observed in all Type I results: the direction of the freezing front does not necessarily coincide with the local direction of inter-droplet freezing. While the bulk motion of the aggregate freezing front typically moved in some general direction, the inter-droplet freezing processes tended to follow a more tortuous path that was clearly dependent on the condensate droplet distribution on the surface. In fact, the direction of the inter-droplet freezing events did not always coincide with the general direction of ice propagation; in many locations, the two are actually opposed to some extent. From these observations, it is evident that the complicated morphology of an aggregate freezing front (such as the one presented in Figure 4.1) is actually the result of the smaller scale droplet-to-droplet interactions which occur on the substrate.

The freezing history and pathline data shown in Figure 4.11 hold a great deal of quantitative information about the inter-droplet freezing process. For a given experiment, the use of Equations 4.23 - 4.30 produced a family of velocities which were computed on a droplet-to-droplet basis. To better understand the significance of these velocities as a group, frequency distributions of the inter-droplet velocities were generated for each experiment. Examples of the frequency distribution, based on total bin counts, for the same SiA1 experiment discussed previously are presented in Figure 4.12 for two different freezing velocity ranges and bin widths ($\Delta\hat{v}_{k,\bar{D}}$).

The histogram shown in Figure 4.12(a) indicates that a relatively wide range of velocities were computed with the data reduction algorithm; however, the well defined peak at the lower end of the velocity spectrum signifies the presence of a dominant set of freezing velocities for these particular test conditions and surface. A subset of the same velocity distribution, shown for a smaller velocity range and bin width in Figure 4.12(b), suggests that the calculated inter-droplet freezing velocities follow a log-normal distribution over the range of $0 \leq \hat{v}_{k,\bar{D}} \leq 25$ μm/s.

The inter-droplet freezing velocity distributions for all Type I experiments conducted in this study were similar to those presented in Figure 4.12. A mean inter-

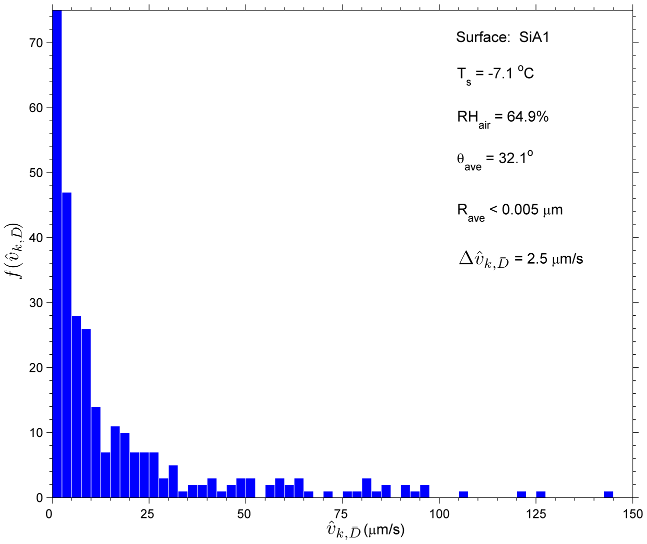

(a)

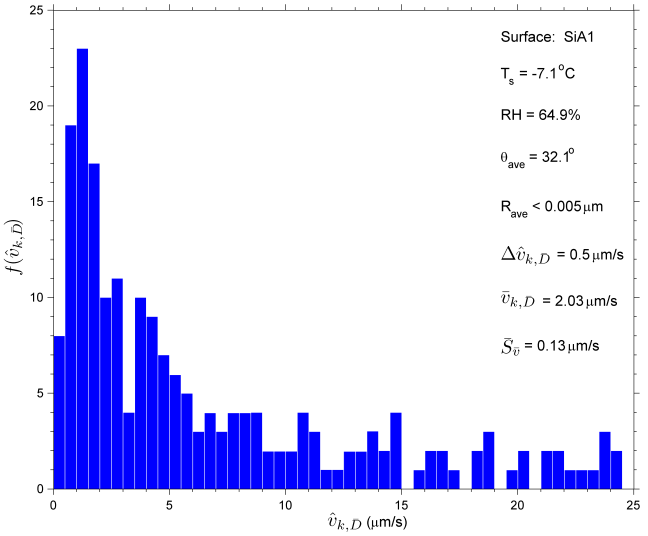

(b)

Figure 4.12: Inter-droplet freezing velocity distribution (total bin count) for surface SiA1 with $T_s = -7.1°\text{C}$, $T_{air} = 5.0°\text{C}$, and $RH = 64.9\%$: for (a) $0 \le \hat{v}_{k,\bar{D}} \le 150$ μm/s with $\Delta\hat{v}_{k,\bar{D}} = 2.5$ μm/s and (b) $0 \le \hat{v}_{k,\bar{D}} \le 25$ μm/s with $\Delta\hat{v}_{k,\bar{D}} = 0.5$ μm/s

droplet freezing velocity representative of the histographic data was defined with a weighted average given by

$$\bar{v}_{k,\bar{D}} = \frac{\displaystyle\int_0^{\hat{v}_\epsilon} f(\hat{v}_{k,\bar{D}})\hat{v}_{k,\bar{D}}\ dv}{\displaystyle\int_0^{\hat{v}_\epsilon} f(\hat{v}_{k,\bar{D}})\ dv} \tag{4.31}$$

where $\hat{v}_\epsilon$ is a cutoff velocity below which ϵ-percent of the total number of calculated velocities reside. Equation 4.31 can be equivalently expressed in discrete form as

$$\bar{v}_{k,\bar{D}} = \frac{\displaystyle\sum_{i=1}^{N_\epsilon} f_i \hat{v}_i}{\displaystyle\sum_{i=1}^{N_\epsilon} f_i} \tag{4.32}$$

where $\hat{v}_i$ is the nominal velocity magnitude associated with bin "i" and N_ϵ is the bin number corresponding to $\hat{v}_\epsilon$.

To minimize the impact that spuriously high values of $\hat{v}_{k,\bar{D}}$ or $\hat{v}_i$ had on Equations 4.31 and 4.32, ϵ was chosen so as to incorporate as large of a sample set as possible into the average freezing velocity calculations without artificially skewing the results. Through a series of comparisons with manual freezing velocity measurements taken from the Type II experiments[1], it was determined that the optimal value for ϵ was 75% for all cases[2]. For the example case shown in Figure 4.12, the corresponding cutoff velocity was $\hat{v}_\epsilon = 5$ μm/s and the resulting value of $\bar{v}_{k,\bar{D}}$ for this case was calculated to be 2.03 μm/s. If the freezing velocity distribution shown in Figure 4.12(b) were assumed to follow a Gaussian profile within the limited range of $0 \leq \hat{v}_{k,\bar{D}} \leq \bar{v}_\epsilon$, the random component of the uncertainty associated with $\bar{v}_{k,\bar{D}}$ could be estimated with

---

[1] The Type II experiments are considered in more detail in §B2 of this chapter.

[2] In other words, all data in the upper quartile of the freezing velocity distributions were excluded from the calculation of $\bar{v}_{k,\bar{D}}$.

the standard error of the sample defined by

$$\bar{S}_{\bar{v}} = \frac{S_{\bar{v}}}{\sqrt{\sum_{i=1}^{N_\epsilon} f_i}} \tag{4.33}$$

where $S_{\bar{v}}$ was the standard deviation of the data subset in the range $0 \leq \hat{v}_{k,\bar{D}} \leq \bar{v}_\epsilon$. For the example case presented in Figure 4.12, this equated to $\bar{S}_{\bar{v}} = 0.13$ μm/s. For a confidence interval of 95% about the weighted sample mean, the associated bounds of uncertainty could be expressed in terms of the standard error as $\mathcal{U}_p = \pm 1.96\bar{S}_{\bar{v}}$ [72], which for the example case considered thus far corresponded to $\mathcal{U}_p = \pm 0.25$ μm/s. Therefore, within this context, $\bar{v}_{k,\bar{D}}$ can be understood as representing the expected mean value of the inter-droplet freezing velocities detected on the surface while $\mathcal{U}_p$ represents an estimate of the precision associated with this mean. The topic of experimental uncertainty is addressed in more detail in Appendix A.

The representative example shown in Figures 4.11 and 4.12 highlights how the methodology outlined in the previous section was used to identify characteristic freezing velocities for each test surface and experimental condition. However, the magnitude of these so-called inter-droplet freezing velocities were much lower than the observed speed with which the aggregate freezing front propagated across the surface. For example, the time required for all droplets to freeze within the ROI shown in Figure 4.11 was 82.7 s. As noted previously, the freezing front in this particular experiment generally followed a path from the lower right to the upper left quadrant of the image. Using the total freeze time along with the minimum and diagonal dimensions of the ROI as lower and upper bounds (see Table 3.4) suggests that an average freezing velocity for this case should fall somewhere between 29.5 and 47.2 μm/s. This was confirmed by manually interrogating the image sequence with the *ImageJ* software and correlating the frame-by-frame freezing front displacement along one principle direction: the measured front velocity in this case was found to be about 41.5 μm/s. This aggregate velocity is more than one order of magnitude larger than the corresponding inter-droplet freezing velocity $\bar{v}_{k,\bar{D}}$ (Figure 4.12). Substantial differences such as these were observed for all experiments. Although these data clearly show that the inter-droplet freezing process plays a fundamental role in the evolution of ice on surfaces, these differences in velocity indicate that the larger scale motion of ice fronts must be dependent on other factors as well. Therefore, to better understand the constituents, the dynamics of aggregate ice fronts needed to be characterized independently.

5. Computation of Aggregate Freezing Velocity Fields

Although the *ImageJ* software was suitable for spot-checking the freezing front velocity as described above, it was virtually impossible to track the evolution of the front with detail due to its generally complicated morphology. Consequently, manual freezing front measurements could not be relied upon to provide any form of local velocity data which was representative of the entire ROI for the Type I experiments. To combat this issue, an implicit front tracking method was developed which exploited the topology of the surface formed by the droplet coordinates and associated freeze times. With this approach, it was possible to resolve the tortuous ice front interfaces with accuracy and calculate a corresponding freezing velocity vector field within the ROI.

The basic concept behind the front tracking method is straightforward: by knowing the x and y coordinates of each droplet as well as the time each droplet froze, the location of the ice phase as a function of time within the ROI was automatically defined. Fortunately, values for the droplet coordinates and freeze times were already available from the filtered data structure $\mathbb{X}(k)$ defined in Equation 4.23, namely the

(x_k, y_k, t_k) triad. The significance of these variables is made clear by plotting x_k, y_k and t_k on a set of three-dimensional coordinate axes. An example of one such plot for the SiA1 substrate example case considered thus far is shown in Figure 4.13.

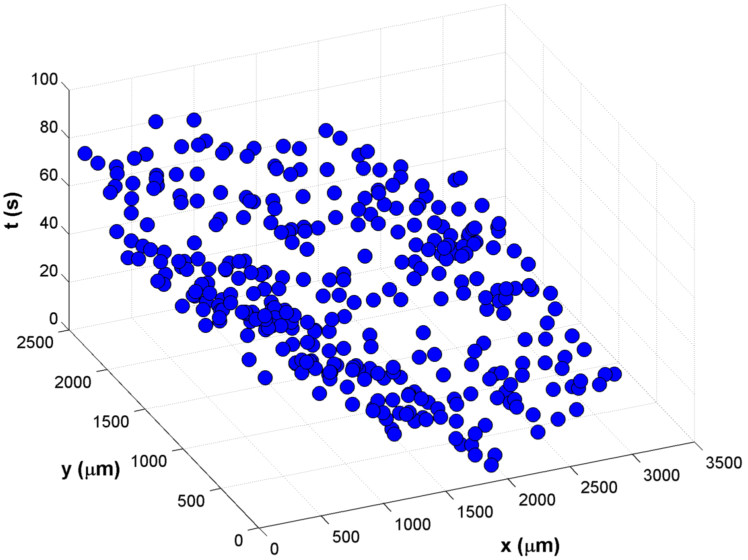

Figure 4.13: Droplet location versus freeze time for substrate SiA1 with $T_s = -7.1$°C, $T_{air} = 5.0$°C, and $RH = 64.9\%$

The evolution of the ice phase within the ROI can be directly inferred from the three-dimensional profile of the data shown in Figure 4.13. The actual location of a particular droplet is defined by the position of each data marker relative to the xy plane; likewise, the freezing time for that droplet is indicated by the data marker's position in the vertical t direction. The resulting trend formed by these data can be cast into a continuous function of two independent variables by determining the mathematical surface which best fits the data. The resulting "surface of best fit" defines an explicit relationship for the freeze time as a function of droplet position, $t_\psi = f(x, y)$. For this study, a surface fitting routine based on the MATLAB function *gridfit*[3] was adapted to the data reduction algorithm to numerically solve for the optimal $t_\psi = f(x,y)$ surface on a 50×50 node computational grid. The underlying surface fitting method used in *gridfit* was based on a linear tensor product interpolation scheme coupled with a Laplacian regularization technique [73]; with this arrangement, it was possible to adjust the degree of smoothness of the resulting surface.

In each case, the coefficient of determination (R^2) was used to assess how well the surface fit the data. By adjusting the smoothness parameter in the surface fitting routine, it was possible to drive the R^2 value towards unity, effectively fitting the surface through every data point. This, however, tended to generate surfaces which were excessively rough and too “noisy” to be meaningful for further analysis. It was found through trial and error that R^2 values falling in the range of 0.80 - 0.92 generally produced the best results; therefore, the topological regression program used in this study was designed to preferentially target R^2 values near 0.90 by iteration. Figure 4.14 shows a representative example of the results of this process applied to the SiA1 dataset previously discussed in conjunction with Figure 4.13.

With the $t_\psi = f(x,y)$ surface established, the bulk motion of the freezing front could be interpreted by projecting isocontours of time from the surface onto the xy plane. An example of the regression-derived contours for the SiA1 experiment considered previously is shown in Figure 4.15. Figure 4.15(a) shows the continuous $t_\psi = f(x,y)$ surface generated from the dataset along with isocontours of time projected onto the xy plane. Locally, these temporal contour projections correspond to the actual position of the ice front at any point in time. A 2-D view of these contours in the xy plane is shown in Figure 4.15(b); in this plot, the contours are labeled and

---

[3] The source code for *gridfit* is available under the FreeBSD open source license from The MathWorks™at `http://www.mathworks.com/matlabcentral/`.

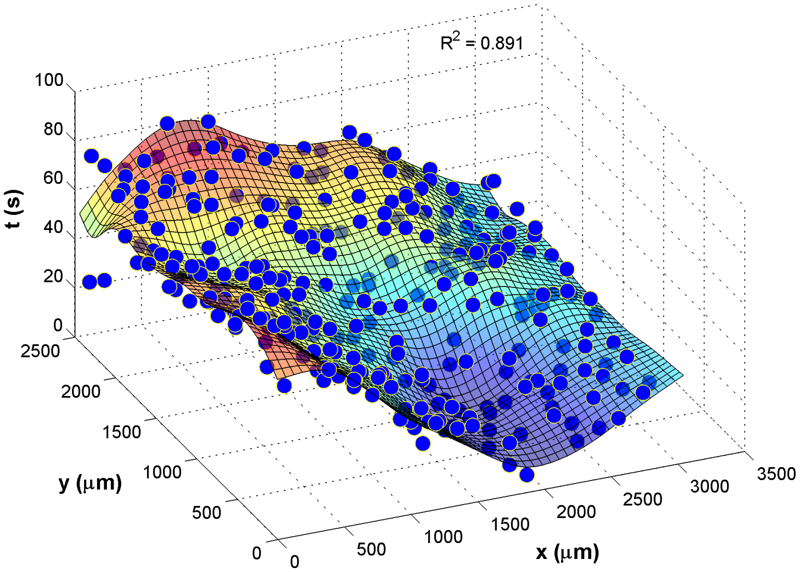

Figure 4.14: Surface of best fit through droplet location and freeze time data for substrate SiA1 with $T_s = -7.1°\text{C}$, $T_{air} = 5.0°\text{C}$, and $RH = 64.9\%$

colored by the freezing time t_ψ.

Compared to the freezing pathline plot shown in Figure 4.11, Figure 4.15(b) provides a more intuitive view of the ice propagation process from an aggregate vantage point. In this plot, the evolution of the individual contours agree with the previous findings which showed that ice generally propagated from the lower right to the upper left quadrant of the ROI for this particular experiment. This plot also reveals that the morphology of the ice front is dynamic and can be quite complicated; information of this sort was not readily obtainable from the results of the inter-droplet freezing velocity calculations. It can also be seen that a single, continuous primary ice front propagated across most of of the ROI; however, discontinuities in the contours at a few different locations indicate the emergence of several smaller ice fronts at the periphery of the ROI. The shape and increasing time value associated with those con-

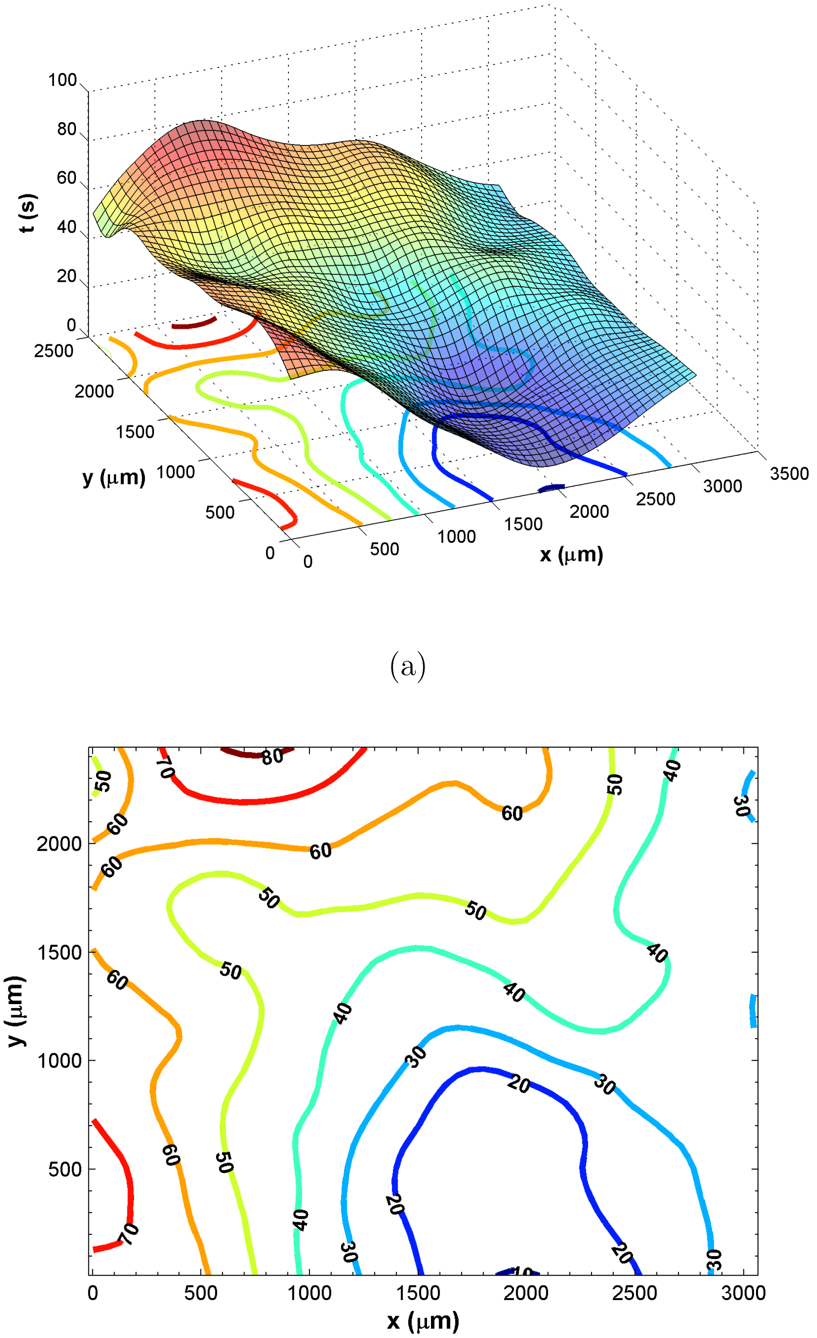

(a)

(b)

Figure 4.15: $t_\psi = f(x, y)$ surface with temporal isocontours (a) and corresponding 2-D projection showing freezing front evolution (b) for substrate SiA1 with $T_s = -7.1°\text{C}$, $T_{air} = 5.0°\text{C}$, and $RH = 64.9\%$

tours shows how the additional freezing fronts eventually merged with the primary front to complete the freezing process. Although it should be noted that the observations presented here are for the particular SiA1 experiment discussed thus far, they are representative of all experiments conducted in this study. The accuracy of the front tracking method was checked by directly comparing the resulting 2-D contour plot for a given experiment (see Figure 4.15(b)) with the appropriate frames of the corresponding raw image sequence: there was excellent agreement between the two in all cases.

Because the temporal isocontours such as those shown in Figure 4.15(b) corresponded directly to the position of the freezing front with time, the spatial separation between them must be proportional to the local velocity of the front. To properly define a front's velocity, its potentially dynamic morphology must be considered. This is illustrated in Figure 4.16 were the shapes of two arbitrarily moving interfaces at times t_1 and t_2 are shown: for comparison, one front has been assumed to be perfectly straight ("planar") while the other features a more complicated profile ("non-planar").

The absolute velocity $\mathbf{V}$ of any point along the fronts shown in Figure 4.16 can be resolved into an orthogonal set of normal and tangential velocity vectors $\mathbf{V}_N$ and $\mathbf{V}_T$, respectively. In this case, the normal velocity $\mathbf{V}_N$ is simply the component of $\mathbf{V}$ which is oriented perpendicular to the front at a given point; as such, it serves as the reference which establishes the orthogonal unit basis vectors aligned in the normal and tangential directions. In order for the shape of the planar front shown in Figure 4.16 to remain unchanged while evolving, $\mathbf{V}_T$ must be zero such that $\mathbf{V} = \mathbf{V}_N$. Accordingly, all points along the interface have the same velocity and the dynamics of the front can be characterized in terms of stable, *translational* motion. For the non-planar front, however, the role of $\mathbf{V}$ is different as it generally does not delineate the perceived

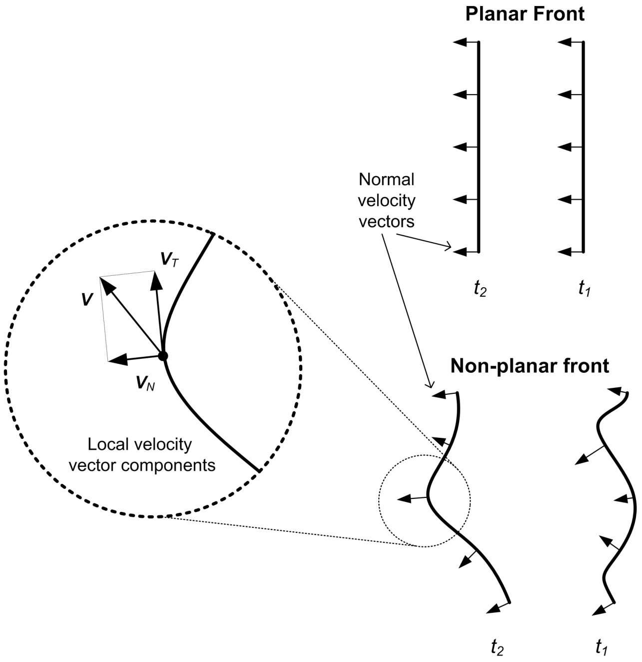

Figure 4.16: Local velocity vector components for planar and non-planar propagating fronts

motion of the interface. This concept is illustrated within the inlay of Figure 4.16 which shows that in regions where the shape of the front changes as it propagates, $\mathbf{V}_T$ must be non-zero to account for the "stretching" or "contraction" of the interface associated with non-zero curvature. Thus, for non-planar fronts, $\mathbf{V} \neq \mathbf{V}_N$ in general both *translational* ($\mathbf{V}_N$) and *distortional* ($\mathbf{V}_T$) velocity components at any point along this unstable interface are required to properly characterize the dynamics of the front. The physical significance of the resultant vector $\mathbf{V}$ can therefore be strictly interpreted as the instantaneous rate and direction with which any *point* along an interface moves.

By extending the previous discussion to a generic phase change process, it may be inferred from Figure 4.16 that the local rate at which a new phase propagates *into* the surrounding parent phase is given exclusively by the normal velocity of the resulting interface. For the substrate freezing processes considered in this study, a central parameter of interest is therefore the local normal velocity of ice fronts like those shown in Figure 4.15. Conceptually, the normal velocity associated with these fronts can be computed by simply measuring the local, point-wise displacement of the ice front between any two time steps. With the position of the ice front know, this could, in theory, be achieved by

1. fitting smooth splines through the xy data at each time step to generate a family of parametric curves which describe the shape and location of the freezing front over time

2. evaluating the sequential, point-wise displacement of these curves from one time step to the next

Unfortunately, there are some principles difficulties inherent to such a method. The generally non-planar shape of the freezing front renders this approach susceptible to considerable error for all but the simplest cases because the curvature of the solid-liquid interface may change significantly over short distances. If $\Gamma(t)$ denotes the parameterized set of xy coordinates along the interface at any time t, then point-wise computation of the associated normal velocity vectors $\mathbf{V}_N(t)$ with this technique would require the use of a discrete finite differencing scheme involving the neighboring contours $\Gamma(t+\delta t)$ and $\Gamma(t-\delta t)$. As the calculations proceed through time, the accuracy of this method would be progressively impacted by truncation error, particularly in regions of rapidly changing curvature. In addition, handling multiple freezing fronts with this approach presents a considerable challenge, particularly in terms of properly tracking and resolving the collision of two or more interfaces.

To circumvent these issues, a more direct method was conceived to compute the local aggregate ice front velocities on the substrate. The resulting technique was based on the premise that all of the information needed to completely resolve the freezing velocity vector field within the ROI is intrinsically contained within the topology of each $t_\psi = f(x, y)$ surface, such as the one shown in Figures 4.14 and 4.15(a). The slope of the t_ψ surface in a direction normal to the temporal isocontours (and thus the freezing fronts) at all points in space and time is defined by the gradient of t_ψ,

$$\nabla t_\psi = \frac{\partial t_\psi}{\partial x}\mathbf{e}_x + \frac{\partial t_\psi}{\partial y}\mathbf{e}_y \tag{4.34}$$

Accordingly, Equation 4.34 may be used to define a unit normal vector at any point by

$$\mathbf{n} = \frac{\nabla t_\psi}{|\nabla t_\psi|} \tag{4.35}$$

and the local curvature of any isocontour may be evaluated with the divergence of $\mathbf{n}$,

$$\kappa = \nabla \cdot \frac{\nabla t_\psi}{|\nabla t_\psi|} \tag{4.36}$$

As long as the vector-valued function given by Equation 4.34 can be parameterized, it can be shown that the x and y components of ∇t_ψ represent the inverse magnitudes of the x and y components of the absolute front velocity, namely

$$\frac{\partial t_\psi}{\partial x} = \left(\frac{\partial x_\Gamma}{\partial t}\right)^{-1}$$
$$\frac{\partial t_\psi}{\partial y} = \left(\frac{\partial y_\Gamma}{\partial t}\right)^{-1}$$

Therefore, the the absolute velocity vector can be defined as

$$\mathbf{V} = \frac{\partial x}{\partial t}\mathbf{e}_x + \frac{\partial y}{\partial t}\mathbf{e}_y = \left(\frac{\partial t}{\partial x}\right)^{-1}\mathbf{e}_x + \left(\frac{\partial t}{\partial y}\right)^{-1}\mathbf{e}_y \tag{4.37}$$

where the subscripts ψ and Γ have been dropped for convenience. The component-wise reciprocity between ∇t and $\mathbf{V}$ indicates that these vectors are defined as long as $\frac{\partial t}{\partial x}$ and $\frac{\partial t}{\partial y}$ are non-zero and that they are co-linear when $\frac{\partial t}{\partial x} = \frac{\partial t}{\partial x}$; otherwise, they differ in direction by the angle β as shown in Figure 4.17 and defined by

$$\beta = \beta_V - \beta_{\nabla t} \tag{4.38}$$

where

$$\beta_V = \tan^{-1}\left(\frac{\left(\frac{\partial y}{\partial t}\right)}{\left(\frac{\partial x}{\partial t}\right)}\right) \tag{4.39}$$

and

$$\beta_{\nabla t} = \tan^{-1}\left(\frac{\left(\frac{\partial t}{\partial y}\right)}{\left(\frac{\partial t}{\partial x}\right)}\right) \tag{4.40}$$

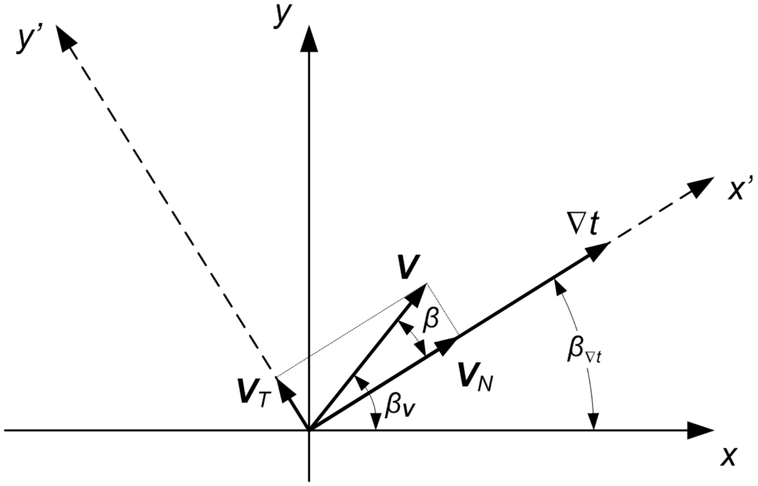

Figure 4.17: Freezing front velocity vectors and coordinate system transformation used for the temporal gradient front tracking technique

Figure 4.17 also shows how $\mathbf{V}$ can be resolved into the normal and tangential components $\mathbf{V}_N$ and $\mathbf{V}_T$, respectively. Recall that it is $\mathbf{V}_N$, not $\mathbf{V}$, that locally defines the speed and direction with which the front propagates. Thus, the focus is shifted towards determining the magnitude and direction of $\mathbf{V}_N$. The direction of $\mathbf{V}_N$ is always the same as ∇t; therefore its direction in the $< x, y >$ coordinate system is simply given by $\beta_{\nabla t}$ defined in Equation 4.40[4]. With finding $|\mathbf{V}_N|$ the only

---

[4] The co-linearity shared between $\mathbf{V}_N$ and ∇t also implies that in a normalized vector space, both vectors can be conceptualized as being eigenvectors of some transformational matrix $\mathbb{M}$ with the eigenvalue λ and for which $\mathbb{M}\vec{\nabla} t = \lambda \nabla t = \mathbf{V}_N$ [74].

remaining task at hand, the problem becomes one of establishing a coordinate-system-independent relationship between ∇t and $\mathbf{V}_N$ in terms of its normal and tangential components.

Considerable simplification to the problem of finding $|\mathbf{V}_N|$ can be achieved by invoking a transformation to the orthogonal coordinate system $< x', y' >$ shown in Figure 4.17. The $< x', y' >$ coordinate system is oriented such that the y' component of ∇t is always zero; as such, this is a rotational transformation only with the angle between the x and x' axes given by $\beta_{\nabla t}$. Equations 4.34 and 4.37 can be rewritten in matrix notation to highlight their equivalence in each coordinate system:

$$\nabla t = \begin{bmatrix} \dfrac{\partial t}{\partial x} & 0 \\ 0 & \dfrac{\partial t}{\partial y} \end{bmatrix} \begin{bmatrix} \mathbf{e}_x \\ \mathbf{e}_y \end{bmatrix} = \begin{bmatrix} \dfrac{\partial t}{\partial x'} & 0 \\ 0 & 0 \end{bmatrix} \begin{bmatrix} \mathbf{e}_{x'} \\ \mathbf{e}_{y'} \end{bmatrix} \tag{4.41}$$

and

$$\mathbf{V} = \begin{bmatrix} \dfrac{\partial x}{\partial t} & 0 \\ 0 & \dfrac{\partial y}{\partial t} \end{bmatrix} \begin{bmatrix} \mathbf{e}_x \\ \mathbf{e}_y \end{bmatrix} = \begin{bmatrix} \dfrac{\partial x'}{\partial t} & 0 \\ 0 & \dfrac{\partial y'}{\partial t} \end{bmatrix} \begin{bmatrix} \mathbf{e}_{x'} \\ \mathbf{e}_{y'} \end{bmatrix} \tag{4.42}$$

In addition, Equation 4.42 can be alternately expressed in terms of the normal and tangential front velocities as

$$\mathbf{V} = \begin{bmatrix} \mathbf{V}_N \\ \mathbf{V}_T \end{bmatrix} = |\mathbf{V}| \begin{bmatrix} \cos\beta & 0 \\ 0 & \sin\beta \end{bmatrix} \begin{bmatrix} \mathbf{e}_{x'} \\ \mathbf{e}_{y'} \end{bmatrix} \tag{4.43}$$

When $\beta = 0$, Equation 4.43 requires that

$$\mathbf{V}\Big|_{\beta=0} = |\mathbf{V}| \begin{bmatrix} 1 & 0 \\ 0 & 0 \end{bmatrix} \begin{bmatrix} \mathbf{e}_{x'} \\ \mathbf{e}_{y'} \end{bmatrix} = \mathbf{V}_N \tag{4.44}$$

Thus, with Equations 4.41 and 4.42

$$\nabla t = \frac{\partial t}{\partial x'} \mathbf{e}_{x'} \tag{4.45}$$

and

$$\mathbf{V}_N = \frac{\partial x'}{\partial t}\mathbf{e}_{x'} \tag{4.46}$$

Because ∇t and $\mathbf{V}_N$ are co-linear, their dot product must be unity:

$$\mathbf{V}_N \cdot \nabla t = |\mathbf{V}_N||\nabla t|\cos(0) = 1 \tag{4.47}$$

This may be further validated by evaluating the product of the vector components given by Equations 4.45 and 4.46, namely

$$|\mathbf{V}_N||\nabla t| = \left(\frac{\partial x'}{\partial t}\,\frac{\partial t}{\partial x'}\right) = 1 \tag{4.48}$$

Equation 4.48 provides an expression for the normal freezing front velocity at all points in space and time that is independent of the coordinate system used. It is rewritten explicitly for convenience here as

$$|\mathbf{V}_N| = \frac{1}{|\nabla t|} \tag{4.49}$$

Equation 4.49 is equivalent to the first order, non-linear partial differential equation (PDE) otherwise known as the eikonal or Hamilton-Jacobi equation, depending on whether the context stems from the subject of geometric optics or classical mechanics, respectively [75–77]. It may be expressed in a more general form as

$$\left(\frac{\partial u}{\partial \zeta}\right)^2 + \left(\frac{\partial u}{\partial \eta}\right)^2 = F(\zeta,\eta)^{-2} \tag{4.50}$$

where $u(\zeta,\eta)$ is generally sought given some function $F(\zeta,\eta)$. A class of level set methods known as fast marching methods can be used to numerically solve this PDE for u given some speed function F; in fact, this technique is well suited for the numerical solution of many types of moving boundary problems featuring complicated, multi-dimensional interface dynamics [78, 79]. In physical terms, the eikonal equation defines the field variable F in terms of the potential u, or vice versa. For the application at hand, u and F in Equation 4.50 correspond to t and $|\mathbf{V}_N|$ in Equation 4.49, respectively. Thus, the relationship given by Equation 4.49 can be understood to equate the normal velocity magnitude of the ice front $|\mathbf{V}_N|$ to the measured "temporal" potential given by t. With t derived from the experimental data acquired in this study, the representative PDE does not need to be solved; rather, $|\mathbf{V}_N|$ is the variable of interest and may be evaluated directly by computing the inverse of the magnitude of ∇t.

For this study, Equation 4.49 was used with the fitted t_ψ surface from each experimental dataset to numerically resolve the local freezing front velocity field over the entire ROI. Use of this approach was critical because it allowed the aggregate freezing dynamics of all experiments to be evaluated locally and compared on an equal footing. An example of the results generated by this analysis is shown in Figure 4.18 for the sample case previously considered: Figures 4.18(a) and (b) show the same vector and contour data, with the latter featuring the addition of the freezing position of the droplets. The vector calculations for all cases were carried out on the same 50×50 node grid used for the t_ψ surface fitting process.

The vector-contour plot shown in Figure 4.18(a) provides a number of intuitive insights into the aggregate freezing process on the substrate. To begin with, the vectors clearly delineate the local trajectory of the freezing front over the entire ROI and are in full agreement with the observations previously noted from Figures 4.11 and 4.15(b). These vectors also reveal that the freezing velocity magnitude was not generally uniform across the substrate, indicating that the ice front experienced acceleration and deceleration as it propagated through certain regions. The most pronounced changes in velocity invariably coincided with locations where the front curvature changed appreciably as well; thus, the generally dynamic, non-planar mor-

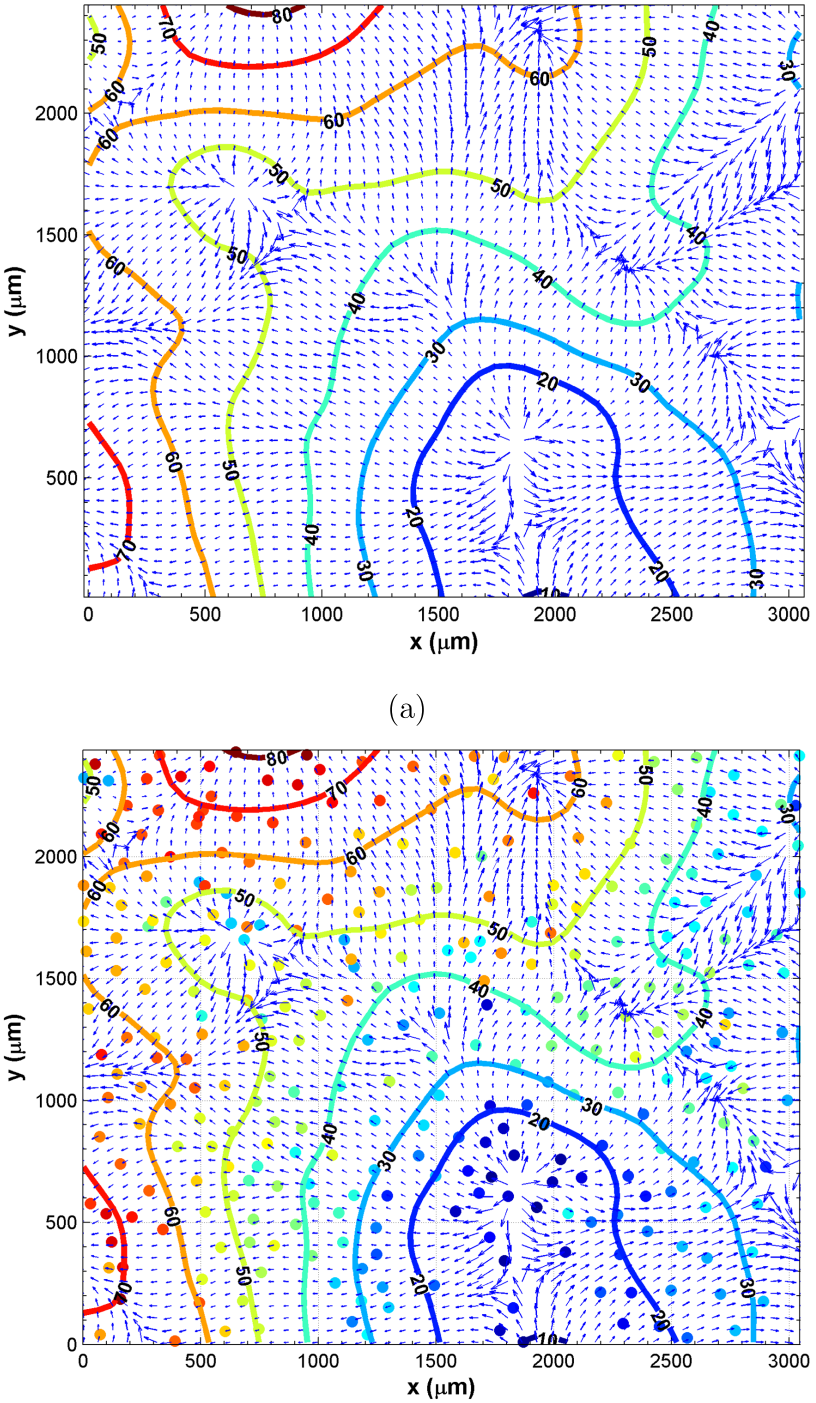

(a)

(b)

Figure 4.18: Freezing front normal velocity vectors $\mathbf{V}_N$ and front position Γ at discrete time intervals without (a) and with (b) droplet positions for substrate SiA1 with $T_s = -7.1°\text{C}$, $T_{air} = 5.0°\text{C}$, and $RH = 64.9\%$

phology of the aggregate ice front can be attributed to localized variations in freezing velocity. Figure 4.18(b) enhances this discussion by showing that the freezing velocity was always higher in regions where the droplets were more closely spaced (i.e. a higher droplet number density). These characteristics were observed for all experiments conducted in this study, suggesting that the local condensate droplet distribution and aggregate freezing velocity are closely related.

With the velocity vectors field resolved, it was possible to compare the aggregate freezing dynamics from one surface and set of test conditions to the others. To do this, an area-weighted average of the local freezing front velocity magnitude was computed as

$$\bar{V}_n = \frac{1}{A_{ROI}} \int_0^X \int_0^Y |\mathbf{V}_N| \, dxdy \tag{4.51}$$

where A_{ROI} is the viewable area of the ROI and X and Y are the geometric extents of the ROI in the x and y directions, respectively. Based on Equation 4.51, the average aggregate freezing velocity magnitude for the example case considered thus far was found to be $\bar{V}_n = 41.7$ μm/s. This magnitude compares very well with the value of 41.5 μm/s measured directly by manual interrogation of the same data (see §A4).

The vector data shown in Figure 4.18 also highlight two important benefits afforded by the front tracking technique developed for this study, namely:

1. accurate resolution of collapsing, colliding, or merging ice fronts
2. identification of locations where spontaneous ice inception occurred

For example, consider the regions in Figure 4.18(a) where the vectors either converge or diverge. Conceptually, areas in which the vectors converge to a point may either indicate the collapse or self-enclosure of a single front[5] or the collision of two or

---

[5] A single non-planar front undergoing significant distortion can repeatedly merge with itself to form so-called “self-enclosed” sub-domains.

more independent fronts; in both cases, the point of convergence represents a local terminus in the droplet freezing process. In some cases, however, the vectors only partially converge to form distinct “ridges” or “seams” in the vector field, indicating that two or more fronts gradually collided while propagating in a generally common direction. On the other hand, vectors which are seen to diverge from a single point signify the emergence of a new ice front at that point brought about by an isolated freezing event. It follows that the locations of these terminal or inceptive singularities can be readily identified by evaluating the divergence of the associated velocity field.

Mathematically, the divergence of the freezing velocity vector field is defined as

$$\nabla \cdot \mathbf{V}_N = \frac{\partial}{\partial x}\left(|\mathbf{V}_{N,x}|\right) + \frac{\partial}{\partial y}\left(|\mathbf{V}_{N,y}|\right) \tag{4.52}$$

where the magnitudes of the x and y components of the normal freezing velocity $\mathbf{V}_N$ are given by

$$\begin{aligned} |\mathbf{V}_{N,x}| &= |\mathbf{V}_N| \cos\beta_{\nabla t} \\ |\mathbf{V}_{N,y}| &= |\mathbf{V}_N| \sin\beta_{\nabla t} \end{aligned} \tag{4.53}$$

The divergence of the vector field for the example case presented in Figure 4.18(a) is shown in Figure 4.19.

For the scalar contour plot shown in Figure 4.19, the value and sign of $\nabla \cdot \mathbf{V}_N$ natively specifies locations where front collision, merging, and inception occur on the substrate. Specifically, the maximum positive values of divergence (dark red) correlate directly with locations where new freezing fronts emerged within the ROI whereas the minimum negative values (dark blue) identify the regions where fronts collided to form a local terminus. These local maxima and minima stand in stark contrast to the near-zero divergence seen throughout most of the ROI. In a few areas, $\nabla \cdot \mathbf{V}_N$ can be seen to take on intermediate positive (yellow to orange) or negative (cyan to light blue) values; these contour levels correspond to regions in which the

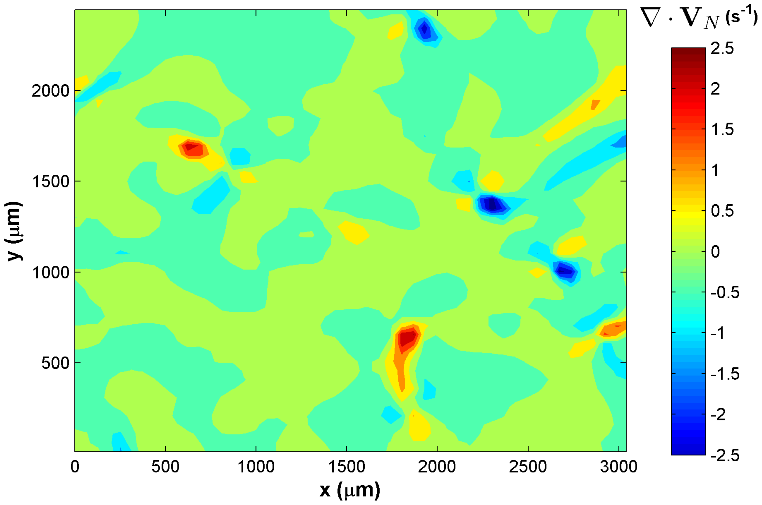

Figure 4.19: $\nabla \cdot \mathbf{V}_N$ for substrate SiA1 with $T_s = -7.1$°C, $T_{air} = 5.0$°C, and $RH = 64.9\%$

freezing front experienced localized acceleration or deceleration in some preferential direction, respectively. For the positive intermediate values, the contours of $\nabla \cdot \mathbf{V}_N$ physically correspond to regions in which the freezing front rapidly propagated into the surrounding unfrozen area in a highly localized fashion. Likewise, negative intermediate values of divergence merely identify the regions where two or more fronts merged while undergoing propagation.

6. Summary

The Type I data reduction and analysis techniques presented in the previous sections were developed specifically to characterize the ice propagation process on horizontal surfaces undergoing dropwise condensation. This methodology made it possible to reliably measure the following parameters within the ROI:

1. discrete inter-droplet freezing velocity magnitudes, $\hat{v}_{k,\bar{D}}$
2. the average inter-droplet freezing velocity magnitude, $\bar{v}_{k,\bar{D}}$
3. local aggregate freezing front velocities, $\mathbf{V}_N$
4. the average aggregate freezing velocity magnitude, $\bar{V}_n$
5. locations of spontaneous ice inception, defined by $(\nabla \cdot \mathbf{V}_N)_{\max}$
6. the total number of droplets involved in freezing, K
7. the average droplet diameter just prior to freezing, $\bar{D}_k$

These parameters were determined for each test surface and condition previously delineated in the test matrix of Table 3.10. Interpretation of these results along with consideration of the associated thermophysics are discussed in subsequent chapters.

B. Type II and III Experiments

The Type I data reduction and analysis methodology developed in the foregoing sections provided a means to quantitatively evaluate two important aspects of ice propagation on surfaces undergoing dropwise condensation: the inter-droplet freezing process and the dynamic behavior of the resulting aggregate freezing fronts. These tools made it possible to characterize the freezing processes on a consistent basis and over a wide range of conditions and surface properties representative of those used in real engineering devices. The Type I experiments were conceived to study the freezing process from a mesoscopic viewpoint with length and time scales on the order of 10^{-4} to 10^{-2} m and 10^{-1} to 10^{1} s, respectively. Although viewed with a magnification of 5X (see Table 3.3, for example), the optical resolution from the Type I perspective was actually not high enough to truly expose the mechanisms responsible for ice propagation amongst supercooled water droplets. And surprisingly, the image acquisition rate of 100 Hz used for the Type I experiments was not nearly fast enough to observe the freezing process within individual droplets. Consequently, the Type II and III experiments were designed to bridge this gap by providing higher magnification glimpses into the underlying phenomena.

A detailed overview of the Type II and III experiments and associated test matrices were provided in the previous chapter (see Tables 3.11 and 3.12). Briefly, the scope of each can be summarized as follows:

- The Type II experiments were designed to utilize the high optical resolving power of the microscope to explore the microscopic *length* scales (on the order of 10^{-7} to 10^{-4} m) associated with *inter*-droplet ice propagation.
- The Type III experiments were crafted to exploit the high speed capabilities of the digital microscopy system to explore the microscopic *time* scales (on the order of 10^{-4} to 10^{-3} s) associated with *intra*-droplet ice propagation.

The following sections outline the analysis techniques used to reduce the image data acquired in these experiments.

1. Type II and III Data Analysis Overview

Compared to the Type I data, the reduction and analysis of the Type II and III image data were very straightforward. This was primarily due to the fact that:

1. The ROI for the Type II experiments was always confined to a small area on the substrate and therefore always focused on only one or two key freezing events at a time.

2. The number of frames acquired for each Type III image sequence was relatively small due to the high speed nature of the intra-droplet freezing process.

Thus, it was practical to manually analyze each image sequence acquired for these types of experiments. This was accomplished by using the *ImageJ* software to condition each image as necessary and then measure the displacement of the evolving ice structures from one frame to the next. With the time step between each frame known, the dynamics of the appropriate ice growth phenomena could be accurately quantified. Perhaps of even more importance, the processed image sequences could be used in a more qualitative fashion to provide more insight into ice propagation at the microscale.

2. Type II Image Analysis

Representative examples of images acquired for the Type II experiments are shown in Figure 4.20 where microscopic condensate droplets on the verge of freezing can be seen at optical magnifications of 20X and 50X, as indicated. These images were acquired from two separate tests conducted on the SiA1 substrate under identical conditions and highlight the considerably smaller length scales able to be studied with the Type II experiments. For example, the smallest droplets visible at 50X power (Figure 4.20(b)) would be completely invisible at 20X (Figure 4.20(a)). Likewise, the smallest droplets able to be resolved at 20X magnification would not be visible at 5X magnification (see Figures 4.1 or 4.9, for example). The Type II test matrix (Table 3.11) was evaluated for each test surface at both the 20X and 50X configurations. And while the 20X images provided a great deal qualitative insight into the inter-droplet freezing dynamics, the 50X image sequences were used exclusively for all quantitative analyses because of the higher spatial resolution they provided.

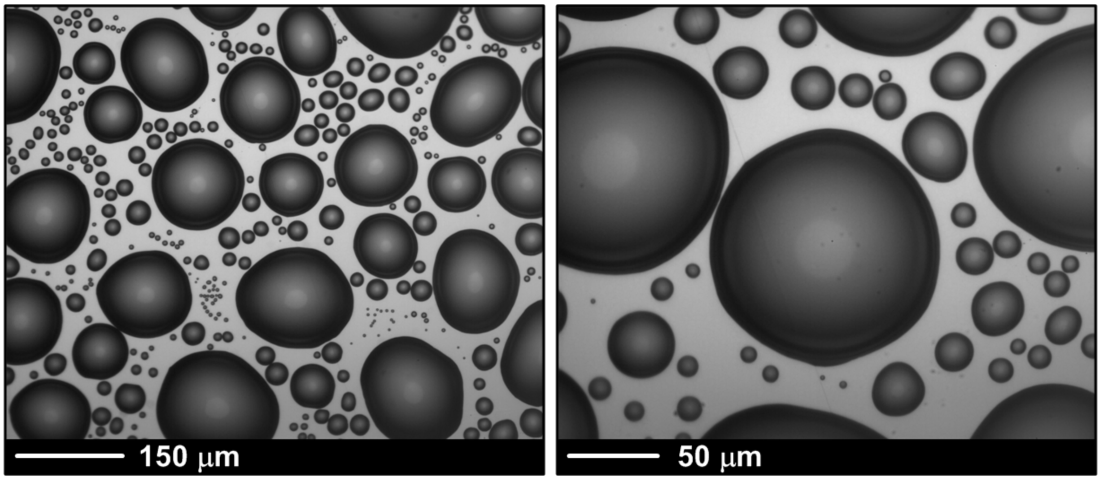

(a) (b)

Figure 4.20: Field of view for Type II experiments at 20X (a) and 50X (b) optical magnification

The clarity with which the droplet edges can be resolved in Figure 4.20 is a result of the the microscope being focused directly on the substrate (as opposed to being focused off-surface as required for the Type I experiments). The benefits of having this level of detail are apparent from the results of a representative Type II test shown in the image sequence of Figure 4.21. In this case, distinct ice crystals can be clearly seen growing between the droplets over time; some of the finer details of this process are highlighted in the magnified inlays. Higher constrast images suitable for extracting quantatative measurements were generated by applying Gaussian smoothing to each image followed by the Sobel edge detection method previously defined in Equation 4.18. Examples of applying these enhancements to the images presented in Figure 4.21 are shown Figure 4.22.

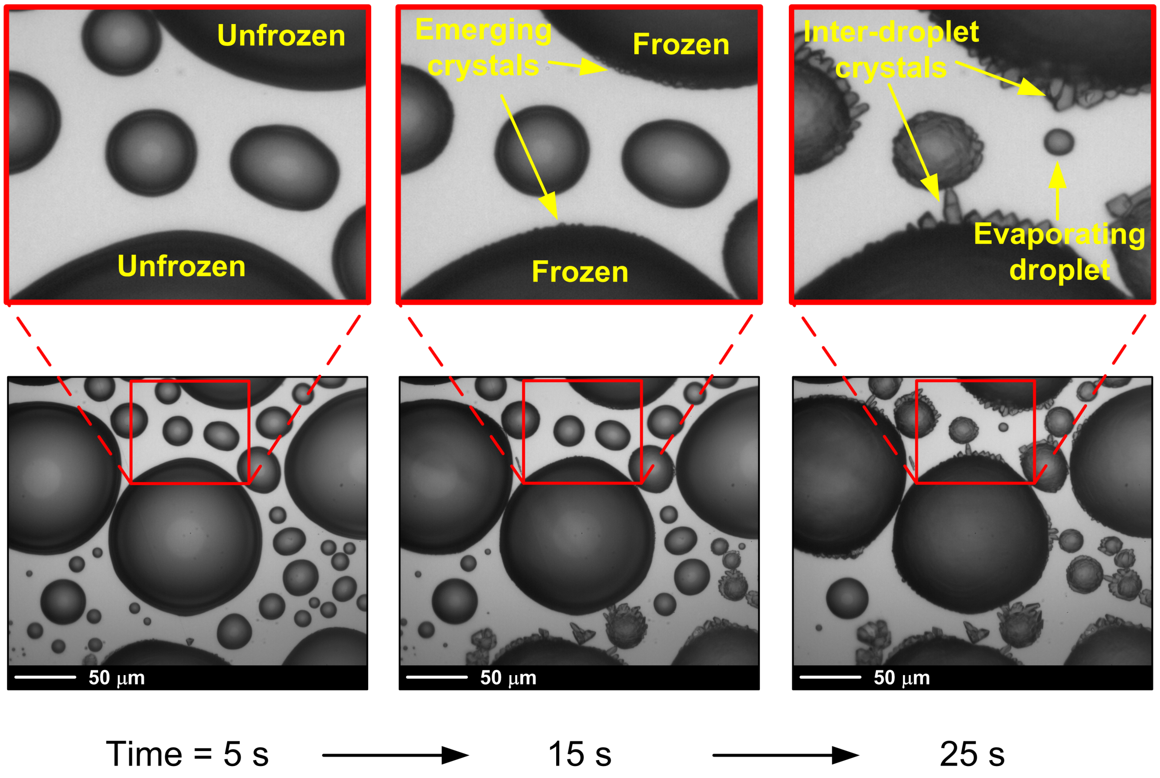

Figure 4.21: Type II image sequence for substrate SiA1 at 50X magnification with $T_s = -10.0°\text{C}$, $T_{air} = 5.1°\text{C}$, and $RH = 65.4\%$

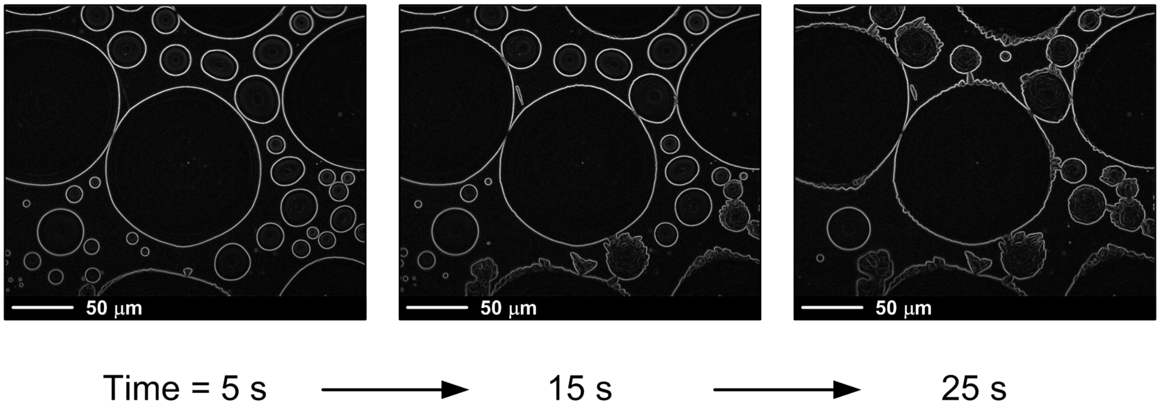

Figure 4.22: Image sequence from Figure 4.21 with Gaussian smoothing and Sobel edge detection

Because the images shown in Figures 4.21 and 4.22 were preferentially focused on the substrate under high magnification, the sudden shift in the droplets' refractive index which accompanies freezing did not generally produce a significant enough optical perturbation to signal ice nucleation. However, the initiation of freezing was clearly revealed by two other indicators: a sudden (albeit small) dilation of the droplets as they begin to transition to the less dense ice phase followed immediately by the emergence of dendritic ice crystals along the periphery of the newly frozen droplets. Repeated observation of this inter-droplet ice crystal growth process for all Type II experiments revealed a number of remarkable characteristics:

1. The ice crystals invariably grew outward from their newly frozen parent droplet towards the nearest unfrozen droplet (referred to henceforth as the "target" droplet). This process occurred independently of the direction of airflow over the test substrate.

2. Upon contacting the target droplet, the ice crystal triggered freezing in that droplet, spawning a new family ice crystals which in turn grew outwards from the newly frozen target droplet. This process was also observed from the broader perspective offered by the 20X images, implying that this process repeated until all droplets on the substrate were frozen.

3. As the ice crystals grew towards their target liquid droplets, the unfrozen droplets showed signs of evaporation. This phenomenon was more pronounced for less massive liquid droplets, as evidenced by the notable shrinking or complete disappearance of a number of the smaller droplets over time in the image sequence shown in Figures 4.21 and 4.22.

4. A given ice crystal continued to grow until

   (a) it grew long enough to contact the target droplet and initiate freezing,
   (b) freezing was induced in the target droplet by another crystal growing from elsewhere, or
   (c) the target droplet or droplets completely evaporated before freezing.

5. Given that the depth of focus for the 50X objective lens was previously calculated to be ± 0.62 μm (Table 3.3), the clarity with which the crystals can be resolved indicate that they were in direct contact with the substrate and on the order of 1 μm thick or less.

An additional item worthy of further discussion pertains to the in-plane (along the substrate) versus out-of-plane (normal to the substrate) growth of ice during propagation. Numerous observations at both 20X and 50X magnification revealed that ice preferentially grew along the subtrate as long as at least one unfrozen droplet remained in the local vicinity of the evolving crystals. Interestingly, once all liquid droplets within a region had frozen, the crystal growth process did not cease, but merely reoriented itself in an upward direction normal to the surface and toward the ambient air stream. Thus, after exhausting the seemingly preferred liquid phase, the ice phase began to grow away from the surface of the droplets and substrate in the form of a thickening crystalline matrix, eventually manifesting as frost at larger length scales.

The enhanced Type II images such as those shown in Figure 4.22 provided a consistent demarcation of the droplet and crystal edges; as such, they were used to carry out local quantitative measurements of individual inter-droplet ice crystal growth rates. The crystal velocity was determined by manually measuring the change in length of a selected crystal between successive frames with the *ImageJ* software. Whenever practical, the target droplet evaporation rate was measured in a similar fashion by tracking the corresponding change in droplet diameter from one frame to the next[6]. Figure 4.23 shows an example of the position of the leading edge of the crystal tip r_c and target droplet diameter D_{td} versus time for the test case presented in Figure 4.22.

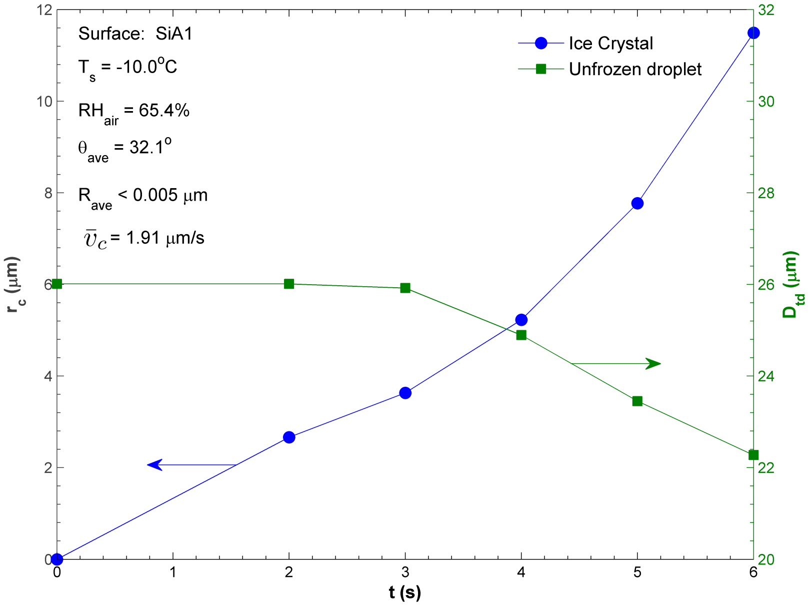

Figure 4.23: Measured inter-droplet ice crystal position and target droplet diameter versus time from enhanced image sequence shown in Figure 4.22

The data shown in Figure 4.23 are representative of all quantitative manual measurements acquired from the Type II experiments. In this plot, the crystal tip position and target droplet diameter over time are given by the left and right ordinate axes, respectively. The crystal tip position at time $t = 0$ s was taken to be at the periphery of the parent droplet just prior to freezing and assigned a reference value of zero. After the freezing process began, the crystal advanced towards the target

---

[6] This was not possible in a number of instances because the target droplet was so large that its diameter did not measurably change before freezing occurred.

droplet with increasing speed until reaching a length of about 11.5 μm. At this point, the crystal contacted and initiated freezing in the target droplet and then ceased growing altogether.

The diametral history shown in Figure 4.23 indicates that the target droplet was essentially unaffected by the encroaching ice phase until the incipient crystal had grown to within about 8 μm of the droplet's edge; it was only after this point that the diameter of the droplet began to measurably decrease, marking the onset of localized evaporation. During evaporation, the diameter of the target droplet decreased from its initial value of approximately 26.1 μm to a terminal freezing value of 22.3 μm. Upon freezing, the diameter of the target droplet did not further change with time. Remarkably, the onset of evaporation for the target droplet coincided with the point in time at which the ice crystal growth rate began to markedly accelerate. This phenomenon was observed for all Type II experiments in which the size of the target droplets were able to be tracked with time, suggesting that the target droplets may act as proximity-dependent mass sources for the inter-droplet crystal growth process. This implies that the inter-droplet crystal growth process occurs as the result of ice deposition from the vapor phase, which in turn indicates that the substrate between droplets is essentially dry during the the freezing process.

The measured inter-droplet crystal growth velocity for all Type II experiments was generally not constant over time and tended to increase as the crystal approached the target droplet, as shown in Figure 4.23. Therefore, in order to properly compare the crystal growth velocities between all test surfaces and conditions, a time-integrated average velocity was used, given by

$$\bar{v}_c = \frac{1}{t_f - t_i} \int_{t_i}^{t_f} v_c \, dt \tag{4.54}$$

where v_c is the instantaneous crystal growth velocity. In practice, v_c was approximated numerically from backward differences of the crystal position versus time data and the integral in Equation 4.54 was evaluated using the trapezoid rule. For the example case considered here, Equation 4.54 yielded an average inter-droplet crystal growth velocity of $\bar{v}_c = 1.91$ μm/s. This value of $\bar{v}_c$ was determined for a substrate temperature of approximately -10°C and ambient relative humidity of around 65% on the SiA1 test surface. As a point of comparison, the Type I inter-droplet freezing velocity calculations previously outlined in §A4 gave a value of $\bar{v}_{k,\bar{D}} = 2.03$ μm/s for the same surface and test conditions. The fact that $\bar{v}_c$ and $\bar{v}_{k,\bar{D}}$ agree to within less than 10% is not coincidental: $\bar{v}_c$ technically represents a single, high resolution "spot-check" measurement of a much larger sample of inter-droplet freezing velocities represented statistically by $\bar{v}_{k,\bar{D}}$.

3. Type III Image Analysis

The field of view for the Type III experiments was scaled back to 5X magnification (the same used for the Type I experiments) while the temporal emphasis was shifted towards observing ice inception and propagation within individual droplets. These phenomena were found to occur over much smaller time scales than the inter-droplet crystal growth process and ultimately, camera frame rates as high as 2367 Hz were required to accurately resolve them. The Type III image data were interrogated with the *ImageJ* software in essentially the same manner as the Type II data; that is, the evolution of the ice phase within a given droplet was tracked manually over time.

After acquisition, all frames in each Type III image sequence were spatially convolved with an exponential kernel to enhance sharpness and contrast for the manual analysis. Three frames of one such sequence is shown in Figure 4.24. In this sequence, the ice phase can be seen to have emanated from a single point of origin at the droplet periphery and evolved rapidly throughout the droplet. The temporal resolution provided by the high speed imaging system is highlighted by the time stamps associated with each image shown; for this case, the time step between successive images is 4.2×10^{-4} s (0.42 ms).

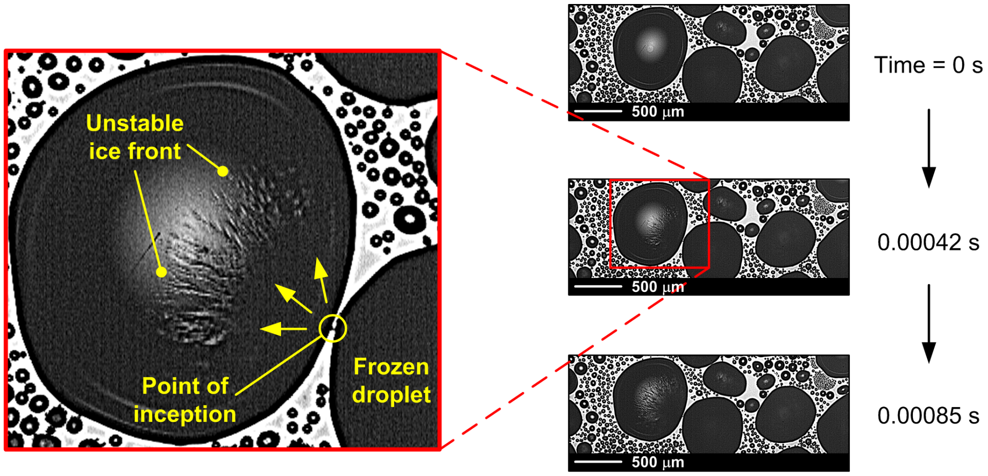

Figure 4.24: Type III image sequence for substrate SiA1 acquired at 2367 Hz and 5X magnification with $T_s = -20.1°\text{C}$, $T_{air} = 4.9°\text{C}$, and $RH = 65.2\%$

The magnified inlay shown in Figure 4.24 illuminates several important characteristics of the intra-droplet freezing process. Perhaps one of the most noticeable features is that the evolving ice front is not defined by a sharp interface, but rather by a “feathery” or “mushy” phase-change region. The difference in refractive index of ice and water suggests that these optically distorted, needle-like structures seen along the leading edge of the front are actually dendritic ice crystals growing into the surrounding liquid phase. This observation is supported by the more general theoretical basis associated with unstable dendritic solidification in supercooled melts [80, 81]. In addition, the fact that the microscope was purposely focused on the substrate beneath the droplet indicates that the ice front propagated along the bottom edge of the droplet (i.e. the droplet-substrate interface) and not within the bulk volume of the interior. Based on the depth of focus offered by the 5X microscope objective lens

(± 2.02 μm; see Table 3.3) the thickness of this ice front was estimated to be no more than 3 μm.

Figure 4.24 also shows that the point of ice inception within the droplet tended to occur along the periphery. As indicated in the inlay, a single ice crystal originating from an adjacent frozen droplet can be seen to have grown across the inter-droplet gap and a contacted the unfrozen droplet, triggering ice nucleation. This phenomenon was observed for the vast majority of the Type III experiments and is consistent with the findings of the the Type II data analysis discussed in the previous section. However, there were a couple of notable instances in which freezing was actually observed to have initiated independently within a particular droplet, without the influence of any obvious external trigger. For the range of surface temperatures considered in this study, kinetic theory suggests that thermodynamic conditions conducive to heterogeneous ice nucleation was likely reached within those droplets [3, 46]. From a considerably broader perspective, spontaneously nucleating droplets such as these account for the emergence of independent aggregate ice fronts on the substrate, as previously demonstrated in Figure 4.19 for the Type I results.

The Type III images like those shown in Figure 4.24 were also used to quantify the intra-droplet ice front propagation velocity. Although the solid-liquid interface was not clearly defined, the displacement of what was estimated to be the leading edge of the ice front was manually tracked from its point of origin from one frame to the next using the *ImageJ* software. The resulting ice front position versus time data for the example case considered in this section is shown in Figure 4.25.

One of the most striking features associated with the data presented in Figure 4.25 is the sheer speed of the intra-droplet freezing front compared to those associated with the inter-droplet and aggregate freezing processes. For comparison, a time-integrated average velocity for the intra-droplet solidification front, $\bar{v}_{sl}$, was

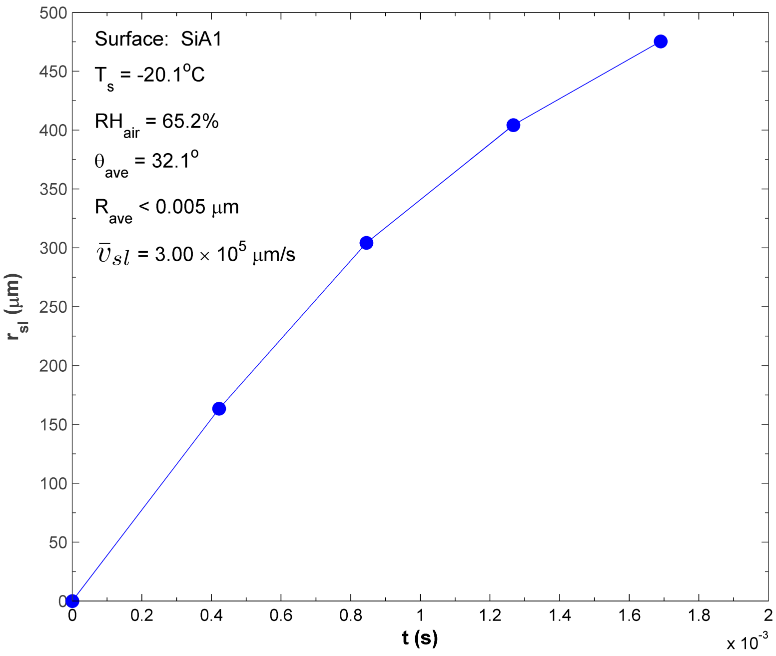

Figure 4.25: Measured intra-droplet ice front position versus time from the enhanced image sequence shown in Figure 4.24

calculated in the same manner as $\bar{v}_c$ previously defined by Equation 4.54. Used with this expression, the data given in Figure 4.25 correspond to $\bar{v}_{sl} = 3.00 \times 10^5$ μm/s, which is several orders of magnitude larger than the *inter-droplet* freezing velocity (given by $\bar{v}_c$ or $\bar{v}_{k,\bar{D}}$) measured for the same test surface and conditions! Considering all Type III experiments conducted, $\bar{v}_{sl}$ was found to vary in the range of 10^4 to 10^5 μm/s, depending on the substrate temperature. In general, the nearly linear instantaneous ice front displacement profile shown in Figure 4.25 was observed consistently throughout the entire Type III dataset.

With a firmer grasp on the dynamics of the intra-droplet freezing process in hand, it should be noted that this process does not correspond to the overall "bulk" solidification of an individual droplet. This so-called bulk freezing process may be envisioned simply as the propagation of the ice phase throughout the volume of the droplet and ending when the entire droplet has frozen. In a previous study, Gong [39] found that this freezing process always begins at the droplet-substrate interface, propagating upwards and away from the substrate through the bulk of the droplet in the form of a distinct ice front. For this process, he measured bulk freezing velocities in the range of 10^2 to 10^3 μm/s in sessile water droplets with base diameters in the range of 2 to 3 mm. A remarkable finding from the Type III experiments conducted in this study, however, was that the high velocity intra-droplet freezing front characterized by $\bar{v}_{sl}$ was observed to propagate along the entire free surface of the droplet prior to the onset of the bulk freezing process. In other words, the nucleation of ice appears to first induce the formation of a very thin ice shell which rapidly encases the entire droplet long before the bulk freezing process begins. This effect is shown in Figure 4.26 with a high speed image sequence acquired for a freezing experiment conducted on a manually implanted water droplet with the microscope oriented in the side-view orientation. Figure 4.26 also shows the bulk freezing process, which can be seen to transpire over a much longer time scale.

4. Summary

The techniques used to reduce and analyze the data acquired from the Type II and III experiments were outlined in the previous sections. The results of these experiments provided a great deal of qualitative and quantitative information about ice propagation on surfaces undergoing dropwise condensation. Specifically:

1. Detailed observations from the Type II image data showed that one distinct ice propagation mechanism for droplet-laden surfaces consists of an inter-droplet crystal growth process in which microscopic ice crystals preferentially grow from

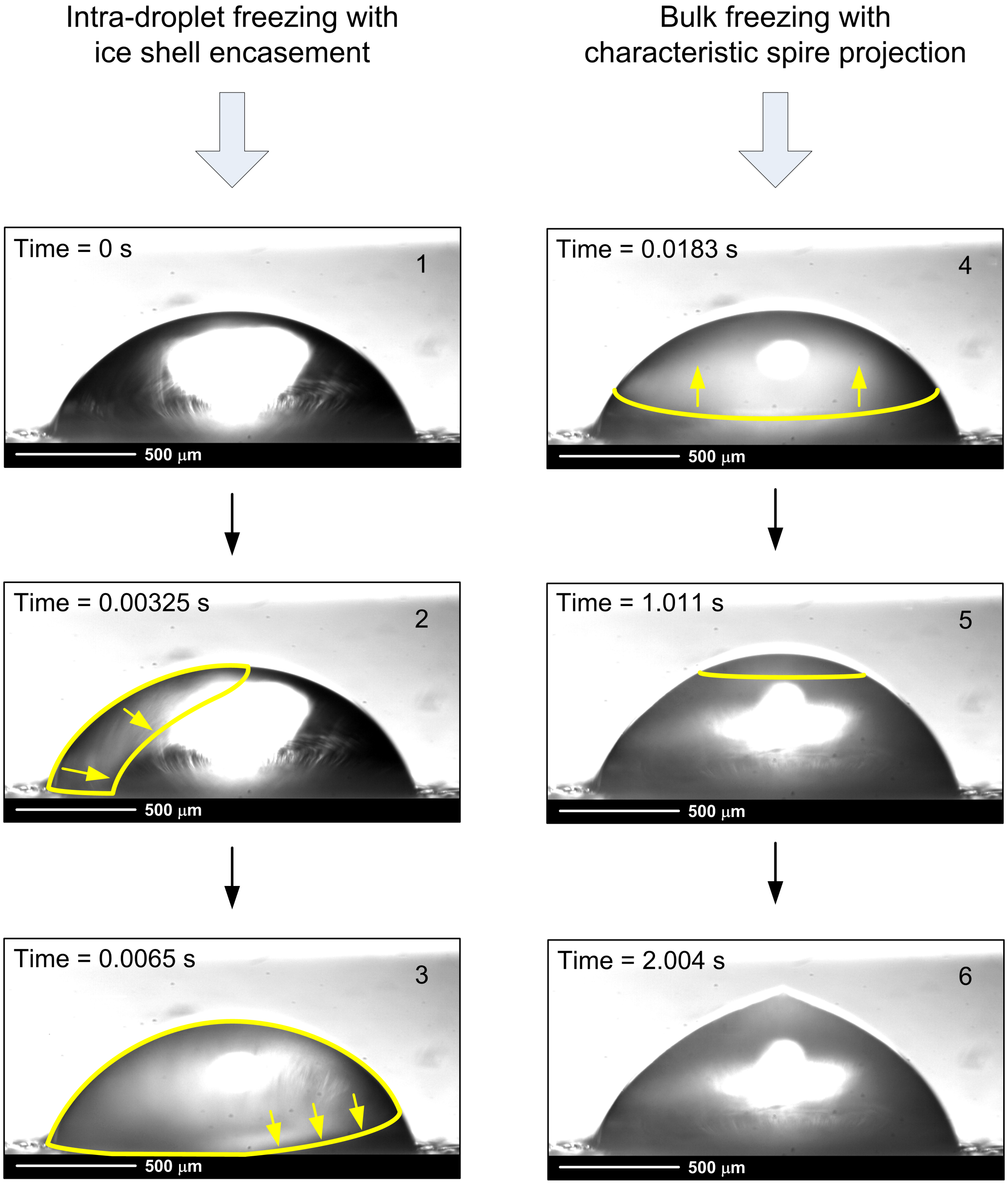

Figure 4.26: High speed image sequence of the intra-droplet and bulk freezing processes for a manually implanted water droplet on the CuA5 substrate; acquired at 2770 Hz and 5X magnification with $T_s = -7.1$°C, $T_{air} = 5.1$°C, and $RH = 64.9\%$

frozen to unfrozen droplets along the substrate by what appears to be deposition.

2. Direct crystal growth velocity measurements ($\bar{v}_c$) taken from the Type II data provided validation for the results of the broader-scoped Type I inter-droplet freezing velocity calculations ($\bar{v}_{k,\bar{D}}$).

3. The Type III experiments revealed that another distinct ice propagation mechanism for droplet-laden surfaces involves a very rapid liquid-to-solid phase transition within individual droplets.

4. Measurements of the intra-droplet freezing process ($\bar{v}_{sl}$) revealed that the crystallization kinetics associated with this mechanism are several orders of magnitude faster than those for the inter-droplet freezing process.

These observations and measurements were carried out for each test surface and condition listed in the Type II and III test matrices presented in Tables 3.11 and 3.12. The full range of results are presented in the next chapter.

C. Summary and Remarks

In order to investigate the complicated and random nature of ice propagation on surfaces undergoing dropwise condensation, three general classes of experiments were developed and conducted: Types I, II, and III. The largest fraction of the work fell into the Type I category and in order to to process the plethora of data that emerged, a set of analysis tools had to be developed. A central element in these experiments was a phase tracking technique which exploited the optical properties of sessile water droplets residing on reflective surfaces. The resulting visualization data were processed with a custom image analysis routine written in MATLAB and fed into a pair of data processing algorithms. One algorithm was designed to systematically detect the droplet-by-droplet freezing progression; this allowed inter-droplet freezing velocities to be evaluated for all droplets residing within the ROI . The other algorithm used a novel temporal gradient scheme which was developed to compute aggregate freezing velocity vectors fields for the entire ROI from the raw image data. These tools allowed key parameters to be measured in a largely automated fashion, providing the fidelity needed to properly quantify and compare them on a consistent basis. Data analysis for the Type II and III experiments was carried out in a largely manual fashion by using the *ImageJ* software package to interrogate the appropriate image sequences on a frame-by-frame basis.

The results of the Type I experiments revealed the presence of a characteristic inter-droplet freezing velocity $\bar{v}_{k,\bar{D}}$ for each test surface and set of conditions (Figure 4.12). This velocity, which was validated with single-point quantitative measurements from the Type II experiments ($\bar{v}_c$), defines the speed with which the ice phase propagates between droplets on the surface. The Type I experiments also showed that the average velocity of the aggregate ice front, $\bar{V}_n$, was considerably greater than $\bar{v}_{k,\bar{D}}$ in all cases. On the other hand, the Type III experiments revealed that the intra-droplet freezing velocity, represented by $\bar{v}_{sl}$, was always substantially greater than both $\bar{v}_{k,\bar{D}}$ and $\bar{V}_n$. These results suggest that the aggregate freezing process may be better understood (and possibly modeled) via superposition of the inter- and intra-droplet freezing mechanisms.

In addition to the quantitative results, the experiments conducted in this study provided a number of qualitative insights into the ice propagation process at the mircoscale. One particularly interesting observation taken from the Type II data was that discrete ice crystals preferentially grew along the substrate from frozen droplets towards unfrozen droplets. However, when all droplets within a given region had frozen, small ice crystals were seen to emerge from the surfaces of the frozen droplets (as well as the substrate) and grow upwards, towards the humid air stream. Another remarkable finding gleaned from the Type III data was that the intra-droplet freezing process operates not just in the plane defined by the droplet-substrate interface, but along the semi-spherical free surface of the droplet as well. As a result of this phenomenon, freezing droplets appear to become encased with a very thin ice shell before the bulk of the droplet freezes.

The present chapter has focused on the development and demonstration of the methodology used to reduce and analyze the data acquired in this study. The full gamut of results are discussed, interpreted, and analyzed in the chapters that follow.

CHAPTER V

DYNAMIC CHARACTERISTICS OF ICE PROPAGATION ON DROPLET-LADEN SURFACES

To characterize the dynamics of ice propagation on surfaces undergoing dropwise condensation, a series of quantitative visualization experiments were conducted in a psychrometric wind tunnel with a high speed digital microscopy system. In total, over 150 experiments were carried out for four different horizontal test surfaces over a wide range of conditions. To investigate the different length and time scales associated with ice propagation phenomena in this configuration, the experimental work was partitioned into three main categories: Types I, II, and III. The details surrounding each type of experiment, along with the associated testing procedures and facilities, were previously outlined in Chapter III. In addition, the techniques used to reduce and analyze the resulting data were presented in Chapter IV. In this chapter, the full spectrum of experimental results for this investigation are reported and discussed.

A. Reduced Freezing Velocity Data

As previously discussed in Chapters III and IV, the three classes of experiments used in this study (Types I, II, and III) were designed to target specific length or time scales associated with the ice propagation process. The Type I experiments were used primarily to characterize the freezing dynamics by tracking the motion of aggregate freezing fronts while simultaneously capturing the individual droplet-to-droplet freezing events with high fidelity. On the other hand, the Type II and III experiments were tailored more towards identifying the underlying mechanisms responsible for the ice propagation phenomenon. For example, the Type II experiments revealed that the ice phase propagates between water droplets by way of microscopic ice crystals that preferentially grow from frozen to unfrozen droplets along the substrate. And the Type III experiments showed that the solidification process associated with the inceptive freezing of individual water droplets proceeds with kinetics that are several orders of magnitude faster than those of the inter-droplet crystal growth process. In addition to these and a number of other qualitative insights, extensive quantitative inter- and intra-droplet freezing velocity data were gleaned from the Type II and III experiments. The resulting quantitative data from all three types of experiments are presented in the following sections. The uncertainty intervals associated with these data are presented with error bars ascribed to the dependent variables; the details of the uncertainty analysis are summarized in Appendix A.

1. Aggregate Freezing Front Velocity

The concept of an aggregate freezing front on a droplet-laden surface was previously introduced in Chapter IV. In that same chapter, the methodology used to reduce and analyze the image data acquired from the Type I visualization experiments was outlined in detail. The parameter ultimately used to characterize the bulk freezing dynamics on a given substrate was the average aggregate freezing velocity magnitude $\bar{V}_n$, defined by Equation 4.51 as an area-integrated average of the local aggregate velocity magnitude $|\mathbf{V}_n|$. Based on the test matrix shown in Table 3.10, there were 32 unique combinations of substrate type (e.g. SiA2), temperature (T_s), and free stream relative humidity (RH) for which values of $\bar{V}_n$ were determined. In practice, each experiment was repeated a minimum of two times, with the results being averaged to produce one representative value of $\bar{V}_n$ for each test condition and surface combination. The resulting values of $\bar{V}_n$ are shown as a function of T_s and RH for each substrate in Figure 5.1. Figure 5.2 presents the same reduced $\bar{V}_n$ data as a function of RH and surface type for each value of T_s considered.

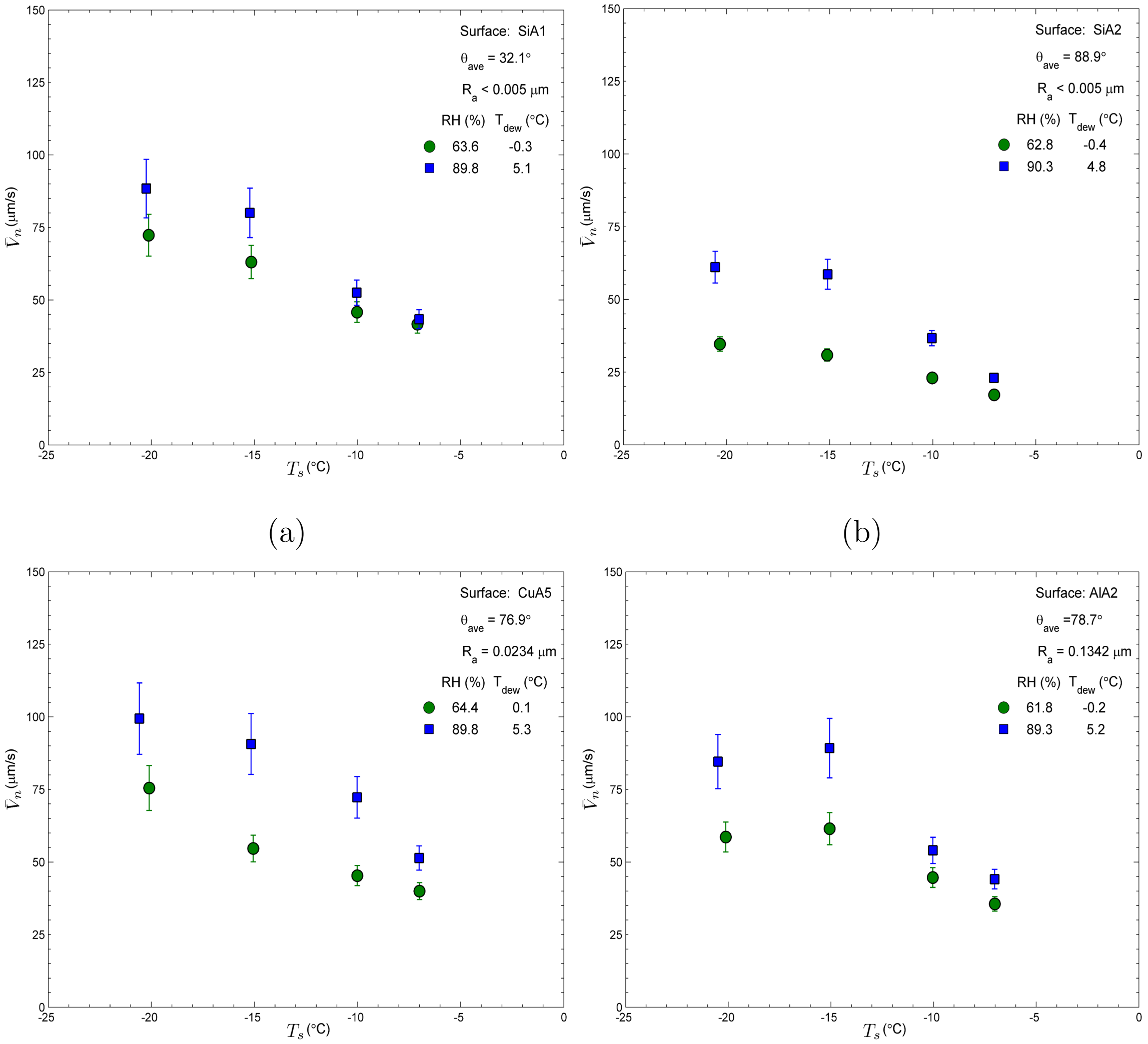

(a)

(b)

(c)

(d)

Figure 5.1: Area-weighted aggregate freezing velocity $\bar{V}_n$ versus substrate temperature T_s with $T_{air} = 5$°C and $U_{air} = 5$ m/s for surfaces (a) SiA1, (b) SiA2, (c) CuA5, and (d) AlA2

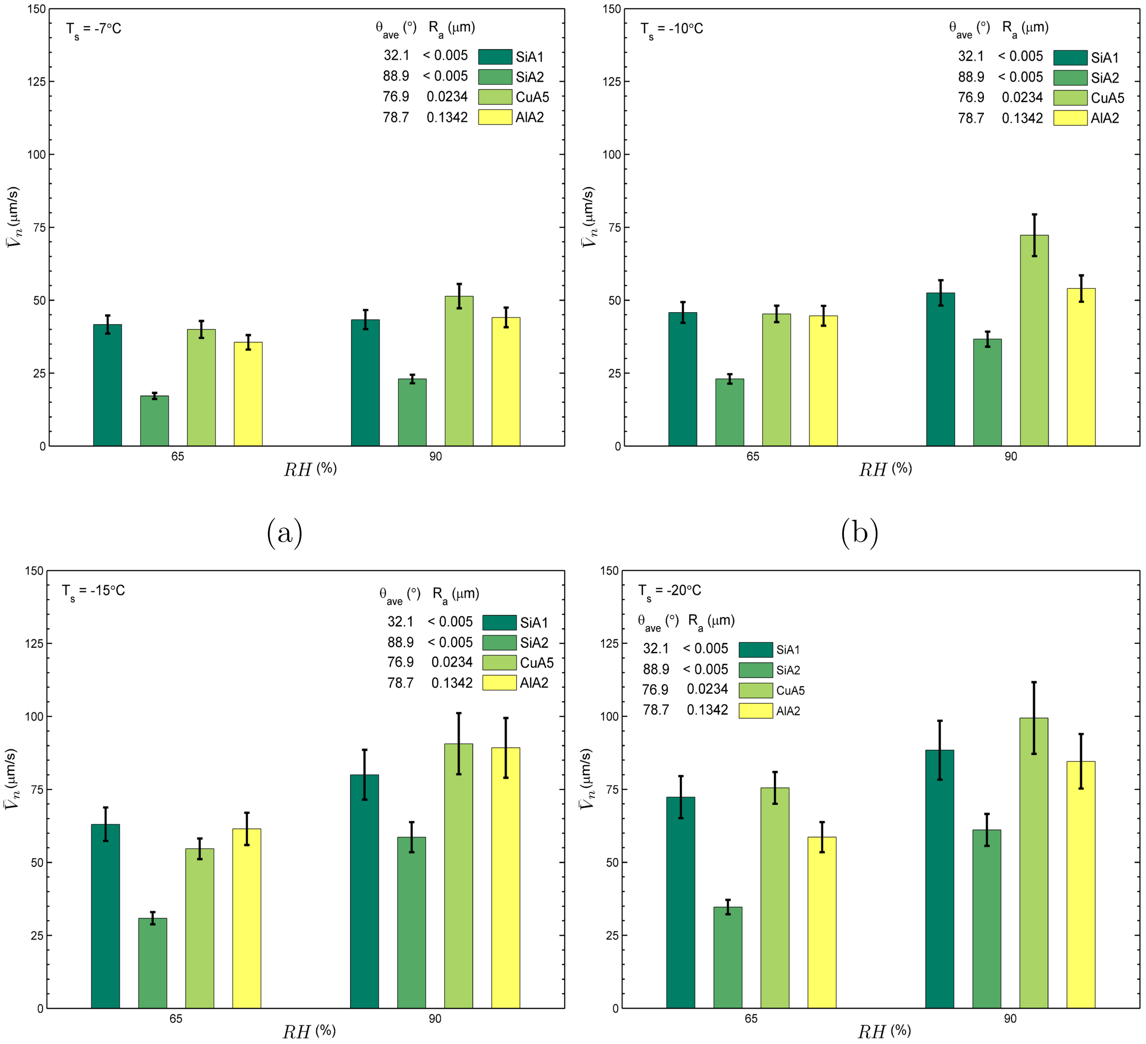

(a) (b)

(c) (d)

Figure 5.2: Area-weighted aggregate freezing velocity $\bar{V}_n$ versus free stream relative humidity RH with $T_{air} = 5°\text{C}$ and $U_{air} = 5$ m/s for nominal substrate temperatures of (a) -7, (b) -10, (c) -15, and (d) $-20°\text{C}$

In Figure 5.1, it can be seen that for a given surface temperature, $\bar{V}_n$ increased with increasing relative humidity, and that for a given humidity, $\bar{V}_n$ increased with decreasing substrate temperature. An interesting trend found in the data was that regardless of the humidity value, $\bar{V}_n$ tended to increase towards an asymptote as T_s decreased. Another noteworthy observation was that for a given surface temperature, the difference between the values of $\bar{V}_n$ associated with the 65 and 90% RH conditions tended to increase with decreasing surface temperature. This latter finding was observed for all test conditions and surfaces and was most pronounced for the SiA1 substrate. In fact, the overlap of the error bars shown in Figure 5.1(a) suggested that for the SiA1 surface, the effects of air stream humidity on $\bar{V}_n$ were essentially negligible for temperatures above -10°C.

The data shown in Figure 5.2 are identical to those presented in Figure 5.1; however, the bar chart arrangement used in Figure 5.2 was better suited for directly comparing the full gamut of aggregate freezing velocity data. In particular, these plots highlight the effects of air stream relative humidity and surface properties on $\bar{V}_n$. Cast in this perspective, these data indicated that the surface type can have a significant effect on the aggregate freezing velocity. For example, the values of $\bar{V}_n$ for the silicon SiA2 surface were found to be, on average, about 45% lower than those for the SiA1 surface at the same conditions. Considering that surface SiA2 was notably more hydrophobic than SiA1 while the roughness values were essentially the same[1], these findings indicate that the free energy of the substrate can have a substantial impact on the aggregate freezing dynamics. Specifically, ice tended to propagate more slowly amongst droplets on hydrophobic substrates (i.e. lower surface energy) than on hydrophillic substrates (i.e. higher surface energy).

---

[1] Nominal values of the average surface roughness R_a and apparent hydrophobicity, given in terms of the average static contact angle θ_{ave}, are reported in Figure 5.2.

The effects of surface roughness on the aggregate freezing dynamics were less clear, however. Extending the previous comparison to include the values of $\bar{V}_n$ for the copper CuA5 and aluminum AlA2 substrates, it must first be recalled that the roughness of the former was about an order of magnitude lower than that of the latter while the apparent hydrophobicity of the two were very nearly the same. Figure 5.2 indicates that $\bar{V}_n$ for the smoother CuA5 surface was generally higher than for the AlA2 substrate. Remarkably, the values of $\bar{V}_n$ for the SiA1, CuA5, and AlA2 surfaces tended to agree to within a few percent for surface temperatures above -10°C and the lower humidity of 65%; at lower surface temperatures and the higher humidity value of 90%, this variation increased to as much as 25%. Considering that the apparent free energy of the SiA1 surface was less than that of the CuA5 or AlA2 specimens, these findings suggested that surface roughness and hydrophobicity were likely to affect the aggregate freezing dynamics in a coupled manner. Unfortunately, the results presented in Figures 5.1 and 5.2 did not offer any additional insights into the relationship between surface roughness and hydrophobicity. Furthermore, these data did not explicitly account for substrate thermophysical properties such as thermal conductivity and heat capacity, attributes which vary substantially among the silicon, copper, and aluminum specimens used. These issues are further addressed in a subsequent section.

2. Inter-Droplet Freezing Velocity

Another key parameter extracted from the results of the Type I experiments was the velocity with which ice propagated from one droplet to the next. With the methods outlined in Chapter IV, discrete values of the inter-droplet freezing velocity $\hat{v}_{k,\bar{D}}$, defined by Equation 4.30, were determined for all droplets detected within the region of interest (ROI) on the substrate during a given test. The values of $\hat{v}_{k,\bar{D}}$ for each case were based on an average droplet diameter $\bar{D}_k$, which was representative of the entire ROI for the particular substrate and test conditions. For a given experiment, the set of inter-droplet velocities given by $\hat{v}_{k,\bar{D}}$ provided a time history of the local freezing process, which in turn allowed the local progression of freezing to be tracked on a droplet-by-droplet basis (see Figure 4.11). In addition, the set of velocities given by $\hat{v}_{k,\bar{D}}$ was found to follow a log-normal distribution such as that shown in Figure 4.12. The mean value of the most frequently measured velocities that fell within a specified interval of the peak was designated as $\bar{v}_{k,\bar{D}}$ and was taken to be the characteristic inter-droplet freezing velocity for the substrate and conditions under test. Values of $\bar{v}_{k,\bar{D}}$ were complied for all of the conditions covered by the average aggregate freezing velocity results previously discussed. In Figure 5.3, the resulting values of $\bar{v}_{k,\bar{D}}$ are shown as a function of T_s and RH for each substrate. The same $\bar{v}_{k,\bar{D}}$ data are displayed alternatively as a function of RH and surface type for each value of T_s considered in Figure 5.4.

One of the more notable features of the data shown in Figure 5.3 is that for a given substrate, the inter-droplet freezing velocity tended to change very little with substrate temperature. Overall, these data showed a very slight upwards trend in $\bar{v}_{k,\bar{D}}$ as T_s decreases. However, within the limits of experimental uncertainty denoted by the error bars shown, $\bar{v}_{k,\bar{D}}$ was essentially independent of the substrate temperature for a given humidity. This finding was somewhat unexpected considering that the aggregate freezing velocity $\bar{V}_n$ was found to be a relatively strong function of T_s (Figures 5.1 and 5.2). The effects of air stream humidity on the inter-droplet freezing dynamics were decidedly clearer: as RH increased, so did $\bar{v}_{k,\bar{D}}$. This behavior is more intuitive because for a given air and substrate temperature, higher humidity values correspond to higher vapor-to-liquid (condensation) and vapor-to-solid (deposition) mass transfer driving potentials. Figure 5.4 indicated that increasing the hydropho-

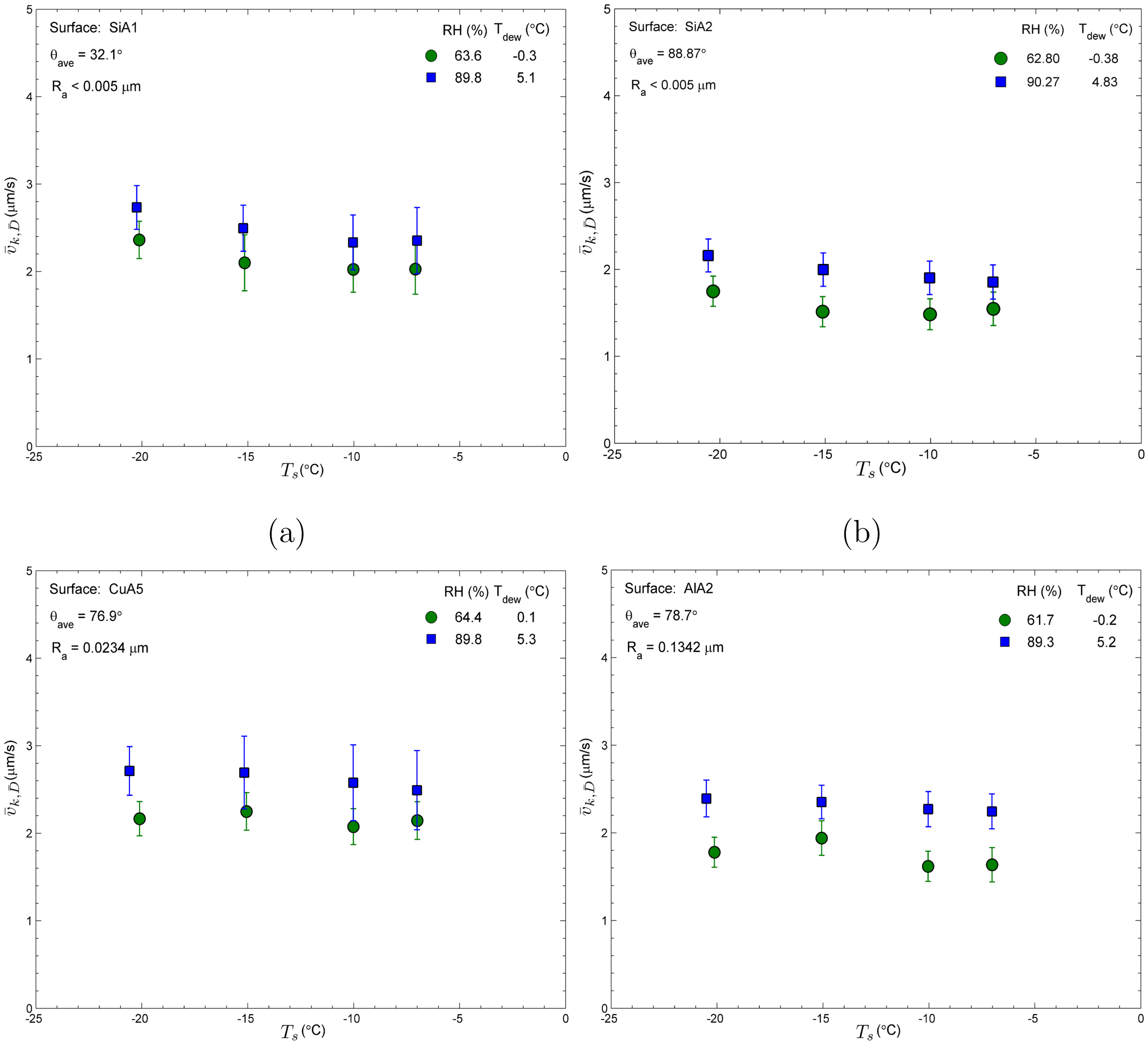

(a) (b)

(c) (d)

Figure 5.3: Inter-droplet freezing velocity $\bar{v}_{k,\bar{D}}$ versus substrate temperature T_s with $T_{air} = 5°\text{C}$ and $U_{air} = 5$ m/s for test surfaces (a) SiA1, (b) SiA2, (c) CuA5, and (d) AlA2

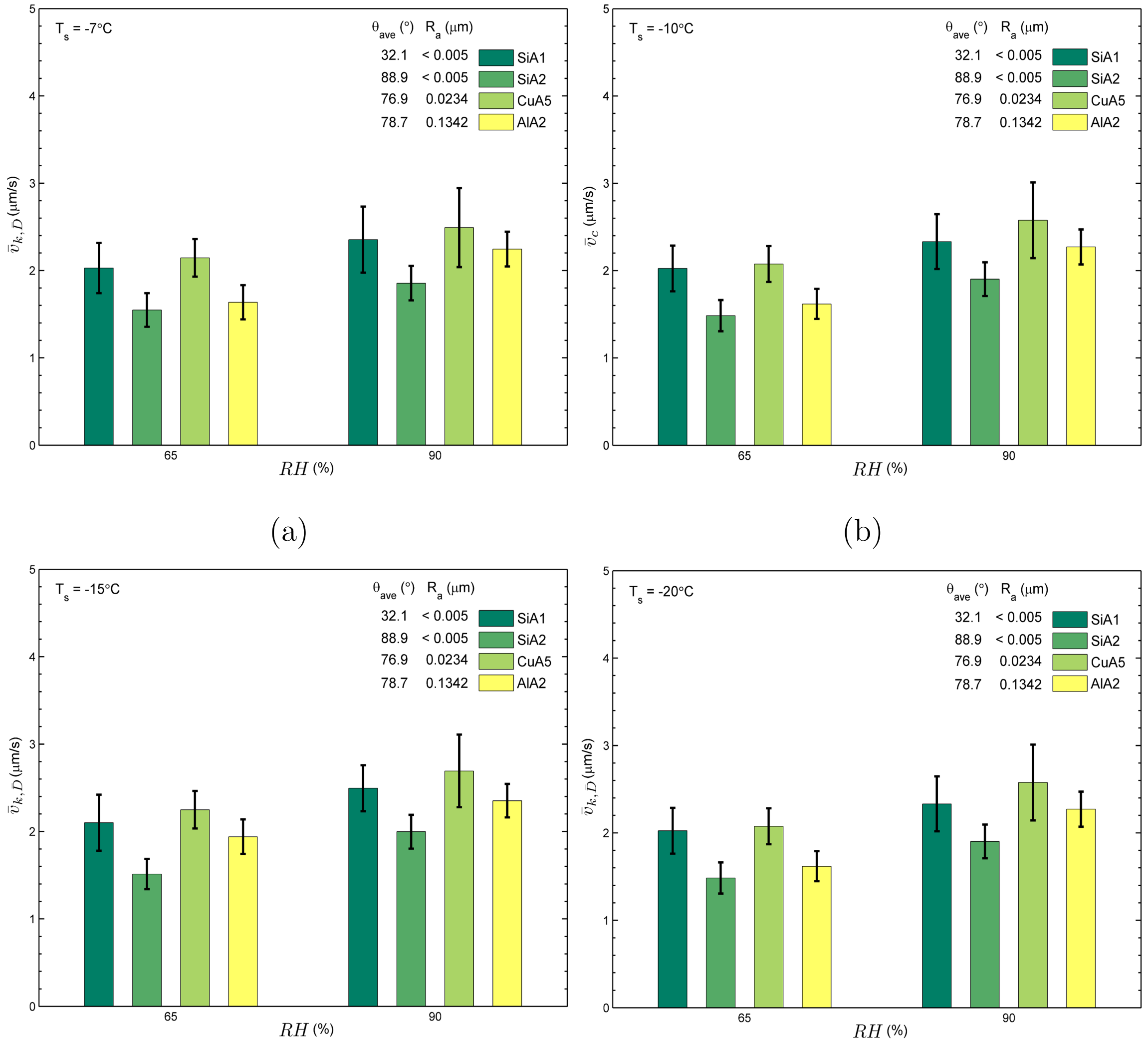

(a) (b)

(c) (d)

Figure 5.4: Mean inter-droplet freezing velocity $\bar{v}_{k,\bar{D}}$ versus free stream relative humidity RH with T_{air} = 5°C and U_{air} = 5 m/s for nominal substrate temperatures of (a) -7, (b) -10, (c) -15, and (d) -20°C

bicity of the substrate consistently decreased the inter-droplet freezing velocity, with $\bar{v}_{k,\bar{D}}$ for SiA2 substrate being on the order of 30% lower than for the SiA1 surface. This observation was consistent with the aggregate freezing velocity data shown previously. In addition, the trends of $\bar{v}_{k,\bar{D}}$ with surface type were similar to those presented in Figure 5.2; as was the case with $\bar{V}_n$, this implied that the isolated impact of surface roughness on $\bar{v}_{k,\bar{D}}$ cannot be readily isolated from the effects of hydrophobicity with these data.

Because the inter-droplet freezing velocity was based on a single average droplet diameter $\bar{D}_k$ for each case, the question naturally arises of whether or not $\bar{v}_{k,\bar{D}}$ accurately represents a true characteristic velocity for the inter-droplet freezing process. To address this concern, a series of quantitative measurements of the underlying inter-droplet crystal growth process were extracted from the Type II data. The resulting data consisted of manual crystal growth rate measurements carried out under high magnification with the digital microscopy system. These growth rates, which were designated as $\bar{v}_c$, were computed as time-integrated averages of the crystal tip displacement over time, as given by Equation 4.54. As the resulting crystal growth velocities were based on fundamental length and time measurements, $\bar{v}_c$ was assumed to be a reliable "spot check" measurement of the statistically-determined values of $\bar{v}_{k,\bar{D}}$ acquired from the much large sample sets associated with the Type I data. The Type II experiments were carried out for each test surface at substrate temperatures of -10 and -20°C and relative humidity values of 65 and 90%. The resulting values of $\bar{v}_c$ are presented in Figure 5.5 as a function of RH and surface type for each value of T_s considered. A direct comparison between $\bar{v}_c$ and $\bar{v}_{k,\bar{D}}$ for data at all matching conditions is shown in Figure 5.6.

In general, Figure 5.5 indicates that the variation of $\bar{v}_c$ with substrate temperature, relative humidity, and surface type was consistent with the matching $\bar{v}_{k,\bar{D}}$ data

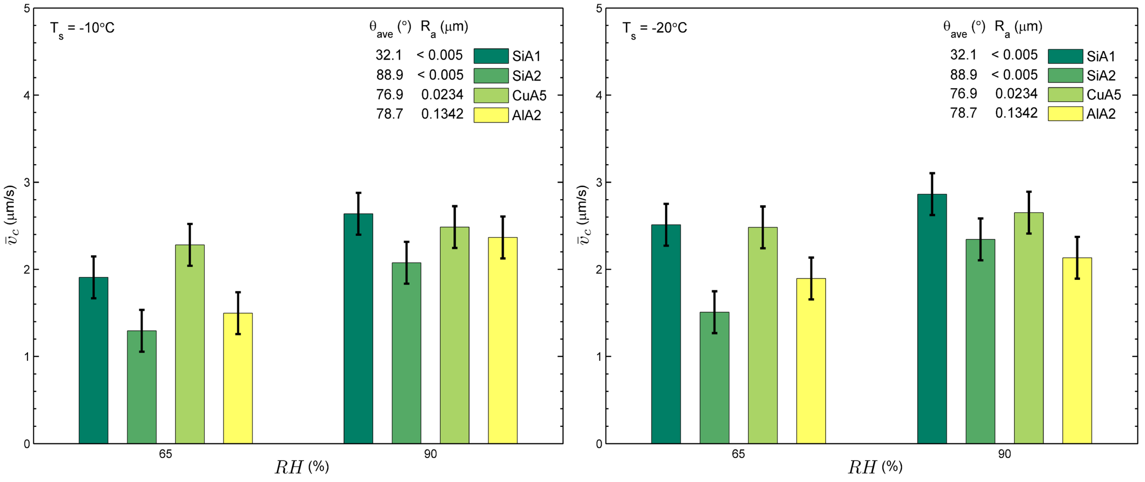

(a) (b)

Figure 5.5: Type II inter-droplet freezing velocity measurements $\bar{v}_c$ versus free stream relative humidity RH $T_{air} = 5$°C and $U_{air} = 5$ m/s for nominal substrate temperatures of (a) -10 and (b) -20°C

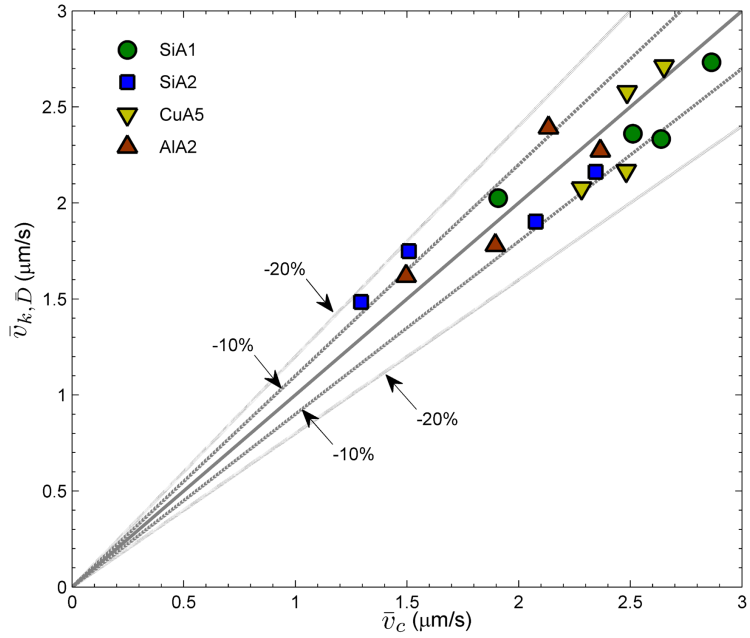

Figure 5.6: $\bar{v}_{k,\bar{D}}$ versus $\bar{v}_c$ for nominal surface temperatures of -10 and -20°C and relative humidity values of 65 and 90% for all test surfaces

presented in Figure 5.4. This observation was further validated by Figure 5.6 which shows that $\bar{v}_{k,\bar{D}}$ and $\bar{v}_c$ agreed to within ± 10% for the majority of the cases directly compared; the velocities agreed to within ± 20% in all instances.

3. Intra-Droplet Freezing Velocity

The primary objective of the Type III experiments was to observe and characterize the internal freezing process associated with individual droplets. High speed imaging of this intra-droplet freezing process revealed that upon the initiation of freezing within a droplet, a dendritic ice front rapidly propagated away from the point of inception along the droplet-substrate and droplet-air interfaces. This process appeared to encase the liquid droplet in a very thin ice shell prior to the onset of freezing in the bulk volume[2]. The velocity with which this encasing ice front propagates was designated as $\bar{v}_{sl}$ and was computed as the time-integrated average of the ice front displacement with time (in a manner analogous to $\bar{v}_c$ and Equation 4.54). Values of $\bar{v}_{sl}$ were determined for the same conditions used in the Type II experiments discussed previously. The resulting values of $\bar{v}_{sl}$ are shown in Figure 5.7 as a function of T_s and RH for each substrate. In Figure 5.8, the same data are displayed in terms of RH and surface type for each value of T_s used.

Perhaps the most remarkable feature of the data shown in Figures 5.7 and 5.8 was the substantial difference in the overall magnitudes of $\bar{v}_{sl}$ compared to $\bar{V}_n$ and $\bar{v}_{k,\bar{D}}$ at comparable conditions. On average, the intra-droplet freezing velocity was determined to be between three and five orders of magnitude greater than either the

---

[2] In this context, "bulk" freezing corresponds to the process by which the majority of the liquid volume within a droplet eventually freezes. Observations have shown that bulk freezing always starts at the droplet-substrate interface and proceeds in a direction normal to the surface until the entire droplet is frozen [39]. A time-lapsed image sequence of this process was shown in Figure 4.26

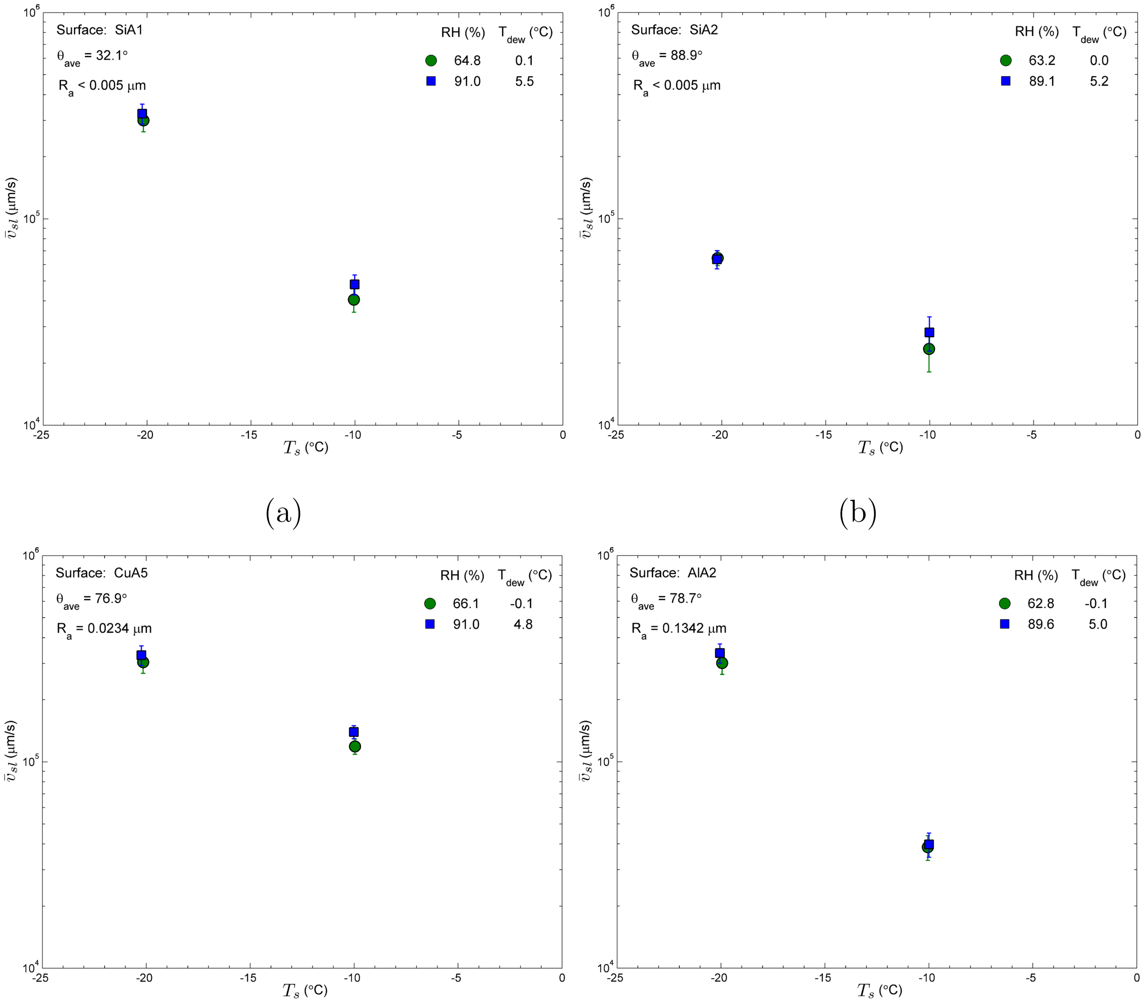

(a) (b)

(c) (d)

Figure 5.7: Type III inter-droplet freezing velocity measurements $\bar{v}_{sl}$ versus substrate temperature T_s with T_{air} = 5°C and U_{air} = 5 m/s for test surfaces (a) SiA1, (b) SiA2, (c) CuA5, and (d) AlA2

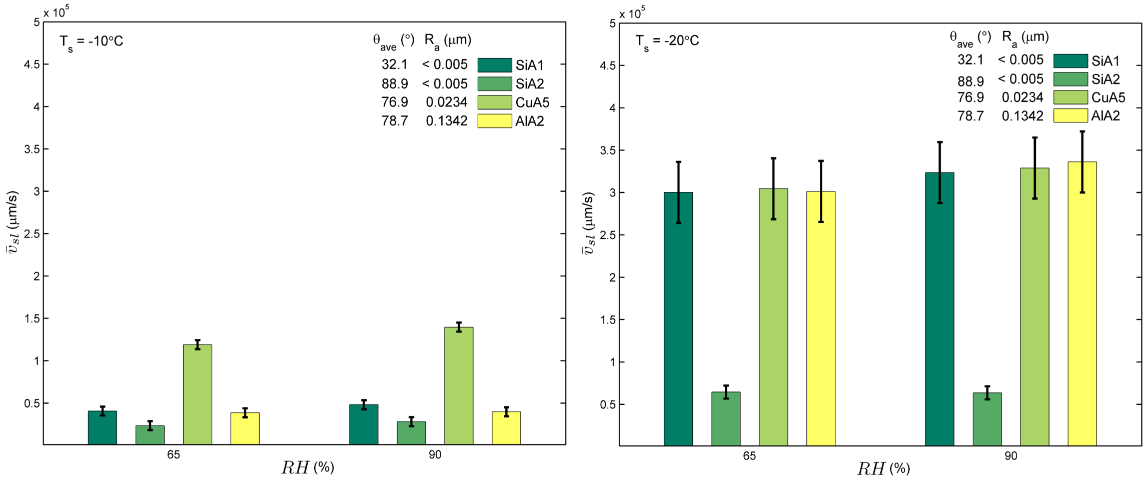

(a) (b)

Figure 5.8: Type III intra-droplet freezing velocity measurements $\bar{v}_{sl}$ versus free stream relative humidity RH with $T_{air} = 5$°C and $U_{air} = 5$ m/s for nominal substrate temperatures of (a) -10 and (b) -20°C

aggregate or inter-droplet freezing velocity for the same surface and set of conditions. Figure 5.7 clearly shows that the intra-droplet freezing velocity was a strong function of the substrate temperature. These data also indicated that $\bar{v}_{sl}$ was essentially independent of the air stream relative humidity. This latter observation was consistent with the expectation that any intra-droplet phenomena occurring along the droplet-substrate interface should be largely isolated from any potential effects associated with the ambient air stream.

The effects of surface properties on the intra-droplet freezing velocity were made clearer in Figure 5.8. These data showed that the isolated impact of substrate hydrophobicity can be quite significant. For example, at $T_s = -10$°C, $\bar{v}_{sl}$ on the SiA2 surface was found to be about 50% less than that for the SiA1 specimen. Interestingly, lowering the substrate temperature to -20°C increased this difference to over 75%. These data also revealed some information about the effects of surface roughness on the intra-droplet freezing process. In Figure 5.8, the magnitudes of $\bar{v}_{sl}$ for the SiA1 (smoothest, lowest R_a) and AlA2 (roughest, largest R_a) substrates agreed to within 5% for all cases. This finding suggested that surface roughness did not appreciably affect the intra-droplet freezing process. The fact that $\bar{v}_{sl}$ for the CuA5 surface at $T_s = -20$°C agreed well with the SiA1 and AlA2 data lent support to this supposition. However, the values of $\bar{v}_{sl}$ for the CuA5 surface at $T_s = -10$°C were as much as 65% higher than those for the SiA1 and AlA2 surfaces at the same conditions. The reason why this discrepancy emerged at the higher surface temperature but disappeared at the lower surface temperature was not immediately clear. Considering the fact that all of the latent heat evolved at the solid-liquid interface during freezing must eventually be conducted through the substrate, it was possible that the thermophysical properties of the substrate played an increasingly important role in the intra-droplet freezing process as the surface temperature increased.

B. Normalized Data and Predictive Correlations

The results presented in the previous section spawned two important questions about the dynamics of ice propgation on surfaces undergoing dropwise condensation:

1. How does the surface roughness (R_a) and apparent hydrophobicity (θ_{ave}) interact in tandem to affect the freezing process?
2. What role do the thermophysical properties of the substrate play in the freezing process, if any?

To addresses these questions, the reduced data presented in Figures 5.1 - 5.8 were modified to account for the variation of the indicated parameters. For greater generality in the ensuing discussion, all temperatures were reported in the corresponding absolute units of Kelvin (K) and all relative humidity values were recast in terms of the absolute humidity ratio, defined as

$$\omega_{air} = 0.622 \frac{P_w}{P_\infty - P_w} \tag{5.1}$$

where P_w is the partial pressure of the water vapor in the air stream and P_∞ is the total ambient air pressure. The units of ω_{air} are g/kg, which is interpreted in this context as *grams of water per kilogram of dry air*. Given that the relative humidity of the air could be defined in terms of the saturation vapor pressure of water $P_{w,sat}$ at a given temperature,

$$RH = \frac{P_w}{P_{w,sat}} \tag{5.2}$$

an explicit relationship between ω_{air} and RH could be cast as

$$\omega_{air} = 0.622 \frac{RH \cdot P_{w,sat}}{P_\infty - RH \cdot P_{w,sat}} \tag{5.3}$$

In an effort to better understand the interplay of surface roughness and free energy, the model of Wenzel [35] previously discussed in Chapter II (Equation 2.15) was assessed as one way to anticipate the true or corrected contact angle θ_w for a droplet that is in perfect contact with a given substrate. The Wenzel formula was given by

$$\cos\theta_w = f_w \cos\theta_{app} \tag{5.4}$$

where θ_{app} was equivalent to the apparent contact angle θ_{ave} reported in the previous section and f_w was the ratio of the actual to projected contact area between the droplet and substrate. Because f_w increases with increasing surface roughness, it follows that for $\theta_{app} < 90°$, $\theta_w \leq \theta_{app}$. Conversely, for $\theta_{ave} > 90°$, Equation 5.4 requires that $\theta_w \geq \theta_{app}$. The implications of these relationships for the problem at hand was as follows. For the experiments conducted in this study, the droplets were always grown from condensation on a dry substrate. However, the apparent contact angles given by θ_{ave} were measured from *implanted* droplets which were manually pipetted onto the test surfaces. Because the condensation process occured at a molecular level, it was reasonable to assume that a droplet grown from water vapor was in better overall contact with the microscopic topology of the surface as compared to an implanted droplet. Thus θ_w in Equation 5.4 represented a logical parameter by which to intrinsically couple the effects of surface roughness and wettability.

In the absence of precise surface profilometry, determining the value of f_w for a substrate would be difficult and subject to considerable uncertainty. To utilize the Wenzel concept in the present analysis, it was more practical to simply measure θ_w directly. To do this, the microscope had to be reconfigured from an top- to side-view orientation such that the test surface could be viewed edge-on. With this arrangement, each test surface was able to be placed on the thermal stage and cooled to condensing temperatures. As droplets grew within the field of view, the digital imaging system was used to acquire multiple images as the droplets grew through sizes comparable to those reported in Figure 3.11. A minimum of 15 condensed contact angle measurements were carried out for each surface with droplet base diameters ranging from about 750 to 2500 μm. In addition, a comparable set of implanted droplet contact angle measurements on the dry surfaces were carried out with the same microscope setup to check for consistency with the previous measurements. The implanted contact angles for each surface were found to be consistent with the apparent values reported in Table 3.9. An example of the differences between condensed and implanted contact angles for the AlA2 surface can be seen in the pair of contrast enhanced images shown in Figure 5.9. Mean values of the condensed (θ_w) and implanted (θ_{app}) contact angles for each surface, along with the nominal contact angle deviation $\Delta\theta = \theta_{app} - \theta_w$ and calculated values of f_w, are are reported in Table

5.1.

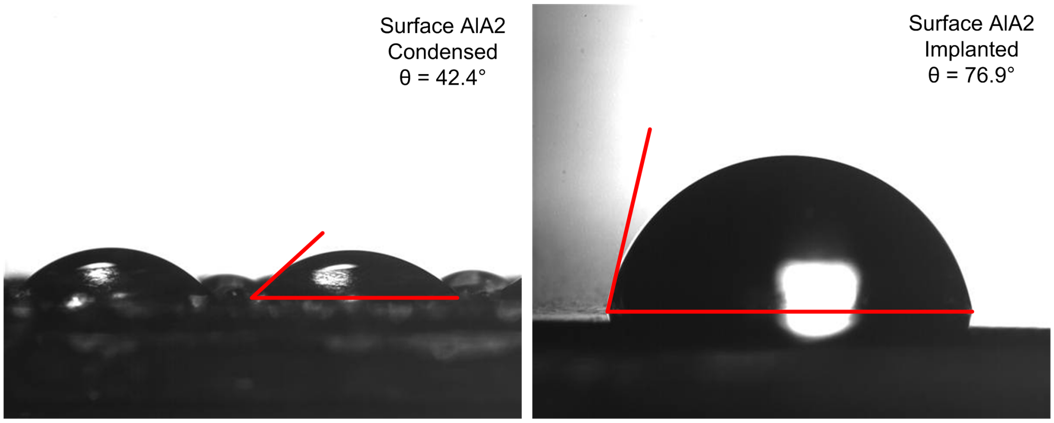

(a) (b)

Figure 5.9: Example of (a) condensed and (b) implanted droplets and resulting contact angles for the AlA2 substrate

Table 5.1: Average condensed and implanted contact angles for all test surfaces

Surface ID	θ_w degrees	θ_{app} degrees	$\Delta\theta$ degrees	f_w
SiA1	25.3	33.6	8.3	1.09
SiA2	83.0	83.9	0.9	1.16
CuA5	57.7	77.7	20.0	2.52
AlA2	41.5	76.4	34.9	3.14

The variation of θ_w with θ_{app} shown in Table 5.1 was consistent with the general relationship given by Equation 5.4: as roughness increased, so did the difference between the apparent and corrected contact angles. For the smoothest SiA1 and SiA2 surfaces, the difference between the corrected and apparent contact angles was relatively small, a fact which was further reflected by the near-unity[3] values of f_w. However, the contact angle deviation for the CuA5 and AlA2 surfaces was considerably higher, indicating that the use of the apparent contact angles θ_{app} or θ_{ave} can be misleading for rougher surfaces. As a result of these findings, the corrected contact angle θ_w was used as the sole parameter for quantifying the combined interfacical properties of roughness and wettablillity for each test substrate.

By design, the testing configuration and conditions used in this study ensured that all latent heat evolved during the freezing process was ultimately conducted away from the phase-change regions and through the substrate. Even though the size of the freezing droplets were quite small compared to the length, width, and thickness of the test surfaces, the question still remained as to what role, if any, the substrate thermophysical properties played in the ice propagation dynamics. For example, the thermal conductivity of copper substrate was more than 2.5 times greater than that of the silicon specimens; thus, latent heat rejected during freezing would be expected to diffuse into and throughout the copper and silicon surfaces in different manners. With this in mind, it was not difficult to envision a scenario in which the heat evolved by a single droplet led to a localized surface temperature fluctuation within its immediate vicinity. A phenomenon such as this occurring many times over on a droplet-laden surface could be a major constituent of the overall freezing dynamics. If this was in fact this case, then the thermophysical properties of the substrate could, by extension, have a considerable impact on the freezing dynamics as well.

Directly measuring or simulating the localized effects of transient heat conduction in the substrate were beyond the scope of this study. However, the effects of the

---

[3] Because the roughness values for surfaces SiA1 and SiA2 were assumed to be essentially the same, one would expect f_w for both surfaces to be effectively identical; they actually differ by about 6%, which falls within the range of uncertainty for the contact angle measurements

properties most relevant to heat conduction in the substrate − thermal conductivity k_s, heat capacity C_s, and density ρ_s − were readily assessed. These three properties can be combined to define the thermal diffusivity of the substrate,

$$\alpha_s = \frac{k_s}{\rho_s C_s} \tag{5.5}$$

Thermal diffusivity may be understood as an indication the efficiency with which a substance conducts heat in relation to its volumetric heat capacity. In general, the higher the thermal diffusivity of a material, the faster it tends to approach thermal equilibrium with its surroundings. The thermal diffusivities of the surfaces used in this study are reported in Table 3.7.

The freezing velocity data presented in Figures 5.1 - 5.8 were normalized with the substrate thermal diffusivities to form a set of dimensionless velocity parameters. These normalized freezing velocities were then appropriately cast as functions of the corrected contact angle, surface temperature, and absolute humidity ratio for each case as

$$\frac{\mathcal{V} \cdot \ell_r}{\alpha_s} = f\left(\theta_w, T_s, \omega_{air}\right) \tag{5.6}$$

where $\mathcal{V}$ is a placeholder for the appropriate freezing velocity ($\bar{V}_n$, $\bar{v}_{k,\bar{D}}$, or $\bar{v}_{sl}$) and ℓ_r is a conduction length scale. Ideally, ℓ_r should be based on the substrate geometry and the effective direction of the heat flux vectors[4], but the latter item can not be determined in practice without local temperature measurements. Therefore, for consistency ℓ_r was assigned a constant value equal to the diagonal dimension of the ROI for all cases. For the 5X microscope objective lens, this corresponded to $\ell_r = 1.902 \times 10^3$ μm.

---

[4] As in accordance with the vector form of Fourier's law, $\mathbf{q}'' = -k\nabla T$.

1. Aggregate Freezing Process

Normalization of the reduced aggregate freezing velocity data presented in Figures 5.1 and 5.2 produced a series of general trends which are shown in Figure 5.10. In these plots, the surface properties of roughness and apparent hydrophobicty are intrinsically represented by the values of θ_w while the nominal substrate temperature is indicated by the data marker type. The normalized aggregate freezing velocity data are presented for humidity ratios of 3.5 and 4.9 g/kg in Figures 5.10(a) and (b), respectively.

The results shown in Figure 5.10 indicate that for a given substrate temperature and humidity ratio, the normalized freezing velocity tracks inversely with the corrected contact angle. This relationship is emphasized by the lines of best fit shown for each substrate temperature in both Figures 5.10(a) and (b). These lines were generated by way of non-linear regression analysis applied to the dataset associated with each substrate temperature and humidity ratio condition. The only constraint applied in the regression analyses was

$$\lim_{\theta_w \to 180^\circ} \bar{V}_n = 0$$

which was predicated on the assumption that for a completely non-wettable surface, the activation energy barrier for ice nucleation was high enough that freezing would not occur within the range of substrate temperatures considered in this study. Considering this constraint, the data profiles suggested a sigmoidal or “S-curve” relationship between the normalized velocity and corrected contact angle. A suitable correlating function was determined to be a three-parameter sigmoid curve of the form

$$\frac{\bar{V}_n \cdot \ell_r}{\alpha_s} = C_1 \left(\frac{1}{1 + e^{\frac{C_3 - \theta_w}{C_2}}} - \Theta_0 \right) \tag{5.7}$$

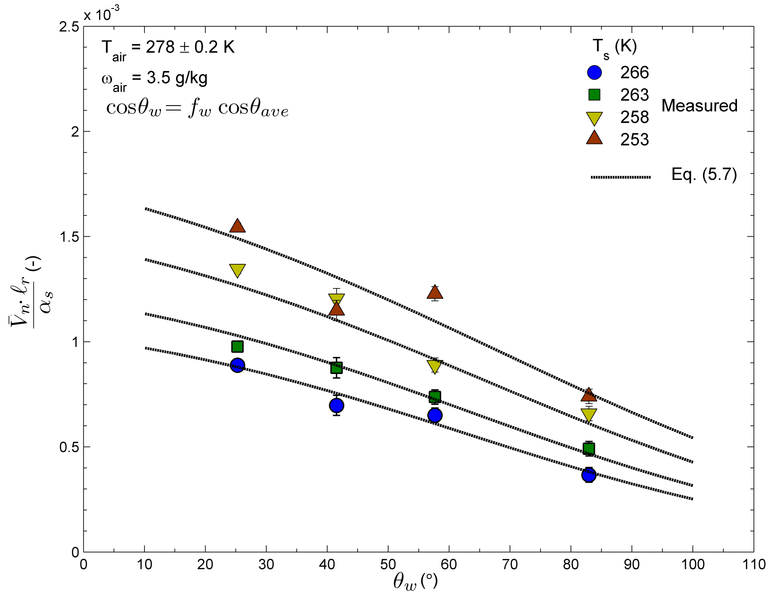

(a)

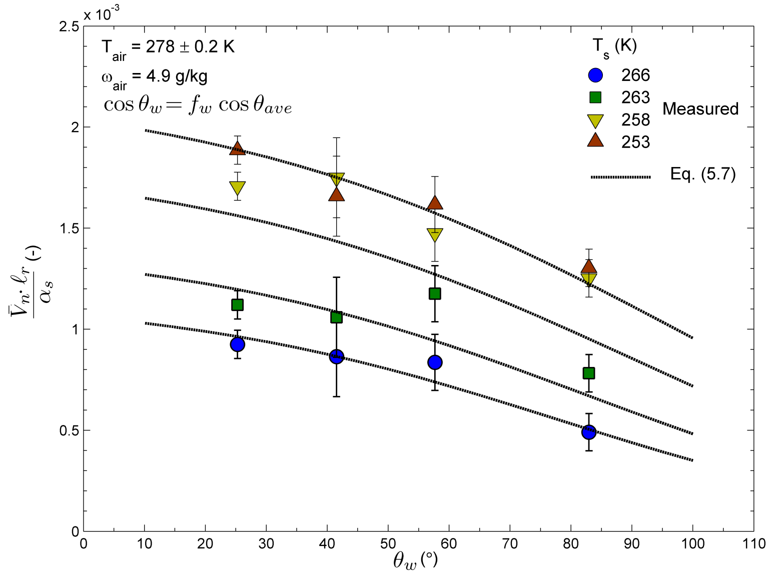

(b)

Figure 5.10: Normalized aggregate freezing front velocity $\frac{\bar{V}_n \cdot \ell_r}{\alpha_s}$ versus corrected contact angle θ_w with $U_{air} = 5$ m/s for all test surfaces and nominal humidity ratios of (a) 3.5 and (b) 4.9 g/kg

where

$$\Theta_0 = \frac{1}{1 + e^{\frac{C_3 - 180}{C_2}}} \tag{5.8}$$

and C_1, C_2 and C_3 were correlating parameters which were functions of the substrate temperature and humidity ratio. Based on the results of a secondary multiple regression analysis, it was found that C_1, C_2 and C_3 could be cast as linear functions of T_s and ω_{air}, leading to the common expression

$$C_n = a_1 \omega_{air} T_s + a_2 T_s + a_3 \omega_{air} + a_4 \tag{5.9}$$

where C_n represented the appropriate correlating parameter used in Equations 5.7 and 5.8 and a_1, a_2, a_3, and a_4 were constants; the values of these constants are listed in Table 5.2.

Table 5.2: Correlating constants for functions C_n given by Equation 5.9

n	a_1	a_2	a_3	a_4
1	-1.901×10^{-5}	-7.000×10^{-6}	5.090×10^{-3}	3.028×10^{-3}
2	1.697×10^{-2}	5.097×10^{-1}	-4.075×10^{0}	-1.693×10^{2}
3	-9.106×10^{-1}	2.766×10^{0}	2.538×10^{2}	-7.140×10^{2}

Considering all layers in this multi-parameter correlation, the coefficient of determination (R^2) for Equation 5.7 was found to be ≥ 0.90 for all but two datasets. Inspection of Figure 5.10(b) revealed that the accuracy of the correlation was lowest at substrate temperatures of 263 and 258 K for the highest humidity ratio considered ($\omega_{air} = 4.9$ g/kg). The overall performance of Equation 5.7 was assessed by directly evaluating the predicted against the corresponding measured values. A comparative plot summarizing these results is shown in Figure 5.11.

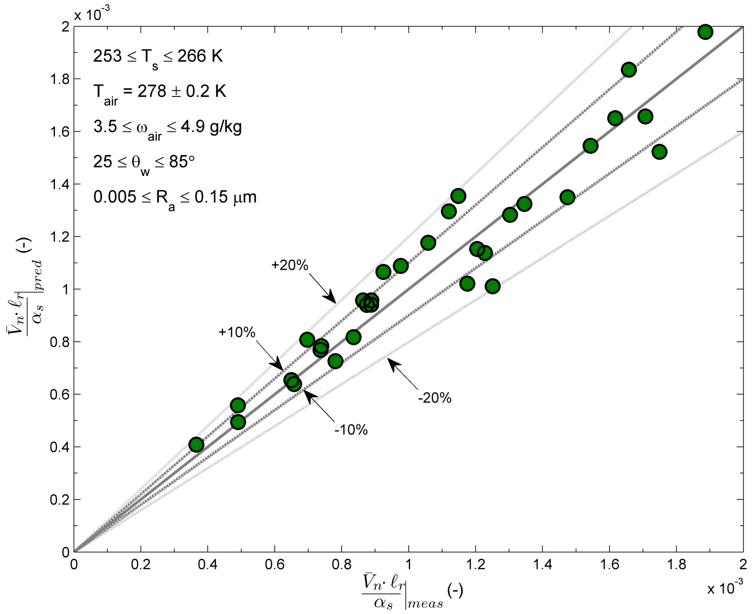

Figure 5.11: Predicted versus measured values of normalized aggregate freezing front velocity $\frac{\bar{V}_n \cdot \ell_r}{\alpha_s}$ for all test surfaces and conditions: based on Equation 5.7

Figure 5.11 indicates that Equation 5.7 predicted 60% of the measured data to within ± 10% and all data to within ± 20%. Based on these results, Equation 5.7 was expected to provide reasonably accurate estimations of the average aggregate freezing velocity within the ranges of substrate and environmental parameters listed in Figure 5.11.

2. Inter-Droplet Freezing Process

The inter-droplet freezing data shown in Figures 5.3 and 5.4 were normalized with the substrate thermal diffusivity in the same manner described in the previous section. The resulting normalized data are presented in Figure 5.12(a) in terms of the corrected contact angle and the two humidity ratios considered. The large degree of overlap seen in each humidity dataset at a given value of θ_w was similar to the previous assessment of the inter-droplet freezing velocity not being very sensitive to the temperature of the substrate. To simplify the analysis, the normalized inter-droplet freezing velocity was assumed to be completely independent of temperature; as such, each constant θ_w and ω_{air} dataset was averaged across all values of T_s to yield a single representative value of $\frac{\bar{v}_{k,\bar{D}} \cdot \ell_r}{\alpha_s}$ for each combination of θ_w and ω_{air}. These temperature-averaged data are shown in Figure 5.12(b).

The results presented in Figure 5.12(b) suggested that for a given humidity ratio, the normalized inter-droplet freezing velocity approached a finite value as $\theta_w \rightarrow 0°$ and decayed asymptotically to a non-zero value as $\theta_w \rightarrow 180°$. The former trend was consistent with the fact that the activation energy barrier for solidification and deposition was less for a hydrophillic surface than a hydrophobic surface. In the absence of data in the upper ranges of θ_w, the physical significance of the latter trend was not as clear. On one hand, it could be argued that $\bar{v}_{k,\bar{D}} \rightarrow 0$ as $\theta_w \rightarrow 180°$ based simply on the premise that such a surface would not be wettable. However, if the dominant mechanism responsible for inter-droplet crystal growth was ice deposition from the vapor phase – the same mechanism responsible for atmospheric ice crystal growth (e.g. snowflakes) [82–84] – it was not clear whether or not such a constraint was even applicable to a completely hydrophobic surface. Nevertheless, the general trends for the range of data shown in Figure 5.12 suggested the relationship between the normalized velocity and corrected contact angle followed one of exponential decay. The lines of best fit included in Figure 5.12 were derived from a non-linear regression analysis based on a three-parameter fitting function of the form

$$\frac{\bar{v}_{k,\bar{D}} \cdot \ell_r}{\alpha_s} = C_4 + C_5 e^{-C_6 \theta_w} \tag{5.10}$$

where C_4, C_5, and C_6 were correlating parameters which were a first order linear function of ω_{air}:

$$C_n = a_5 \omega_{air} + a_6 \tag{5.11}$$

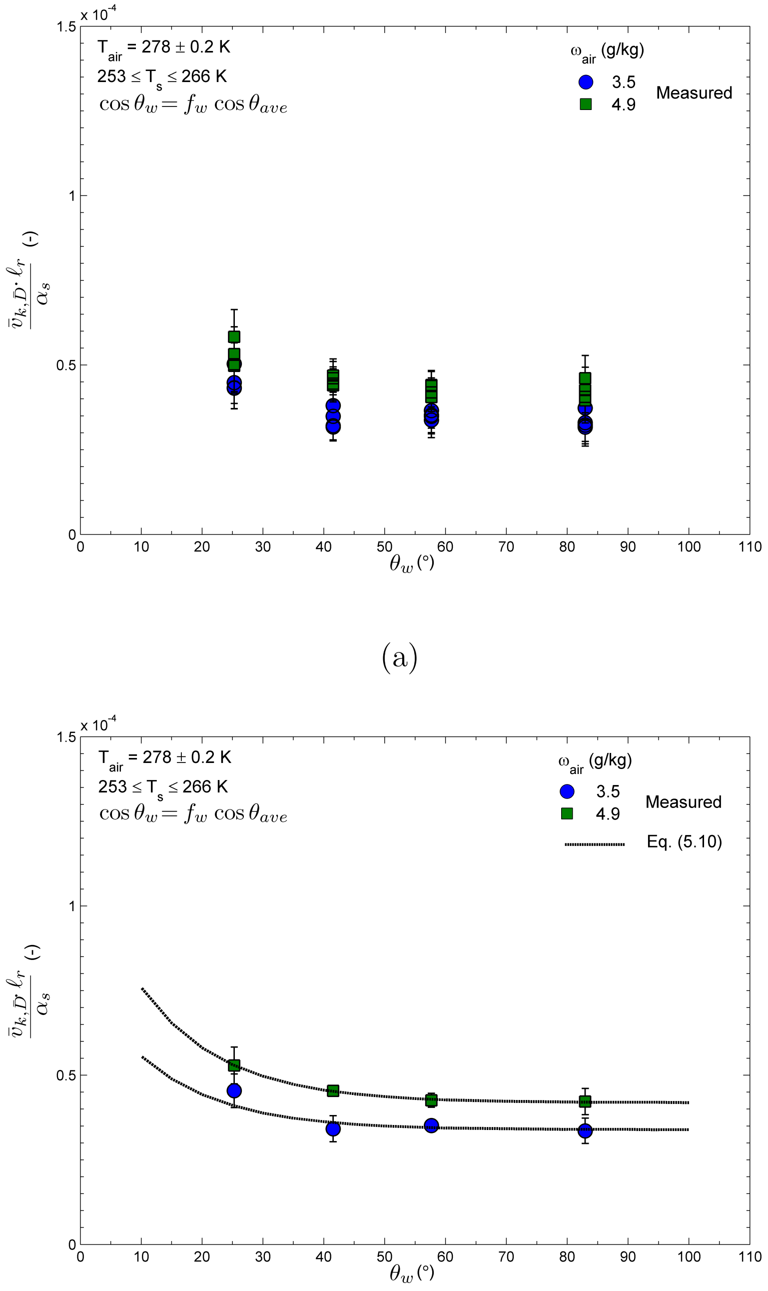

(a)

(b)

Figure 5.12: Normalized inter-droplet freezing velocity $\frac{\bar{v}_{k,\bar{D}} \cdot \ell_r}{\alpha_s}$ versus corrected contact angle θ_w with U_{air} = 5 m/s for all test surfaces and nominal humidity ratios of 3.5 and 4.9 g/kg: (a) all and (b) T_s-averaged data

The values of the constants a_5 and a_6 used in Equation 5.11 are given in Table 5.3.

Table 5.3: Correlating constants for functions C_n given by Equation 5.11

n	a_5	a_6
4	6.000×10^{-6}	1.300×10^{-5}
5	1.900×10^{-5}	-2.100×10^{-5}
6	0	7.380×10^{-2}

The lines of best fit shown in Figure 5.12(b) indicated generally good agreement between the data and Equation 5.10 ($R^2 \geq 0.95$). The accuracy of Equation 5.10 was assessed by contrasting the predicted and corresponding measured values for all of the data shown in Figure 5.12(a). This results of this evaluation are presented in Figure 5.13.

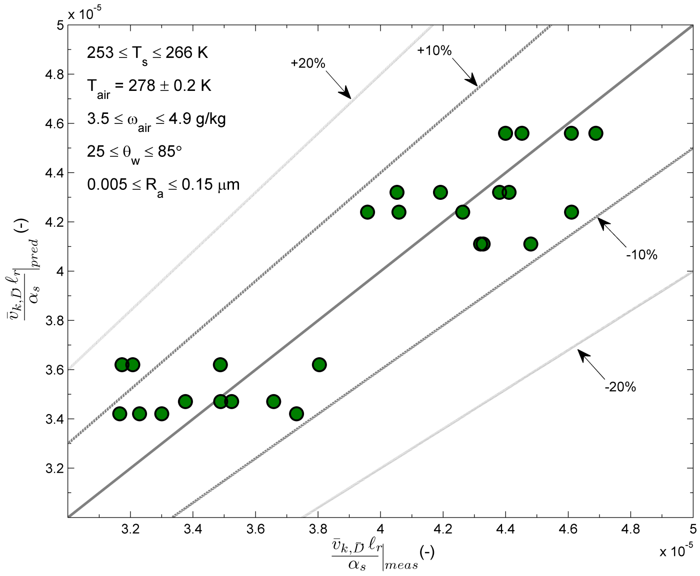

Figure 5.13: Predicted versus measured values of normalized inter-droplet freezing velocity $\frac{\bar{v}_{k,\bar{D}}\cdot\ell_r}{\alpha_s}$ for all test surfaces and conditions: based on Equation 5.10

Figure 5.13 shows that Equation 5.10 accurately captured the subtle impact of humidity ratio and corrected contact angle on the normalized inter-droplet freezing velocity. Specifically, this correlation predicted 90% of the measured data to within ± 10% and all data to within ± 20%.

3. Intra-Droplet Freezing Process

The normalized intra-droplet freezing velocity data, based on the reduced values reported in Figures 5.7 and 5.8, are shown in Figure 5.14. The normalized data were presented in terms of the corrected contact angle and substrate temperature only. The effect of humidity on the intra-droplet freezing process was found to be negligible and was not considered further.

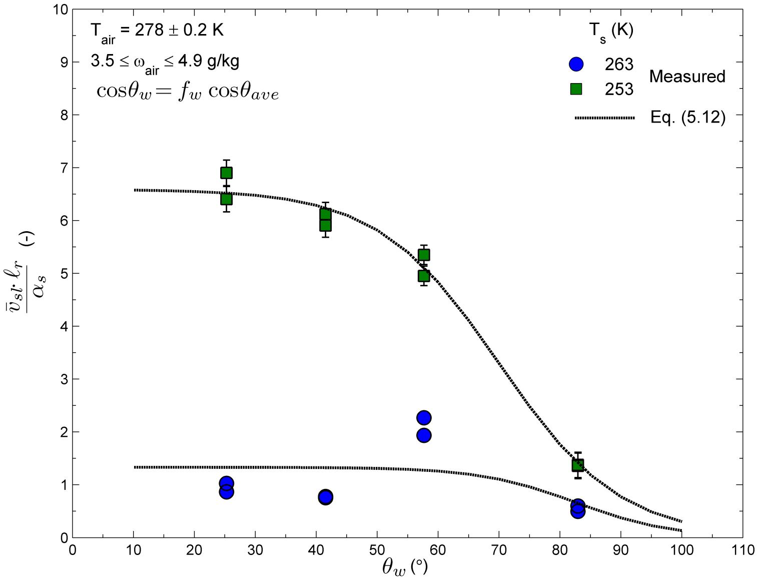

Figure 5.14: Normalized intra-droplet freezing velocity $\frac{\bar{v}_{sl}\cdot\ell_r}{\alpha_s}$ versus corrected contact angle θ_w for all test surfaces at nominal surface temperatures of 263 and 253 K and humidity ratios of 3.5 and 4.9 g/kg

Figure 5.14 indicated that for a given substrate temperature, the normalized intra-droplet freezing velocity decreased monotonically from a finite asymptotic value as the corrected contact angle increased. Assuming that ice nucleation would not occur on a completely hydrophobic surface within the range of substrate temperatures considered in this investigation, the general shape of these trends suggested a sigmoidal relationship between the normalized velocity and corrected contact angle. The lines of best fit shown in Figure 5.14 were derived from a non-linear regression analysis similar to that previously carried out for the normalized aggregate freezing velocity data. Invoking the constraint defined by

$$\lim_{\theta_w \to 180^\circ} \bar{v}_{sl} = 0$$

the optimal correlating function was determined to be a sigmoid curve similar to Equation 5.7, namely

$$\frac{\bar{v}_{sl} \cdot \ell_r}{\alpha_s} = C_7 \left(\frac{1}{1 + e^{\frac{C_9 - \theta_w}{C_8}}} - \Theta_1 \right) \tag{5.12}$$

where

$$\Theta_1 = \frac{1}{1 + e^{\frac{C_9 - 180}{C_8}}} \tag{5.13}$$

The correlating parameters C_7, C_8, and C_9 were assumed to be functions of T_s only. A generic first order linear function for these parameters was used:

$$C_n = a_7 T_s + a_8 \tag{5.14}$$

The values of the constants a_7 and a_8 used in Equation 5.14 are listed in Table 5.4.

The R^2 values associated with Equation 5.12 were determined to be 0.71 and 0.98 for the substrate temperature conditions of 263 and 253 K, respectively. A comparison between the predicted and measured values is shown in Figure 5.15.

Overall, Equation 5.12 predicted about 60% of the measured data to within

Table 5.4: Correlating constants for functions C_n given by Equation 5.14

n	a_7	a_8
7	-5.259×10^{-1}	1.397×10^{2}
8	2.000×10^{-1}	-6.053×10^{1}
9	1.250×10^{0}	-2.463×10^{2}

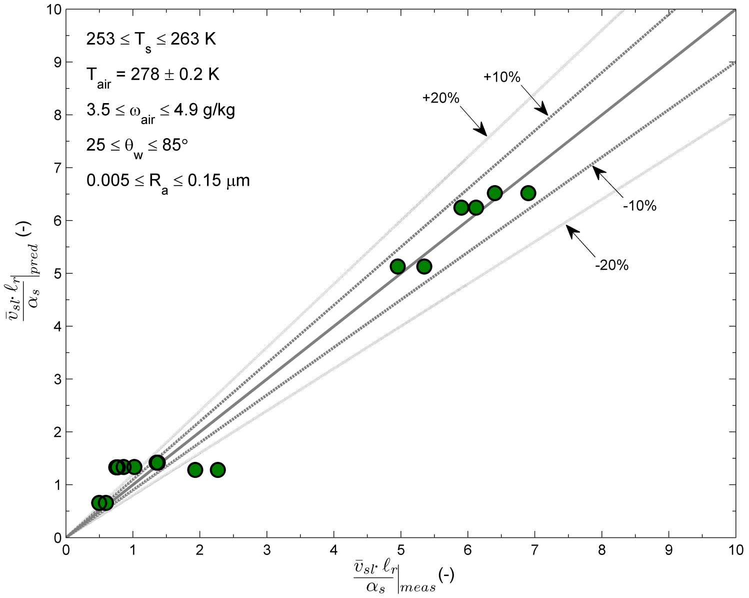

Figure 5.15: Predicted versus measured values of normalized intra-droplet freezing velocity $\frac{\bar{v}_{sl} \cdot \ell_r}{\alpha_s}$ for all test surfaces and conditions: based on Equation 5.12

$\pm 20\%$. The poorer agreement between the predicted and measured values for the higher temperature condition can be largely attributed to the data points located at $\theta_w = 57.7^\circ$, which where measured to have values that were, on average, about 70% higher than implied by the trend. The underlying reason for this discrepancy was not known, but two distinct possibilities include

1. microscopic defects, including contamination or oxidation, along the droplet-substrate interface that may have had the net effect of accelerating the crystallization kinetics at higher temperatures (in a manner somewhat analogous to ice nuclei), or
2. localized fluctuations in substrate temperature.

C. Summary and Remarks

Three unique sets of freezing velocity data were used characterize the dynamics of ice propagation on surfaces undergoing dropwise condensation. The dependent variables of interest consisted of the average aggregate freezing velocity $\bar{V}_n$, the average inter-droplet freezing velocity $\bar{v}_{k,\bar{D}}$, and the average intra-droplet freezing velocity $\bar{v}_{sl}$. These parameters were normalized with the thermal diffusivities of the substrates and modeled as functions of three independent variables quantified in or by the experiments: the substrate temperature T_s, the absolute humidity ratio of the air stream ω_{air}, and the combined effects of surface roughness and hydrophobicity, as given by the corrected contact angle θ_w. Generalized correlations were developed which predicted the normalized velocities with reasonable accuracy: the resulting methods were found to match at least 75% of the measured data from the aggregate, inter-droplet, and intra-droplet freezing experiments to within $\pm 15\%$, $\pm 10\%$, and $\pm 35\%$, respectively.

The correlations for the aggregate (Equation 5.7) and inter-droplet freezing velocities (Equation 5.10) were found to provide accurate results over the following ranges of substrate and environmental parameters:

- $253 \leq T_s \leq 266$ K
- $3.5 \leq \omega_{air} \leq 4.9$ g/kg
- $25 \leq \theta_w \leq 85^\circ$
- $8.9 \times 10^{-5} \leq \alpha_s \leq 1.2 \times 10^{-4}$ m^2/s

The correlation for the intra-droplet freezing velocity (Equation 5.12) was applicable over the same ranges of these parameters except for the substrate temperature; this relationship has not been validated for $T_s \geq 263$ K. The effects of air stream temperature and velocity were not explicitly considered in this study.

It is worth noting that the effects of condensation and condensate distribution have been implicitly incorporated into the aggregate freezing data. Inasmuch, Equation 5.7 can be thought of as type of higher level phenomenological model that could eventually be reformulated to study the condensation process with greater detail. The data reduction and analysis methods developed in Chapter IV would certainly be conducive to such an investigation.

CHAPTER VI

EVIDENCE FOR ICE PROPAGATION MECHANISMS ON DROPLET-LADEN SURFACES

The results presented in the previous two chapters suggest that ice propagates across surfaces undergoing dropwise condensation due to the combined effects of two distinct mechanisms: inter- and intra-droplet ice crystal growth. A series of experimental procedures and analysis techniques outlined in Chapters III and IV allowed these mechanisms, as well as the resulting aggregate freezing dynamics, to be characterized independently as functions of surface properties and environmental parameters. The resulting freezing velocity data, along with a set of predictive correlations, were presented and discussed in Chapter V. As an extension to the reported methods and results, it was desirable to evaluate the primary mechanisms of ice crystal growth in terms of more fundamental principles. The benefits of such an analysis include:

1. Being able to explain the experimental results and observations within a more fundamental framework provides further validation that the basic mechanisms have been correctly identified.
2. Analyzing the ice propagation process at a basic level is a critical first step towards developing a more comprehensive dynamical model.
3. A better understanding of the theoretical underpinnings associated with these mechanisms ultimately contributes to the body of fundamental knowledge in the areas of nucleation, crystallization kinetics, and surface science.

In this chapter, the aggregate freezing process is analyzed in terms of the constituent crystal growth mechanisms and the thermophysics associated with these mechanisms are analyzed and compared with the experimental data, where possible.

A. Phenomenological Decomposition of the Aggregate Freezing Process

Numerous quantitative and qualitative observations reported in this study indicated that the aggregate ice propagation process on droplet-laden surfaces can be described as the manifestation of two distinct crystal growth mechanisms which operated over a range of microscopic length and time scales. The first mechanism, referred to as the inter-droplet freezing process, was responsible for the propagation of the ice phase from one droplet to the next and appeared to operate exclusively along the substrate between neighboring droplets. The second mechanism, branded the intra-droplet freezing process, dictated the rate at which ice propagated throughout individual supercooled droplets. Notwithstanding the fact that some droplets on the surface naturally underwent spontaneous ice nucleation, the combined interaction of these mechanisms eventually led to the freezing of all droplets within a given region, which was found to be a necessary precursor to the localized formation of frost. The interaction between these two mechanisms for an ideal, one-dimensional aggregate freezing process is illustrated in Figure 6.1.

The results presented in Chapter V showed that the speed at which the intra-droplet mechanism propagated ($\bar{v}_{sl}$) was as many as five orders of magnitude higher than that of the inter-droplet freezing process ($\bar{v}_{k,\bar{D}}$). Consequently, the manner in which these two mechanisms affected the aggregate freezing process was considerably different. As depicted in Figure 6.1, the slower inter-droplet mechanism controlled the rate at which the ice phase migrated *between* droplets; as such, $\bar{v}_{k,\bar{D}}$ acted exclusively through length scales consistent with the local inter-droplet separation and defined a lower limit for the average aggregate freezing velocity $\bar{V}_n$ as long as droplets are present on the surface. On the other hand, the significantly faster intra-droplet mechanism defined the rate at which the ice phase propagated *across* individual supercooled liquid

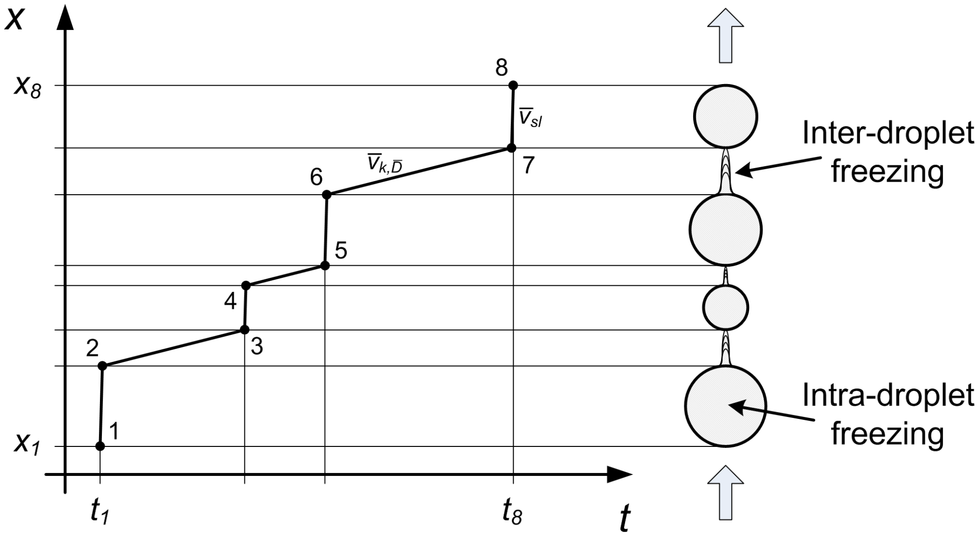

Figure 6.1: Illustration of an ideal 1-D aggregate freezing process in terms of the local ice phase position versus time for the constituent inter- and intra-droplet ice crystal growth mechanisms

droplets, (i.e. from one side to the other); $\bar{v}_{sl}$ therefore operated at the diametral length scales associated with individual droplets and served as an upper limit for the aggregate freezing velocity. Assuming that the characteristic quantities given by $\bar{v}_{k,\bar{D}}$ and $\bar{v}_{sl}$ did not vary appreciably over the surface, the aggregate freezing velocity magnitude in any local region can be cast as a function of these two constituent velocities, as well as two parameters that specified the distribution of condensate on the substrate:

$$V_n = f\left(\bar{v}_{k,\bar{D}}, \bar{v}_{sl}, D, \Delta r\right) \tag{6.1}$$

In Equation 6.1, D and Δr were the local droplet diameter and inter-droplet separation just prior to freezing, respectively. With regard to Figure 6.1, the droplet diameter could be written as $D = x_2 - x_1$ or $D = x_8 - x_7$, depending on the position of the ice phase at any time t. Likewise, the inter-droplet separation distance could be expressed as $\Delta r = x_3 - x_2$ or $\Delta r = x_7 - x_6$, and so on.

In considering the simple one-dimensional case depicted in Figure 6.1, a suitable basis emerged for defining the aggregate freezing velocity in terms of the constituent mechanisms. The most localized definition of V_n was based on the variable unit length

$$\Delta x_\psi = D + \Delta r \tag{6.2}$$

where the size of Δx_ψ was such that the inter- and intra-droplet crystal growth mechanisms were incorporated into the formulation just once. For example, V_n could be defined between the points 1 and 3 or 6 and 8 shown in Figure 6.1, but not between 3 and 4 as the latter would simply be $\bar{v}_{sl}$. Within this framework, V_n varied locally according to the droplet size and spatial distributions of the condensate droplets as

$$V_n(x) = \frac{\Delta x_\psi}{\Delta t_\psi} \tag{6.3}$$

where Δt_ψ was the unit time scale associated with Δx_ψ defined by

$$\Delta t_\psi = \Delta t_{inter} + \Delta t_{intra} = \frac{\Delta r}{\bar{v}_{k,\bar{D}}} + \frac{D}{\bar{v}_{sl}} \tag{6.4}$$

Substituting the expressions for Δx_ψ and Δt_ψ into Equation 6.3 yielded

$$V_n(x) = \frac{D + \Delta r}{\frac{\Delta r}{\bar{v}_{k,\bar{D}}} + \frac{D}{\bar{v}_{sl}}} \tag{6.5}$$

The partial fraction in Equation 6.5 can be further simplified by recalling that $\bar{v}_{sl} \gg \bar{v}_{k,\bar{D}}$; therefore, $\frac{D}{\bar{v}_{sl}} \ll \frac{\Delta r}{\bar{v}_{k,\bar{D}}}$ and the local aggregate freezing velocity can be reduced to

$$V_n(x) = \bar{v}_{k,\bar{D}} \left(1 + \frac{D}{\Delta r}\right) \tag{6.6}$$

By extending the foregoing analysis to include all unit length and time increments present, an overall or average aggregate freezing velocity could be evaluated. For the simple 1-D case shown in Figure 6.1, there were always N unit increments associated with a total of $2N-2$ droplets. Therefore, an average aggregate velocity $\bar{V}_n$ could be expressed in terms of the local values $V_{n,i}$ for each increment $i = 1 \ldots N$ by the general relationship

$$\bar{V}_n = \frac{1}{N}\sum_{i=1}^{N} V_{n,i}(x) = \frac{1}{N}\sum_{i=1}^{N} \frac{x_{i+2}-x_i}{t_{i+2}-t_i} \tag{6.7}$$

It can be shown that an equally valid expression for Equation 6.7 is

$$\bar{V}_n = \frac{\bar{v}_{k,\bar{D}}}{N}\sum_{i=1}^{N}\left(1+\frac{D_i}{\Delta r_i}\right) \tag{6.8}$$

Although Equations 6.7 and 6.8 can be applied directly to the ideal 1-D scenario depicted in Figure 6.1, they were not generally valid for the more realistic situation in which the freezing process occurs in two spatial dimensions. This was due primarily to the fact that for 2-D freezing, ice can propagate along any number of freezing pathlines within a field of droplets (see Figure 4.11), in which case the number of corresponding unit increments N would not typically correlate with the number of droplets. Furthermore, evaluating Equation 6.8 for any region would require knowledge of the local condensate droplet size (D_i) and spatial distribution (Δr_i). Accurately resolving these parameters was beyond the scope of this study.

Equation 6.6, on the other hand, can be applied to the 2-D ice propagation problem because it was based on a local formulation. This relationship revealed an important aspect of the aggregate freezing process in general: the magnitude of the intra-droplet freezing velocity $\bar{v}_{sl}$ did not significantly affect the dynamics of the aggregate freezing process. Equation 6.6 indicated that for a given value of $\bar{v}_{k,\bar{D}}$, the aggregate freezing velocity increased with increasing D and decreasing Δr. The results presented in Chapter V showed that the average aggregate freezing velocity $\bar{V}_n$ was dependent on three parameters: the substrate temperature (T_s), the free stream humidity (RH or ω_{air}), and the interfacial surface properties (as captured by θ_w, defined by Equation 5.4). Interestingly, the same dataset revealed that $\bar{v}_{k,\bar{D}}$ was nearly independent of T_s and very weakly dependent on ω_{air} and θ_w. Equation 6.6 therefore implied that it was the distribution of condensate on the surface that controlled the dynamics of the aggregate freezing process, not the kinetics of the underlying phase change mechanisms. The relative droplet size and spatial distributions of the condensate were locally characterized by the ratio $\frac{D}{\Delta r}$. In addition, D and Δr were inversely coupled[1] and stemmed directly from the condensation process, which was dependent on T_s, ω_{air} and θ_w. Therefore, $\bar{V}_n$ can be understood to be a function of T_s, ω_{air}, and θ_w as a consequence of the fact that D and Δr were dependent on the same parameters.

B. The Kinetics of Ice Crystal Growth within Supercooled Water Droplets

Using high speed digital microscopy, the solidification process for individual water droplets was found to occur in two sequential steps:

1. an unstable, dendritic ice front that rapidly propagated away from the point of inception along the droplet-substrate and droplet-air interface, and
2. a slower, more planar ice front that propagated upwards through the bulk of the remaining liquid, eventually freezing the entire droplet.

Numerous observations made in this study have shown that the crystal growth process in first stage effectively encases the supercooled liquid droplet with a very thin "ice shell" prior to onset of bulk freezing in the second stage. Toward the end of the second stage, the upward displacement of the remaining liquid phase above the solidification

---

[1] Consider that for a fixed number of droplets within an arbitrary region on the surface, the separation distance between droplets (Δr) must decrease as the size of the droplets (D) increase.

front produced an inflected "spire" at the top of the droplet[2]. The rate at which the encasement process occured was, on average, about two orders of magnitude greater than the bulk freezing process. For example, the dynamics of the dendritic ice fronts associated with the first stage were characterized by $\bar{v}_{sl}$ and reported as a function of substrate temperature and surface properties in Chapter V; the magnitude of $\bar{v}_{sl}$ was found to fall in the range of 10^4 to 10^5 μm/s for the conditions studied. The dynamics of the bulk freezing process associated with the second stage were previously characterized in an earlier study by Gong [39] in which he reported bulk freezing velocities on the order of 10^2 to 10^3 μm/s under comparable conditions. As such, the bulk freezing process was not considered further and the remaining discussion focuses exclusively on the overall thermophysics of the inceptive crystallization mechanism.

A molecular analysis of the liquid-to-solid phase change process associated with the intra-droplet crystal growth mechanism required the framework of statistical thermodynamics. As discussed in Chapter II, the condition of stable equilibrium within any system undergoing a phase-change process at a fixed temperature T and pressure P requires that the Gibbs free energy G of each phase are equal. For a liquid-solid system, this condition specifically requires that

$$G_l(T_M, P) = G_s(T_M, P) \tag{6.9}$$

where T_M is the equilibrium melting point temperature of the solid phase at pressure P and the subscripts s and l denoted the solid and liquid phases, respectively. The equilibrium condition given by Equation 6.9 can be alternately expressed in terms of

---

[2] Examples of these processes may be seen in a series of selected frames from a high speed image sequence in Figure 4.26

the enthalpies and entropies of each phase as

$$H_l - T_M S_l = H_s - T_M S_s \tag{6.10}$$

The expression given by Equation 6.10 can be rearranged to reveal the definition of the enthalpy of formation associated with the phase change process, namely

$$H_l - H_s = T_M \Delta S = \mathcal{L}_{sl} \tag{6.11}$$

or on a molecular basis as,

$$\hat{h}_l - \hat{h}_s = T_M \Delta \hat{s} = \hat{l}_{sl} \tag{6.12}$$

Because $\mathcal{L}_{sl}$ and $\hat{l}_{sl}$ are representative of an isothermal change in energy, these parameters have historically been referred to as *latent* heats of formation. For a melting or solidification process, these terms are more generally labeled as *latent heats of fusion.*

At temperatures above the melting point, $G_s > G_l$; hence, the liquid phase is the more thermodynamically stable of the two phases for $T > T_M$. Conversely, for $T < T_M$, $G_s < G_l$ and the existence of the solid is more thermodynamically favorable. The variation of the Gibbs free energy with temperature for each phase is illustrated in Figure 6.2.

The existence of the liquid phase for temperatures below T_M is the result of phenomenon known as supercooling and represents a metastable thermodynamic condition. As shown in Figure 6.2, a Gibbs free energy potential $\Delta G_{sl} = G_l(T, P) - G_s(T, P)$ exists between the liquid phase and the absent solid phase for all $T < T_M$. For a given pressure, this potential energy increases with the degree of supercooling $\Delta T = T_M - T$ until a critical nucleation limit is reached, at which point a stable ice nucleus forms and the supercooled liquid begins to crystallize. The Gibbs potential for this process

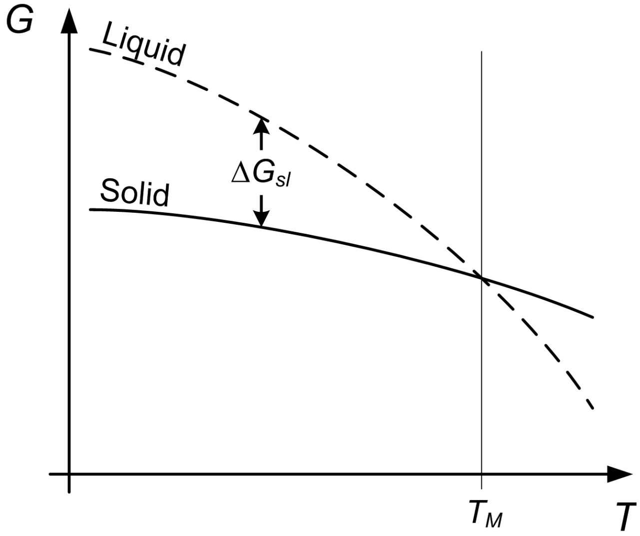

Figure 6.2: Illustration of the isobaric variation of Gibb's free energy with temperature for solid and liquid phases

may be approximated by a first order expansion in temperature as

$$\Delta G_{sl} \approx \left(\frac{\partial G_l}{\partial T}\right)_P \Delta T - \left(\frac{\partial G_s}{\partial T}\right)_P \Delta T \tag{6.13}$$

Using Equation 6.11 with the thermodynamic relation $S = -\left(\frac{\partial G}{\partial T}\right)_P$ [85], Equation 6.13 becomes

$$\Delta G_{sl} = \mathcal{L}_{sl}\frac{\Delta T}{T_M} \tag{6.14}$$

Equation 6.14 is a fundamental relationship for the thermodynamic driving potential for crystal growth within the supercooled liquid phase. It can also be expressed on a molecular basis as

$$\Delta\mu = \hat{l}_{sl}\frac{\Delta T}{T_M} \tag{6.15}$$

where $\mu = \frac{G}{N_m}$ is often referred to as the chemical potential. It should be noted that because of the metastable conditions for which they were defined, Equations 6.13 - 6.15 are inherently non-equilibrium relationships.

For an ice crystal to evolve within the liquid phase, water molecules must overcome an activation energy barrier associated with molecular diffusion to freely adsorb onto and properly reorient with a crystalline surface. If the diffusion energy barrier is represented by $\mathcal{E}_{ad}$, the probability that a given molecule will exceed this energy barrier is proportional to the Boltzmann weight given by [86]

$$\mathcal{P} \propto e^{\frac{-\mathcal{E}_{ad}}{k_B T}}$$

where k_B is Boltzmann's constant. If the water molecules vibrate around their average position with a frequency ν, then the average molecular adsorption flux at the crystalline interface is given by

$$f_{ad} = \nu e^{\frac{-\mathcal{E}_{ad}}{k_B T}} \tag{6.16}$$

The adsorption of water molecules at the crystalline interface is met with some degree of desorption (melting), represented by f_{ds}. The molecular fluxes of adsorption and desorption can be shown to differ by the factor [80]

$$\frac{f_{ad}}{f_{ds}} = e^{\frac{-\Delta\mu}{k_B T}}$$

where $\Delta\mu$ is the chemical driving potential given by Equation 6.15. Therefore, the net growth rate of the crystal is given by

$$v_{WF} = d_m \nu e^{\frac{-\mathcal{E}_{ad}}{k_B T}} \left[1 - e^{\frac{-\Delta\mu}{k_B T}}\right] \tag{6.17}$$

where d_m is the molecular diameter. Equation 6.17 is known as the Wilson-Frenkel formula and describes the evolution rate of crystals from their melt. The leading terms in Equation 6.17 may be equated with the Brownian diffusion coefficient $\mathcal{D}$ given by the Einstein-Stokes relation [87],

$$\mathcal{D} = \frac{k_B T}{3\pi\eta d_m} = d_m^2 \nu e^{\frac{-\mathcal{E}_{ad}}{k_B T}} \tag{6.18}$$

This allows Equation 6.17 to be rewritten in terms of the liquid dynamic viscosity η as

$$v_{WF} = \frac{k_B T}{6\pi\eta d_m^2}\left[1 - e^{\frac{-\Delta\mu}{k_B T}}\right] \tag{6.19}$$

For moderate degrees of supercooling, Equations 6.17 and 6.19 have been shown to be approximated by [88]

$$v_{WF} \approx K_T \Delta T \tag{6.20}$$

where K_T is a kinetic coefficient defined by

$$K_T = \frac{\hat{l}_{sl}}{6\pi\eta d_m^2 T_M} \tag{6.21}$$

The liquid viscosity η, molecular diameter d_m, and latent heat per molecule $\hat{l}_{sl}$ must be known to evaluate Equations 6.19 or 6.20. For water and ice-I$_\mathrm{h}$, $d_m = 2.8\text{Å} = 2.8 \times 10^{-10}$ m and $\hat{l}_{sv} = 9.97 \times 10^{-21}$ J/molecule are taken as reasonable values [89]. Viscosity data for supercooled liquids were found to be scarce; however, measurements of η for water have been reported for temperatures down to 248 K by Hallett [90]. These data, shown in Figure 6.3, were found to correlate well with the general relationship given by

$$\eta = \eta_0 + \frac{a_1}{T} + \frac{a_2}{T^2} + \frac{a_3}{T^3} \tag{6.22}$$

where

$$\eta_0 = -2.47 \times 10^3$$

$$a_1 = 2.00 \times 10^6$$

$$a_2 = -5.41 \times 10^8$$

$$a_3 = 4.89 \times 10^{10}$$

Figure 6.3 shows that the viscosity of supercooled water can vary markedly with the degree of supercooling, increasing rapidly with decreasing temperature. The

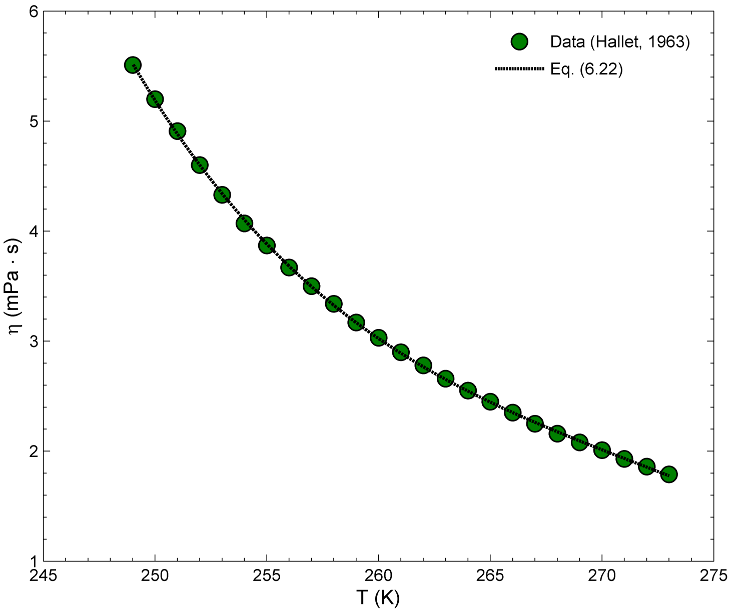

Figure 6.3: Variation of dynamic viscosity with temperature for supercooled water; from Hallett [90]

general forms of Equations 6.19 and 6.20 indicated that the crystal growth rate can be substantially reduced at larger supercooling because of the increase in liquid viscosity. However, the results of early molecular dynamics study of the crystallization process for a Lennard-Jones liquid [91] suggested that the molecular mobility in the melt does not appreciably affect the crystal growth rate due to a “pre-aligning” effect in the region near the liquid-solid interface. Indeed, using the variable viscosity relation (Equation 6.22) in Equations 6.19 or 6.20 was found to produce physically unrealistic crystal growth velocities for the larger values of ΔT considered in this study. However, if an constant value of η was used, evaluated at the average substrate temperature spanned by the experimental data reported in this study (for $T_{s,ave} = 260$ K, $\eta = 3.01$ mPa·s), Equations 6.19 and 6.20 produced more reasonable velocities over the full range of substrate temperatures considered in this study. The corresponding values of the intra-droplet freezing velocity $\bar{v}_{sl}$ taken from the Type III experimental data could then be directly compared with these predictions. The results of this analysis are shown in Figure 6.4.

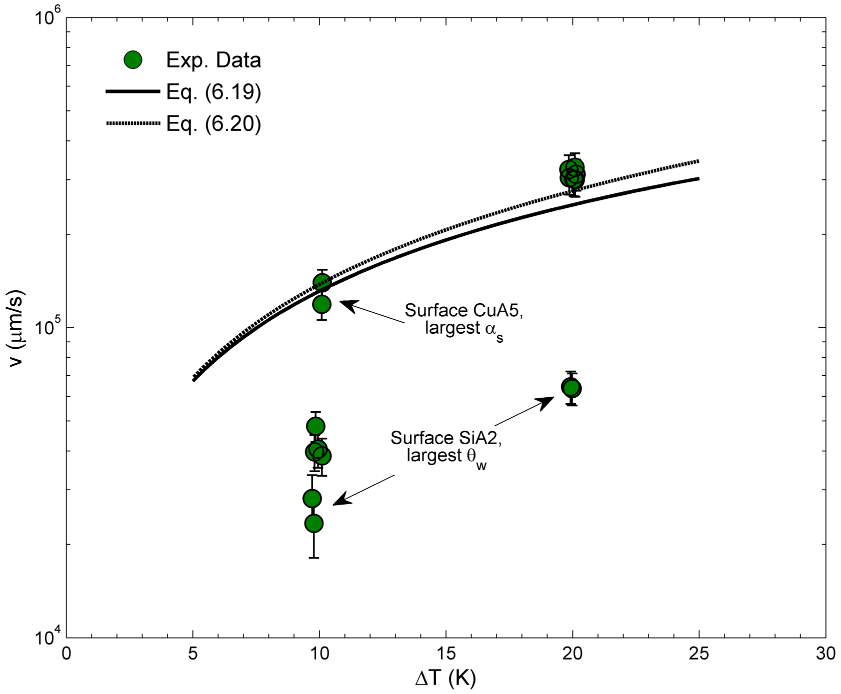

Figure 6.4: Rate of crystal growth in melt versus degree of supercooling given by Equations 6.19 and 6.20 with Type III experimental data

The results presented in Figure 6.4, which provide a direct comparison between theory and experiment, demonstrated that the dynamics of the intra-droplet freezing process were consistent with those of the crystal growth mechanism in supercooled melts. This observation was underscored by the remarkably good agreement between the experimental data and the predictions of Equations 6.19 and 6.20 seen for higher values of the supercooling ΔT. And as indicated in the plot annotations, the lower ΔT data acquired for the CuA5 test surface compared favorably with these predictions as well. However, Figure 6.4 also showed that with the exception of the CuA5 data, Equations 6.19 and 6.20 over-predicted all of the lower ΔT data by about a factor of four, on average. The same relative over-prediction was observed for the SiA2 data for the higher ΔT condition.

There were a number of potential explanations for the differences observed between theory and experiment in these results. The possibilities range from unexpected bias in the data due to factors such as surface contamination to the application of an overly simplistic theoretical model. It should be noted that only the kinetics of the crystallization process were considered in this analysis; the interaction between the substrate, ice, and supercooled water was not incorporated into the theoretical model. Furthermore, deeper-seeded effects such as those associated with morphological instabilities in the evolving solid-liquid interface, spontaneous ice nucleation, and thermal effects associated with local heat conduction into the substrate were not considered. Nonetheless, this analysis was carried out with the intention of demonstrating that the intra-droplet freezing process is consistent with and amenable to further analysis with established theory.

Aside from the overall kinetic arguments presented in the foregoing analysis, a fascinating question remains: why does the intra-droplet freezing process rapidly encase the droplet in an ice shell prior to the onset of bulk freezing? One possible explanation for this interesting phenomenon can be framed in the context of molecular interactions within the confines of a liquid. Any molecule residing within the bulk interior of a liquid will experience inter-molecular forces of attraction from neighboring molecules in essentially all directions, resulting in a net force of zero acting on that molecule. Conversely, a molecule located along or near the liquid-vapor interface will experience these attractive forces from one side only, resulting in a non-zero net force acting towards the bulk interior. It is this resulting force imbalance along the interface that gives rise to the phenomenon of surface tension. Because the molecules along the surface experience fewer interactions with other molecules, they naturally possess, on average, higher free energies than those in bulk liquid. Therefore, based on the free energy minimization principles discussed previously, it is logical to speculate that once ice nucleation occurs, regions with higher free energy potentials ΔG_{sl} (e.g. the droplet-air interface) are more likely to undergo freezing before those with lower free potentials (e.g. the bulk interior of the droplet). This ice encasement phenomenon is also consistent with results reported in two investigations in which the solidification process was modeled with molecular dynamics simulations [62, 91].

C. The Kinetics of Ice Crystal Growth between Supercooled Water Droplets

High resolution microscopy used in conjunction with a novel image analysis technique revealed that the inter-droplet freezing process occured as the result of targeted ice crystal growth along the substrate between neighboring droplets. The data showed that once a given droplet began to freeze, an ice crystal emerged from its periphery and began to grow along the substrate directly toward the nearest unfrozen droplets (for example, see Figure 4.21). In many instances, the so-called “target droplets” that the crystals grew towards showed signs of evaporation and this process always tracked consistently with the local crystal tip velocity. This later observation suggested that the basic inter-droplet ice propagation mechanism was fundamentally based on that of crystal growth from the vapor phase. Remarkably, this also implied that the mass source for crystal growth may in fact be vapor that was derived from the evaporation of a proximal liquid phase. Thus, the inter-droplet crystal growth phenomenon may very well be the result of a complicated *three-phase* heat and mass transfer process.

In general, the basic mechanisms which determine dynamics of ice crystal growth from the vapor phase are poorly understood. The growth of any crystal from its vapor is an incredibly complex process which depends on many factors, including temperature, vapor pressure, as well as the underlying lattice structure of the atoms or molecules in the solid phase. At the most fundamental level, the evolution of crystals are thought to occur through the adsorption and incorporation of vapor atoms or molecules into sub-microscopic steps and kinks on the advancing solid-vapor interface [92]. Depending on the substance and conditions, the process by which the atoms or molecules are incorporated into the kinks can occur as the result of several distinct mechanisms, including surface diffusion, circular or spiral step growth, and two-dimensional nucleation [88]. Additional complications arise in the case of the ice-water vapor system because, owing to the hexagonal structure of ice-$\mathrm{I_h}$, growth can occur in a direction normal to two principle crystallographic planes: the basal and prism facets [89].

Despite the complexities noted above, a more general analysis, formulated in terms of ideal kinetics, can provide considerable insight into the purported inter-droplet ice crystal growth mechanism. For a dilute, ideal gas, the probability that a given molecule has a velocity somewhere within the region $dv_x dv_y dv_z$ around the central value of $\mathbf{v} = v_x\mathbf{e}_i + v_y\mathbf{e}_j + v_z\mathbf{e}_k$ in velocity space is given by the Maxwell velocity distribution [93]

$$\mathcal{P}(\mathbf{v})d\mathbf{v} = \left(\frac{m}{2\pi k_B T}\right)^{3/2} e^{-\frac{m\mathbf{v}^2}{2k_B T}} d\mathbf{v} \tag{6.23}$$

For simplicity, it will be assumed that the solid-vapor interface of the growing crystal is a perfectly flat, two-dimensional surface oriented parallel to the yz plane, initially located at $x = 0$, and growing in the positive x-direction. In a unit time dt, the flux of molecules impinging on the surface may be evaluated by

$$f = \int_{-\infty}^{\infty}\int_{-\infty}^{\infty}\int_{-\infty}^{0} n|\mathbf{v}_x|\mathcal{P}(\mathbf{v})\ dv_x dv_y dv_z \tag{6.24}$$

where n is the mean number density of the vapor molecules given by

$$n = \frac{P}{k_B T} \tag{6.25}$$

and P is the parital pressure of the vapor phase. Evaluating Equation 6.24 provides the molecular adsorption flux

$$f_{ad} = \frac{P}{\sqrt{2\pi m k_B T}} \tag{6.26}$$

For a given temperature and pressure, the adsorption of vapor molecules at the surface is met with some degree of sublimation or desorption. For an ideal gas, the desorption flux is independent of the adsorption flux and may be evaluated by Equation 6.26 when $P = P_{sat}(T)$, which is the saturation or equilibrium vapor pressure at the temperature T:

$$f_{sat} = \frac{P_{sat}}{\sqrt{2\pi m k_B T}} = f_{ds} \tag{6.27}$$

Now, in an infinitesimal timespan dt, the crystal face advances a distance dx in the positive x-direction due to the progressive impingment and "stacking" of vapor molecules of diameter d_m onto the surface. Therefore, the advancement rate $\frac{dx}{dt}$ of the crystal surface can be equated to the net molecular flux as

$$v_{HK} = d_m^3 \left(f_{ad} - f_{ds}\right) = \frac{d_m^3 \left(P - P_{sat}\right)}{\sqrt{2\pi m k_B T}} \tag{6.28}$$

Equation 6.28 is known as the Hertz-Knudsen formula. With the supersaturation ratio σ defined by

$$\sigma = \frac{P - P_{sat}}{P_{sat}} \tag{6.29}$$

the Hertz-Knudsen formula may also be written as

$$v_{HK} = \frac{d_m^3 \sigma P_{sat}}{\sqrt{2\pi m k_B T}} \tag{6.30}$$

Using arguments similar to those presented in association with Figure 6.2, Equation 6.28 can be alternatively expressed in terms of the chemical driving potential μ:

$$v_{HK} = d_m^3 f_{sat} \left[e^{-\frac{\Delta\mu}{k_B T}} - 1 \right] \tag{6.31}$$

Experiments have shown that due to kinetic-limiting effects associated with basal and prism facet growth, formulations such as Equation 6.28 tend to overpredict measured vapor growth rates for ice crystals under normal atmospheric conditions [83]. To address this issue, Equation 6.28 may be modified with the addition of a semi-empirical parameter known as the condensation coefficient α_{cond} to yield and expression of the form

$$v_{HK} = \alpha_{cond} \frac{d_m^3 \left(P - P_{sat}\right)}{\sqrt{2\pi m k_B T}} \tag{6.32}$$

for which $\alpha_{cond} \leq 1$. The condensation coefficient is a function of the local vapor pressure and temperature; Libbrecht [83] reported that measured values of α_{cond} correlated well with σ through the functional form given by

$$\alpha_{cond} = A e^{-\frac{\sigma_0}{\sigma}} \tag{6.33}$$

From reported values of these coefficients, A and σ_0 can be approximated by a linear function of the supercooling degree ΔT with

$$\begin{aligned} A &= 0.0038\Delta T - 0.0377 \\ \sigma_0 &= 0.0069\Delta T + 0.0514 \end{aligned}$$

The crystal growth velocities predicted by Equations 6.28 through 6.32 are directly proportional to the vapor pressure imbalance relative to saturated conditions and inversely proportional to the square root of the temperature. The saturation pressure of water vapor above an ice surface is less than that above liquid water, a fact which is demonstrated in Figure 6.5 with the saturation pressure versus temperature profiles for ice and water derived from the thermodynamic formulations of the IAPWS[3]. Figure 6.5 shows the variation in P_{sat} for both water and ice with the degree of supercooling ΔT. Recall that for the inter-droplet freezing process observed in this study, ice crystals were observed to preferentially grow along the substrate away from newly frozen droplets toward nearby unfrozen droplets. Thus, the directional crystal growth observed for the inter-droplet freezing process can be explained by phase-induced vapor pressure gradients. In this process, newly frozen and unfrozen

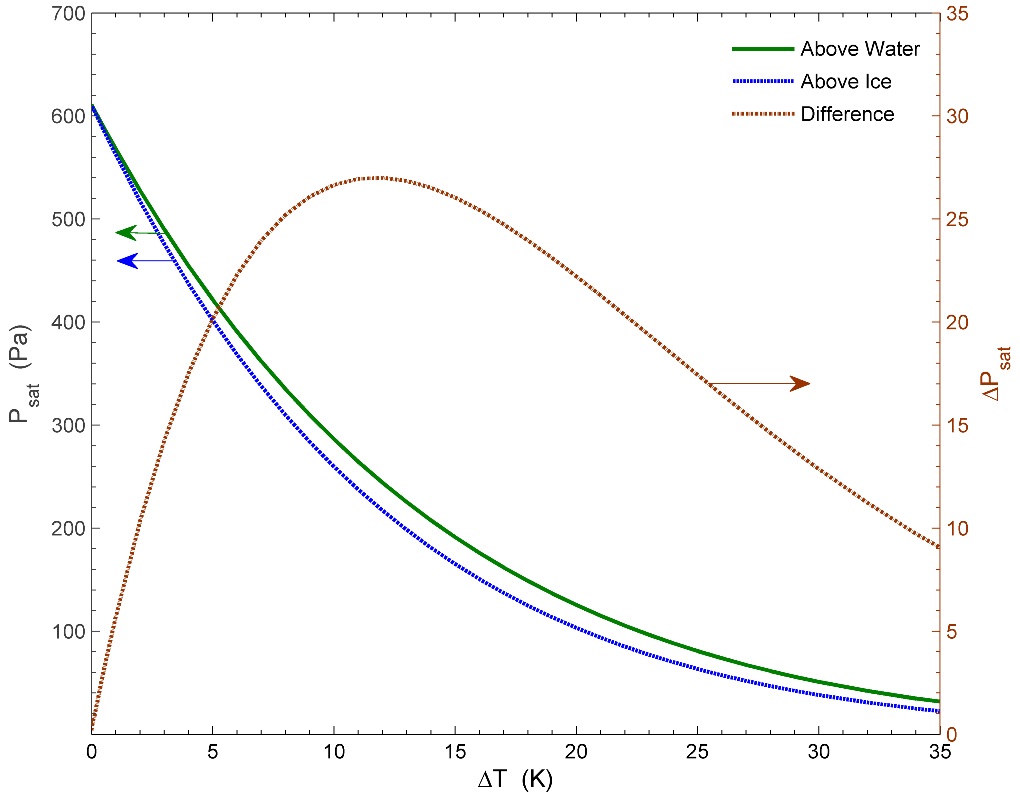

Figure 6.5: Saturation vapor pressures of water vapor above water and ice as a function of supercooling degree (based on IAPWS)

---

[3] The International Association for the Properties of Water and Steam

droplets on the substrate assume the roles of mass *sinks* and *sources*, respectively, with the former drawing water molecules from the latter via evaporation. The evaporation process itself can be explained by the vapor pressure imbalance resulting from the segregated liquid and solid phases coexisting with subsaturated vapor at temperatures below the triple point. It is also possible that latent heat conduction through the substrate contributes to this process to some extent.

The secondary axis shown in Figure 6.5 displays the relative difference between the saturation vapor pressures for each phase; a maximum value for ΔP_{sat} occurs for $\Delta T \approx 12$ K. This particular curve provided some indications as to how the dynamics of the crystal growth process was affected by temperature: considering the impact of the temperature term in the denominator, the crystal growth rate predicted by Equation 6.32 can be expected to peak for $\Delta T \geq 12$ and then monotonically decrease with increasing ΔT beyond that point. To assess how well Equation 6.32 compared with the inter-droplet freezing velocity data collected in this study ($\bar{v}_{k,\bar{D}}$), the following assumptions were made:

1. The driving force in Equation 6.32 was based on the difference between the saturation pressures of water and ice at a given temperature: $P_{w,sat}(T) - P_{i,sat}(T)$.
2. The leading edge or tip of the inter-droplet crystal modeled by Equation 6.32 was assumed to behave as a flat interface that was oriented perpendicular to the substrate along which it grew.
3. Despite having a thickness of the order of microns, the overall dimensions of this idealized interface were assumed to be several orders of magnitude larger than the size of an individual water molecule
4. Because the thickness of the crystal was relatively small compared to the thick-

ness of the substrate, the ice temperature in a region near the interface was assumed to be effectively the same as that of the test substrate. As such, any thermal effects at the interface due to the evolution of latent heating were ignored.

Using the appropriate values for d_m and m along with the saturation pressures shown in Figure 6.5, Equation 6.32 was evaluated over the range of substrate temperatures considered in this study. Corresponding values of the inter-droplet freezing velocity $\bar{v}_{k,\bar{D}}$ taken from the Type I experimental data were compared with this prediction. The results of the analysis are presented in Figure 6.6.

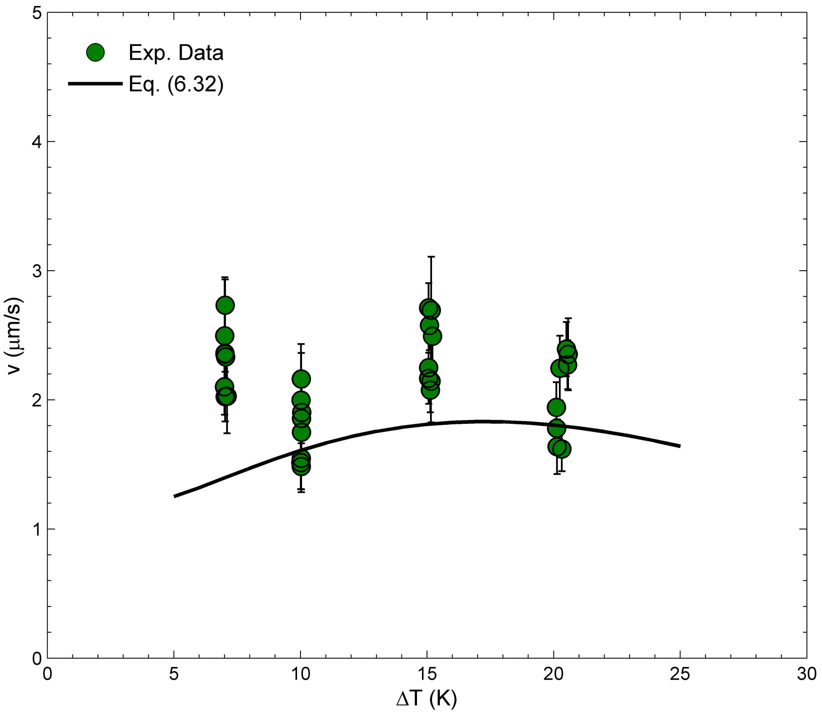

Figure 6.6: Rate of crystal growth from vapor versus degree of supercooling given by Equation 6.32 with measured values of $\bar{v}_{k,\bar{D}}$ from Type I experimental data

The comparison shown in Figure 6.6 indicated that the modified Hertz-Knudsen formula predicted the measured values of $\bar{v}_{k,\bar{D}}$ reasonably well, with Equation 6.32 falling about 20% short of the inter-droplet freezing velocity data, on average. Figure 6.6 also showed that the predicted crystal growth velocity reached a maximum value at $\Delta T \approx 18$ K. The experimental data for nominal ΔT values of 10, 15, and 20 K appeared to follow this trend. However, the freezing velocity data for $\Delta T = 7$ K were over 60% higher than the predicted value and did not support the extension of this trend into higher substrate temperatures. The reason for this discrepancy was not entirely clear, although Libbrecht [83] had noted that the effects of latent heating at the solid-vapor interface may begin to impact the dynamics of the real crystal growth process for $\Delta T < 10$ K. The results of this analysis suggested that the dynamics of the inter-droplet freezing process were consistent with the basic mechanism of crystal growth from vapor. Furthermore, the fact that such consistency was obtained by using the difference in water and ice saturation vapor pressures as the driving force for crystal growth lent support to the notion that the inter-droplet crystals grew as a result of a vapor pressure gradients generated by a three-phase freezing-evaporation-deposition cycle.

The results of this analysis also raised two important questions. First of all, why did the direction of airflow over the test surface not have a discernible impact on the direction of the inter-droplet freezing velocities? Second, why did the relative humidity have such a minor effect on this process? Reasonable explanations for both of these questions can be found from a qualitative consideration of the air boundary-layer development over the test surface. In order to discuss the possible boundary-layer effects, the following assumptions were made:

1. the dimensions of the test section duct were much larger than the air boundary-layer thickness in the vicinity of the test surface; thus, locally, airflow over the

test surface could be approximated as external flow

2. the boundary-layer started to form at the leading edge of the test surface,

For incompressible laminar flow over a flat plate, the streamwise velocity boundary-layer thickness $\delta(x)$ may be approximated by the relation [94]

$$\delta(x) \approx 5\sqrt{\frac{\nu x}{U_\infty}} = \frac{5x}{\sqrt{\mathrm{Re}_x}} \tag{6.34}$$

where U_∞ is the free stream longitudinal velocity of the air, ν is the kinematic viscosity of the air, x is the location downstream from the leading edge of the plate, and Re_x is the local Reynolds number of the airflow based on the free steam velocity. Assuming that the measured test section centerline air velocity U_{air} was representative of U_∞, for the conditions prescribed in these experiments (see Chapter III), $\delta(x)$ was found to be on the order of about 1000 μm at the downstream location corresponding to the optical region of interest (ROI). The presence of droplets on the substrate undoubtedly affected the development of the boundary-layer to some extent, particularly near the leading edge where the boundary-layer was thin; however, the largest droplets observed prior to freezing for any experiment conducted in this study were on the order of 100 μm in diameter. It was therefore likely that all of the droplets within the ROI were fully enveloped within some form of a “primary” boundary-layer, the thickness of which was many times greater than the protrusion height of the droplets from the surface. With regard to the flow field near the substrate, there is ample theoretical, numerical, and experimental evidence to suggest that the formation and separation of secondary boundary-layers would have tended to generate vortices and other coherent flow structures in the wake region of each droplet [95,96]. A simplified illustration of this concept applied to a two-droplet system is shown in Figure 6.7.

If the flow field within the larger primary boundary-layer was predominantly

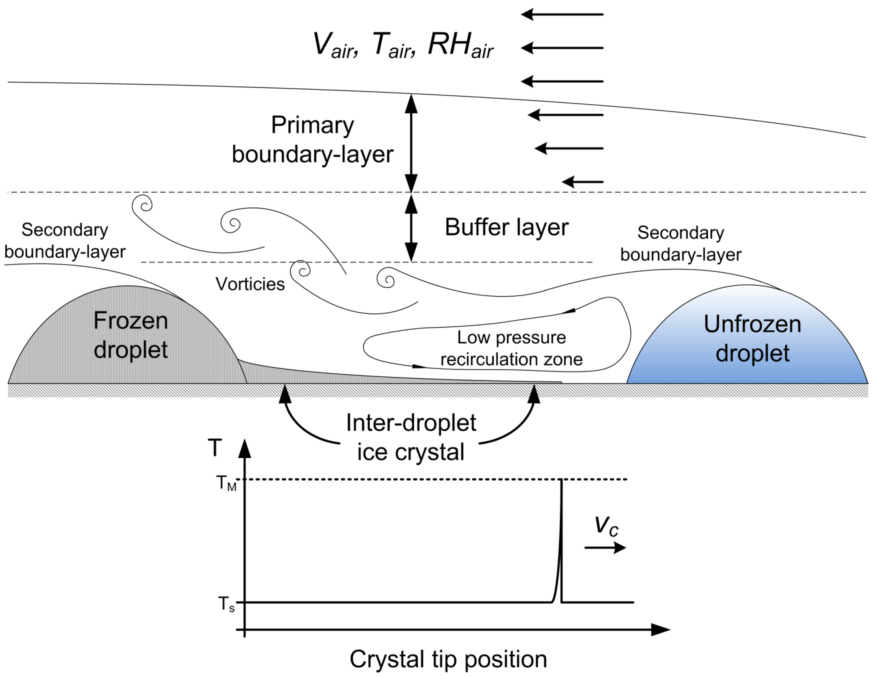

Figure 6.7: Illustration of possible intra-boundary-layer phenomena associated with inter-droplet freezing process (not to scale)

streamwise, the more complex secondary flow field associated with the near-droplet region would tend to be suppressed or smoothed by the bulk airflow at some height above the droplet field. The interaction of these two flow fields would probably have produced an interfacial shear or buffer layer, as depicted in Figure 6.7. The thickness of the inter-droplet ice crystals were consistently measured to be on the order of 1 μm (Chapter IV). Accordingly, the inter-droplet crystal growth process would have always been confined to a lower-pressure recirculation zone in between neighboring droplets, far below the buffer layer. It therefore stands to reason that the buffer layer could have served to effectively "shield" the evolving inter-droplet ice crystals from any effects associated with the direction of the free stream airflow. And due to the effects of intra-boundary layer mixing and advection, this buffer layer could have had the added effect of imposing what was essentially a mass transfer resistance for condensation or deposition. Although measuring or simulating these effects were beyond the scope of this investigation, these explanations were consistent with the experimental observations that the magnitude of the inter-droplet freezing velocity $\bar{v}_{k,\bar{D}}$ was 1) independent of the airflow direction and 2) increased slightly with increasing humidity ratio ω_{air}.

As an extension to the previous discussion, Figure 6.7 also illustrates some potential thermal effects that the evolution of the crystal could have had on the substrate. As the leading tip of the crystal propagated from left to right, the local substrate temperature may have increased to some extent due to the rejection of latent heat associated with the deposition process. In principle, evaluating the extent of these substrate temperature fluctuations would require knowing the local convective thermal boundary conditions as well as the molecular kinetics at the solid-vapor interface. For kinetic-limited conditions, the increase in substrate temperature in the vicinity of the crystal tip might not be substantial. For very fast crystal growth kinetics, however, the local substrate temperature could increase enough to affect a change in the local saturation vapor pressure for ice, which in turn would alter the deposition process.

D. Summary and Remarks

To obtain a better understanding of the thermophysics of ice propagation on droplet-laden surfaces, the three principle freezing processes discovered in this study − the aggregate, inter-, and intra-droplet freezing processes − were analyzed from a mechanistic standpoint. Based on the results of this analysis, the aggregate freezing process did not appear to be a basic ice propagation mechanism itself, but rather comprised of two constituent mechanisms: the inter- and intra-droplet freezing processes. A more detailed analysis of the inter- and intra-droplet freezing processes revealed that these mechanisms were capable of being understood in terms of molecular kinetics.

A phenomenological breakdown of the aggregate freezing process in terms of its constituents showed that the aggregate freezing velocity was dependent on the inter-droplet freezing velocity as well as the size and spatial distribution of the condensate droplets just prior to the onset of freezing. Surprisingly, it was found that the magnitude of the intra-droplet freezing velocity did not directly affect the dynamics of the aggregate freezing process. This later finding could be explained with the simple fact that intra-droplet freezing velocity was, on average, about five orders of magnitude faster than that of inter-droplet freezing process. Because the intra-droplet freezing process acted over the diametral length scales associated with individual droplets, it only affected the aggregate freezing process indirectly by significantly shortening the corresponding diametral freezing time scales.

The dynamics of the inter- and intra-droplet freezing mechanisms were found to be consistent with the kinetics of crystal growth from the vapor and liquid phases, respectively. Experimental measurements of the intra-droplet freezing velocity compared favorably with predictions from a simplified form of the Wilson-Frenkel formula for crystal growth in melts. Likewise, a modified form of the Hertz-Knudsen formula was found to agree quite well with inter-droplet freezing velocity data. In addition to increasing confidence that these dropwise ice propagation mechanisms were in fact fundamental, these results could serve as a starting point for more detailed investigations in the future.

CHAPTER VII

CONCLUSIONS AND RECOMMENDATIONS

The primary objective of this investigation was to determine and characterize the mechanisms responsible for ice propagation on surfaces undergoing dropwise condensation. To study the underlying phenomena responsible for this freezing process, a series of visualization experiments were conducted for four test surfaces. These experiments were carried out for a wide range of carefully controlled environmental conditions in an apparatus that was capable of simulating psychrometric airflows typically encountered in sub-freezing refrigeration applications. The experiments were divided into three classes of tests, each designed to utilize certain capabilities of the high speed digital microscopy system built to observe the freezing process *in situ* over various length and time scales. To analyze the large volumes of visualization data that were generated, a set of image and data analysis methods were developed which allowed the freezing dynamics from each experiment to be quantified on a consistent basis.

Based on the results of this study, three primary freezing events were identified: they were designated as the 1) inter-droplet, 2) intra-droplet, and 3) aggregate freezing processes. The inter-droplet freezing process served as the dominant mode of of ice propagation between neighboring droplets; it was observed to occur as the result of directional ice crystal growth from the vapor phase along the substrate. The intra-droplet freezing process was responsible for the evolution of ice within individual supercooled droplets; it was found to operate at rates as many as five orders of magnitude faster than the inter-droplet process. The aggregate freezing process was determined to be a larger scale manifestation of the inter- and intra-droplet freezing processes operating together.

The dynamics of these three freezing processes were quantified by reduced freezing velocities that were normalized with the substrate thermal diffusivity (α_s) and correlated with the independent variables of substrate roughness and hydrophobicity (collectively represented by the corrected contact angle θ_w), substrate temperature (T_s), and the free stream humidity ratio (ω_{air}). The normalized aggregate freezing velocity was determined to be dependent on all of these parameters; however, the normalized inter- and intra-droplet freezing velocities were found to be essentially independent of T_s and ω_{air}, respectively. A set of predictive correlations were developed from the normalized data corresponding to each process and in general, they predicted the dynamics of these phenomena quite well.

Through mechanistic analyses of the underlying thermophysics, the dynamics of the inter- and intra-droplet freezing processes were found to be consistent with the kinetics of generic crystal growth from the vapor and supercooled liquid phases, respectively. Furthermore, the aggregate freezing process was broken down and analyzed in terms of the constituent inter- and intra-droplet crystal growth mechanisms. The results of those analyses should provide a good starting point for more fundamental studies in this area in the future.

A. Conclusions

A number of conclusions can be drawn from the results of this investigation:

1. A comparison between the experimental data and the results of generalized kinetic analyses showed that the dynamcis of the inter- and intra-droplet freezing processes were consistent with the basic mechanisms of crystal growth from the vapor and liquid phases, respectively. Therefore, these freezing processes appeared to be fundamental ice propagation mechanisms for surfaces undergoing

dropwise condensation.

2. Based on the reduced data, the aggregate freezing dynamics were found to be dependent on T_s, ω_{air}, and θ_w. An analysis of the aggregate freezing process in terms of its constituent mechanisms showed that the aggregate freezing velocity was dependent on the magnitude of the inter-droplet freezing velocity as well the distribution of condensate on the surface. However, the inter-droplet freezing velocity was found to be independent of T_s and only weakly dependent on ω_{air}. Therefore, the reason that the aggregate freezing dynamics were affected by the substrate temperature and the humidity ratio of the air was because the dropwise condensation process was strongly dependent on these parameters.
3. The dynamics of the inter-droplet freezing mechanism were found to be weakly dependent on the free stream humidity ratio and independent of the airflow direction. A simple boundary-layer analysis revealed that the thickness of the free flow or primary boundary-layer was several times greater than the radius of the largest droplets measured in this study. Given that the flow field near and amongst the droplets would tend to be quite complicated (Figure 6.7), it was possible that a shear or buffer layer could have formed just above the droplets and effectively isolated the inter-droplet crystal growth mechanism from the effects of the free stream airflow.
4. For a given surface roughness value, an increase in the contact angle was observed to significantly slow the propagation of ice. The data indicated that the inter- and intra-droplet freezing velocities were greatly reduced after a hydrophobic coating was applied to one of the smoothest test substrates. Measurements also showed that the aggregate freezing velocity decreased with increasing surface hydrophobicity as well. The manner in which hydrophobicity impacted

the fundamental ice propagation mechanisms was not clear. However, the effects of hydrophobicity on the aggregate freezing process can be understood, to some extent, as being due to the alteration of the condensate distribution prior to the onset of freezing.

5. According to Song et al. [50], a liquid film with a thickness on the order of microns coexists amongst the droplets on surfaces undergoing dropwise condensation. However, the dynamics of the inter-droplet ice propagation mechanism were determined to be very consistent with those of crystal growth from the vapor phase. These results do not necessarily preclude the possibility that a condensate film can exist amongst the droplets prior to the onset of freezing. They do, however, imply that for the range of substrate properties and environmental conditions considered in this study, the exposed substrate area between individual condensate droplets was actually dry during the freezing process. If such a liquid film was present during freezing, the measured inter-droplet freezing velocities would have compared more favorably with the much faster kinetics associated with crystal growth in melts.

B. Recommendations

The results obtained in this study have prompted the following recommendations for future work:

1. The manner in which surface energy affects the fundamental inter- and intra-droplet freezing processes is not well understood. Thus, a logical extension to this work would be to conduct similar freezing experiments for hydrophobic and superhydrophoic surfaces. Broadening the range of this parameter could provide further insights into the relationship between the surface energy of the

substrate and the freezing dynamics.

2. The inter-droplet freezing and condensation processes could be studied with greater precision if the diameter of each droplet within the optical region of interest (ROI) could be reliably measured and tracked in an automated fashion. Several attempts were made to incorporate this functionality into the image processing algorithms used in this study and unfortunately, all were met with limited success. Due to the lens-like geometry inherent to sessile water droplets, it may be possible to correlate the shapes and contact angles of individual droplets with the size and intensity of the corresponding magnified light cones.

3. Additional non-invasive thermal measurements of the inter- and intra-droplet freezing processes could reveal important details about the crystallization kinetics associated with these mechanisms. One way this could be accomplished is by integrating a diagnostic-quality infrared camera into the digital microscopy system; this would provide real time and continuous temperature measurements of the exposed side of the test surface during the freezing process. Another type of instrument that could be employed to do this is a high frequency thin-film thermocouple (TFT) integrated into the substrate itself.

4. The impact that the flow of latent heat into the substrate could have on the fundamental freezing mechanisms is not currently known and has only been roughly accounted for in this study by normalizing the appropriate freezing velocities with the thermal diffusivity of the substrate. A detailed study of this transient phenomenon could provide valuable information about the local dynamics of the fundamental freezing mechanisms.

REFERENCES

[1] Emery, A. F. and Siegel, B. L., "Experimental Measurements of the Effects of Frost Formation on Heat Exchanger Performance," *ASME HTD-Heat and Mass Transfer in Frost and Ice, Packed Beds, and Environmental Discharge*, Vol. 139, 1990, pp. 1–8.

[2] Georgiadis, J. G., "Microscopic Study of Frost Inception," *Proceedings of the* 2^{nd} *European Thermal-Sciences and* 14^{th} *UIT National Heat Transfer Conference*, Rome, Italy, May 29-31, 1990.

[3] Hobbs, P. V., *Ice Physics*, Clarendon Press, Oxford, England, 1974.

[4] Jones, B. W. and Parker, J. D., "Frost Formation with Varying Environmental Parameters," *ASME Journal of Heat Transfer*, Vol. 97, 1975, pp. 255–259.

[5] Schneider, H. W., "Equation of the Growth Rate of Frost Forming on Cooled Surfaces," *International Journal of Heat and Mass Transfer*, Vol. 21, 1978, pp. 1019–1024.

[6] O'Neal, D. L. and Tree, D. R., "Measurement of Frost Growth and Density in a Parallel Plate Geometry," *ASHRAE Transactions*, Vol. 2A, 1984, pp. 287–290.

[7] Mao, Y., Besant, R. W., and Rezkallah, K. S., "Measurement and Correlations of Frost Properties with Airflow Over a Flat Plate," *ASHRAE Transactions*, Vol. 98, No. 2, 1992, pp. 1–14.

[8] Sherif, S. A., Raju, S. P., Padki, M. M., and Chan, A. B., "A Semi-Empirical Transient Method for Modeling Frost Formation on a Flat Plate," *International Journal of Refrigeration*, Vol. 16, 1993, pp. 321–329.

[9] Tao, Y. X., Besant, R. W., and Rezkallah, K. S., "A Mathematical Model for Predicting the Densification and Growth of Frost on a Flat Plate," *International Journal of Heat and Mass Transfer*, Vol. 36, 1993, pp. 353–363.

[10] le Gall, R. and Grillot, J. M., "Modeling of Frost Growth and Densification," *International Journal of Heat and Mass Transfer*, Vol. 40, No. 3, 1997, pp. 3177–3187.

[11] Lee, K. S., Kim, W. S., and Lee, T. H., "A One-Dimensional Model for Frost Formation on a Cold Flat Surface," *International Journal of Heat and Mass Transfer*, Vol. 40, 1997, pp. 4359–4365.

[12] Chen, H., Besant, R. W., and Tao, Y. X., "Frost Characteristics and Heat Transfer on a Flat Plate Under Freezer Operating Conditions: Part II, Numerical Modeling and Comparison with Data," *ASHRAE Transactions*, Vol. 105, No. 2, 1999, pp. 252–259.

[13] Ismail, K. A. R. and Salinas, C. S., "Modeling of Frost Formation Over Parallel Cold Plates," *International Journal of Refrigeration*, Vol. 22, 1999, pp. 425–441.

[14] Mao, Y., Besant, R. W., and Chen, H., "Frost Characteristics and Heat Transfer on a Flat Plate Under Freezer Operating Conditions," *ASHRAE Transactions*, Vol. 105, No. 2, 1999, pp. 231–251.

[15] Cheng, C. H. and Shiu, C. C., "Frost Formation and Frost Crystal Growth on a Cold Plate in Atmospheric Air Flow," *International Journal of Heat and Mass Transfer*, Vol. 45, 2002, pp. 4289–4303.

[16] Yun, R., Kim, Y., and Min, M. K., "Modeling of Frost Growth and Frost Properties with Airflow Over a Flat Plate," *International Journal of Refrigeration*,

Vol. 25, 2002, pp. 326–371.

[17] Lee, K. S., Jhee, S., and Yang, D. K., “Prediction of the Frost Formation on a Cold Flat Surface,” *International Journal of Heat and Mass Transfer*, Vol. 46, 2003, pp. 3789–3796.

[18] Mago, P. J. and Sherif, S. A., “Heat and Mass Transfer on a Cylinder Surface in Cross Flow Under Supersaturated Conditions,” *International Journal of Refrigeration*, Vol. 26, 2003, pp. 889–899.

[19] Na, B. and Webb, R. L., “Mass Transfer On and Within a Frost Layer,” *International Journal of Heat and Mass Transfer*, Vol. 47, 2004, pp. 899–911.

[20] Na, B. and Webb, R. L., “New Model for Frost Growth Rate,” *International Journal of Heat and Mass Transfer*, Vol. 47, 2004, pp. 925–936.

[21] Yang, D. K. and Lee, K. S., “Modeling of Frosting Behavior on a Cold Plate,” *International Journal of Refrigeration*, Vol. 28, 2005, pp. 396–402.

[22] Qu, K., Komori, S., and Jiang, Y., “Local Variation of Frost Layer Thickness and Morphology,” *International Journal of Thermal Sciences*, Vol. 45, 2006, pp. 116–123.

[23] Hermes, C. J. L., Piucco, R. O., Jr., J. R. B., and Melo, C., “A Study of Frost Growth and Densification on Flat Surfaces,” *Experimental Thermal and Fluid Science*, Vol. 33, 2009, pp. 371–379.

[24] Dyer, J. M., Jacobi, A. M., Storey, B. D., Georgiadis, J. G., and Hoke, J. L., “An Experimental Investigation of the Effect of Hydrophobicity on the Rate of Frost Growth in Laminar Channel Flows,” *ASHRAE Transactions*, Vol. 106, No. 1, 2000, pp. 143–151.

[25] Shin, J., Tikhonov, A. V., and Kim, C., "Experimental Study on Frost Structure on Surfaces with Different Hydrophobicity: Density and Thermal Conductivity," *ASME Journal of Heat Transfer*, Vol. 125, 2003, pp. 84–94.

[26] Georgiadis, J. G. and Hoke, J. L., "Quantitative Visualization of Early Frost Growth via Scanning Confocal Microscopy," *Brazilian Congress of Thermal Engineering and Science*, Rio de Janeiro, Brazil, November 30-December 4, 2004.

[27] Bryant, J. A., *Effects of Hydrophobic Surface Treatments on Dropwise Condensation and Freezing of Water*, Ph.D. thesis, Texas A&M University, College Station, Texas, 1995.

[28] Hoke, J. L., *The Interaction Between the Substrate and Frost Layer Through Condensate Distribution*, Ph.D. thesis, University of Illinois at Urbana-Champaign, Urbana, Illinois, 2001.

[29] Hoke, J. L., Georgiadis, J. G., and Jacobi, A. M., "Effect of Substrate Wetability on Frost Properties," *AIAA Journal of Thermophysics and Heat Transfer*, Vol. 18, No. 2, 2004, pp. 228–235.

[30] Carey, V. P., *Liquid-Vapor Phase Change Phenomena*, Hemisphere, New York, 1992.

[31] Lock, G. H. S., *The Growth and Decay of Ice*, Cambridge University Press, New York, 1990.

[32] Lock, G. H. S., *Latent Heat Transfer*, Oxford University Press, Oxford, England, 1996.

[33] Stefan, J., "Üeber die Theorie der Eisbildung, Inbesondere über die Eisbildung im Polarmeere," *Annalen der Physik*, Vol. 42, 1891, pp. 269–286.

[34] de Gennes, P.-G., Brochard-Wyart, F., and Quéré, D., *Capillarity and Wetting Phenomena - Drops, Bubbles, Pearls, and Waves*, Springer, New York, 2003.

[35] Wenzel, R. N., "Surface Roughness and Contact Angle," *Industrial and Engineering Chemistry*, Vol. 28, 1936, pp. 988–994.

[36] Cassie, A. B. and Baxter, S., "Wettability of Porous Surfaces," *Transactions of the Faraday Society*, Vol. 76, 1944, pp. 546–551.

[37] Pruppacher, H. R., "A New Look at Homogeneous Ice Nucleation in Supercooled Water Droplets," *Journal of the Atmospheric Sciences*, Vol. 11, 1995, pp. 1924–1933.

[38] Na, B. and Webb, R. L., "A Fundamental Understanding of Factors Affecting Frost Nucleation," *International Journal of Heat and Mass Transfer*, Vol. 46, 2003, pp. 3797–3808.

[39] Gong, Y., *An Investigation on Heat Transfer During the Freezing of Condensate Droplets*, Ph.D. thesis, Texas A&M University, College Station, Texas, 1996.

[40] Horibe, A., Fukusako, M., Yamada, M., Tago, M., and Okagaki, O., "Freezing Characteristics of an Aqueous Solution Droplet Installed on a Wall," *The 6th International Symposium on Transport Phenomena in Thermal Engineering*, Seoul, South Korea, May 9-13, 1993, pp. 326–331.

[41] Wang, J., Liu, Z., Gou, Y., and Zhang, X., "Deformation of Freezing Water Droplets on a Cold Copper Surface," *Science in China Series E: Technological Sciences*, Vol. 49, 2006, pp. 590–600.

[42] Tao, Y. X., Besant, R. W., and Mao, Y., "Characteristics of Frost Growth on a Flat Plate During the Early Growth Period," *ASHRAE Transactions*, Vol. 99, No. 1, 1993, pp. 746–753.

[43] Seki, N., Fukusako, S., Matsuo, K., and Uemura, S., "An Analysis of Incipient Frost Formation," *Wärme- und Stoffübertragung*, Vol. 19, 1985, pp. 9–18.

[44] Olsen, W. A. and Hilding, W. E., "Three-Phase Heat Transfer: Transient Condensing and Freezing from a Pure Vapor onto a Cold Horizontal Plate - Analysis and Experiment," *International Journal of Heat and Mass Transfer*, Vol. 15, 1972, pp. 1887–1903.

[45] Na, B., *Analysis of Frost Formation in an Evaporator*, Ph.D. thesis, The Pennsylvania State University, University Park, Pennsylvania, 2003.

[46] Fletcher, N. H., *The Chemical Physics of Ice*, Cambridge University Press, New York, 1970.

[47] Hayashi, Y., Aoki, A., Adachi, S., and Horl, K., "Study of Frost Properties Correlating with Frost Formation Types," *ASME Journal of Heat Transfer*, Vol. 99, 1977, pp. 239–245.

[48] Tao, Y. X. and Besant, R. W., "Frost Growth on a Flat Plate Subject to a Developed Laminar Flow," *92-WA/HT-8 Presented at the Winter Annual Meeting of the AMSE*, Anaheim, California, November 8-13, 1992.

[49] Lee, H., Shin, J., Ha, S., Choi, B., and Lee, J., "Frost Formation on a Plate with Different Surface Hydrophobicity," *International Journal of Heat and Mass Transfer*, Vol. 47, 2004, pp. 4881–4893.

[50] Song, Y., Xu, D., Lin, J., and Tsian, S., "A Study on the Mechanism of Dropwise Condensation," *International Journal of Heat and Mass Transfer*, Vol. 34, 1991, pp. 2827–2831.

[51] Marto, P. J., Looney, D. J., Rose, J. W., and Wanniarachchi, A. S., "Evaluation of Organic Coatings for the Promotion of Dropwise Condensation of Steam," *International Journal of Heat and Mass Transfer*, Vol. 98, No. 2, 1986, pp. 1–14.

[52] Hannemann, R. J. and Mikic, B. B., "An Experimental Investigation into the Effect of Surface Thermal Conductivity on the Rate of Heat Transfer in Dropwise Condensation," *International Journal of Heat and Mass Transfer*, Vol. 19, No. 11, 1976, pp. 1309–1317.

[53] Tsuruta, T., Tananka, H., and Togashi, S., "A Theoretical Study on the Constriction Resistance in Dropwise Condensation," *International Journal of Heat and Mass Transfer*, Vol. 34, 1991, pp. 2779–2786.

[54] Umur, A. and Griffith, P., "Mechanism of Dropwise Condensation," *ASME Journal of Heat Transfer*, Vol. 87, 1965, pp. 275–282.

[55] Welch, J. F. and Westwater, J. W., "Microscopic Study of Dropwise Condensation," *Proceedings of the 1961-1962 International Heat Transfer Conference*, ASME, Part II, 1961, pp. 302–309.

[56] Lynch, D. K., Sassen, K., Starr, D. O., and Stephens, G., *Cirrus*, Oxford University Press, New York, 2002.

[57] Gokhale, N. R. and Goold, J., "Droplet Freezing by Surface Nucleation," *Journal of Applied Meteorology*, Vol. 7, No. 5, 1968, pp. 870–874.

[58] Fukata, N., "A Study of the Mechanism of Contact Ice Nucleation," *Journal of the Atmospheric Sciences*, Vol. 32, No. 8, 1975, pp. 1597–1603.

[59] Shaw, R. A., Durant, A. J., and Mi, Y., "Heterogeneous Surface Crystallization Observed in Undercooled Water," *Journal of Physical Chemistry*, Vol. 109, 1993, pp. 9865–9868.

[60] Durant, A. J. and Shaw, R. A., "Evaporation Freezing by Contact Nucleation Inside-Out," *Geophysical Research Letters*, Vol. 32, 2005.

[61] Chushak, Y. and Bartell, L. S., "Crystal Nucleation and Growth in Large Clusters of SeF_6," *Journal of Physical Chemistry A*, Vol. 104, 2000, pp. 9328–9336.

[62] Vrbka, L. and Jungwirth, P., "Homogeneous Freezing of Water Starts in the Subsurface," *Journal of Physical Chemistry B*, Vol. 110, 2006, pp. 18126–18129.

[63] Feuillebois, F., Lasek, A., Creismeas, P., Pigeonneau, F., and Szaniawski, A., "Freezing of a Subcooled Liquid Droplet," *Journal of Colloid and Interface Science*, Vol. 169, 1995, pp. 90–102.

[64] Tabakova, S. and Fueillebois, F., "On the Solidification of a Supercooled Liquid Droplet Lying on a Surface," *Journal of Colloid and Interface Science*, Vol. 272, 2004, pp. 225–234.

[65] Zhong, Y., *Condensation and Freezing Front Propagation on Surfaces with Topographic and Chemical Modifications*, Ph.D. thesis, University of Illinois at Urbana-Champaign, Urbana, Illinois, 2008.

[66] *CRC Handbook of Chemistry and Physics*, edited by D. R. Lide, chap. 6, Taylor and Francis, Boca Raton, Florida, 89th ed., 1995.

[67] Sinha, N., *Design, Fabrication, Packaging, and Testing of Thin Film Thermocouples for Boiling Studies*, M.S. thesis, Texas A&M University, College Station, Texas, 2006.

[68] Lau, K. K. S., Bico, J., Teo, K. B. K., Chhowalla, M., Amaratunga, G. A. J., Milne, W. I., McKinley, G. H., and Gleason, K. K., "Superhydrophbobic Carbon Nanotube Forests," *Nano Letters*, Vol. 3, No. 12, 2003, pp. 1701–1705.

[69] Incropera, F. P. and DeWitt, D. P., *Fundamentals of Heat and Mass Transfer*, John Wiley & Sons, Hoboken, New Jersey, 5th ed., 2002, pp. 385–438.

[70] Hecht, E., *Optics*, Addison Wesley, San Francisco, California, 4th ed., 2002.

[71] Gonzalez, R. C., Woods, R. E., and Eddins, S. L., *Digital Image Processing Using MATLAB*, Pearson Prentice Hall, Upper Saddle River, New Jersey, 2004.

[72] Miller, I. and Freund, J. E., *Probability and Statistics for Engineers*, Prentice-Hall, Englewood Cliffs, New Jersey, 1985.

[73] Lancaster, P. and Šalkauskas, K., *Curve and Surface Fitting: An Introduction*, Academic Press, London, England, 1986.

[74] Larson, R. E. and Edwards, B. H., *Elementary Linear Algebra*, D. C. Heath and Company, Lexington, Massachusetts, 2nd ed., 1991.

[75] Landau, L. D. and Lifshitz, E. M., *The Classical Theory of Fields*, Elsevier Butterworth-Heinemann, Oxford, England, 4th ed., 1975.

[76] Arfken, G. B. and Weber, H. J., *Mathematical Methods for Physicists*, Elsevier Academic Press, Burlington, Massachusetts, 6th ed., 2005.

[77] Bleecker, D. and Csordas, G., *Basic Partial Differential Equations*, International Press, Somerville, Massachusetts, 2003.

[78] Sethian, J. A., *Level Set Methods and Fast Marching Methods*, Cambridge University Press, New York, 1999.

[79] Osher, S. and Fedkiw, R., *Level Set Methods and Dynamic Implicit Surfaces*, Springer-Verlag, New York, 2000.

[80] Kurz, W. and Fisher, D. J., *Fundamentals of Solidificaiton*, Trans Tech Publications, Zürich, Switzerland, 1998.

[81] Fornea, A. P., Brooks, S. D., Dooley, J. B., and Saha, A., "Heterogeneous Freezing of Ice on Atmospheric Aerosols Containing Ash, Soot, and Soil," *Journal of Geophysical Research - Atmospheres*, Vol. 114, 2009.

[82] Wood, S. E., Baker, M. B., and Calhoun, D., "New Model for the Vapor Growth of Hexagonal Ice Crystals in the Atmosphere," *Journal of Geophysical Research*, Vol. 106, No. D5, 2001, pp. 4845–4870.

[83] Libbrecht, K. G., "Growth Rates of the Principal Facets of Ice Between $-10°$C and $-40°$C," *Journal of Crystal Growth*, Vol. 247, 2003, pp. 530–540.

[84] Libbrecht, K. G., "The Physics of Snow Crystals," *Reports on Progress in Physics*, Vol. 68, No. 4, 2005, pp. 855–895.

[85] Moran, M. J. and Shaprio, H. N., *Fundamentals of Engineering Thermodynamics*, John Wiley & Sons, New York, 4th ed., 2000.

[86] Baierlein, R., *Thermal Physics*, Cambridge University Press, New York, 1999.

[87] Seinfeld, J. H. and Pandis, S. N., *Atmospheric Chemistry and Physics*, John Wiley & Sons, New York, 1998.

[88] Saito, Y., *Statistical Physics of Crystal Growth*, World Scientific, River Edge, New Jersey, 1996.

[89] Petrenko, V. F. and Whitworth, R. W., *Physics of Ice*, Oxford University Press, New York, 1999.

[90] Hallett, J., "The Temperature Dependence of the Viscosity of Supercooled Water," *Proceedings of the Physical Society*, Vol. 82, 1963, pp. 1046–1050.

[91] Broughton, J. Q., Gilmer, G. H., and Jackson, K. A., "Crystallization Rates of a Lennard-Jones Liquid," *Physical Review Letters*, Vol. 49, 1983, pp. 1496–1500.

[92] Burton, W. K., Cabrera, N., and Frank, F. C., "The Growth of Crystals and the Equilibrium Structure of Their Surfaces," *Philosophical Transactions of the Royal Society of London - Series A*, Vol. 243, 1951, pp. 299–358.

[93] Landau, L. D. and Lifshitz, E. M., *Statistical Physics*, Elsevier Butterworth-Heinemann, Oxford, England, 1951.

[94] Schlichting, H. and Gersten, K., *Boundary-Layer Theory*, Springer-Verlag, Berlin, Germany, 2000.

[95] Acarlar, M. S. and Smith, C. R., "A Study of Hairpin Vortices in a Laminar Boundary Layer. Part 1. Hairpin Vortices Generated by a Hemisphere Protuberance," *Journal of Fluid Mechanics*, Vol. 175, 1987, pp. 1–41.

[96] Sugiyama, K. and Sbragaglia, M., "Linear Shear Flow Past a Hemispherical Droplet Adhereing to a Solid Surface," *Journal of Engineering Mathematics*, Vol. 62, 2008, pp. 35–50.

[97] Abernethy, R. B., Benedict, R. P., and Dowdell, R. B., "ASME Measurement Uncertainty," *Journal of Fluids Engineering*, Vol. 107, 1985, pp. 161–164.

[98] Kline, S. J., "The Purposes of Uncertainty Analysis," *Journal of Fluids Engineering*, Vol. 107, 1985, pp. 153–160.

[99] Coleman, H. W. and W. Glenn Steele, J., *Experimentation and Uncertainty Analysis for Engineers*, John Wiley & Sons, New York, 1989.

[100] Kline, S. J. and McClintock, F. A., "Describing Uncertainties in Single-Sample Experiments," *Mechanical Engineering*, Vol. 75, 1953, pp. 3–9.

[101] Moffat, R. J., "Using Uncertainty Analysis in the Planning of an Experiment," *Journal of Fluids Engineering*, Vol. 107, 1985, pp. 173–178.

APPENDIX A

ANALYSIS OF UNCERTAINTY

The overall uncertainties associated with the data presented in this study were reported in terms of error bars affixed to the dependent variables. The methodology used to determine these uncertainty intervals is outlined in this appendix.

Assessment of Systematic and Random Components of Overall Uncertainty

The overall limits of uncertainty $\mathcal{U}_Y$ associated with a measured variable Y can be ascribed to two primary components [97]:

1. a bias limit, $\mathcal{U}_b$, resulting from systematic errors that remain constant from one measurement of the variable to the next (e.g. calibration, offset, or anticipated drift errors)
2. a precision limit, $\mathcal{U}_p$, resulting from random errors associated with repeated measurements of the variable

In these definitions, use of the term *error* implies that the true value of the variable in question is precisely known; in practice, however, this is never the case, so the operative term *limit* is applied to these components to denote that the true and measured values are expected to fall within some interval of confidence. The size of this interval can vary, but the most commonly accepted value for experiments in the engineering sciences is based on 20:1 odds, or a 95% confidence level [98]. This implies that for a fixed set of conditions, 19 out of every 20 measurements of Y are expected to fall within the bounds defined by $\pm\mathcal{U}_Y$

For a set of N independent measurements of Y, the precision limit $\mathcal{U}_p$ can be defined from the statistics of the sample set taken from an assumed Gaussian parent population as

$$\mathcal{U}_p = \pm\, t\bar{S}_{\bar{R}} \tag{A.1}$$

where t is a value from the t-distribution that yields a particular confidence level and $\bar{S}_{\bar{Y}}$ is the sample standard error defined by

$$\bar{S}_{\bar{Y}} = \frac{S_{\bar{Y}}}{\sqrt{N}} \tag{A.2}$$

In Equation A.2, $S_{\bar{Y}}$ is the sample standard deviation given by

$$S_{\bar{Y}} = \left[\frac{1}{N-1}\sum_{i=1}^{N}\left(Y_i - \bar{Y}\right)^2\right]^{1/2} \tag{A.3}$$

where Y_i and $\bar{Y}$ are the individual and mean values of the sample set, respectively. The value of t used in Equation A.1 is a function of the degrees of freedom used in calculating $S_{\bar{Y}}$; for large samples ($N > 30$), a constant value of $t = 1.96$ corresponds to a 95% confidence level [72].

Unlike the precision limit, the bias limit $\mathcal{U}_b$ does not necessarily have a comparable statistical basis and must often be estimated from other sources with some degree of judgment. A reasonable estimate for $\mathcal{U}_b$ might stem from the calibrated repeatability or reported accuracy of a particular instrument with respect to a traceable standard. In such cases, the determined or assumed bias limit may be based on the statistical precision associated with repeated trial measurements taken with respect to some reference value and therefore subject to its own confidence interval.

With the bias and precision limits defined, the question remains of how to combine the two into an overall measure of uncertainty. Two accepted methods include one of straight addition,

$$\mathcal{U}_{Y,ADD} = \mathcal{U}_b + \mathcal{U}_p \tag{A.4}$$

and another based on the root-sum-square (RSS) of the component uncertainties,

$$\mathcal{U}_{Y,RSS} = \left(\mathcal{U}_b^2 + \mathcal{U}_p^2\right)^{1/2} \tag{A.5}$$

If $\mathcal{U}_b$ and $\mathcal{U}_p$ are both based on 95% confidence levels, then Equation A.4 represents a 95% to 99% confidence interval for the measured variable Y, depending on the relative magnitudes of the components[1] [99]. On the other hand, Equation A.5 provides an overall confidence interval of 95% for all cases. In this investigation, the RSS method given by Equation A.5 was used exclusively to quantify the uncertainty of all variables.

Statistical samples of repeated measurements may not be practical or even possible to obtain, particularly for single-sample experiments; therefore the true precision limits (Equation A.1) for such measurements are not generally known. The overall uncertainty intervals for such variables are often determined from an estimate of the bias limit which may include some form of a precision index. For example, the uncalibrated accuracy of a certain type of temperature probe may be reported by its manufacturer to be, based on a presumed 95% confidence level, ± 0.5°C within some specified temperature range. In this case, the overall uncertainty of the temperature measurement, including the bias and precision limits, would simply be taken to be $\mathcal{U}_{probe} = \pm 0.5$°C. If the end user calibrates the temperature probe with a known standard of much higher accuracy and precision than the probe itself (thereby reducing the bias limit) and subsequently compiles a number of calibrated sensitivity measure-

---

[1] If $\mathcal{O}(\mathcal{U}_b) \approx \mathcal{O}(\mathcal{U}_p)$, then $\mathcal{U}_{Y,ADD}$ represents a confidence interval about Y that approaches 99%. However, if one component is negligible compared to the other, then the overall confidence level approaches that of the non-negligible component, which would be 95% in this case.

ments at a fixed value of that standard (thereby quantifying the calibrated precision limit), then the overall uncertainty of the temperature measurement may be able to be reduced considerably.

Propagation of Uncertainty into Dependent Variables

The uncertainty interval for a calculated variable R that is a function of n independent variables, $R = f(x_1, x_2, \ldots, x_n)$, can be expressed as [100]

$$\mathcal{U}_R = \left[\left(\frac{\partial R}{\partial x_1} \mathcal{U}_{x_1} \right)^2 + \left(\frac{\partial R}{\partial x_2} \mathcal{U}_{x_2} \right)^2 + \cdots + \left(\frac{\partial R}{\partial x_n} \mathcal{U}_{x_n} \right)^2 \right]^{1/2} \tag{A.6}$$

where $\mathcal{U}_{x_1}, \mathcal{U}_{x_2}, \ldots, \mathcal{U}_{x_n}$ are the uncertainty intervals associated with each independent variable x_n. If the relationship for R can be expressed as a continuous product of the form

$$R = x_1^a x_2^b \cdots x_n^n \tag{A.7}$$

then Equation A.6 can be used to define an closed-form expression for the uncertainty interval, namely

$$\mathcal{U}_R = R \left[\left(a \frac{\mathcal{U}_{x_1}}{x_1} \right)^2 + \left(b \frac{\mathcal{U}_{x_2}}{x_2} \right)^2 + \cdots + \left(n \frac{\mathcal{U}_{x_n}}{x_n} \right)^2 \right]^{1/2} \tag{A.8}$$

or in relative terms as

$$\frac{\mathcal{U}_R}{R} = \left[\left(a \frac{\mathcal{U}_{x_1}}{x_1} \right)^2 + \left(b \frac{\mathcal{U}_{x_2}}{x_2} \right)^2 + \cdots + \left(n \frac{\mathcal{U}_{x_n}}{x_n} \right)^2 \right]^{1/2} \tag{A.9}$$

Although Equation A.6 is conceptually straightforward, evaluating the partial derivatives can become unwieldy for cases in which R happens to be a complicated function of many independent variables. This difficulty can be circumvented in practice by recognizing that with the definition of the derivative operator,

$$\frac{\partial R}{\partial x_i} = \lim_{\Delta x_i \to 0} \frac{R(x_i + \Delta x_i) - R(x_i)}{\Delta x_i} \tag{A.10}$$

the exact derivative can be approximated with a finite perturbation δx_i of the independent variable x_i by

$$\frac{\partial R}{\partial x_i} \approx \frac{R(x_i + \delta x_i) - R(x_i)}{\delta x_i} \tag{A.11}$$

If it is assumed that $\delta x_i \approx \mathcal{U}_{x_i}$, then Equation A.11 can be expressed as [101]

$$\frac{\partial R}{\partial x_i}\mathcal{U}_{x_i} \approx R(x_i + \mathcal{U}_{x_i}) - R(x_i) \tag{A.12}$$

Equation A.12 has the same form as each squared term on the right hand side of Equation A.6. Therefore, $\mathcal{U}_R$ may be approximated by sequentially perturbing each independent variable x_i by its uncertainty $\mathcal{U}_{x_i}$ and computing the root-sum-square of the resulting contributions:

$$\mathcal{U}_R = \left[\mathcal{U}_{R,x_1}^2 + \mathcal{U}_{R,x_2}^2 + \cdots + \mathcal{U}_{R,x_n}^2\right]^{1/2} \tag{A.13}$$

where $\mathcal{U}_{R,x_1}, \mathcal{U}_{R,x_2}, \ldots, \mathcal{U}_{R,x_n}$ are appropriately referred to as the sensitivity components of R, given by

$$\begin{aligned}
\mathcal{U}_{R,x_1} &= R(x_1 + \mathcal{U}_{x_1}, x_2, \ldots, x_n) - R(x_1, x_2, \ldots, x_n) \\
\mathcal{U}_{R,x_2} &= R(x_1, x_2 + \mathcal{U}_{x_2}, \ldots, x_n) - R(x_1, x_2, \ldots, x_n) \\
&\vdots \\
\mathcal{U}_{R,x_n} &= R(x_1, x_2, \ldots, x_n + \mathcal{U}_{x_n}) - R(x_1, x_2, \ldots, x_n)
\end{aligned} \tag{A.14}$$

Example Calculations

The following sections present representative examples of how the overall uncertainty intervals were determined for the dependent variables in this investigation. For congruity, these calculations correspond directly to the example cases previously discussed throughout Chapter IV.

Average Inter-Droplet Freezing Velocity Magnitude, $\bar{v}_{k,\bar{D}}$

The overall uncertainty of $\bar{v}_{k,\bar{D}}$ was assumed to consist of two primary components: random ($\mathcal{U}_{p,\bar{v}_{k,\bar{D}}}$) and systematic ($\mathcal{U}_{b,\bar{v}_{k,\bar{D}}}$) uncertainty. Although the full spectrum of inter-droplet freezing velocities calculated for all test conditions and surfaces were found to follow log-normal distributions (Figure 4.12), it was shown that the average inter-droplet freezing velocity $\bar{v}_{k,\bar{D}}$ could be calculated as a weighted mean over a range limited to the most dominant velocities (Equations 4.31 and 4.32). Within this range, the velocity distribution was assumed to be Gaussian[2]; therefore, for the example case presented in Figure 4.12, the random component of uncertainty associated with $\bar{v}_{k,\bar{D}}$ was previously shown to be $\mathcal{U}_{p,\bar{v}_{k,\bar{D}}} = \pm\, 0.25\ \mu\text{m/s}$.

The fundamental relationship used to calculate the discrete value of the inter-droplet freezing velocity was given by Equations 4.28 and 4.29, presented here in simplified form as

$$\hat{v}_{k,\bar{D}} = \frac{\Delta\bar{r}}{\Delta\bar{t}} \tag{A.15}$$

where $\Delta\bar{r} = \bar{r} - \bar{D}$ is the average inter-droplet spacing for the region of interest (Figure 4.10) based on the average center-to-center droplet spacing $\bar{r}$ and the average droplet diameter $\bar{D}$. The systematic component of uncertainty for $\bar{v}_{k,\bar{D}}$ was evaluated

---

[2] The effects of non-Gaussian sample distributions on the evaluation of precision limits are generally negligible expect for cases in which the tails of the distributions are important [99, 100].

by applying Equation A.8 to Equation A.15, resulting in

$$\mathcal{U}_{b,\bar{v}_{k,\bar{D}}} = \bar{v}_{k,\bar{D}} \left[\left(\frac{\mathcal{U}_{\Delta\bar{r}}}{\Delta\bar{r}} \right)^2 + \left(-\frac{\mathcal{U}_{\Delta\hat{t}}}{\Delta\hat{t}} \right)^2 \right]^{1/2} \tag{A.16}$$

For the example case shown in Figure 4.12,

$$\begin{aligned} \bar{v}_{k,\bar{D}} &= 2.03\,\mu\text{m/s} \\ \Delta\bar{r} &= 64.4\,\mu\text{m} \\ \Delta\hat{t} &= 0.05\,\text{s} \\ \mathcal{U}_{\Delta\bar{r}} &= 4.91\,\mu\text{m} \\ \mathcal{U}_{\Delta\hat{t}} &= 0.005\,\text{s} \end{aligned}$$

where the value of $\mathcal{U}_{\Delta\bar{r}}$ accounted for the optical resolving power of the digital microscopy system as well as the bias and precision limits associated with the mean values of $\bar{r} = 130.3$ μm and $\bar{D} = 65.9$ μm. The values of $\Delta\hat{t}$ and $\mathcal{U}_{\Delta\hat{t}}$ were based on the computational time steps used in the data reduction algorithm and the image acquisition speed, respectively. Using these values in Equation A.16 yielded $\mathcal{U}_{b,\bar{v}_{k,\bar{D}}} = 0.12\,\mu$m/s. With $\mathcal{U}_{b,\bar{v}_{k,\bar{D}}}$ and $\mathcal{U}_{p,\bar{v}_{k,\bar{D}}}$ known, the overall uncertainty for $\bar{v}_{k,\bar{D}}$ was determined to be

$$\mathcal{U}_{\bar{v}_{k,\bar{D}}} = \left[\left(\mathcal{U}_{b,\bar{v}_{k,\bar{D}}} \right)^2 + \left(\mathcal{U}_{p,\bar{v}_{k,\bar{D}}} \right)^2 \right]^{1/2} = \left[(0.12)^2 + (0.25)^2 \right]^{1/2} = \pm\,0.27\,\mu\text{m/s} \tag{A.17}$$

or in relative terms,

$$\frac{\mathcal{U}_{\bar{v}_{k,\bar{D}}}}{\bar{v}_{k,\bar{D}}} = \pm\,0.137\ (13.7\%) \tag{A.18}$$

The relative uncertainty given by Equation A.18 varied from approximately 7 to 15% for all inter-droplet freezing velocity data compiled in this study. In general, the lower the surface temperature for an experiment, the lower the corresponding uncertainty value. This occurred because for given surface and set of environmental conditions, lower surface temperatures typically produced larger numbers of droplets within the region of interest before freezing occurred.

Average Aggregate Freezing Velocity Magnitude, $\bar{V}_n$

As in the previous example calculation, the overall uncertainty associated with $\bar{V}_n$ was assumed to be a combination of systematic ($\mathcal{U}_{b,\bar{V}_n}$) and random ($\mathcal{U}_{p,\bar{V}_n}$) uncertainties. The value of $\bar{V}_n$ determined for each experiment was evaluated as the area weighted average (Equation 4.51) of the local freezing velocity magnitude $|\mathbf{V}_N|$ computed on a 50×50 grid (Figure 4.18); thus, the correspondingly large sample of local velocities could be used to evaluate $\mathcal{U}_{p,\bar{V}_n}$. For the example case presented in Figure 4.18, the sample standard deviation was determined to be $S_{\bar{V}_n} = 12.81$ μm/s. With $N = 2500$, this equated to a sample standard error of $\bar{S}_{\bar{V}_n} = 0.26$ μm/s for which Equation A.1 gave the random component of uncertainty to be $\mathcal{U}_{p,\bar{V}_n} = \pm\, 0.50$ μm/s.

An estimate for $\mathcal{U}_{b,\bar{V}_n}$ was obtained by evaluating the propagation of uncertainty through the eikonal equation used to compute the magnitudes of the local freezing velocity vectors (Equation 4.49), rewritten here as

$$|\mathbf{V}_N| = \frac{1}{|\nabla t|} \tag{A.19}$$

The systematic uncertainty associated with the local freezing velocity $|\mathbf{V}_N|$ was assumed to be constant for a given experiment and therefore representative of the systematic uncertainty associated with the aggregate velocity $\bar{V}_n$. Applying Equation A.8 to Equation A.19 yields

$$\mathcal{U}_{b,\bar{V}_n} = \bar{V}_n \left[\left(-\frac{\mathcal{U}_{|\nabla t|}}{|\nabla t|} \right)^2 \right] = \bar{V}_n \left(\frac{\mathcal{U}_{|\nabla t|}}{|\nabla t|} \right) \tag{A.20}$$

In order to determine $\mathcal{U}_{b,\bar{V}_n}$, the uncertainty associated with $|\nabla t|$ needed to be evaluated. The magnitude of the gradient of t was defined by

$$|\nabla t| = \left[\left(\frac{\partial t}{\partial x}\right)^2 + \left(\frac{\partial t}{\partial y}\right)^2\right]^{1/2} \tag{A.21}$$

which may be equivalently expressed in discrete form as

$$|\nabla t| = \left[\left(\frac{\Delta t}{\Delta x}\right)^2 + \left(\frac{\Delta t}{\Delta y}\right)^2\right]^{1/2} \tag{A.22}$$

Equation A.8 could not be applied to Equations A.21 or A.22 because of their non-product form. The uncertainty interval for $|\nabla t|$ could have been evaluated with the general analytical form given by Equation A.6, but evaluating the partial derivatives would have been complicated and prone to error due to the common variable ∂t or Δt embedded in the root of the summed square. Therefore, the perturbation technique defined by Equation A.13 was used to determine $\mathcal{U}_{|\nabla t|}$. Using Equation A.22 as the basis, the sensitivity components defined by Equation A.14 were cast as

$$\begin{aligned}
\mathcal{U}_{|\nabla t|,\Delta x} &= \left[\left(\frac{\Delta t}{\Delta x - \mathcal{U}_{\Delta x}}\right)^2 + \left(\frac{\Delta t}{\Delta y}\right)^2\right]^{1/2} - |\nabla t| \\[2ex]
\mathcal{U}_{|\nabla t|,\Delta y} &= \left[\left(\frac{\Delta t}{\Delta x}\right)^2 + \left(\frac{\Delta t}{\Delta y - \mathcal{U}_{\Delta y}}\right)^2\right]^{1/2} - |\nabla t| \qquad \text{(A.23)} \\[2ex]
\mathcal{U}_{|\nabla t|,\Delta t} &= \left[\left(\frac{\Delta t - \mathcal{U}_{\Delta t}}{\Delta x}\right)^2 + \left(\frac{\Delta t - \mathcal{U}_{\Delta t}}{\Delta y}\right)^2\right]^{1/2} - |\nabla t|
\end{aligned}$$

where $|\nabla t|$ was a nominal value given by Equation A.22. For the example case shown in Figure 4.18,

$$\begin{aligned}\bar{V}_n &= 41.7\,\mu\text{m/s}\\ \Delta x &= 60.9\,\mu\text{m}\\ \Delta y &= 51.4\,\mu\text{m}\\ \Delta t &= 0.94\,\text{s}\\ \mathcal{U}_{\Delta x} = \mathcal{U}_{\Delta y} &= 3.36\,\mu\text{m}\\ \mathcal{U}_{\Delta t} &= 0.025\,\text{s}\end{aligned}$$

The values of Δx, Δy, and Δt represented the unit size of the computational grid used to numerically compute ∇t while $\mathcal{U}_{\Delta x}$, $\mathcal{U}_{\Delta y}$, and $\mathcal{U}_{\Delta t}$ accounted for the spatial and temporal resolution of the discrete experimental data points superimposed onto that grid (Figures 4.13 and 4.14). With the exception of Δt, all of these parameters were fixed for all experiments. The value of Δt used in Equations A.22 and A.23 varied from one experiment to the next based on the speed of the detected aggregate freezing front and was calculated as

$$\Delta t = \frac{1}{\bar{V}_n}\left[\frac{1}{(\Delta x)^{-2} + (\Delta y)^{-2}}\right]^{1/2} \tag{A.24}$$

With the values listed above, Equation A.23 yielded the following values for the sensitivity components:

$$\begin{aligned}\mathcal{U}_{|\nabla t|,\Delta x} &= -5.14 \times 10^{-4}\ \text{s}/\mu\text{m}\\ \mathcal{U}_{|\nabla t|,\Delta y} &= -8.49 \times 10^{-4}\ \text{s}/\mu\text{m}\\ \mathcal{U}_{|\nabla t|,\Delta t} &= 6.36 \times 10^{-4}\ \text{s}/\mu\text{m}\end{aligned} \tag{A.25}$$

From Equation A.13, $\mathcal{U}_{|\nabla t|}$ was determined to be

$$\begin{aligned} \mathcal{U}_{|\nabla t|} &= \left[\left(\mathcal{U}_{|\nabla t|,\Delta x}\right)^2 + \left(\mathcal{U}_{|\nabla t|,\Delta y}\right)^2 + \left(\mathcal{U}_{|\nabla t|,\Delta t}\right)^2\right]^2 \\ &= \left[\left(-5.14 \times 10^{-4}\right)^2 + \left(-8.49 \times 10^{-4}\right)^2 + \left(6.36 \times 10^{-4}\right)^2\right]^{1/2} \\ &= 1.18 \times 10^{-3}\,\mathrm{s}/\mu\mathrm{m} \end{aligned} \tag{A.26}$$

Using this value in Equation A.20, the systematic component of uncertainty was determined to be $\mathcal{U}_{b,\bar{V}_n} = 2.04\,\mu\mathrm{m/s}$. With $\mathcal{U}_{b,\bar{V}_n}$ and $\mathcal{U}_{p,\bar{V}_n}$ known, the overall uncertainty associated with $\bar{V}_n$ was found to be

$$\mathcal{U}_{\bar{V}_n} = \left[\left(\mathcal{U}_{b,\bar{V}_n}\right)^2 + \left(\mathcal{U}_{p,\bar{V}_n}\right)^2\right]^{1/2} = \left[(2.04)^2 + (0.50)^2\right]^{1/2} = \pm\,2.10\,\mu\mathrm{m/s} \tag{A.27}$$

or in relative terms,

$$\frac{\mathcal{U}_{\bar{V}_n}}{\bar{V}_n} = \pm\,0.051\ (5.1\%) \tag{A.28}$$

The overall relative uncertainty for $\bar{V}_n$ varied from approximately 5 to 13% for all data acquired in this investigation. The uncertainty interval tended toward the lower values within this range for tests that exhibited smooth, semi-planar aggregate freezing fronts. Conversely, fronts with more complicated morphologies generally corresponded to uncertainty intervals in the higher end of this range.

Inter- and Intra-Droplet Crystal Growth Rates, $\bar{v}_c$ and $\bar{v}_{sl}$

Because $\bar{v}_c$ and $\bar{v}_{sl}$ were determined from direct optical measurements, the corresponding uncertainty intervals $\mathcal{U}_{\bar{v}_c}$ and $\mathcal{U}_{\bar{v}_{sl}}$ were assumed to consist of systematic components only. These velocities were computed as numerically-integrated averages of the instantaneous crystal tip velocity over a characteristic timespan $t_f - t_i$ (Equation 4.54), rewritten here in generic form as

$$\bar{v} = \frac{1}{t_f - t_i}\int_{t_i}^{t_f} v\;dt \tag{A.29}$$

where the instantaneous velocity v was computed for each discrete time step Δt corresponding to direct measurements of the crystal displacement Δr by the relationship

$$v = \frac{\Delta r}{\Delta t} \tag{A.30}$$

On a relative basis, the uncertainty associated with v and $\bar{v}$ was assumed to be the same; therefore, Equation A.8 was applied to Equation A.30 to yield the following expression for $\mathcal{U}_{\bar{v}}$:

$$\mathcal{U}_{\bar{v}} = \bar{v}\left[\left(\frac{\mathcal{U}_{\Delta r}}{\Delta r}\right)^2 + \left(-\frac{\mathcal{U}_{\Delta t}}{\Delta t}\right)^2\right]^{1/2} \tag{A.31}$$

For the example cases shown in Figures 4.23 and 4.25,

$$\begin{array}{rclrcl}
\bar{v}_c & = & 1.91\,\mu\text{m/s} & \bar{v}_{sl} & = & 3.00\times10^5\,\mu\text{m/s} \\
\Delta r_{\bar{v}_c} & = & 2.30\,\mu\text{m} & \Delta r_{\bar{v}_{sl}} & = & 476.3\,\mu\text{m} \\
\Delta t_{\bar{v}_c} & = & 1.20\,\text{s} & \Delta t_{\bar{v}_{sl}} & = & 0.0017\,\text{s} \\
\mathcal{U}_{\Delta r_{\bar{v}_c}} & = & 0.34\,\mu\text{m} & \mathcal{U}_{\Delta r_{\bar{v}_{sl}}} & = & 3.36\,\mu\text{m} \\
\mathcal{U}_{\Delta t_{\bar{v}_c}} & = & 0.005\,\text{s} & \mathcal{U}_{\Delta t_{\bar{v}_{sl}}} & = & 0.0002\,\text{s}
\end{array}$$

The values of Δr and Δt listed above corresponded to the average displacements and time steps used in the calculation of $\bar{v}_c$ and $\bar{v}_{sl}$. Likewise, $\mathcal{U}_{\Delta r}$ and $\mathcal{U}_{\Delta t}$ represented the respective spatial and temporal resolution of the digital microscopy system. Using these values in Equation A.31, the uncertainty intervals associated with the inter- and intra-droplet crystal growth rates were found to be

$$\mathcal{U}_{\bar{v}_c} = \pm\,0.28\,\mu\text{m/s} \tag{A.32}$$

$$\mathcal{U}_{\bar{v}_{sl}} = \pm\,3.53\times10^4\,\mu\text{m/s} \tag{A.33}$$

or in relative terms,

$$\frac{\mathcal{U}_{\bar{v}_c}}{\bar{v}_c} = \pm 0.148\,(14.8\%) \tag{A.34}$$

$$\frac{\mathcal{U}_{\bar{v}_{sl}}}{\bar{v}_{sl}} = \pm 0.118\,(11.8\%) \tag{A.35}$$

The overall relative uncertainties for $\bar{v}_c$ and $\bar{v}_{sl}$ for all experiments varied from approximately 7 to 15% and 9 to 16%, respectively.

Normalized Freezing Velocity Correlations

The propagation of uncertainty through the predictive methods developed from the normalized freezing velocity data presented in Figures 5.10, 5.12, and 5.14 were also considered. The modeling equations for the normalized aggregate, inter-, and intra-droplet freezing velocities were given by Equations 5.7, 5.10, and 5.12, respectively. These correlations have been rewritten here in explicit terms of the appropriate velocity as

$$\bar{V}_n|_{pred} = \frac{C_1 \alpha_s}{\ell_r} \left(\frac{1}{1 + e^{\frac{C_3 - \theta_w}{C_2}}} - \Theta_0 \right) = f\left(T_s, \omega_{air}, \theta_w, \alpha_s, \ell_r\right) \tag{A.36}$$

$$\bar{v}_{k,\bar{D}}|_{pred} = \frac{\alpha_s}{\ell_r} \left(C_4 + C_5 e^{-C_6 \theta_w} \right) = f\left(\omega_{air}, \theta_w, \alpha_s, \ell_r\right) \tag{A.37}$$

$$\bar{v}_{sl}|_{pred} = \frac{C_7 \alpha_s}{\ell_r} \left(\frac{1}{1 + e^{\frac{C_9 - \theta_w}{C_8}}} - \Theta_1 \right) = f\left(T_s, \theta_w, \alpha_s, \ell_r\right) \tag{A.38}$$

where α_s was the substrate thermal diffusivity, ℓ_r was a latent heat conduction length scale, θ_w was the corrected droplet contact angle, and Θ_0 and Θ_1 were offset parameters defined by Equations 5.8 and 5.13, respectively. The correlating parameters C_1 - C_9 were cast as functions of the absolute substrate temperature T_s and humidity ratio ω_{air}, depending on the correlation; they were defined by Equations 5.9, 5.11, and 5.14 along with Tables 5.2, 5.3, and 5.4.

To demonstrate a representative uncertainty interval for the predicted aggregate, inter- and intra-droplet freezing velocities, the following values of the independent variables along with conservative estimates of their respective uncertainties were used:

$$\begin{aligned} T_s &= 260\,\mathrm{K} & \mathcal{U}_{T_s} &= 0.5\,\mathrm{K} \\ \omega_{air} &= 4.0\,\mathrm{g/kg} & \mathcal{U}_{\omega air} &= 0.1\,\mathrm{g/kg} \\ \theta_w &= 60^\circ & \mathcal{U}_{\theta_w} &= 3^\circ \\ \alpha_s &= 8.92 \times 10^{-5}\,\tfrac{\mathrm{m}^2}{\mathrm{s}} & \mathcal{U}_{\alpha_s} &= 7.5 \times 10^{-6}\,\tfrac{\mathrm{m}^2}{\mathrm{s}} \\ \ell_r &= 1.90 \times 10^3\,\mu\mathrm{m} & \mathcal{U}_{\ell_r} &= 3.36\,\mu\mathrm{m} \end{aligned}$$

Using these values in Equations A.36 - A.38, the following values for $\bar{V}_n$, $\bar{v}_{k,\bar{D}}$, and $\bar{v}_{sl}$ were calculated:

$$\bar{V}_n|_{pred} = 46.2\,\mu\mathrm{m/s} \tag{A.39}$$

$$\bar{v}_{k,\bar{D}}|_{pred} = 1.74\,\mu\mathrm{m/s} \tag{A.40}$$

$$\bar{v}_{sl}|_{pred} = 1.26 \times 10^5\,\mu\mathrm{m/s} \tag{A.41}$$

Applying the sequential perturbation method given by Equations A.13 and A.14 to those same equations, the corresponding uncertainty intervals for the predicted freezing velocities were found to be

$$\mathcal{U}_{\bar{V}_n}|_{pred} = \pm\,5.13\,\mu\mathrm{m/s} \tag{A.42}$$

$$\mathcal{U}_{\bar{v}_{k,\bar{D}}}|_{pred} = \pm\,0.15\,\mu\mathrm{m/s} \tag{A.43}$$

$$\mathcal{U}_{\bar{v}_{sl}}|_{pred} = \pm\,1.73 \times 10^4\,\mu\mathrm{m/s} \tag{A.44}$$

In relative terms, these intervals corresponded to

$$\left.\frac{\mathcal{U}_{\bar{V}_n}}{\bar{V}_n}\right|_{pred} = \pm\,0.111\,(11.1\%) \tag{A.45}$$

$$\left.\frac{\mathcal{U}_{\bar{v}_{k,\bar{D}}}}{\bar{v}_{k,\bar{D}}}\right|_{pred} = \pm\,0.086\,(8.6\%) \tag{A.46}$$

$$\left.\frac{\mathcal{U}_{\bar{v}_{sl}}}{\bar{v}_{sl}}\right|_{pred} = \pm\,0.137\,(13.7\%) \tag{A.47}$$

VITA

Jeffrey Brandon Dooley was born on January 16, 1979 in Dallas, Texas. He was raised in the town of Lone Oak, Texas and graduated from Lone Oak High School in 1997. In 2002, he graduated with honors from Texas A&M University in College Station with a bachelor's degree in mechanical engineering. After graduation, Dooley worked as a field engineer for the Energy Systems Laboratory at the Texas Engineering Experiment Station (TEES). He began graduate studies at Texas A&M in 2003, earning a master's degree in mechanical engineering in 2004. In 2005, he began pursuing a doctorate in the same discipline. He joined the technical staff at Heat Transfer Research, Inc. (HTRI) in 2006, where he worked as a research engineer while completing his dissertation in tandem. He is currently employed at HTRI where he studies fundamental thermal-hydraulic phenomena pertinent to the design and analysis of heat exchangers.

Dooley has previously conducted research at Los Alamos National Laboratory and Sandia National Laboratories, both in New Mexico, and has taught classes in thermodynamics, fluid mechanics, heat transfer, and numerical methods. His research interests include heat exchanger technology, energy systems, microscale heat transfer, experimental and computational methods for single- and multi-phase thermal-fluid problems, and interfacial and phase-change phenomena in condensed matter physics. He is a member of the American Society of Mechanical Engineers (ASME), the American Society of Heating, Refrigeration, and Air-Conditioning Engineers (ASHRAE), and the American Physical Society (APS).

He can be reached via Dr. Dennis O'Neal in the mechanical engineering department at Texas A&M University, mail stop 3123, College Station, TX 77843.

The typist for this dissertation was J. Brandon Dooley.